THE KINEMATICS OF A FREE PITCHING FLEXIBLE CANTILEVER NACA 0012 WING AT TRANSITIONAL REYNOLDS NUMBERS

CINÉMATIQUE D'UNE AILE NACA 0012 EN PORTE-À-FAUX FLEXIBLE ET EN ROTATION LIBRE À DES NOMBRES DE REYNOLDS TRANSITOIRES

A Thesis Submitted to the Division of Graduate Studies
of the Royal Military College of Canada
by

Crystal Sharilene Itwar Barrett, B.Eng (Mechanical)

In Partial Fulfillment of the Requirements for the Degree of
Master of Applied Science in Mechanical Engineering

October, 2020

Acknowledgements

First and foremost, I'd like to thank my husband, Simon, to whom I owe everything: neither words nor actions could ever convey my love and gratitude. From the bottom of my heart, I'd like to thank my family for their years of love and support: Mom and Dad, who taught me the value of independence, hard work and persistence, and provided me with the opportunities to broaden my horizons. I owe much to Al for being such a worthy and inspiring role model. Finally, the love, laughs and positive words from Elena, Evan, Alex, Des and Sally made all the difference, both academically and personally. I am greatly indebted to and humbled by the patience, teaching, mentorship and guidance I have received from my supervisor, Dr. Dominique Poirel. I am also thankful for the skillful advice of Dr. Asad Asghar, Dr. David DuQuesnay, Dr. Azemi Benaissa, Dr. Diane Wowk, and M. Lavoie. Finally, I would like to say a heartfelt thanks to all the professors, graduate students and technicians at RMC who helped me along the way, and made my time here truly rewarding and joyous.

Abstract

A series of experiments were performed on a flexible cantilever NACA 0012 wing to study the complex physics which occur in the transitional Reynolds number region of $7.9 \times 10^4 < Re_c < 1.7 \times 10^5$. The wing is free to move in pitch, is flexible in bending and torsion, has 3D effects in the aerodynamics and the structures, and exhibits significant non-linearities. A steel beam is located inside in the wing. The beam provides the structural stiffness, and the wing outer shell provides the aerodynamic loading. The pitch stiffness is also provided via linear springs located at the root of the wing. The flexural centre and pitch axis are aligned with the quarter chord point. On the other hand, the sectional centre of mass is located aft of the pitch and flexural axes, giving rise to inertial coupling. This work builds on previous research performed with a free-rotating, rigid NACA 0012 wing. Data were collected using accelerometers, bending and torsion strain gauges and a potentiometer. The experiments yielded information on Limit Cycle Oscillation (LCO) amplitudes and frequencies, for two different types of beams. These LCO's were characterized by significant pitch motion, as well as flapwise bending motion. Two distinct branches of LCO's were found in the bifurcation diagrams: small amplitude oscillations (SAO) and large amplitude oscillations (LAO). Evidence of hysteresis was also found. The data were compared to previous results of the rigid wing quasi-2D configuration, and suggested that SAO is possibly due to laminar separation flutter (LSF). The LAO shows characteristics of both coupled flutter and stall flutter, and hence further study is required to elucidate its physical origin. The frequency data were also compared to Euler-Bernoulli uncoupled natural frequencies, and finite difference method (FDM) results for the first three modes of the system. In addition, the experimental results briefly provided further insight into the effects of plastic deformation, change in beam material, ambient conditions, and changes in the structural properties of the system via mass moment of inertia, dry friction and freeplay, on the LCO amplitudes and frequencies.

Résumé

Une série d'expériences a été réalisée sur une aile NACA 0012 en porte-à-faux flexible pour étudier la physique complexe qui se produit dans la région du nombre de Reynolds transitionnel de 7,9 $\times 10^4 < Re_c < 1,7 \times 10^5$. L'aile est libre de se déplacer en tangage, est flexible en flexion et en torsion, a des effets 3D sur l'aérodynamique et les structures, et présente des non-linéarités importantes. Une poutre en acier est située à l'intérieur de l'aile. La poutre assure la libre structurelle et la coque extérieure de l'aile assure la charge aérodynamique. La rigidité de tangage est également assurée par des ressorts linéaires situés au pied de l'aile. Le centre de flexion et l'axe de tangage sont alignés avec le quart de corde. En revanche, le centre de masse en coupe est situé en arrière des axes de tangage et de flexion, donnant lieu à un couplage inertiel. Ce travail s'appuie sur des recherches antérieures effectuées avec une aile rigide NACA 0012 à rotation libre. Les données ont été recueillies à l'aide d'accéléromètres, de jauges de déformation de flexion et de torsion et d'un potentiomètre. Les expériences ont fourni des informations sur les amplitudes et fréquences d'oscillation à cycle limite (LCO), pour deux types différents de poutre. Ces LCO étaient caractérisés par un mouvement de tangage significatif, ainsi que par un mouvement de flexion par volet. Deux branches distinctes de LCO ont été trouvées dans les diagrammes de bifurcation: les oscillations de petite amplitude (SAO) et les oscillations de grande amplitude (LAO). Des signes d'hystérésis ont également été trouvés. Les données ont été comparées aux résultats précédents de la configuration quasi-2D de l'aile rigide, et ont suggéré que le SAO est probablement dû au flottement de séparation laminaire (LSF). Le LAO présente les caractéristiques du flottement couplé et du flottement de décrochage, et donc une étude plus approfondie est nécessaire pour élucider son origine physique. Les données de fréquence ont également été comparées aux fréquences propres découplées d'Euler-Bernoulli et aux résultats de la méthode des différences finies (FDM) pour les trois premiers modes du système. En outre, les résultats expérimentaux ont brièvement fourni des informations supplémentaires sur les effets de la déformation plastique, du changement de matériau de la poutre, des conditions ambiantes et des changements dans les propriétés structurelles du système via le moment d'inertie de masse, le frottement sec et le jeu libre, sur les amplitudes LCO et fréquences.

Contents

List of Tables

List of Figures

Nomenclature

Abbreviations

$A.R.$	Aspect Ratio
DOF	Degrees of Freedom
LAO	Large Amplitude Oscillations
LCO	Limit Cycle Oscillations
LSB	Laminar Separation Bubble
LSF	Laminar Separation Flutter
$P.A.$	Pitch Axis (Location in Percent of Chord)
SAO	Small Amplitude Oscillations
C.G.	Centre of Gravity
CFD	Computational Fluid Dynamics
E.A.	Elastic Axis (Location as percent of chord)
EI	Bending (Flexural) Rigidity (Nm^2)
FDM	Finite Difference Method
FDT	Free Decay Test
FEA	Finite Element Analysis
GJ	Torsional Rigidity (Nm^2)
GVT	Ground Vibration Tests
HALE	High Altitude Long Endurance
I.C.	Initial Condition
L.E.	Leading Edge
LCO	Limit Cycle Oscillation
LES	Large Eddy Simulation
LSB	Laminar Separation Bubble
NRC	National Research Council of Canada
PSD	Power Spectral Density
RPM	Rotations Per Minute

SHM	Simple Harmonic Motion
T.E.	Trailing Edge
TAT	Thin Airfoil Theory
VLAO	Very Large Amplitude Oscillations

Roman Symbols

$\#f$	Superharmonic
ΔP	Pressure Difference (Pa)
b	Half Chord (m)
c	Chord (m)
k	Reduced Frequency (*Aeroelasticity*)
M	Mach Number
R^2	Total Variance
S	Wing Span (m)
U	Airspeed (m/s)
C	Aerodynamic Damping
c/4	Quarter-Chord Point
D	Diameter
d	Distance Between C.G. (wing/beam) and c/4
E	Young's Modulus (N/m^2)
G	Shear Modulus (GPa)
g	Gravity (m/s^2)
J	Polar Second Moment of Area (m^4)
J	Polar Second Moment of Area (m^4)
K	Aerodynamic Stiffness
L	Length (m)
M	Mach Number
m	Mass (kg)
N	Number of Springs
P	Pressure (Pa)
R	Ideal Gas Constant (Air)(J/kg K)
r	Radius of Pulley (m)
St	Strouhal Number
T	Temperature (K or $^\circ$)
t	Time (s)

Tu	Turbulence Intensity (%)
U	Airspeed (m/s)
V	Voltage
w	Flapwise Bending Deflection (cm)
y	Distance from Neutral Axis (m)

Greek Symbols

α	Angle of Attack (AOA) (Deg)
$\bar{\alpha}$	Mean Angle of Attack (Deg)
$\bar{\delta}$	Average Deviation (Deg)
$\bar{\omega}$	Frequency Ratio
ϵ	Strain (m/m)
μ	Viscosity of Air (*Aerodynamics*)$(kg/(m \cdot s))$
ν	Kinematic Viscosity of Air (*Aerodynamics*) (m^2/s)
ν	Poisson's Ratio (*Structural Dynamics*)
ω	Frequency (Hz)
ϕ	Torsion (Deg)
ρ	Density (kg/m^3)
σ	Stress (N/m^2)
θ	Pitch (Deg)
ζ	Damping Ratio

Subscripts

$(S_{el})_{steel}$	Elastic Limit of Steel (MPa)
α_o	Initial Angle of Attack (Deg)
α_{stall}	Stall Angle (Deg)
$\bar{\theta}_{peak}$	Average Height of Individual Pitch Peak (Deg)
δ_{max}	Maximum Tip Bending Deflection (m)
ω_h	Uncoupled Heave Natural Frequency (Hz)
ω_θ	Uncoupled Pitch Natural Frequency (Hz)
σ_y	Yield Strength (MPa)
σ_{UTS}	Ultimate Tensile Strength (MPa)
θ_{eq}	Equilibrium Angle (Deg)
θ_{peak}	Height of Individual Pitch Peak (Deg)
A_0	Initial Area (m^2)
C_L	Lift Coefficient

$C_{Mc/4}$	Quarter-Chord Moment Coefficient
D_θ	Damping Coefficient for Pitch $({}^{kgm^2}/_{2})$
$F_{applied}$	Applied Force (N)
F_{max}	Maximum Bending Force (N)
F_{pass}	Low-Pass Filter Passband Frequency (Hz)
F_{stop}	Low-Pass Filter Stopband Frequency (Hz)
G_T	Tangent Modulus (GPa)
I_p	Area Polar Moment of Area (m^4)
I_y	Area Moment of Inertia (About the y-axis)(m^4)
I_θ	Mass Moment of Inertia in Pitch (kgm^2)
K_h	Stiffness in Heave (N/m)
K_θ	Stiffness in Pitch (Nm)
k_θ	Total Pitch Stiffness(Nm/rad)
m_w	Mass of Wing (kg)
M_{EA}	Moment (About the Elastic Axis)
Re_c	Chord Based Reynolds Number
Re_x	Length Based Reynolds Number
t_{beam}	Beam Thickness (m)
U_f	Flutter Speed (m/s)
U_∞	Freestream Airspeed (m/s)
U_{div}	Divergence Airspeed (m/s)
V_0	Initial Voltage
w_{beam}	Beam Width (m)
x_θ	Static Imbalance (Chordwise)

1 Introduction

1.1 Overall Context

The current experimental work performed at the Royal Military College of Canada (RMC) focussed on testing a flexible, cantilever NACA 0012 airfoil at low airspeeds in order to study the aeroelastic physics manifested in the transitional Reynolds number regime. The test apparatus is designed to allow free pitching, as well as flexible movement, most significantly in flapwise bending and in torsion. As a continuation, and in contrast, to previous research done at RMC on a free pitch-plunge rigid NACA 0012 quasi-2D wing, this work exhibits significant 3D characteristics. The airfoil subsequently experiences flutter-induced oscillations of limited amplitude. There are aerodynamic, geometric and material non-linearities present, as well as inertial and aerodynamic coupling.

1.2 Literature Review

The literature review is divided into two main components. First, a retrospective of related work performed in the scientific community is provided. This is followed by a summary of relevant work performed specifically at the Royal Military College of Canada in the Aeroelasticity Lab.

1.2.1 External Retrospective

1.2.1.1 Low Speed Non-Linear Aerodynamics

It is well known that static stall occurs at the stall angle, α_{stall}. For high Reynolds numbers, and for $\alpha \ll \alpha_{stall}$, the aerodynamic lift and moment will follow unsteady linear thin airfoil theory (TAT). However, the aerodynamic lift and moment can become highly non-linear in the vicinity of α_{stall}. Dynamic stall exhibits non-linearities, as well as significant hysteresis with respect to the angle of attack, but with more pronounced effects than seen for static stall.

Dynamic Stall

In 1981, McCroskey [1] provided a detailed account of the mechanisms and types of dynamic stall, which were classified as either light or deep. Overall, dynamic stall is associated with the generation, passage and shedding of a vortex-like structure over the airfoil's suction surface, which creates a non-linear pressure distribution, affecting the aerodynamic lift and moment. Since this vortex-like disturbance moves slower than the freestream velocity, there is a time lag in the re-attachment of the flow, as well as asymmetry in the pressure distribution, which creates the hysteresis. This hysteresis induces aerodynamic damping. If the aerodynamic damping in pitch is negative, the airfoil extracts energy from the airflow, and the pitch oscillations tend to increase in amplitude, which leads to stall flutter. Furthermore, for an airfoil with an added plunge degree of freedom, the plunge may intensify the amplitude of oscillations.

Depending on the overall characteristics of the airfoil, either leading edge (L.E.) or trailing edge (T.E.) stall can occur. For a moderately sharp L.E., there will be a severe adverse pressure gradient occurring over the first few percent of the chord and there will be abrupt boundary layer separation, causing L.E stall. The ensuing vortex at the L.E. causes significant changes in the aerodynamic lift, moment and drag, as the wing is oscillating in and out of stall. The strength of the L.E. vortex is dependent upon a number of factors, including the reduced frequency, k (Equation 1.1), which provides a measure of the unsteady effects i.e. the effects of fluid inertia and lag [2].

$$k = \frac{\omega b}{U_\infty} \tag{1.1}$$

Reynolds Number Effects

As previously mentioned, the order of magnitude of the Reynolds number is of great importance. In 1985, Lissaman and Mueller [3] discussed that in the transitional Reynolds number region (approximately $10^4 < Re_c < 10^6$), the laminar boundary layer does not have enough momentum to overcome the adverse pressure gradient and separation occurs. However, the unstable nature of the laminar free shear layer causes turbulent entrainment and hence re-attachment, which creates a "bubble" of reversed flow or dead air. This boundary layer separation and transition are greatly affected by the Reynolds number, as well as freestream conditions and airfoil surface effects.

At higher Reynolds numbers, a loss of lift accompanies the bursting of this bubble past α_{stall}. However, at lower Reynolds numbers there is loss of lift, as well as hysteresis. The hysteresis is exhibited via the aerodynamic lift and moment, where there is a delay in the effects of the bubble depending on the airfoil motion (pitching nose-up or nose-down), and whether the freestream airspeed was increasing or decreasing. The hysteresis is represented by a fold bifurcation (which will be defined in Section 2.1).

Finally, Lissaman and Mueller discussed the case of a finite wing versus an infinite wing. They found that as aspect ratio (A.R., defined as ${}^{Span^2}\!/_{WingArea}$) increases, the slope of the lift curve decreases, the minimum drag decreases, the stall angle increases, and the range of the hysteresis loop increases.

In 1994, Schreck and Helin [4] performed tests on a finite NACA 0015 wing at low Reynolds numbers (water tunnel, $Re_c = 5.6 \times 10^4$ and wind tunnel $Re_c = 6.9 \times 10^4$). The wing was fitted with pressure transducers and a splitter plate, and dye was injected into the boundary layer. The pitch axis (P.A.) was located at 33% of the chord. This set-up was used to study the vortices present on the suction surface of a pitching airfoil. The results showed evidence of a large L.E. vortex, initially attached to the surface, which then detaches at the mid-chord point. This vortex creates counter-rotating vortices, moving from the mid-chord point towards the T.E. This was further confirmed by the Computational Fluid Dynamics (CFD) modelling performed by Poirel and Yuan in 2009 [5], albeit for a slightly different configuration.

In 1995, Huang and Lin [6] conducted extremely detailed tests, predominantly using smoke streaks and surface oil. The wing half-span was 1 m, and the elastic axis (E.A.) was located at 50% of the chord, and coincident with the centre of gravity (C.G.). The flapwise rigidity (EI) and torsional rigidity (GJ) were given as 2 $\times 10^4$ Nm^2 and 1 $\times 10^4$ Nm^2, respectively. Based on the data provided, it is estimated that their Reynolds number range was 1.17 $\times 10^5 < Re_c <$ 1.22 $\times 10^5$. Their results clearly illustrated the process of flow separation, as well as key phenomena occurring on the surface, such as the location and subsequent movement of the transition point and reattachment points, separated flow, vortices, wall effects, boundary layer effects, as well as the relationship of these phenomena to Reynolds number and root AOA. The results also demonstrated the non-linear relationship between lift and moment, with respect to angle of attack values which were well below α_{stall}.

1.2.1.2 Low Speed Non-Linear Aeroelasticity

Classical Versus Non-Classical Flutter

In 1992, Dunn and Dugundji [7] performed tests which focussed on the phenomenon of stall flutter. This work appeared to be an extension of the work done by Dunn in 1985 [8], and thus it is inferred that the E.A. of Dunn's experimental wing was located near the midchord point (E.A. at $\approx$ 50% of the chord). Dunn and Dugundi used different types of material compositions of a NACA 0012 wing, which allowed investigation of the change in the flutter mechanisms, i.e. stall versus classical flutter, as well as boundaries as related to the variation of free vibration frequency characteristics (a detailed explanation distinguishing between classical and stall flutter will be discussed in Section 2). The wings were outfitted with strain gauges, which were used to obtain the experimental data. By utilizing both experiments and the ONERA model (a low-order unsteady non-linear aerodynamic model), Dunn and Dugundji sought to study the transition from linear to non-linear behaviour (i.e. the change from classical flutter to stall flutter). When considering only the 1^{st} modal frequency results, the experimental and analytical models showed good correlation for the lift and moment curves. Their results also indicated the relationships and sensitivity between the onset of flutter, the dominant mode, and the relative difference in magnitude between the linear flutter speed and divergence airspeed.

Non-Linearities and Initial Conditions

In 1993, Tang and Dowell [9] studied the experimental behaviour of a flexible rotor blade. Similar to Dunn and Dugindji, they also used a corresponding mathematical/analytical model (which was valid for beam deflection magnitudes less than the beam length). However the model used by Tang and Dowell included higher order structural terms and freeplay non-linearities. Unfortunately, the Reynolds number range was not given, but is is known that tests were performed in the Duke University low speed wind tunnel. Tang and Dowell showed that LCO's were sensitive to *initial conditions and airspeed*, and that mostly *periodic* motion was encountered when a perturbation was applied to the root pitch angle. Some important observations concluded that firstly, the linear model only held for relatively small AOA, since geometric non-linearities occur from larger deflections. Secondly, the pitch movement was dominated by the 1^{st} modal frequency. Thirdly, for lower airspeeds and initial pitch angle, the freeplay non-linearity was greater than the geometric non-linearity; however, for higher airspeeds and initial pitch angle, the freeplay non-linearity was less than the geometric non-linearity.

In 2000, Tang and Dowell [10] focussed on a specific type of non-linearity, related to large deflections and material non-linearities, which were relevant to high A.R. wings. They presented and elaborated on the work of Von Karman, which explained that when the wing bends, this creates an in-plane tension which causes it to stiffen quadratically, leading to a structural non-linearity (specifically geometric), which limits the amplitude of oscillations past the classical flutter speed. They used the ONERA model, and the wing's E.A. and C.G. were coincident, and located at 50 % chord. The flapwise and torsional rigidities were provided as, $2 \times 10^4 \; Nm^2$ and $1 \times 10^4 \; Nm^2$, respectively. Tang and Dowell noted that when there were linear geometric characteristics and non-linear aerodynamics present, the LCO response displayed two dominant frequencies. When geometric structural non-linearities were included in the model, no LCO's occurred when the freestream velocity was greater than the flutter speed i.e. $U_\infty > U_f$ (for no initial tip or torsional displacements). Finally, they found that the structurally non-linear force decreased the system stiffness and hence its stability, and so the effects of the *structural* non-linearity dominated over the weaker *aerodynamic* non-linearity and hence did not lead to new a new steady-state LCO.

In 2002, Dowell and Tang [11] again discussed non-linearities, and touched on the topics of aerodynamic and structural effects on varying types of wing characteristics such as delta shapes, high A.R.'s, and other considerations. In general, Dowell and Tang discussed that, where a linear system might predict self-sustained growing oscillations, the presence of non-linear effects would serve to create steady-state LCO's. The magnitude of a perturbation used to trigger these oscillations was of importance, as a locally stable system can experience loss of stability for a large enough initial condition (I.C.). They also noted that LCO amplitudes are proportional to the magnitude of freeplay in the system.

In 2009, Dimitriadis and Li [12] studied a quasi-2D pitch-Plunge NACA 0012 wing with a P.A. located at 38.3 %, and A.R. of 3, undergoing stall flutter in the transitional Reynolds number regime. They found evidence of dynamic stall occurring at $Re_c = 5.1 \times 10^4$, which was especially evident from the aerodynamic moment (about the P.A.), but also seen in the lift where there was an apparent "bow-tie shape" due to hysteresis. The onset of stall flutter was triggered by a large perturbation at 12.2 m/s, with a marked increase in the heave magnitude. However, the flutter was triggered by a simple change in airspeed at 13 m/s. Past the onset of stall flutter (confirmed to be triggered by the pitch DOF going unstable), the LCO amplitude increased with airspeed, while the frequency decreased.

.

In 2011, Razak et al. [13] studied a rectangular NACA 0018 wing (where there were 3D effects present, as the wing horizontally spanned only 50% of the tunnel height, and it was clearly stated that no end plates were installed to ensure the flow over the wing was 3D) at low airspeeds in a wind tunnel, specifically investigating stall flutter. They noted that the mode which goes unstable first tended to be torsion (or rigid pitch) dominant. Their work was important because it strove to locate the boundary between classical and stall flutter, based on the change in static angle of attack, as well as to categorize the types of bifurcations evident. For the tests performed by Razak et al., the turbulence intensity of the wind tunnel was 0.15 %, and the maximum blockage was 5 %. The airspeed test range was 8 m/s $< U <$ 22.5 m/s (assuming standard air density, $1.94 \times 10^5 < Re_c < 5.46 \times 10^5$). The wing had an A.R. of 2.78, K_θ of 755 N/m, and the location of its main spar was at 37 % of the chord. The C.G. was located at 40 % of the chord (indicating the presence of inertial coupling) The decoupled pitch and heave natural frequencies were 4.57 Hz and 5.95 Hz, respectively.

Effects of Freeplay

In 2004 Marsden and Price [14] performed experimental tests with a 2 DOF pitch-plunge NACA 0012 quasi-2D wing, which had an E.A. located at 35 % of the chord, and a frequency ratio less than 1 ($\bar{\omega} < 1$). The chosen frequency ratio is defined in Equation 1.2, where ω_h and ω_θ are the uncoupled, undamped structural natural frequencies in heave and pitch, respectively. Their results demonstrated that freeplay affected the pitch and plunge logarithmic decrements, pitch frequency, and LCO amplitudes but found that the plunge frequency was not as greatly affected. The results of Marsden and Price serve to demonstrate the importance and effects of freeplay on the system.

$$\bar{\omega} = \frac{\omega_h}{\omega_\theta} \tag{1.2}$$

The work discussed in this section was performed external to the Royal Military College, but nevertheless provides a good basis for the understanding of many aerodynamic, aeroelastic, structural and dynamical phenomena. However, it is important to give these studies purpose and context. The notes from Telecon meetings dated August 1^{st} 2019 discussed the importance of the ability to make accurate aeroelastic predictions, and emphasized the importance of the X-56 aeroelastic demonstrator, used by NASA to determine more accurate flutter boundaries in tandem with FEM and CFD models. In addition, the work done at the Royal Military College of Canada provides an important focus on Reynolds number effects, by ensuring that the wind tunnel turbulence intensity was low enough, as well as looking at the effect of various parameters such as varying the frequency ratio, and the effect of bias. Given the recent interest in understanding and predicting the nature of a flexible wing in the transitional Reynolds number regime, a detailed discussion on the rigorous aeroelastic studies and results performed internal to the Royal Military College of Canada will be presented in the next section.

1.2.2 Investigations Conducted at the Royal Military College of Canada

1.2.2.1 Rigid Wing 1 DOF (Pure Pitch) Flutter

In 2006, Poirel et al. [15] performed an experimental study with a single DOF (pitch only), rigid NACA 0012 wing operating in the Reynolds number range of $5\times10^4 < Re_c < 1.2\times10^5$, with varying pitch stiffnesses. By using a hot wire, they proved that there was no periodicity in the upstream flow and therefore the oscillations were self-sustaining and appeared to be simple harmonic motion (SHM). The freestream turbulence intensity was measured to be 0.16%. The results from Poirel et al. showed the appearance of LCO's in the range of 5 m/s $< U <$ 11 m/s . The behaviour of the wing could be further subdivided into two sections based on their observations ($U <$ 8 m/s and $U >$ 8 m/s), seen in Table 1.1. The oscillations were sensitive to temperature, as well as sustained disturbances in the upstream flow. Most significantly, they affirmed that the pitch oscillations were due to non-linear coupling between the airfoil and flow, and *not* vortex shedding or flow periodicity.

Table 1.1: Summary of Results for Pitch Motion Only [15]

$U < 8m/s$	$U > 8m/s$
• pitch sensitive to flow conditions • as pitch stiffness increases, pitch amplitude decreases • $2f$ dominant frequency • pitch oscillations follow airfoil natural frequency	• amplitude independent of spring stiffness • $3f$ and $5f$ frequencies dominant

In 2007, Harris [2] performed tests on a rigid NACA 0012 wing moving in pitch only. The number of springs (pitch stiffnesses) and E.A. positions were varied, which yielded plots of pitch LCO amplitude versus the airspeed, for both increasing and decreasing airspeeds. Harris found both low and high amplitude LCO's. In general, the LCO pitch amplitudes for each curve were nearly congruent, especially as the airspeed increased, and regardless of the pitch stiffness; Harris stated this was a result of the combination of the structural stiffness coupled with the higher aerodynamic stiffness (Note that the notion of an aerodynamic stiffness is purely for the case of linear aerodynamics; for non-linear unsteady aerodynamics, there is an effective aerodynamic stiffness). Also, as pitch stiffness increased, the LCO amplitudes spanned across a wider range of airspeeds. The configuration where the E.A. was aligned with the quarter-chord point yielded the largest pitch amplitudes. The LCO frequencies increased with increasing pitch stiffness and airspeed and appeared to be converging very slowly. Using a PSD analysis, he also found the presence of notable superharmonic peaks with increasing airspeed. While relatively large magnitude odd superharmonics were connected to the non-linearities of the system at higher airspeeds, the data showed that the fundamental frequency peak was relatively higher than the superharmonic peaks, and therefore it was reasonable to assume SHM. It was also observed that there was a difference between LCO amplitudes for a given airspeed and configuration depending on whether the data were gained while ascending versus descending in airspeed. Additionally, Harris noted that even for identical test configurations, the Reynolds number varied, and that both temperature and mean pitch angle appeared to affect the LCO pitch amplitude. Finally, he found that the effective aerodynamic stiffness was sensitive to Reynolds number at small AOA. Harris noted that the "frequencies of LCO's in a non-linear system, are an extension of the eigenfrequencies in the corresponding linear model." This underlines that finding the linear system's eigenvalues is still of relative importance. As previously discussed by Dowell and Tang [16], Harris confirmed the effects of I.C.'s, and also noted that by tripping the boundary layer to create turbulent flow, there was an absence of oscillations, indicating that the oscillations likely occurred due to laminar separation effects.

Recognition and Study of Laminar Separation Flutter

In 2009, Poirel and Yuan [5] performed experimental, analytical and LES modelling in order to study a NACA 0012 wing moving in pure pitch, for $Re_c = 7.7 \times 10^4$. The wing had an E.A. located at 18.6 % chord, an A.R. of 3.9 and was set-up to be quasi-2D. The wind tunnel had a turbulence intensity of $< 0.2\%$ and when the wing was situated in the wind tunnel, there was a blockage ratio of 5%. Through the use of hot-wire anemometry, they confirmed that there was no periodicity in the upstream flow or wake; this was consistent with previous findings by Poirel et al. [15]. The test results yielded some important information regarding the occurrence of LCO's and frequency data, as well as relation to the structural stiffness. SHM was observed, with one dominant frequency and its corresponding even harmonics (caused by asymmetries in the test set-up), and there was a peak at 30 Hz due to motor noise. It was found that neither Von Karman vortex shedding, nor wake structures impacted the pitch LCO's, and the LCO's occurred for an airspeed range of 4.5 m/s$< U <$ 12 m/s. Finally, the oscillation frequencies were related to the structural stiffness. An analytical model was also used to compare with the experimental and LES model data. The moment of inertia of the structure was $I_\theta = 0.00135 kgm^2$, the stiffness in pitch was $K_\theta = 0.30 Nm/rad$ and the damping was $D_\theta = 0.002\ {}^{kgm^2}\!/_{s}$. The results showed that for the relevant pitch angles and rates, the aerodynamic moment was non-linear (due to Reynolds number effects). These quasi-2D analytical results were compared to the 3D work of Huang et al., who had performed a similar analysis, and found to be reasonable despite the differences in models (quasi-2D versus 3D, and differing locations of elastic axis). In terms of the frequency results, when comparing experimental results to analytical results, it was evident that the even harmonics were caused by misalignment, while odd harmonics were an indicator of the non-linear aerodynamic moment. There was also $3f$ dominance, with a magnitude comparable to magnitude of $1f$. In regards to the the aerodynamic moment, the plot showed a transition region where oscillations died out (small amplitude loops) and where the motion settled on limit cycles oscillations (large loops); the large amplitude loops also indicated where the airfoil extracted energy from the flow, as well as negative aerodynamic damping. Finally, they found that the aerodynamic stiffness decreased with pitch angle. CFD was done using an LES-based method, for $Re_c = 7.7 \times 10^4$. The CFD results clearly showed 3D structures moving spanwise and towards the trailing edge. They also showed that while the aerodynamic lift data were nearly SHM, the aerodynamic moment data exhibited behaviour with noticeable odd superharmonics (i.e. $3f$). The model also predicted self-sustained oscillations, and showed good correlation with experimental results for unsteady non-linear aerodynamics. For the range of angles of attack analysed, there was a laminar separation bubble present (except for $0° AOA$ where there was a region of dead air, which has the same effect as the laminar separation bubble i.e. it lowers the suction peak, creating a nose down moment. This plateau in the moment is what causes negative aerodynamic damping).

In 2009, Metivier et al. [17] experimentally studied the effects of inertia and boundary layer tripping on an airfoil which was self-excited, and oscillating in pitch in the transitional Reynolds number regime of $5.0 \times 10^4 - 1.2 \times 10^5$. The chord was 0.156 m, the moment of inertia was $I_\theta = 0.0014 kgm^2$, the pitch stiffness was $K_\theta = 0.3 Nm/rad$, the damping coefficient was $D_\theta = 0.002 {}^{kgm^2}\!/_{s}$, and the static imbalance was $x_\theta = 0.075c$ where $x_\theta = {}^{2\times|C.G.-E.A|}\!/_{c}$). The wing experienced LCO amplitudes of 5° in this particular Reynolds number regime. When the motion was periodic, the observed pitch oscillations were essentially SHM. The frequency of oscillations could be related to the aeroelastic natural frequency of set-up, and did not correspond to the Von Karman vortex shedding frequency in the wake. Numerical studies confirmed that the laminar separation of the boundary layer near the trailing edge played a critical role in initiating pitch oscillations. The high frequencies from the shed instabilities (i.e. separated boundary layer and wake) were not crucial nor necessary to maintaining the motion. The energy was transferred from the airflow to the airfoil, and thus there was positive work done per the aerodynamic moment. A moderate increase in the moment of inertia of the rotating parts had a significant impact on the characteristics of the oscillations, especially in terms of the frequency, and the decrease in the reduced pitch frequency was associated with the decrease in the natural frequency of the rotating parts of the set-up for each moment of inertia tested. The time dependent behaviour of laminar separation, seen in the experiments, suggested that the turbulent boundary layer (over both surfaces of the airfoil) prevented development of the oscillations and that the laminar boundary layer triggered oscillations.

Recognition of LCO Branches

In 2012, Poirel [18] provided a summary of the important phenomena occurring in the transitional Reynolds number region. Poirel generally discussed the difference between what occurs at high versus low Reynolds numbers, especially in regards to boundary layer effects and the laminar separation bubble, by using validation, verifications and analysis. Experimental results were found by testing varying airspeeds, using hot-wires, and some tests were done with the wing being motor-driven; the results were compared with analytical and numerical results and thus conclusions were drawn and summarized. The experimental tests showed that when the boundary layer was tripped, oscillations did not occur, and so Von Karman vortex shedding had no impact, while multiple attractors were observed. The pitch and heave LCO responses were plotted over time, and the results demonstrated two regions. For this particular configuration, it was stated that first region of small amplitude oscillations were due to laminar separation flutter (LSF), and the second region of large amplitude oscillations were due to coalescence flutter. The heave was found to be the driving factor in terms of energy transferred to the airfoil. Finally, numerical simulations provide insight into the separation and attachment which occurred with varying airspeeds and angles of attack.

In 2014, Peristy [19] performed experimental testing on a NACA 0012 airfoil moving in pure pitch, for a varying range of structural stiffnesses. The elastic axis was located at 35% of the chord, with a range of airspeeds of $5.2 < U < 10.3$ m/s ($5.3 \times 10^4 < Re_c < 11 \times 10^5$). He found two branches which were dependent upon I.C.'s. The small amplitude oscillations (SAO) were less than 3° and the large amplitude oscillations (LAO) were greater than 25°.

1.2.2.2 Rigid Wing 2 DOF (Pitch-Plunge) Flutter

Variation of Frequency Ratios and Elastic Axis Positions

In 2014, Poirel and Mendes [20] performed tests on a rigid NACA 0012 airfoil moving in pitch-plunge, with the elastic axis at locations ranging from $10\% < E.A. < 35\%$, and a frequency ratio range of $0.72 < \bar{\omega} < 1.63$. Tests were performed in the transitional Reynolds number region of $5.5 \times 10^4 \leq Re_c \leq 1.25 \times 10^5$. Poirel and Mendes discussed that the basic source of energy that feeds an LCO is from pitch-heave coupling (coupled flutter), and not negative aerodynamic damping (stall flutter). One would also find that depending on I.C.'s, two steady-state oscillations were possible: SAO and LAO, indicating the existence of non-linearities. The origin of SAO is LSF, while the origin of LAO is coalescence flutter, limited by flow separation at large angles of attack (for this particular case). This was opposite to the findings of Razak et al. [13], who determined that the LAO which occurred in their experiments were caused by stall flutter. They found that LAO's followed the heave dominated modal frequency, while SAO followed the pitch dominated modal frequency. Finally, for $\bar{\omega} > 1$, the frequency of the pitch dominated mode was lower than the heave dominated mode.

In 2016, Mendes [21] performed experiments on a rigid pitch-plunge NACA 0012 wing, for a Reynolds numbers range of $5 \times 10^4 \leq Re_c \leq 1.2 \times 10^5$, with a turbulence intensity of $Tu = 0.2\%$, a pitch stiffness of $K_\theta = 0.3 Nm/rad$, heave stiffness range of $K_h = 300 - 1480 N/m$, frequency ratio of $0.72 < \bar{\omega} < 1.63$, and E.A. locations of $10 - 35\%$. Two potentiometers were used, in order to capture data at the wing root and wing tip. The experiments were performed to capture both small and large oscillation amplitudes. Tests were performed in both 1 and 2 DOF, with the focus on studying LSF. In general, for $\bar{\omega} > 1$, there was an increase in heave and pitch LCO amplitudes with increasing airspeed, indicating that they were functions of the airspeed. When the E.A. was located across the range of $10\% - 27\%$, pitch driven SAO occurred (for both 1 and 2 DOF). When the E.A. was located at 27%, both SAO and LAO were possible (due to multiple attractors), with SAO occurring at the lower end of transitional Reynolds number region. Mendes stated that there was a "...tendency to jump to large amplitudes at higher airspeeds," which was dependent upon initial conditions, and also noted that a significant change in the phase difference occurred as the Reynolds numbers increased. While Mendes used Harris' work to compare, validate and draw conclusions, it is important to note (especially for the sake of the effects of hysteresis) that while Harris' results were all for ascending airspeeds, Mendes' results are a combination for mixed ascending/descending. For the LCO frequencies, Mendes found that $2f$ and $3f$ peaks were evident but were relatively smaller in magnitude compared to the fundamental frequency. The values of the first three frequencies were: $1f = 2.77$ Hz, $2f = 5.52$ Hz $3f = 8.30$ Hz (pitch mode). The heave frequency peaks were, in order of magnitude, $1f$, $3f$, then $2f$. The LCO frequencies were found to be related to the aeroelastic stiffness, especially the pitch LCO frequency. Mendes concluded that LAO occurred in pure pitch at both E.A. locations of 27% and 35%. It was confirmed that coupled flutter occurred when the E.A. was located at 27%, and stall flutter occurred when the E.A. was located at 35%. Finally, Mendes' results showed three types of flutter with distinct characteristics: a) Stall Flutter: where the oscillation amplitudes increase with increasing airspeed, b) Laminar Separation Flutter: where the oscillation amplitudes increase with increasing airspeed up to a point, then decrease with increasing airspeed, and c) Coupled Flutter: where one mode's amplitude increases with increasing airspeed, while the other decreases with increasing airspeed, and the frequency of the LCO oscillations increase when the E.A. is behind the quarter-chord point.

Study of Coupled Flutter Versus Stall Flutter

In 2018, Goyaniuk [22] performed experimental tests on a rigid NACA 0012 wing, moving in quasi-2D pitch-plunge motion. Expanding on the previous work done at RMC by Harris, Da Costa Mendes, Rocha Da Costa, and Peristy, Goyaniuk's purpose was to further understand and distinguish between the different mechanisms of flutter, namely stall and coupled flutter, and in doing so, she discussed a unique method of power generation by means of the energy extracted from the flow by the flapping wing. Goyaniuk was specifically focussed on the difference between the mechanisms and characteristics of coupled flutter and stall flutter LCO's, as well as the sensitivity of pitch and heave LCO amplitudes and LCO frequencies to changes in angle of attack, initial conditions, Reynolds number and frequency ratio.

Coupled Flutter

For the coupled flutter tests, the following details were noted: E.A. located at 27% chord, $3.65m/s \leq U \leq 14.0m/s$, $3.7 \times 10^4 \leq Re_c \leq 1.45 \times 10^5$, divergence airspeed, $U_{div} = 16.37$ m/s, $K_\theta = 0.3Nm/rad$, and $x_\theta = 0.093$ (indicating significant inertial coupling). The airfoil moved in two degrees of freedom (DOF), pitch and heave. The divergence airspeed was not within the range of test airspeeds. Goyaniuk found the existence of both SAO's and LAO's for the same airspeed and it was noted the appearance of SAO is a sign of Reynolds number effects. The experimental and analytical flutter speeds were close, indicating that this was most likely coupled flutter and tests confirmed that no 1 DOF flutter occurred for either pitch or heave. Goyaniuk observed SHM, and a constant amplitude (both pitch and heave), and a near zero baseline for pitch, for all tests (i.e. symmetrical). For all tests, the fundamental frequency, $1f$ was most prominent, however there was also a significant $3f$ peak as well in pitch. It was determined that the motion was pitch driven based on the phase angles for pitch and heave. By comparing with a 3 DOF aeroelastic model, using Wagner's function, it was found that for a $\bar{\omega} > 1$, the experimental flutter speed was lower than predicted by the model due to a stiffening in pitch, and indicated the presence of non-linearities. Analysis determined that the heave mode went unstable first and that the flutter was mild (Appendix C.1). In terms of the aerodynamic lift and moment, hysteresis was more evident in the aerodynamic moment curves than the aerodynamic lift curves (as mentioned by Harris) - this revealed that the aerodynamic moment curve, as well as the heave were more non-linear. There were also no asymmetric LCO's, likely due to the stiffening in pitch.

Stall Flutter (1 DOF)

The 1 DOF (Pitch) stall flutter tests had the following parameters: E.A. located at 35% chord, $5.4m/s \leq U \leq 12m/s$, $5.7 \times 10^4 \leq Re_c \leq 1.3 \times 10^5$, $U_{div} = 7.3m/s$, $K_\theta = 0.3Nm/rad$, $x_\theta = 0.004$ (indicating trivial inertial coupling). The divergence airspeed was within the range of test airspeeds. It was noted that coupled flutter was not predicted for this configuration per the analytical model, and that multiple attractors were present. During testing, pitch driven LAO's occurred and the oscillations decayed below the divergence airspeed, however there were LCO's present above the divergence airspeed. There were also SAO at small AOA, with non-zero baselines. The LCO's were determined to be caused by stall flutter since only 1 DOF was required for flutter to occur and there was no coupled flutter predicted analytically. The behaviour was SHM, with a near zero baseline for pitch. It is very important to state that reports on oscillations about a symmetric zero baseline have been sparse for stall flutter. The frequencies showed prominent $2f$ and $3f$ peaks (indicating asymmetries and non-linearities, respectively). However, no asymmetric LCO's occurred.

Stall Flutter (2 DOF)

The 2 DOF stall flutter tests had the following parameters: E.A. located at 35%, $5.4m/s \leq U \leq 12m/s$, $5.7 \times 10^4 \leq Re_c \leq 1.3 \times 10^5$, $U_{div} = 7.3$, $K_\theta = 0.3Nm/rad$, $x_\theta = 0.004$, $0.68 < \bar{\omega} < 1.43$. For the 2 DOF results, with $\bar{\omega}$ not close to 1, small heave amplitudes were noted. An aerodynamic load analysis showed that the pitch drove the motion in heave, and that the heave had less dominant non-linearities; the aerodynamic lift does most of the work. For $\bar{\omega} = 1.43$, the analytical predictions called for negative work done over the cycle, while the experiments showed positive work done over a cycle. The pitch and heave oscillations were almost in phase. An important note which Goyaniuk cited from Fung [23] was that for the overall work done on the airfoil to remain positive, the pitch and heave needed to be in opposite directions (i.e. out of phase) for a large part of the cycle. This phase difference is also a crucial criterion to produce flutter. Further, she noted that Pigolotti et al. [24] found that a small static imbalance (introduced by virtue of inertial coupling), served to enhance the vibration intensity and thus the energy extraction from the flow. Finally, Goyaniuk found that when the frequency ratio is greater than 1.24, the pitch oscillations became enhanced (while the heave basically remained the same), and there was increased structural damping in heave.

1.2.2.3 Investigation of the Laminar Separation Bubble

In 2013, Rudmin et al. [25] performed experimental work using hot-films, hot-wire anemometry, and a potentiometer for both a static and quasi-static NACA 0012 airfoil to track the movement of a laminar separation bubble (LSB). The hot-films were placed from the L.E. to 89% of the chord. The turbulence intensity was $Tu < 0.2\%$, the set-up was quasi-2D, and the wing parameters were $c = 0.0156m$, $S = 61cm$, with a P.A. located at 18.6%, with the motion powered by a motor. The three test points were $Re_c = 6.2 \times 10^4, 8.2 \times 10^4, 1.1 \times 10^5$, with a pitch angle range of $0 - 5°$. For steady aerodynamics only, it was confirmed that the separation bubble reduced in size and moved towards the L.E. when the angle of attack increased and Reynolds number increased. There were some discrepancies between these results compared to previous work, however this was attributed to 2D versus 3D effects and differing turbulence intensities.

In 2015, Poels [26] performed tests which were an extension of the work of Rudmin et al. [25]. She used the same wing and sensors as Rudmin, but with a dynamically pitching wing, driven by a motor. It was confirmed that the behaviour of the driven wing performed in a satisfactory manner when compared to a free-pitching wing. Once again, data were collected at three Reynolds numbers in the transitional region ($Re_c = 6.2 \times 10^4, 8.2 \times 10^4, 1.1 \times 10^5$). Poels found that there was a notable difference in the movement of the separation and transition points between the upper and lower airfoil surfaces, and between Reynolds numbers.

1.2.2.4 Flexible Wing Initial Tests and Modelling

Initial Tests

In 2016 Da Costa [27] performed experiments using the first incarnation of the flexible NACA 0012 wing, as well as analytical modelling using non-linear equations of motion (See Appendix C.2) for elastic bending-torsion with rigid pitch motion, structural non-linear terms and unsteady aerodynamics. This was for a Reynolds number range of $4.5 \times 10^4 \leq Re_c \leq 1.3 \times 10^5$, and $A.R. = 3$; Initially, a wing with an aluminum beam core was used, but quickly experienced plastic deformation; a steel beam was then used in its place. The airfoil exhibited structural non-linearities in free vibration tests i.e. a dependence of damping and frequency on structural displacements. The damping non-linearities appeared to be due to freeplay between the wing and beam. He also noted the evidence of these structural non-linearities (which were restoring) based on the superharmonics observed in the PSD's for the tests. Da Costa found 2 types of LCOs, which were dominated by the pitch mode. He also noted that SAO exhibited a strong dependence on airspeed, as opposed to LAO where this was not the case. He concluded that for a given airspeed, the I.C.'s would determine if SAO or LAO would occur. Finally, LAO appeared to be a result of the coalescence flutter instability (flapwise bending and pitch) and SAO appeared to be due to Reynolds number effects via the laminar boundary layer separation.

Modelling

In 2018, Robinson [28] sought to create a model which could provide numerical results to compare in tandem to the experimental results performed at RMC; his work was focussed on geometric non-linearities and dynamic instabilities. Robinson modelled a flexible cantilever wing, which underwent axial deformation, edgewise (in-plane) bending, flapwise (out of plane) bending, torsion, and was physically coupled with rigid body pitch rotation by means of a support mechanism. Robinson noted that experimental data indicated large oscillation angles between the chord of wing and freestream airflow, which meant a non-linear coupling between the structural displacement and the aerodynamic forcing. By explicating the work of Da Costa [27], who extrapolated the work of Hodges and Dowell [29], Robinson developed a numerical model where the P.A. was not coincident with the E.A., and there was coupling between the rigid body mode and flexible modes. The model included unsteady aerodynamic and 3D effects, as well as rigid body pitch motion. Robinson assumed the aerodynamics to be linear below an angle of attack of 12°, and ensured that that his low amplitude results were consistent with this work's experimental SAO results. Once the model was developed, he applied a large initial condition to the model. The results of an eigenvalue analysis showed that the pitch and 1^{st} bending modes coalesced, and that the 1^{st} bending mode went unstable first, with a flutter speed of 12.67 m/s, and a flutter frequency of 5.59 Hz; he noted that it was moderately unstable and that the 1^{st} bending mode and rigid body pitch modes coalesced. In order to draw conclusions about the effects of the structural non-linearities, he performed analyses on the structural model for three different test points corresponding to $U < U_f$, $U = U_f$, $U > U_f$. It was found that for $U < U_f$, non-linear effects were negligible. For $U = U_f$, all modes had positive damping, except the 1^{st} bending mode, which had zero damping (as expected); the structural non-linearities appeared to have caused a supercritical bifurcation and raised the flutter speed higher than it's linear analogue but the linear and non-linear models still had similar LCO amplitudes and frequencies. However, for $U > U_f$, the linear system exhibited growing oscillations, whereas the non-linear system experienced LCO's due to structural non-linearities, as was consistent with experimental observations. A sensitivity analysis drew the conclusions that structural damping did not affect the flutter speed for moderate flutter; however, the effects would be much more pronounced for mild flutter (Appendix C, Subsection C.1). He also tested the affects of changing the stiffness of the torsional spring, and deduced that changing the pitch stiffness would have a more profound effect on the system behaviour than a change in the mass properties. Finally, Robinson's work produced results for the LCO amplitudes of rigid body pitch and 1^{st} flapwise bending and the corresponding frequencies. The results showed a maximum LCO amplitude of about 25° for rigid body pitch, and 1.5 cm for the 1^{st} flapwise bending. The equations of motion for this system can be seen in Appendix C, Subsection C.2 and clearly display many non-linear terms.

1.3 Objectives

Classical non-linear aeroelastic behaviour is in a large part focussed on transonic problems due to shock waves, which lead to LCO's for fighter aircraft, and there is an abundance of work dedicated to the aforementioned research. However, for certain types of aircraft/operating conditions and wind turbines, low Reynolds number effects are encountered, such as the laminar separation bubble (LSB). Studies conducted in the transitional Reynolds number field of research are relatively sparse. Even for general Reynolds number problems, the literature on stall flutter is not as developed as for transonic flutter. There still remain many aspects to be studied, such as the coupling between rigid and flexible body modes. In addition, most stall flutter studies are focussed on oscillations at a high angle of attack, in the vicinity of the static stall angle. Moreover, the interplay between structural non-linearities and aerodynamic non-linearities is still not well understood.

Figure 1.1 illustrates a plot of the two canonical non-dimensional numbers in aerodynamics: chord based Reynolds number and Mach number. As indicated by the orange highlighted portion of the plot, the pertinent region of interest as related to this current experimental work is $10^4 < Re_c < 10^6$ and $0.01 < M < 0.3$

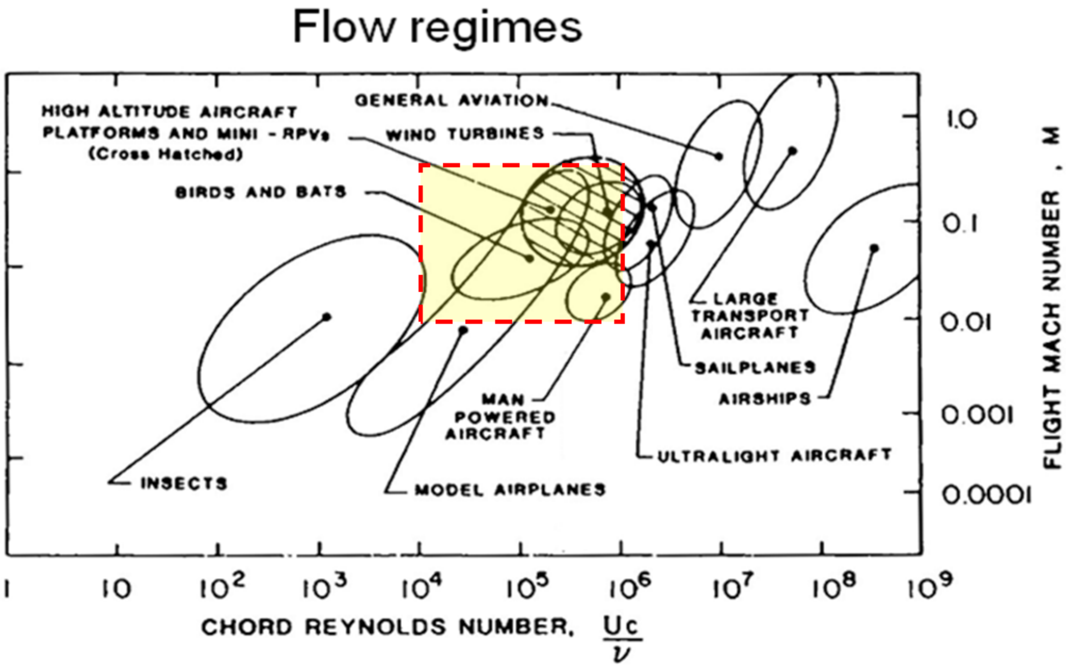

Figure 1.1: Flow Regimes Adapted from [3]

This works builds on the previous work performed with a rigid wing under the direction of the aeroelastic lab at the Royal Military College of Canada. As seen in Figure 1.2, while the rigid wing has 2 DOF (pitch and heave) and is quasi-2D, the flexible wing investigated in this work has an infinite number of DOF, in addition to free pitch motion at its root.

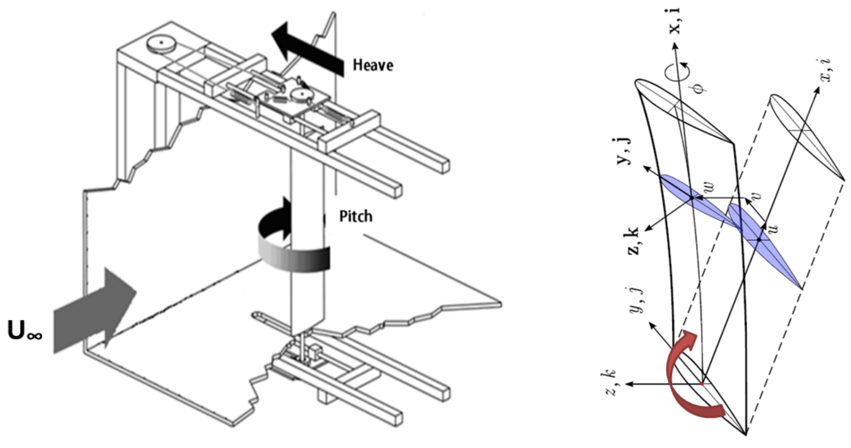

Figure 1.2: Comparison of Rigid Pitch-Plunge Wing and Flexible Wing Adapted from [22] [28]

The experimental work at the Royal Military College of Canada was performed in tandem with Carleton University, which studied the analytical development of the non-linear structure, and NRC (National Research Council of Canada), who focussed on the CFD (Computational Fluid Dynamics) simulation of non-linear aerodynamics. The overall goal of this research is to describe the motion of a flexible wing at transitional Reynolds numbers and will serve as the benchmark model for studies investigating:

1. rigid body mode interacting with flexible body modes
2. the relative importance of structural (due to large deformation) versus aerodynamic (flow separation due to low Reynolds number and high angle of attack) non-linearities
3. the study of three different dynamic aeroelastic instabilites: laminar separation flutter, coupled flutter and stall flutter

2 Theoretical Background

This research being multidisciplinary, it is necessary to introduce a number of basic concepts, ranging from non-linear dynamics to aerodynamics, structural dynamics and aeroelasticity.

2.1 Bifurcation Theory

A bifurcation is a topological description of a qualitative change of behaviour of some dynamic measure, due to a particular parameter, the bifurcation parameter. In this research the bifurcation parameters is the airspeed or the Reynolds number. Considering a physical systems, the qualitative change to the solutions can be illustrated by simple mathematical equations. Some pertinent local bifurcation examples are discussed below [20] [30][31] .

A relevant example of a type of bifurcation is divergence, which is shown as a supercritical pitchfork bifurcation, seen in Figure 2.1 [22], where the equilibrium angle is plotted versus the airspeed, and stability is lost past the divergence airspeed. Another prime example is stall flutter, which is often described as a subcritical Hopf bifurcation, whereas coupled flutter usually leads to a supercritical Hopf bifurcation [13] seen in Figure 2.2. Comparatively, supercritical Hopf bifurcations are considered "Good LCO's" as no flutter occurs below the flutter speed, whereas subcritical Hopf bifurcations are considered "Bad LCO's" since flutter can occur unexpectedly below the flutter speed.

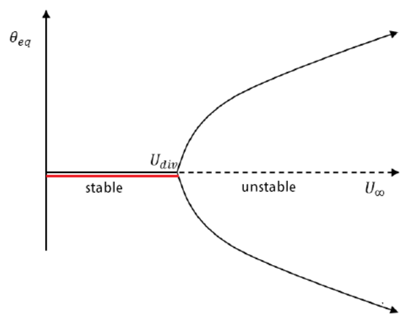

Figure 2.1: Supercritical Pitchfork Bifurcation Example: Divergence Adapted from [22]

Figure 2.2 shows examples of the two broad types of LCO's which can occur, as were previously mentioned. Not only is it evident that the LCO amplitude can change depending on the strength of the non-linearity, we also see that different types of bifurcations may occur due to the effects of non-linearities arising from the aerodynamics and structural effects. [11] [12] [13] [32] [33]

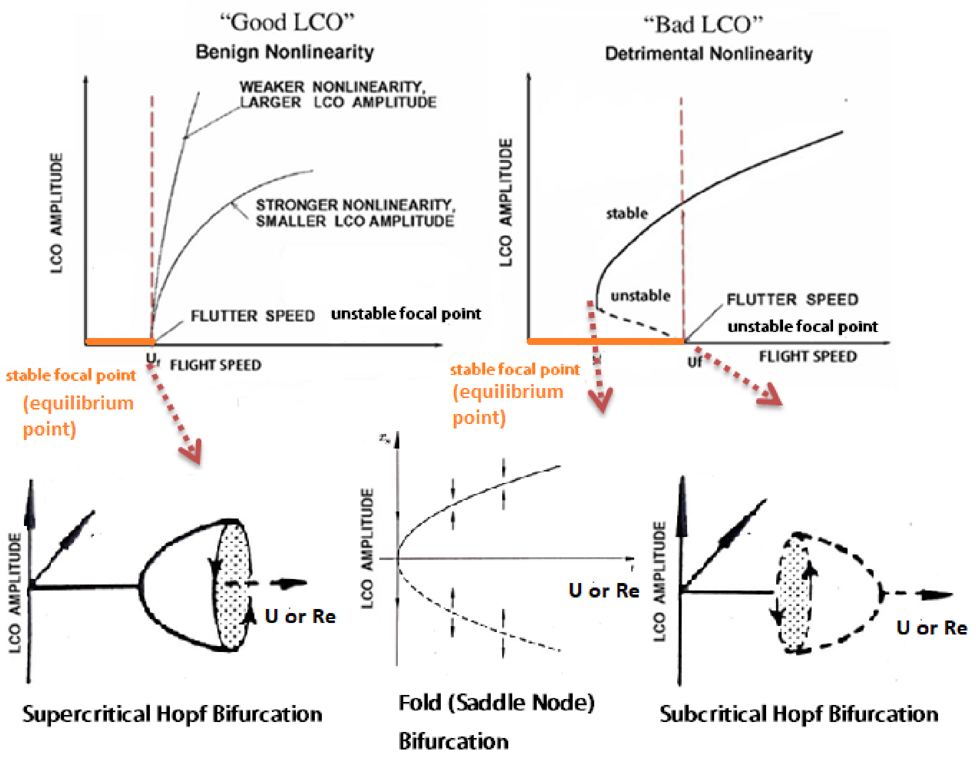

Figure 2.2: LCO's with Limiting Non-Linearities as Related to Bifurcations; Adapted from [11] [32]

2.2 Aerodynamics

2.2.1 Reynolds Number Effect on Lift and Moment

In the transitional Reynolds number region, non-linear dynamics occur due to the Reynolds number effects, mainly local flow separation, causing the aerodynamic lift and moment to become non-linear functions of the angle of attack even at small angles of attack. Considering the static case, for high Reynolds numbers, the lift (Figure 2.3) and moment are linear functions of the AOA right up until stall. Figures 2.4 and 2.5 illustrate the effects of the physics occurring at low Reynolds numbers.

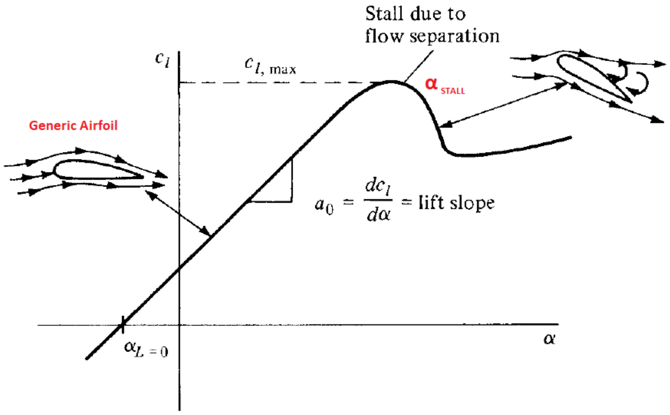

Figure 2.3: Aerodynamic Section Lift Coefficient Versus Angle of Attack at High Reynolds Numbers; Adapted from [34]

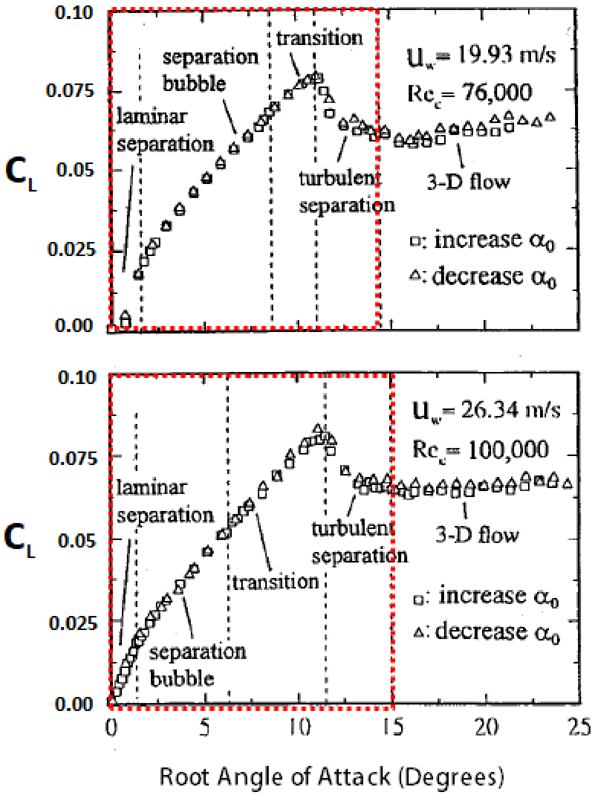

Figure 2.4: Aerodynamic Lift Coefficient Versus Angle of Attack; Adapted from [35]

In the range of $0° < \alpha < 2°$, the lift and moment are non-linear functions of the angle of attack due to the formation and growth/bursting of the separation bubble (Figure 2.6). Above $\alpha = 2°$, the flow becomes 3D, as massive separation occurs.

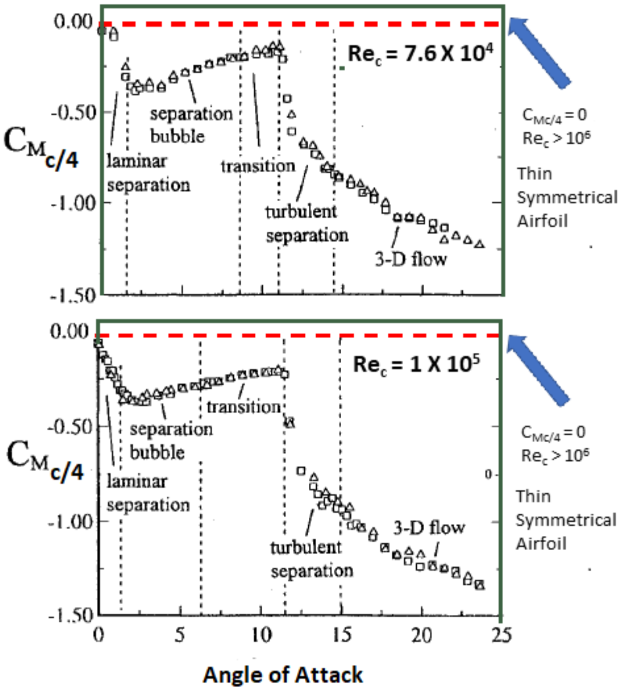

Figure 2.5: Aerodynamic Moment Coefficient Versus Angle of Attack; Adapted from [35]

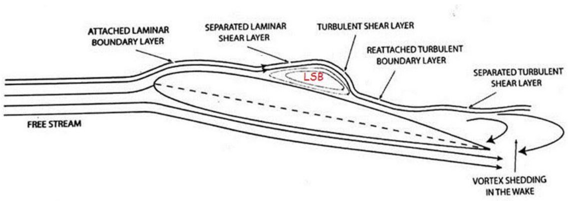

Figure 2.6: Laminar Separation Bubble; Adapted from [35]

2.2.2 Dynamic Stall

Dynamic stall is an unsteady aerodynamic phenomenon [22] [36]. It occurs due to the wing oscillating in and out of the static stall regime, where there is flow separation at high angles of attack and the possibility of negative aerodynamic damping. There are two types of stall per McCroskey: light stall and deep stall. Figure 2.7 indicates the corresponding effect of the types of stall on the damping.

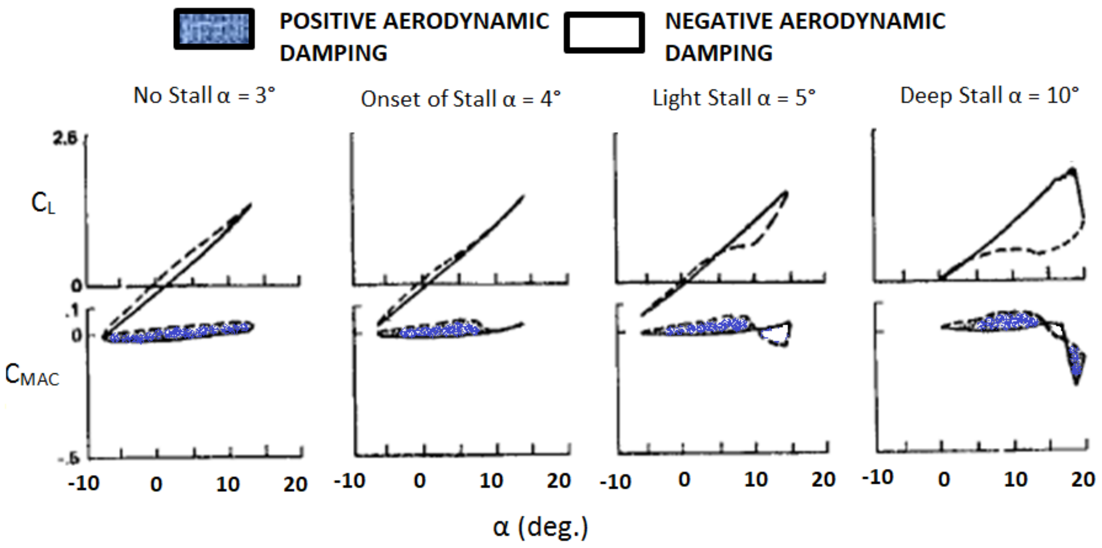

Figure 2.7: Damping During Dynamic Stall; Adapted from [1]

Depending on the direction of the moment loop (Figure 2.8), the work will either be negative or positive; when the work is positive, there is a net positive transfer of energy from the airflow to the airfoil. Furthermore, when a loop is rotating in the clockwise direction, the motion will be unstable, and when it is rotating counter-clockwise, the motion is stable [36].

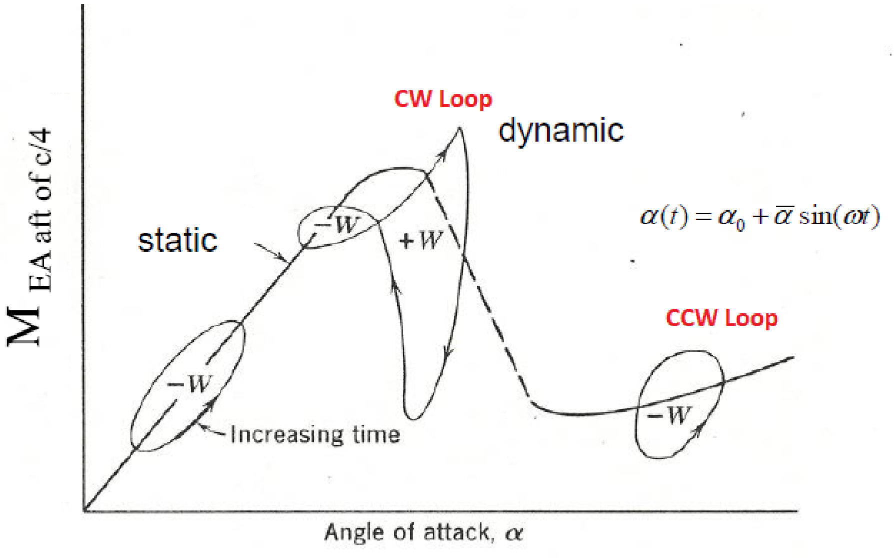

Figure 2.8: Dynamic Stall; Adapted from [36] [37]

2.3 Aeroelasticity

The field of aeroelasticity deals with the interaction between a flexible structure and a fluid (namely a wing and airflow) in terms of instabilities, both static (divergence) and dynamic (flutter), as well as the response.

2.3.1 Static Instability: Divergence

Divergence is a static instability whereby the total stiffness of the system goes to zero. It is a linear aeroelastic problem. For the case of the flexible wing , where the flexural centre and quarter-chord point coincide, $U_{div} = \infty$, since e = 0 (e is the distance between the A.C. and c/4)

2.3.2 Dynamic Instability: Flutter

There are two main types of flutter, Coupled Flutter and Stall Flutter. In addition, because this work is related to low Reynolds numbers, a third type of flutter is being observed, Laminar Separation Flutter (LSF).

2.3.2.1 Coupled Flutter

Coupled flutter occurs when there is a coupling between two DOF (or modes). For an aircraft, this is usually bending-torsion; however, given that the experimental apparatus is simply a free pitching flexible wing, pitch is essentially "rigid torsion." This translates to the onset of flutter possibly being the result of rigid and flexible body modes coupling together, i.e. pitch-bending or pitch-torsion. The binary flutter speed is the critical speed where two frequencies coalesce after one of the modes becomes unstable and experiences negative aeroelastic damping which induces an instability (Figure 2.9); there are self-sustained growing oscillations due to a net positive transfer of energy from the airflow to the airfoil (i.e. positive work done as a result of a large phase difference between the two modes (assuming SHM) [23].

Coupled flutter is mainly sensitive to the structural stiffness (and hence frequency ratio), as the well the relative positions and distance between the elastic axis and aerodynamic centre [21][22]. Coupled flutter is essentially a linear problem.

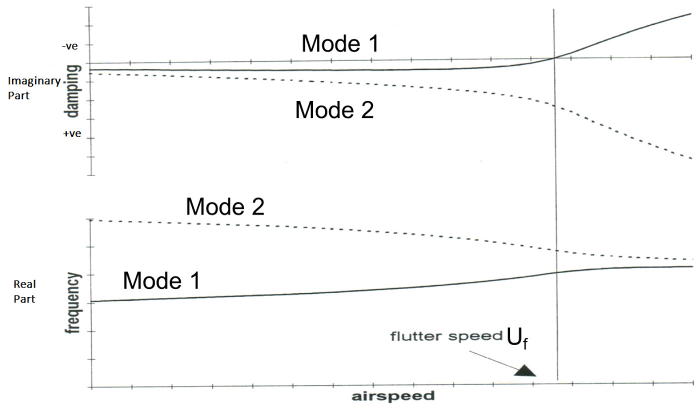

Figure 2.9: V-g-f Diagram of Coupled Flutter; Adapted from [36]

2.3.2.2 Stall Flutter

Stall flutter is an aeroelastic phenomenon, which occurs for a free wing due to flow separation at high AOA, leading to negative aerodynamic damping (as related to dynamic stall) and large amplitudes and thus loss of stability [1]. Stall flutter is essentially a non-linear problem. During one cycle the aerodynamic damping will oscillate between positive and negative value such that the initial loss of stability, followed by re-stabilization on an LCO. However, if the structural damping is greater than the aerodynamic damping, stall flutter cannot occur. Stall flutter can occur in 1 or 2 DOF, and it is mainly sensitive to structural damping [22][36].

Referring back to the work of Poirel and Yuan [5] and considering the equation of motion for pure pitch (Equation 2.1)(where the terms $a_1 - a_{10}$ originate from a least-squares fit to the experimental data, with a third order polynomial; when terms a_8 and a_{10} become dominant (both are negative and provide positive damping), the oscillations are restabilized on an LCO. The experimental results suggested that once LCO's were initiated, the laminar separation bubble produced higher order aerodynamic damping terms, where $a_3({}^{\rho U^2}\!/_2 \times Sc^2) > D_s$ which meant that the aerodynamic damping term is greater than the structural damping and therefore there is a loss of stability, negative aerodynamic damping and the onset of flutter. [5]

$$I_s\ddot{\theta} + [D_s - {}^1\!/_2\rho U^2 sc^2(a_3 + a_8\theta^2 + a_{10}\dot{\theta}^2)]\dot{\theta} \\ + [K_s - {}^1\!/_2\rho U^2 sc^2(a_2 + a_7\theta^2 + a_9\dot{\theta}^2)]\theta = 0 \quad (2.1)$$

For a 3D aircraft, it is usually the torsional vibrations which marry with the dynamic stall; however, for our experiments it is likely be the rigid pitch dominated mode, as it is in essence ”rigid torsion.” The work of Razak et al. [13] found that the interaction between a non-linearity and static divergence can result in a saddle connection bifurcation, and this can cause asymmetric LCO’s even if the wing is set at 0° angle of attack and is symmetrical. The results from Razak et al. also showed that LCO’s appeared below the linear flutter speed; hence they concluded that the cause was stall flutter. Razak et al. concluded that low amplitude LCO’s were due to light stall [1] [13], and that low amplitude LCO’s had a varying amplitude over time, while high amplitude LCO’s were self-excited with steady amplitudes [13]. Goyaniuk also noted that for the case of stall flutter, low amplitude LCO’s could become large amplitude LCO’s if triggered by a large perturbation, due to the non-linearities.

2.3.2.3 Laminar Separation Flutter

There is another type of flutter which occurs from flow separation at low AOA due to Reynolds number effects; it is damping driven and is also a non-linear aerodynamic problem. This type of flutter was coined laminar separation flutter by Poirel and Yuan [5], who investigated this phenomenon in detail. Poirel and Yuan found self-sustained oscillations about the 0° pitch position, for a quasi-2D rigid NACA 0012 wing (elastic axis located at 18.6 %) moving in pitch-plunge, for the range of $5.0 \times 10^4 \leq Re_c \leq 1.3 \times 10^5$ i.e. in the transitional Reynolds number regime. At low airspeeds, the laminar boundary layer does not have enough momentum to overcome the adverse pressure gradient which causes flow separation; thus, a laminar separation bubble (LSB) is formed. Figure 2.10 shows the change in sign of the aerodynamic moment (and thus work done) for various experimental, analytical and numerical results. The results clearly show the non-linearities in the aerodynamic moment due to the LSB at low AOA.

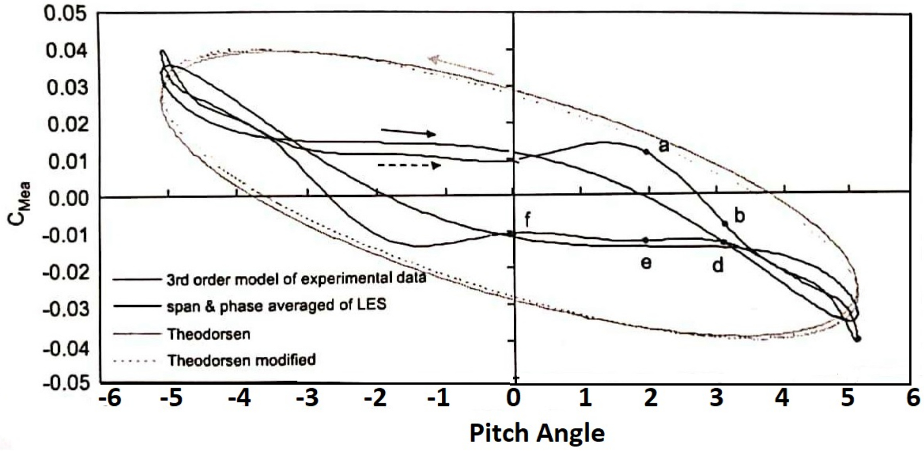

Figure 2.10: Aerodynamic Moment; Adapted from [5]

2.3.2.4 Comparison of Stall vs. Laminar Separation Flutter

Both stall flutter and LSF are caused by flow separation leading to negative aerodynamic damping. In order to demonstrate this, it is useful to use a simple vibration model, such as the Van Der Pol model (with zero angle of incidence). Per Figure 2.11, if the structural damping (D) is larger than the (negative) aerodynamic damping (A), then no flutter will occur. Conversely, if $|A| > |D|$ (A is positive, B is negative), then flutter will occur. At high AOA (stall flutter), stability will be lost due to turbulent flow separation, and then the motion will re-stabilize on an LCO. At low AOA (LSF), the flow will separate due to the laminar boundary layer not having enough momentum to overcome the adverse pressure gradient, followed by re-attachment, (creating the aforementioned LSB). The coupling between the wing structure and the movement of the LSB leads to an LCO.

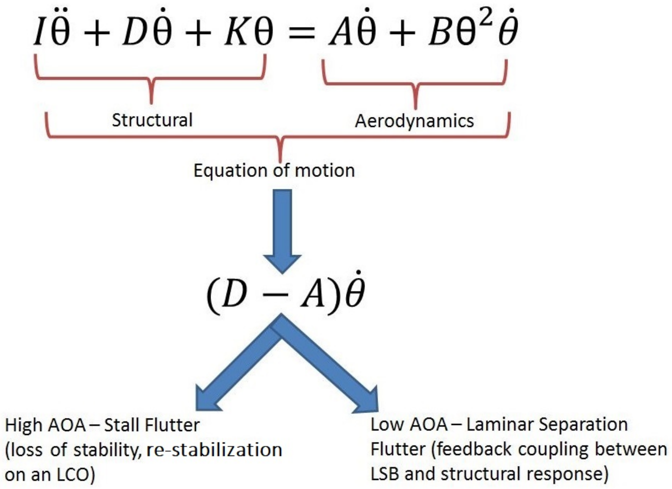

Figure 2.11: Stall and Laminar Separation Flutter Using Van Der Pol's Model Partially; Adapted from [1] [5]

2.4 Structural Mechanics and Vibrations

2.4.1 Mode Shapes of a Cantilever Beam

It is useful to briefly touch on the theory of mode shapes. As opposed to the rigid quasi-2D wing with pitch and heave DOF (i.e discrete system with only rigid body modes), this test apparatus is composed of both a flexible steel core and flexible airfoil and thus is a continuous system with an infinite number of DOF. A cantilever beam can experience different mode shapes, depending on the I.C. applied. Given that the initial conditions (I.C.'s) for the flexible wing experiments were applied via airspeed change, or perturbation at the root, all modes would only be excited for a brief period of time in the transient region. Past this transient region, the effects of the higher frequency modes (Modes 2 and greater) would die down, leaving mainly the effects of the first mode shape (Mode 1). Thus, it is reasonable to assume that the deflection of the wing/beam follows the first mode shape (Mode 1), per Figure 2.4.1.

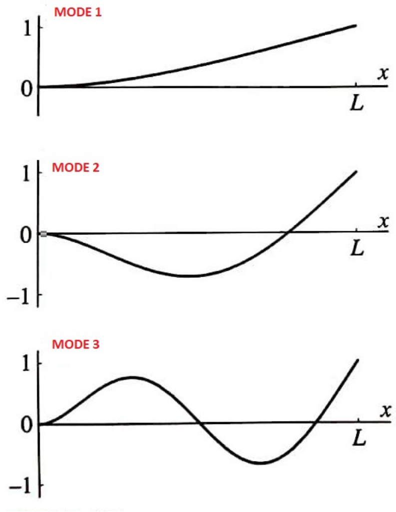

Figure 2.12: Mode Shapes of a Cantilever Beam; Adapted from [38]

2.4.2 Mode Shapes of a Flexible, Cantilever Wing

Jaworski and Dowell [39] performed analyses on a flexible, cantilever HALE-type NACA 0012 wing, made of composite materials. The mode shapes of the HALE wing with tip stores were determined by three different methods, i.e. impact testing, ANSYS FEA modelling and uniform beam theory. The results of these analyses can be seen in Figures 2.13 and 2.14 [39], and illustrated that all methods produce similar results. This work is important as it shows that computational modelling could be used to determine four mode shapes and their corresponding frequencies, for a HALE-type wing composed of several materials, and comprising details such as tip stores, spars, etc. Furthermore, note that the shape of the deflection in Figure 2.13 is similar to the deflection seen in Figure 2.4.1.

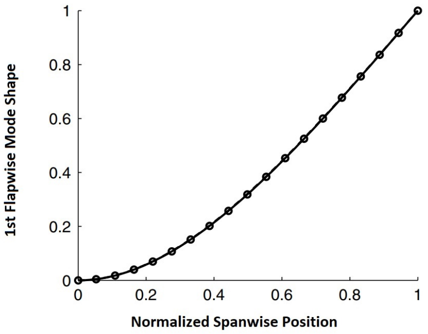

Figure 2.13: 1^{st} Flapwise Mode Shape; Adapted from [39]

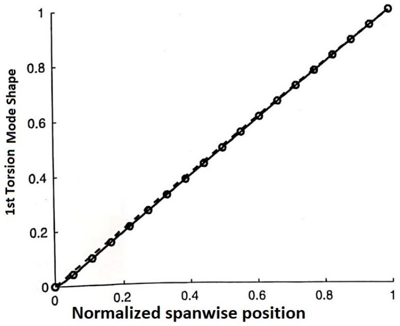

Figure 2.14: 1^{st} Torsion Mode Shape; Adapted from [39]

2.4.2.1 Rigid Body Mode Versus Flexible Modes

Rigid body mode represents the motion of a discrete system, where only the motion of the C.G. of the rigid body is considered. Conversely, flexible body modes move relative to the C.G. of the rigid body, for example as seen in Figure 2.15.

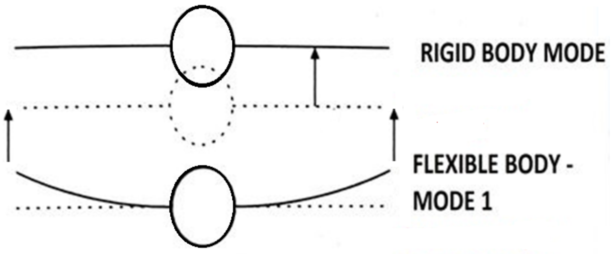

Figure 2.15: Rigid Body Mode versus Flexible Modes; Adapted from [40]

2.4.3 Euler-Bernoulli Beam Theory

2.4.3.1 Bending Natural Frequencies

For decoupled free vibration of a cantilever beam (clamped-free case) and assuming SHM, we can use Equations 2.2, 2.3 and 2.4 to find the first three uncoupled bending natural frequencies (where I_y is calculated per Equation A.6, in Appendix A, Section A.3, Subsection A.3.1 [41]), shown here. Given that all the beam structural properties are known values (except for damping), the frequencies can be calculated [38] for bending and torsion.

$$\omega_1 = 3.5160\sqrt{\frac{EI_y}{mL^4}} \tag{2.2}$$

$$\omega_2 = 22.0345\sqrt{\frac{EI_y}{mL^4}} \tag{2.3}$$

$$\omega_3 = 61.6972\sqrt{\frac{EI_y}{mL^4}} \tag{2.4}$$

2.4.3.2 Torsion Natural Frequencies

For the clamped-free case, and assuming SHM, the first three decoupled torsion natural frequencies can be found by using Equation 2.5 [42]. The polar second moment of area and area polar moment of inertia are calculated by using Equations A.7 and A.8, respectively, (Appendix A, Sections A.3.2 and A.3.3).

$$\omega_n = \frac{(2i-1)}{2l}\sqrt{\frac{GJ}{\rho I_p}}, i = 1, 2, 3.. \tag{2.5}$$

2.4.4 Maximum Pure Bending Stress

Equations 2.6 and 2.7 are used to calculate the maximum bending load and maximum bending stress, respectively, for a cantilever beam [41] with a load applied at the tip. Appendix A, Section A.1.

$$F_{max} = \frac{\delta_{max} 3EI_y}{L^3} \tag{2.6}$$

$$|\sigma_{max}| = \frac{F_{max}Ly}{I_y} \tag{2.7}$$

2.4.5 Elastic-Plastic Material Considerations

The microscopic effects of strain hardening are pictured in Figure 2.16, where both larger and smaller atoms can be seen. The smaller atoms occur due to the cold working of the material as it bends and twists. The original un-worked larger grains at the core exert a pressure on these smaller grains, creating tension within the material and this collectively serves to increase the yield strength of the material (σ_u versus σ_y) seen in Figures 2.17 and 2.18.

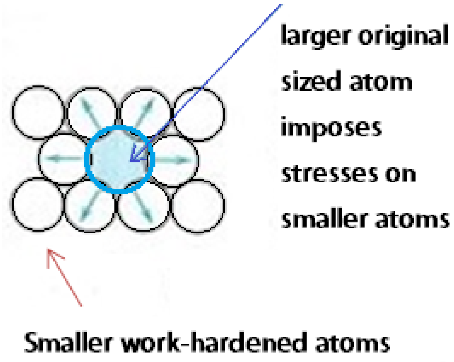

Figure 2.16: Microscopic Example of Strain Hardening; Adapted from [43]

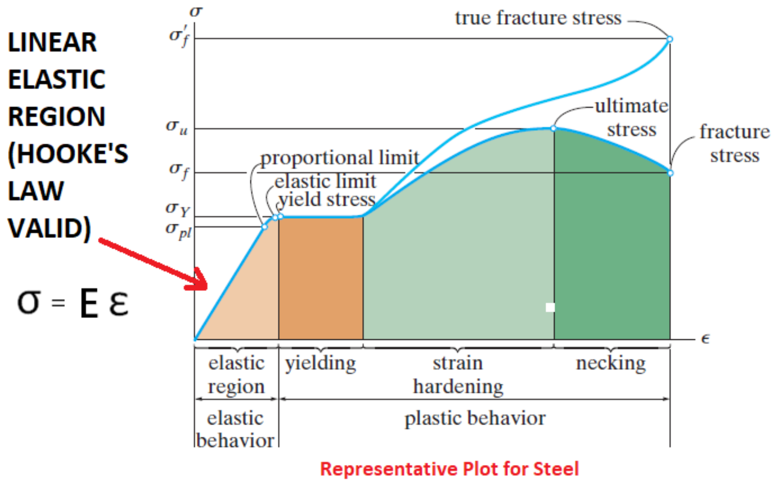

Figure 2.17: Illustration of Strain Hardening on Stress-Strain Curve; Adapted from [44]

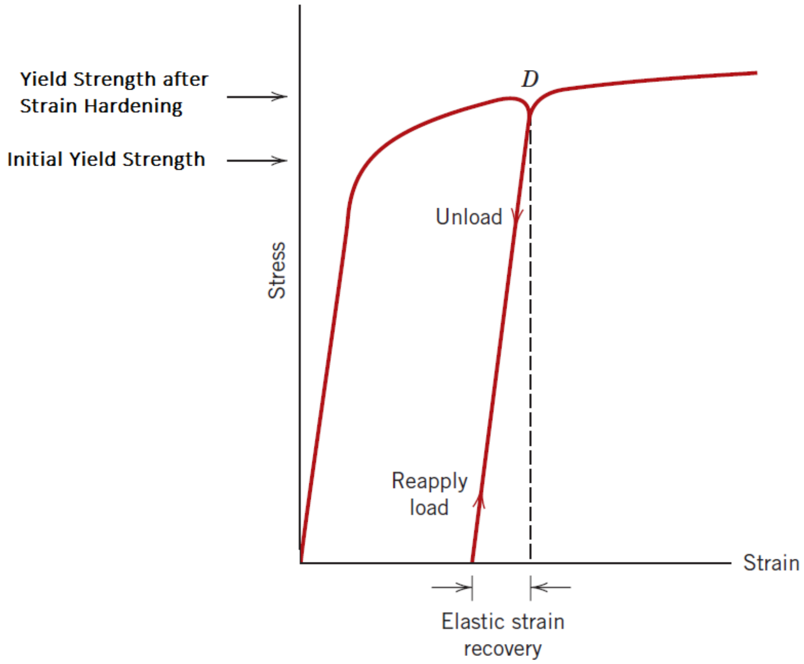

Figure 2.18: Illustration of Elastic Strain Recovery on Stress-Strain Curve; Adapted from [43]

Figure 2.17 succinctly illustrates the regions of elastic and plastic behaviour for a standard steel. Note that past the elastic region, there is plastic deformation occurring, with the effects of the aforementioned strain hardening clearly demonstrated on the (static) stress-strain curve.

Since the wing motion is cyclic (assuming SHM for the LCO), the material undergoes many tension-compression cycles, causing the material to reach its fatigue limit after a certain number of cycles. Figure 2.19 shows that for steel, the endurance limit is 186 MPa at higher numbers of cycles. Thus, it is obvious that the material's endurance limit is even more important than the yield strength or ultimate stress, due to the cyclic motion of the wing/beam.

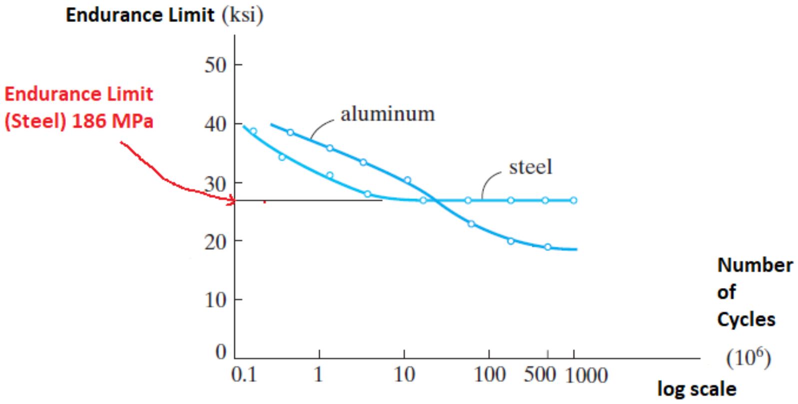

Figure 2.19: S-N Diagram [44]

3 Methodology

3.1 Wind Tunnel

The wind tunnel tests were performed in the large wind tunnel at the Royal Military College of Canada (Figure 3.1). It is a closed circuit low speed wind tunnel, powered by a 75 kW three-phase motor and the flow velocity is controlled by varying the fan speed. The freestream velocity is measured with a pitot static tube, which is located approximately nine chord lengths upstream of the airfoil, and is connected to an analog pressure transducer (and in some cases, is also connected to a DAQ card which allows recording of the pressure transducer data via Labview). The test section inner dimensions are 1.07 m × 0.76 m and the turbulence intensity of the tunnel is less than 0.2% [15]. The magnitude of the turbulence intensity is very important as discussed by Lissaman [3], since a higher turbulence intensity would cause the flow to transition from laminar to turbulent at the leading edge, thus eliminating the low Reynolds number effects. There is also a safety grid located approximately three chord lengths downstream from the wing. Based on previous tests, we anticipate that the apparatus is capable of experiencing various types of flutter in the wind tunnel.

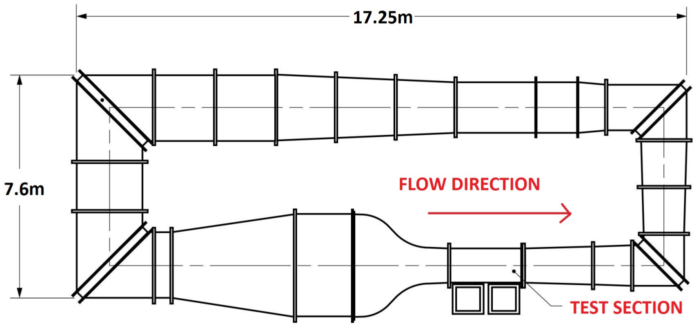

Figure 3.1: RMC Wind Tunnel; Adapted from [21]

The global test apparatus is comprised of the wing apparatus, the support cradle and spacer bar supports which hold the support cradle in place at the correct height (Figure 3.2). It is bolted into the wind tunnel support frame for safety and ease of mobility of the entire system; the wing apparatus, specifically, can be seen in Figure 3.3. While the support cradle was pre-existent, the spacer bar supports were designed and fabricated for these series of tests. Modifications were done to ensure a proper fit for the springs and potentiometer encoder body to fit snugly with the proper tolerances, without creating added dry friction. It was confirmed that the tip of the wing/beam apparatus was not affected by the boundary layer, per Appendix B, Section B.1. The vortex shedding frequencies were calculated, and found to be above the magnitude of expected dominant frequency of oscillations per Appendix B, Section B.2. The wingspan was chosen to be analogous to the rigid wing and appeared reasonable per the rule of thumb seen in Appendix B, Section B.3. Finally, the blockage encountered due to the wing motion was calculated to be 1.0% − 8.3%, per Appendix B, Section B.4.

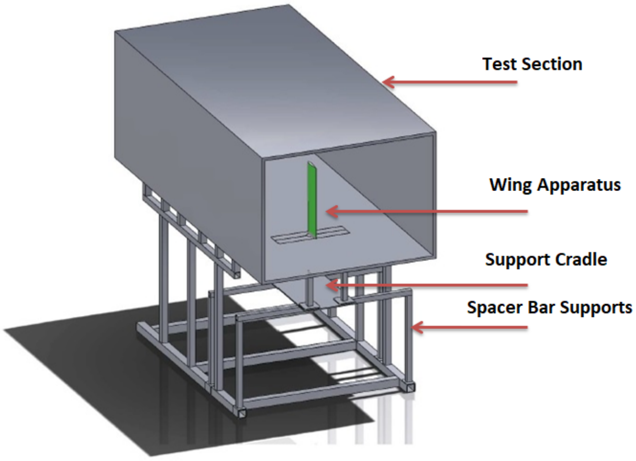

Figure 3.2: Wind Tunnel with Wing Apparatus, Support Cradle and Spacer Bars Installed

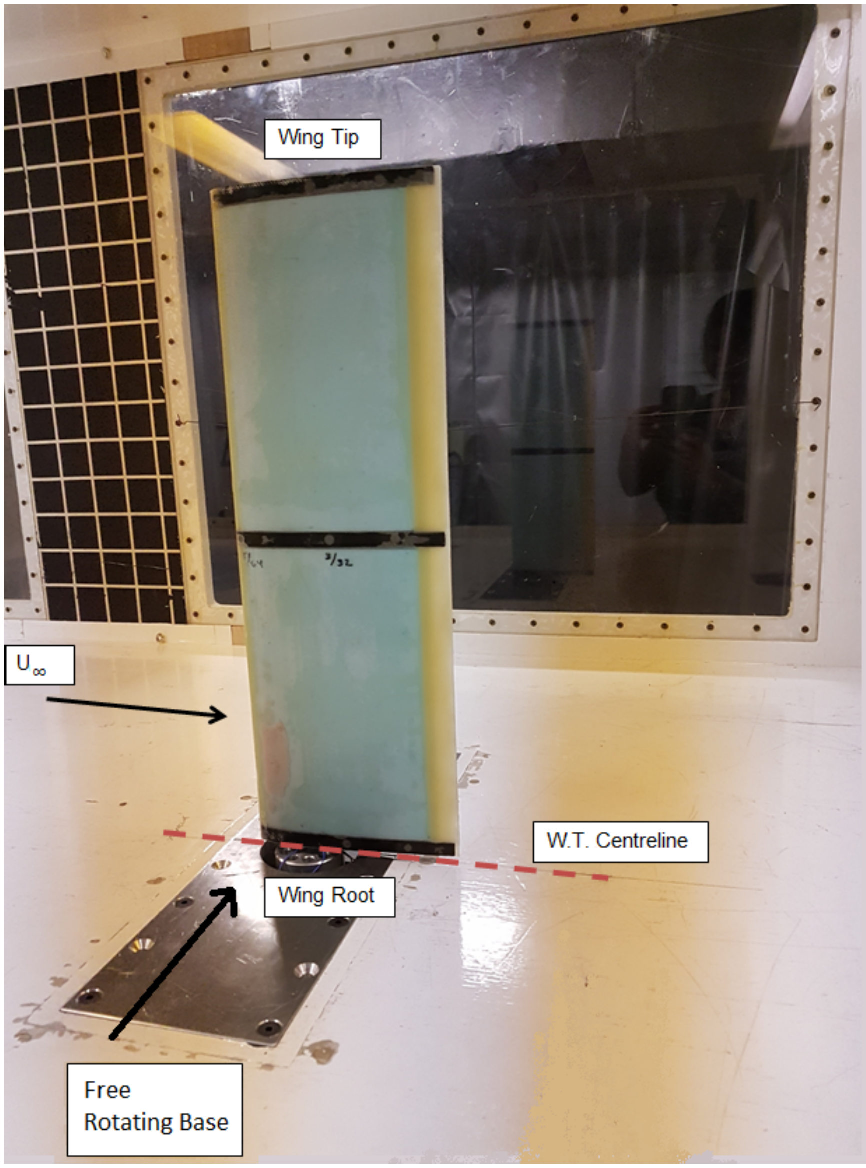

Figure 3.3: $s4^*$ Configuration in Wind Tunnel

In this current flexible wing experimental investigation, the wing testing apparatus consisted of the flexible cantilever NACA 0012 wing, mounted over a thin steel beam. There are two types of beam material which were used: Normalized AISI 01 and Tempered 1095 Spring Steel. The wing/beam combination was mounted on a free rotating base, which constituted the rigid pitch mode. The free rotary base that held the beam was connected to translational springs on a pulley (Figure 3.4) (View from below floor). A detailed view of the pulley mechanism, located underneath the wind tunnel, and housed in the support cradle can be seen in Figure 3.5. The beam provided the structural stiffness, while the wing provided the aerodynamic loads. The wing apparatus can move in rigid pitch, bending, and torsion. (Figure 3.6)

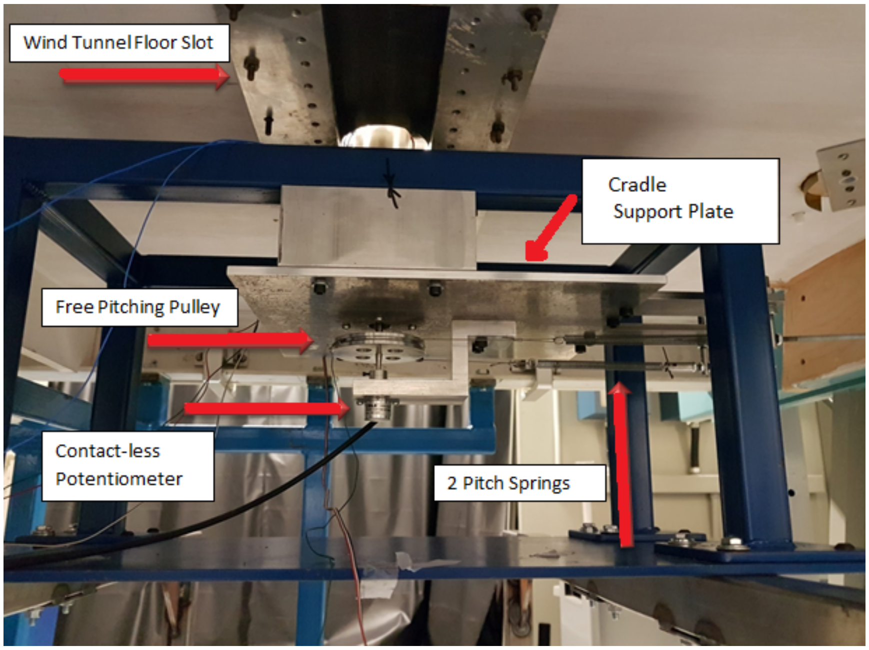

Figure 3.4: Pitch Springs Connected to $s4^*$ Configuration

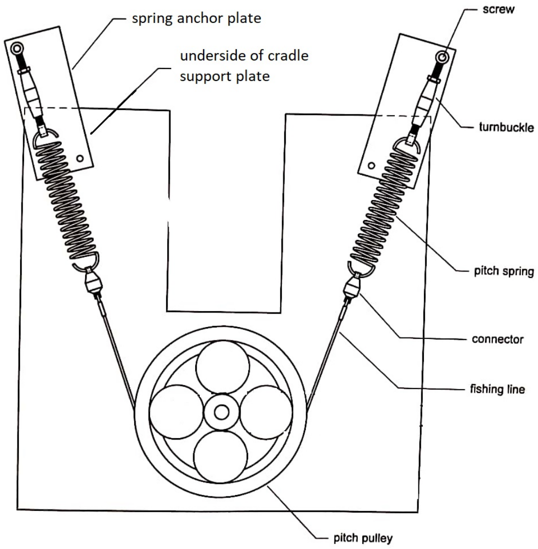

Figure 3.5: Pitch Pulley System; Adapted from [2]

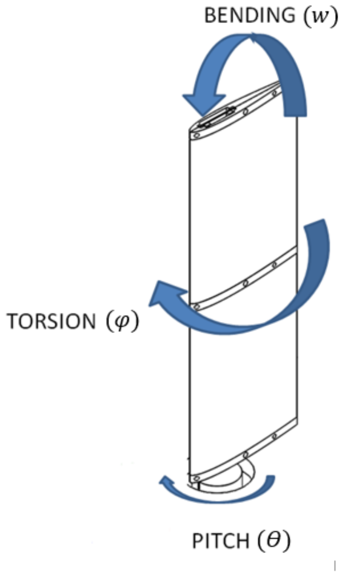

Figure 3.6: Flexible Wing Motion; Adapted from [28]

Referring to Figure 3.7, we see that the quarter-chord point, P.A. and flexural centre were aligned. However, the C.G of the wing-beam combination is not aligned with quarter-chord point, the P.A. or flexural centre, and thus there is inertial coupling between the rigid pitch mode and flexible modes.

It is important to note that the distance between the C.G. of the beam-wing combination and the quarter-chord point is different for Beams-01,-02 and -03 (defined as d_1 = 0.02 m for Beams-01,-02 and d_2 = 0.006 m, for Beam-03). The non-dimensionalized values are d_1/c = 0.1 and d_2/c= 0.04, respectively. The C.G. of the wing and beam was found by using a simple gravity test, suspending the wing by means of rope and adjusting until the wing was at $0° AOA$, and the location of the rope point of contact measured to find the C.G. relative to the L.E. Once the wing and beam C.G. was known, simple geometry was used to estimate the location of the wing and beam C.G. relative to the quarter-chord point, as all other wing and beam geometric values were known.

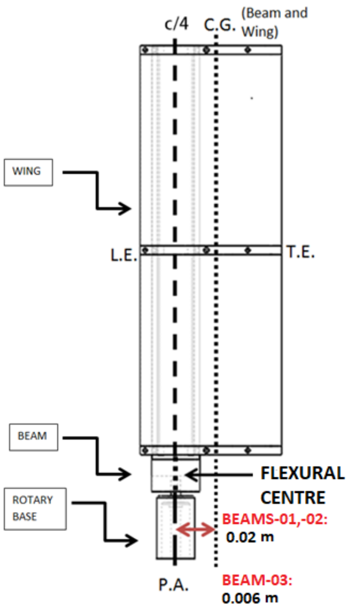

Figure 3.7: Relevant Axes

3.2 Test Rig

Figure 3.8 shows a general schematic of the test apparatus along with the instrumentation. The potentiometer is located at the bottom and is installed so that the top of the free rotating support is just flush with the wind tunnel floor. There is a beam located inside the pictured wing (Figure 3.9), outfitted with four bending strain gauges and four torsion strain gauges located as shown in Figure 3.9, as well as two accelerometers at the tip placed at approximately ≈ 1.3 cm away on either side of the P.A. The sensors are fed by their respective power supplies; the output of the strain gauges and accelerometers are fed through their conditioners, and all the data are then passed through the DAQ unit, to be processed and viewed by the computer with Labview. Labview output limits are set for each piece of instrumentation.

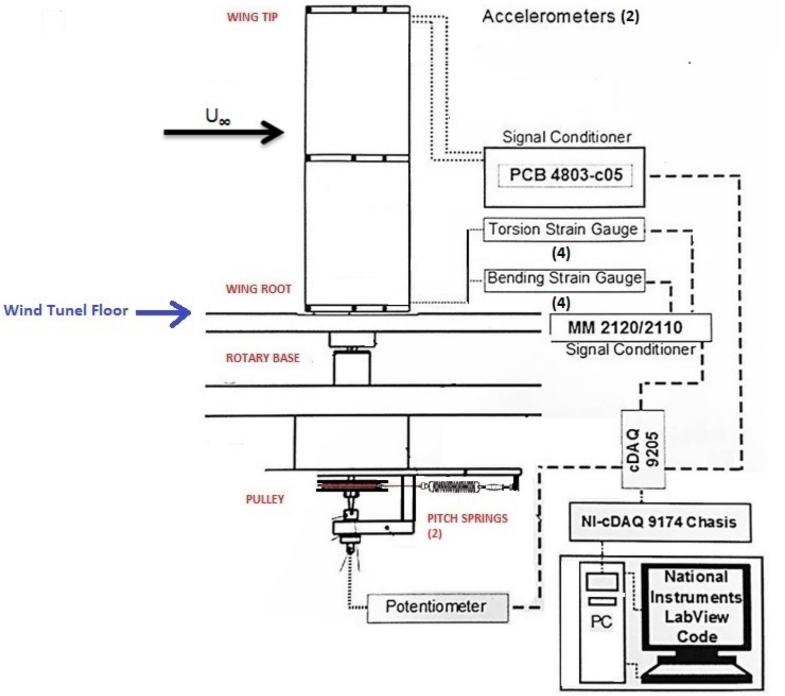

Figure 3.8: Schematic of Test Set-Up; Adapted from [2][27]

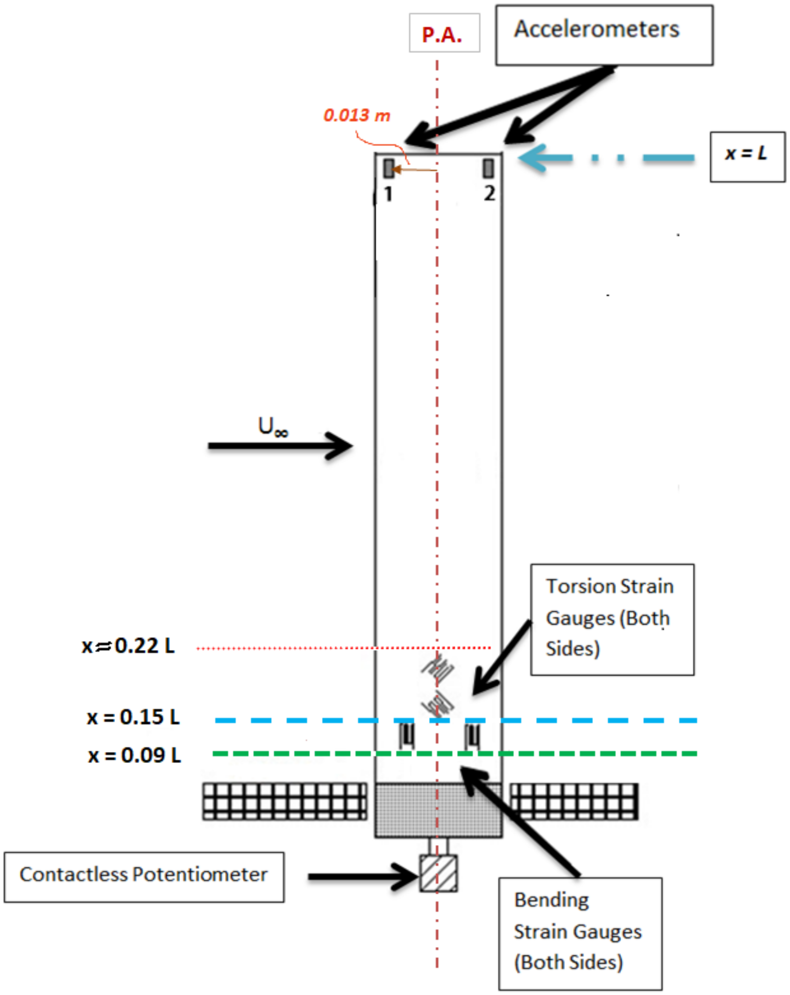

Figure 3.9: Instrumentation Installed on Beam; Adapted from [27]

3.2.1 Configurations

There are five types of test configurations: $s1$, $s2$, $s3$, $s4$ and $s4^*$, as listed below; only three are relevant for the presented results ($s1$, $s2$, and $s4^*$). The $s3$ and $s4$ configurations are only defined as they are relevant for the trial tests (and hence no images are provided); to be clear, no final results for the $s3$ or $s4$ configurations are presented. For all the cases, the position of the electric wires was deemed relatively trivial based on the sensitivity analysis presented in Appendix A, Subsection A.6. Figures 3.10, 3.11 and 3.12 illustrate physical views of the $s1$, $s2$ and $s4^*$ configurations, respectively.

- $s1$: Rotary base, shaft, pulley, potentiometer encoder and body, wires

- $s2$: Rotary base, shaft, pulley, potentiometer encoder and body, steel beam, 8 strain gauges, 2 accelerometers, wires, adhesives

- $s3$: Rotary base, shaft, pulley, potentiometer encoder and body, steel beam, 8 strain gauges, 2 accelerometers, wires, adhesives, flexible NACA 0012 wing, screws

- $s4$: Rotary base, shaft, pulley, potentiometer encoder and body, steel beam, 8 strain gauges, 2 accelerometers, wires, adhesives, flexible NACA 0012 wing, screws, surface putty

- $s4^*$: Rotary base, shaft, pulley, potentiometer encoder and body, steel beam, 8 strain gauges, 2 accelerometers, wires, adhesives, flexible NACA 0012 wing, screws, adhesive to reduce beam/wing freeplay, surface putty

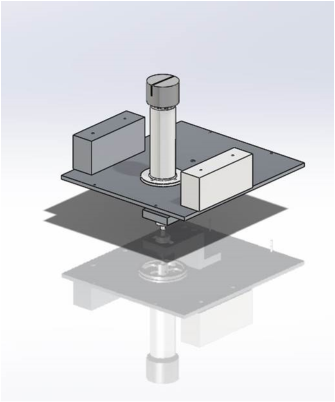

Figure 3.10: $s1$ Configuration

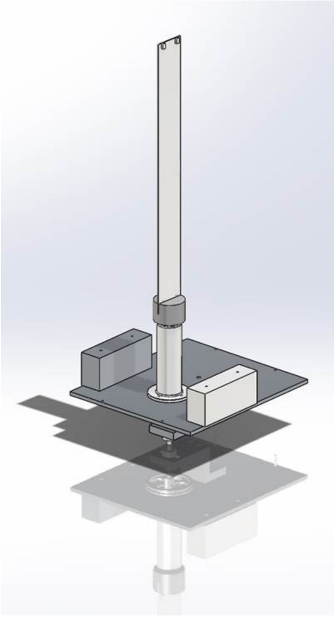

Figure 3.11: $s2$ Configuration

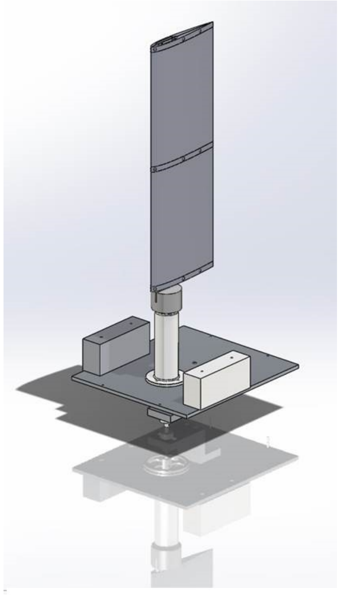

Figure 3.12: $s4^*$ Configuration

These configurations were used to characterize the structural dynamics of the system, namely the system's natural frequencies and damping via free decay tests as discussed in Section 3.5 and some of the inertial properties. Referring back to the work of Mendes [21] in Section 1.2.2, these free decay tests are also important because they provide information on the wing alignment and offset, and indicate if the system properties may have changed during testing.

3.2.2 Wing Characteristics

The flexible wing was designed to be analogous to the rigid wing, in terms of profile, chord, and structural frequencies of the lower modes. While the rigid wing moves in two DOF and is quasi-2D, the flexible wing moves in pitch, bending and torsion, and experiences 3D aerodynamic and structural effects. Both rigid body mode and flexible modes are illustrated in Figure 3.13. The two analogous modes for the rigid and flexible wings can be seen in Table 3.1.

The flexible wing is made of fibreglass, epoxy and foam and its dimensions can be seen in Table 3.2. Specifically, the wing spars were rapid-prototyped out of ASA/ABS plastic. The outer portion of the wing shell is composed of fibreglass resin covered in shrink-wrapped plastic, while the inside of the wing is made of foam and adhesive. The mass moment of inertia of the wing only for each test is provided in Section 3.5.3.2.

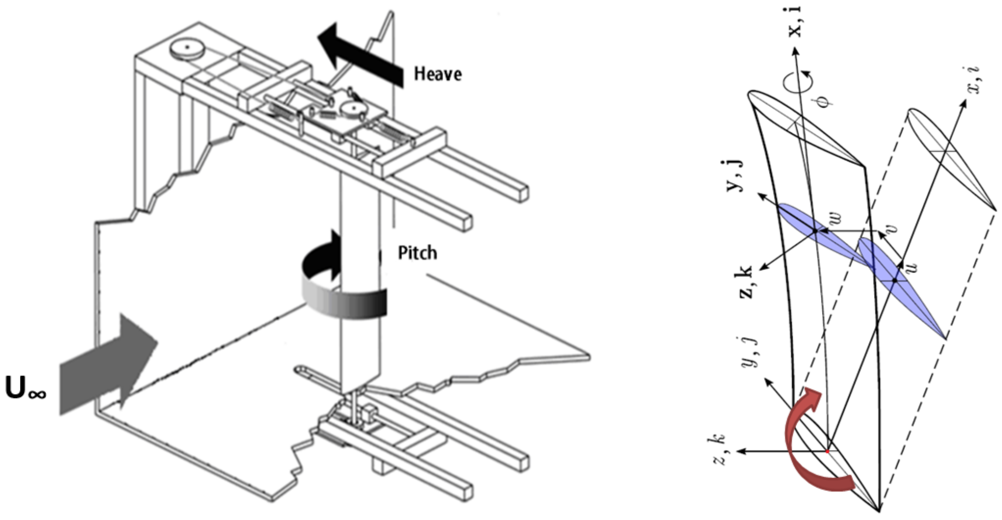

Figure 3.13: Rigid Wing versus Flexible Wing; Adapted from [22][28]

Table 3.1: Rigid Wing and Flexible Wing Analogous Modes

Quasi-2D Pitch-Plunge Wing	Flexible Wing
Pitch (θ)	Rigid Pitch Dominated Mode (θ)
Heave (h)	1^{st} Flapwise Bending Dominated Mode (w)

Table 3.2: Wing Only Paramaters

Material	fibreglass, epoxy and foam
S	0.445 m
c	0.15 m
m	0.145 kg
A.R.	3
C.G.	53% of chord

3.2.3 Beam Physical Properties

The physical parameters of the beams used for testing can be seen in Tables 3.3 and 3.4. The properties of Beams-01 and -02 were determined through tests, as seen in Appendix A.4; this was not required for Beam-03 as the required information was more readily available from the manufacturer. The basic differences between Beams -01,-02, and Beam-03 are thickness, respectively 0.0014 m and 0.0016 m, and material. Additionally, as seen in Figure 3.7, the distance between the wing and beam C.G. and P.A. is affected by the beam parameters. It can be seen that these simple changes in material type and thickness shows some appreciable differences in the beam parameters such as density, mass moment of inertia and polar moment of area. The values from Tables 3.3 and 3.4 indicate that the torsional rigidity (GJ) for each type of beam is 3.51 Nm^2 and 4.99 Nm^2 for Beams-01,-02 and Beam-03, respectively. Similarly, Tables 3.3 and 3.4 show that the flexural rigidity (EI_y) for each type of beam is 2.33 Nm^2 and 3.32 Nm^2 for Beams-01,-02 and Beam-03, respectively. Despite the physical differences between Beams-01,-02 and Beam-03, the difference in the uncoupled modal frequency results was not drastic.

Table 3.3: Average Structural Properties of Beam-01 and Beam-02

Material	Normalized AISI O1 Steel
Length	0.468 m (total beam length)/ 0.445 m (exposed when clamped)
Thickness	0.0014 m
Width	0.051 m
Density	6628 kg/m^3
Mass	0.22 kg
Mass/Unit Length	0.49 kg/m
Young's Modulus	$2X10^{11}$ Pa
Shear Modulus	$7.5X10^{10}$ Pa
Area Moment of Inertia	$1.2X10^{-11}m^4$
Area Polar Moment of Inertia	$1.6X10^{-8}m^4$
Polar Second Moment of Area	$4.7X10^{-11}m^4$
Mass Moment of Inertia	$4.8X10^{-5}kgm^2$
Bending (Flexural) Rigidity (EI_y)	2.33 Nm^2
Torsional Rigidity (GJ)	3.51 Nm^2

Table 3.4: Average Structural Properties of Beam-03

Material	Tempered 1095 Spring Steel
Length	0.468 m (total beam length)/ 0.445 m (exposed when clamped)
Thickness	0.0016 m
Width	0.051 m
Density	7707 kg/m^3
Mass	0.29 kg
Mass/Unit Length	0.64 kg/m
Young's Modulus	$2X10^{11}Pa$
Shear Modulus	$7.5X10^{10}Pa$
Area Moment of Inertia	$1.7X10^{-11}m^4$
Area Polar Moment of Inertia	$1.7X10^{-8}m^4$
Polar Second Moment of Area	$6.6X10^{-11}m^4$
Mass Moment of Inertia	$6.3X10^{-5}kgm^2$
Bending (Flexural) Rigidity (EI_y)	3.32 Nm^2
Torsional Rigidity (GJ)	4.99 Nm^2

3.3 Estimates of Combined Properties of Wing/Beam Combination

In order to determine estimations for the Euler-Bernoulli uncoupled bending and torsion frequencies for the $s4^*$ *configuration* (Sections 3.3.1, and 3.3.2), some simple approximations were made. First, it was assumed that there was no inertial coupling. Second, the wing was approximated as a flat plate, as seen in Equation 3.1 (specifically for this equation, c is the chord, t_{max} is the maximum thickness of the chord, and S the span) which was used to find the density of the beam/wing combination. Third, as stated earlier, it was assumed that the structural stiffness properties were derived solely from the beam, i.e. the wing was assumed to not provide any structural stiffness. The combined properties of the wing/beam combination are thus summarized in Table 3.5.

$$Volume_{wing} = c \times t_{max} \times S \tag{3.1}$$

Table 3.5: Estimated $s4^*$ Combined Wing/Beam Properties for Beams-01,-02,-03

Configuration	$s2$	$s2$	$s4^*$	$s4^*$			
Beam #	Mass of Beam+Wing (kg)	Mass/Length (kg/m)	Flexural Stiffness of Beam (Nm^2)	Torsional Rigidity of Beam (Nm^2)	Volume of Wing (m^3)	Density of Beam+Wing (kg/m^3)	Area Polar Moment of Inertia of Wing (m^4)
01,02	0.3665	0.82	2.3324	3.5079	$1.2X10^{-3}$	6749	$2.9X10^{-7}$
03	0.4347	0.98	2.3324	3.5079	$1.2X10^{-3}$	7828	$2.9X10^{-7}$

It can be seen that the addition of the wing ($s4^*$ versus $s2$ configuration), drastically lowers the frequencies of the torsion modes, but not so much for the bending modes.

3.3.1 Euler-Bernoulli Uncoupled Bending Natural Frequencies

Using the Equations from Section 2.4.3, Subsection 2.4.3.1, the first three $s2$ modal frequencies for the uncoupled bending modes were found for all beams, as seen in Table 3.6. Estimations for the $s4^*$ bending modes (Table 3.6, last two columns) were made per Section 3.3, and using the combined mass per unit length of each beam/wing, as well as the flexural rigidity of the beams (Tables 3.3 and 3.4).

3.3.2 Euler-Bernoulli Uncoupled Torsion Natural Frequencies

Using the Equations from Section 2.4.3, Subsection 2.4.3.2, the first three $s2$ modal frequencies for the uncoupled torsion modes were found for all beams (i.e. $s2$ configuration) and can be seen in Table 3.7. Estimations for the $s4^*$ torsion modes (Table 3.7, last two columns) were made by using the density of the combined wing/beam per Section 3.3,

Table 3.6: Uncoupled Bending Natural Frequencies of $s2$ and $s4^*$ Configurations, All Beams

Configuration	$s2$	$s2$	$s4^*$	$s4^*$
Modes	f (Hz) Beams-01,-02	f (Hz) Beam-03	f (Hz) Wing and Beams-01,-02	f (Hz) Wing and Beam-03
1	6	6	5	4
2	38	40	30	27
3	107	112	83	77

as well as the the estimated polar second moment of area (I_p) per Equation 3.2, and the torsional rigidity of the beam (Table 3.7).

$$I_p = \frac{1}{3}c(t_{max})^3 \tag{3.2}$$

Table 3.7: Uncoupled Torsion Natural Frequencies of $s2$ and $s4^*$ Configurations, All Beams

Configuration	$s2$	$s2$	$s4^*$	$s4^*$
Modes	f (Hz) Beams-01,-02	f (Hz) Beam-03	f (Hz) Wing and Beams-01,-02	f (Hz) Wing and Beam-03
1	104	108	24	22
2	312	325	71	66
3	519	542	118	110

3.3.3 Finite Difference Method Modal Frequencies for Beams-01,02, wing and Rotary Base Configuration

A finite difference method (FDM) model of the wing/beam combination and rotary base was solved using a time-dependent model to find the natural frequencies of the $s4^*$ configuration (recall that the C.G. is not aligned with the P.A. (Figure 3.7). The natural frequencies of the system were found using arbitrary pitch initial conditions yet, despite only being given pitch initial conditions, all modes were excited due to inertial coupling. The FDM model was validated against the Euler-Bernoulli analytical frequencies for the $s2$ configuration (no inertial coupling, P.A. and beam C.G. aligned) and $s4^*$ configuration (inertial coupling present, P.A. not aligned with Wing/Beam C.G.). The FDM model $s4^*$ results can be seen in Table 3.8; the dominant modes were inferred from the Euler-Bernoulli results.

Table 3.8: $s4^*$ Configuration (Beams-01,-02) Natural Frequencies (Hz)

Modes	f (Hz)	Dominant Motion
1	2.56	Pitch
2	5.0	1^{st} Bending
3	29.4	Unknown

3.4 Instrumentation

A total of eight valid tests, A-H, and their results are presented in this thesis, the specific details of which can be seen in Appendix E.4. Table 3.9 indicates the types of information recorded for each specific test; note that an 'x' in a cell indicates that either the data were not recorded, or not considered valid. Details on the no-flow free decay data obtained from the instrumentation will be explained in Section 3.5.

Table 3.9: Wind Tunnel Tests: Recorded Sensor/Instrumentation Data

Test	Torsion Strain Gauge	Bending Strain Gauge	Potentiometer	Accelerometer	Pressure Transducer Readout	Beam #	# Pitch Springs
Test A	x	x	✓	✓	Multimeter	01	2
Test B	x	x	✓	✓	Multimeter	01	2
Test C	x	x	✓	✓	Multimeter	01	2
Test D	x	x	✓	✓	Multimeter	01	2
Test E	x	x	✓	✓	Multimeter	01	2
Test F	x	✓	✓	✓	Labview via USB	02	2
Test G	x	✓	✓	✓	Labview via USB	03	2
Test H	x	x	✓	x	Labview via USB	03	0

The conditioned strain gauge and accelerometer data, along with the potentiometer data, were wired into the National Instruments NI-9205 C Series Voltage Input Module, which in turn fed into the National Instruments NI CDAQ-9174 NI CompactDAQ (limiting value of 10V) which connected to the computer and LabVIEW via USB. As will be further discussed in Section 5.8, no torsion data is presented, as the validity of the data were questioned due to the likely effects of saturation of the strain gauges themselves, as well as damage to the wires connecting to the strain gauge box. Valid bending strain gauge data were not obtained for Tests A-E due to issues with saturation and inadequate gain settings as a result of larger than expected deflections at the tip; nevertheless, qualitative bending deflections were observed. Bending strain gauge data were obtained for Tests F-G. Similarly, accelerometer data were recorded for Tests A-G. However, in terms of strain gauge and accelerometer data, only the results of Test F are included in this thesis, since empirical data provided by the trial tests, and Tests A-E meant that the motion of the wing/beam-01,-02 combination was fairly well understood and relatively predictable. Potentiometer and pressure transducer data were captured for all tests.

The overall goal of the instrumentation (strain gauges, potentiometer, and accelerometers) was to document and analyse the dynamics of the wing, and in particular, the motion at the root and the tip. These three types of sensors will now be explored in greater detail.

3.4.1 Strain Gauges

Placement

Jehan wrote that researchers typically use the directives which stipulate that, ”When choosing a sensor location, one can either place a sensor to maximize the measurement of a specific mode independent of others; place more than one sensor, each targeting specific modes; or place a sensor in a location that optimally detects ‘all’ important modes.” [45] The strain gauges were placed per the second directive, at appropriate locations to capture bending and torsion, separately.

The strain gauges were placed at 0.09 L and 0.15 L (end of bending strain gauges, and end of torsion strain gauges, respectively), since they needed to be nestled in a location unexposed and intended to facilitate resistance to being damaged by the pressure exerted on the beam by the enclosing wing shell per Figure 3.15. Based on the work of Jehan, who applied several different solution methods (such as FEM, Rayleigh-Ritz, etc.) to obtain the mode shapes of a non-dimensional cantilever beam (Figure 3.14), the locations of the strain gauges do not coincide with any node for the first eight mode shapes (for a thin, flexible cantilever beam). This is important, as a sensor placed ”in the vicinity of a node will produce erroneous information about the contribution of this mode to the system response [46] [45],” and thus the sensors were placed as carefully as possible to meet all criteria mentioned.

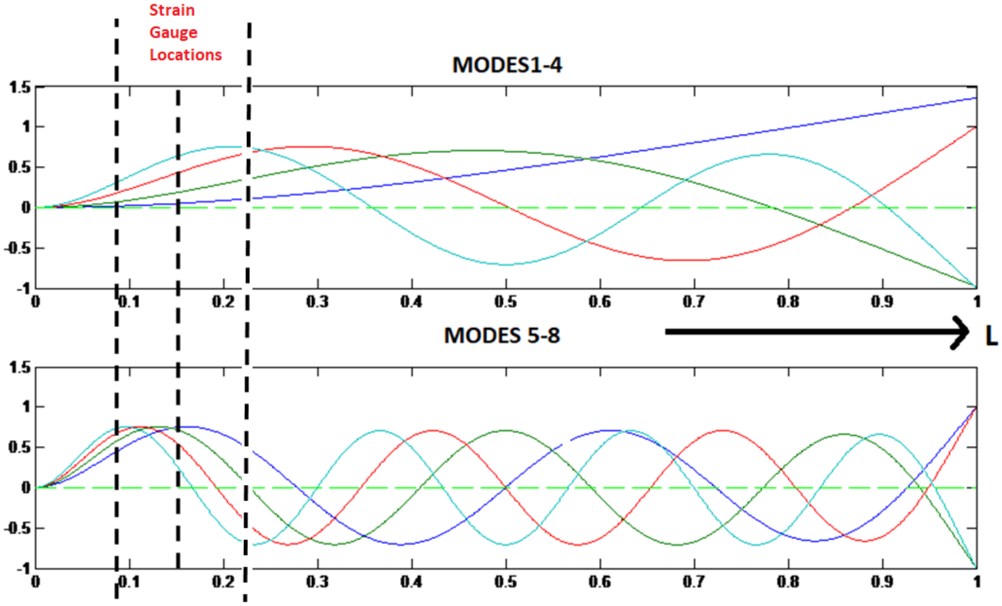

Figure 3.14: Location of Nodes for Eight Mode Shapes of a Thin, Cantilever Beam of Unit Length; Adapted from [45]

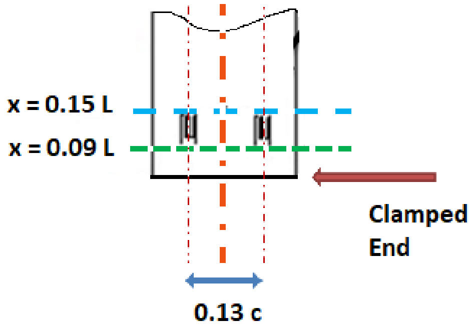

Figure 3.15: Relative Location of Bending Strain Gauges; Adapted from [21]

The strain gauges were placed in full bridge configuration, in such a way to compensate for temperature effects. The bending strain gauges were positioned as seen in Figure 3.16, to compensate for torsion effects; the torsion strain gauges were positioned as seen in Figure 3.17, which compensated for bending effects.

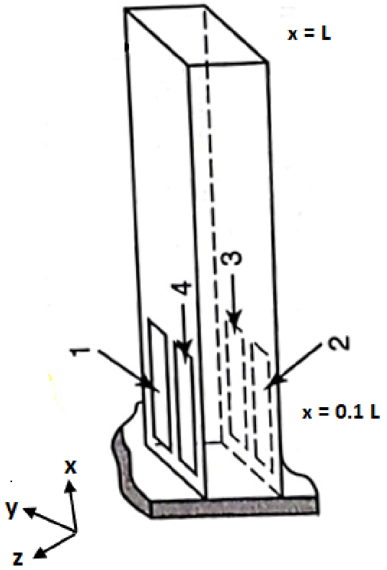

Figure 3.16: Full Bridge Bending Strain Gauge Application; Adapted from [47]

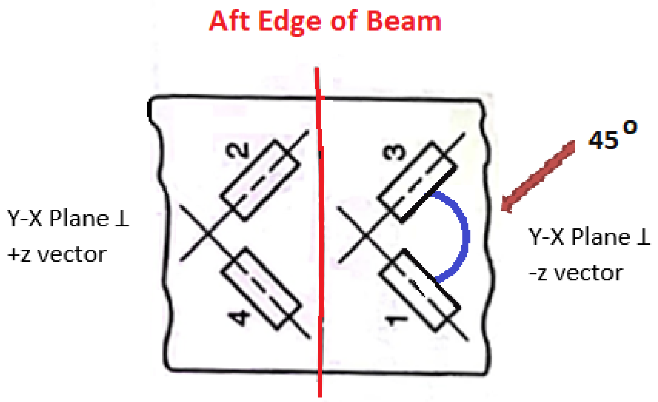

Figure 3.17: Full Bridge Torsion Strain Gauge Application; Adapted from [47]

Model Numbers and Settings

The strain gauge model numbers and their parameters can be seen in Table 3.10. A new model was used for tests G-H simply because the model used in tests A-F had become discontinued. The gains for Tests A-E were set at 10.5 (bending) and 10.5 (torsion), however, analysis of the results showed that amplifying the bending deflection by 10.5 caused the results to exceed the Labview and DAQ limits, abruptly truncating the peaks of the signal. Thus, a sensitivity analysis was done, and it was determined that the optimal bending gain setting was 2 (the torsion remained at 10.5). In general, a gain of greater than 1 is desired to obtain an adequate resolution of the data.

Table 3.10: Strain Gauge Models

Model/Type	Resistance (Ω)	Gage Factor	Excitation Voltage (V)	Tests
Vishay EA-06-240LZ-120	$120.0 \pm 0.3\%$	$2.045 \pm 0.5\% @ 75°C$	3	A-F
Showa N11-FA-5-120-11	$120 \pm 0.3\%$	$2.11 \pm 1\%$	3	G-H

The strain gauge box consisted of a Vishay Measurements Group Model 2150, comprised of a 2110 Power Supply of 4V, 2130 Output Display, set on Channel 5 with × Attenuation, and a 2120 strain gauge conditioner. The 2120 conditioner provided the means to balance the strain gauges to "zero" strain by using balancing knobs and calibration switches. The gain could also be adjusted. A 2130 digital readout was used to switch on the strain gauges, and set the channel as well as view the strain values; the attenuation was set to 1. The Labview limits were set to $\pm 10V$.

Damage and Re-Applications

Prior to testing, the first set of strain gauges were applied by our colleagues at Carleton University, and remained as applied for Tests A-E. However after the failure of the beam after Trial Test 10 (Appendix E.3.5), new strain gauges were applied in-house at RMC. Subsequent Tests F-H required several more re-applications due to damage caused by testing (compression of gauges, and issues with saturation). Thus, each time the old strain gauges needed to be scraped off, and new ones applied. Since the strain gauge placement, bonding and materials were all adequately similar, it was inferred that a new calibration curve could likely be as close as 98% accurate in relation to the old calibration curve [48] and indeed, no appreciable differences were noted.

Calibration to Convert Voltage Strain to Tip Displacement

The strain gauge outputs were strain in voltage, and so a calibration routine was needed. The calibration was performed by using a specially designed in-house calibration jig (Appendix D, Figures D.1 and D.2). The jig was installed in the section, and a small light was used to project the zero degree baseline onto a protractor placed on the wind tunnel ceiling. When the upper bolts were locked, the beam could be twisted in torsion, up to a maximum of about $3 - 5°$ due to the high stiffness in torsion. For bending, for each side, one bolt would be screwed in, pushing the tip of the beam by a prescribed deflection measured by a ruler, and the ensuing voltage recorded.

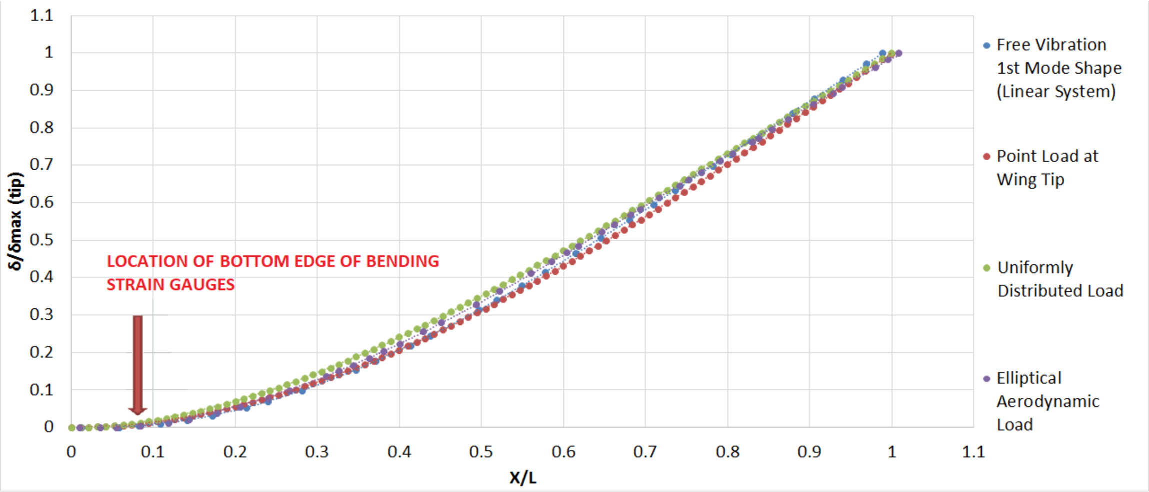

Figure 3.18: Strain Gauge Tip Bending Deflection Calibration

Figure 3.18 shows comparisons between the tip deflection due to: a) free vibration of the 1^{st} mode, b) a point load at the wing tip, c) a uniformly distributed load (UDL), and d) an elliptical aerodynamic load. Cases b-d all appear to be good approximations of the shape of the free vibration of the 1^{st} mode (especially when comparing the points of the curve at around 0.12 L). Thus, the calibration curve in Figure D.6 was found by using Equation D.3.

3.4.2 Potentiometers

Model Numbers and Settings

The rigid pitch data at the root were measured using a potentiometer, i.e. a contactless rotary magnetic actuator, and the corresponding encoder body. The two different models utilized for testing are seen in Table 3.11. The RLS model was used mostly to capture SAO and the Contelec model used mostly to capture LAO, which are the two types of expected LCO's which are being investigated (recall that SAO stands for small amplitude oscillations and LAO stands for large amplitude oscillations). Since the Contelec model has better resolution, the PSD's generated with its data will yield more distinct peaks than that of the RLS model. Both potentiometers were powered by an Agilent U8002A Single Output DC Power Supply, set at 5V and 0.02A resistance, and the Labview limits were set to $\pm 5.00V$.

Table 3.11: Potentiometers

Make/Model	LCO Captured	Resolution (*deg*)	Tests
RLS RMA05A3A00 (actuator) with RM22VA0010B10F1B00 (encoder body)	SAO	0.5	A-E
Contelec Co-Vert-X 22E2 836 221 505 78107 1307 1 (actuator and encoder body)	LAO	0.18	F-H

Calibration to Convert Voltage to Degrees

The calibration was performed by using a protractor on the floor of the wind tunnel. The rotary base was systematically turned to $\pm 0°, \pm 30°, \pm 60°$, and $\pm 90°$ and held until steady, while the potentiometer output voltage was recorded. This allowed for a direct correlation between the root rigid pitch angle and the voltage output. The potentiometer $0° AOA$ baseline was set to 2.5 V by careful installation, in order to allow the full range of motion of 0-5V $(0 - 90°)$. As no valid LCO amplitude exceeded 90°, this calibration routine was suitable and valid. The results of the calibrations can be seen in Appendix D, Subsection D.1.

3.4.3 Accelerometers

Model Numbers and Settings

The tip acceleration at two positions was measured using two accelerometers. Both were model PCB Electronics 352C22 Accelerometers. The details of these accelerometers can be seen in Table 3.12. The accelerometers were conditioned by a PCB electronics 483C05 signal conditioner (conditioner gain factory-set to 1, Labview gain set in-house to 1), and the output was in volts. The Labview limits were set to $\pm 0.20V$.

Placement and Calibration to Convert Voltage to Acceleration

The accelerometers are installed on the beam tip, as seen in Figure 3.9. The accelerations were recorded during testing, and post-processed by multiplying by the manufacturer-provided sensitivity (Table 3.12), filtering and then truncating the signal to the appropriate window of time to capture the information obtained during each steady-state LCO. The accelerometers were placed on only one side of the beam, approximately ±0.013 m away from the pitch axis, per Figure 3.19 and in such a way that the top of each accelerometer was aligned with the top of the beam at location x = L.

Table 3.12: Accelerometer Parameters and Locations

Serial Number	Sensitivity @ 100 Hz ($mV/m/s^2$)	Tests	Position
151335	1.038	F-H	1
151336	1.068	A-H	2
151337	1.064	A-E	1

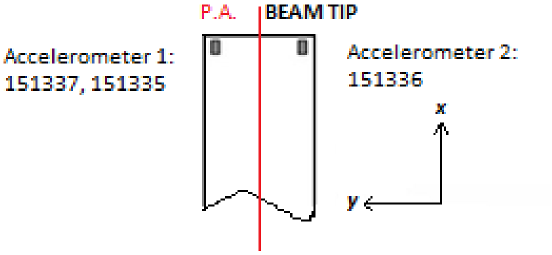

Figure 3.19: Placement of Accelerometers 1 and 2; Adapted from [27]

3.4.4 Pressure Transducer

A pitot static tube recorded the total and static pressures. The pressure transducer, was composed of an Agilent 34401A 6 1/2 Digit Multimeter output (s/n MY41026264) and an Agilent E3615A DC Power Supply, set at 21.6 V (the effects of a small change in voltage supply was tested and the pressure transducer results were found to change by only a negligible amount.) The power supply was linked to the Omega Engineering Inc. Pressure Tranducer, PX154-O10DI, Serial # 35534-1T10. For tests A-E, the results of the pressure transducer were read off the multimeter once the LCO had reached steady-state. However, for Tests F-H, the data were recorded through Labview via USB in order to gain more accurate readings.

3.5 No-Flow (Free Decay) Tests

No-flow free decay tests were performed before and after testing. The purpose was to determine a) the measuring noise characteristics, b) the pre-test no-flow bias which captures the exact orientation of the wing, and c) the modal characteristics frequency content of the system i.e. frequency and damping. These tests are equivalent to GVT (Ground Vibration Tests) performed on full-scale test aircraft, whose results are used to calibrate a finite element model. In our case, these tests will also be used to calibrate FDM results used at The Royal Military College of Canada and Carleton University. The steps for obtaining the free decay data are listed below, in the proper sequence as they are implemented during each series of wind tunnel testing. Note that the wind tunnel motor and clutch are referenced below; the clutch ON indicates that the clutch is engaged. The purpose of performing FDT1 was to check that the wing apparatus properties had not changed, and the purpose of performing FDT2 was to characterize the flutter apparatus.

1. Noise Data:

    a) $s4^*$ configuration; **pitch lock OFF**; **wind tunnel OFF**
    b) $s4^*$ configuration; **pitch lock OFF**; **motor ON**
    c) $s4^*$ configuration; **pitch lock OFF**; **motor and clutch ON (zero RPM)**

2. Free Decay 1 (FDT1):
    a) $s4^*$ configuration; **pitch lock ON**; **motor and clutch ON (zero RPM)**; apply bending initial condition at wing tip (Performed Twice)
    b) $s4^*$ configuration; **pitch lock OFF**; **motor and clutch ON (zero RPM)**; apply pitch initial condition at wing root (Performed Twice)

3. TESTING

4. Free Decay 1 (FDT1):
    a) $s4^*$ configuration; **pitch lock OFF**; **motor and clutch ON (zero RPM)**; apply pitch initial condition at wing root (Performed Twice)

   b) $s4^*$ configuration; **pitch lock ON**; **motor and clutch ON (zero RPM)**; apply bending initial condition at wing tip (Performed Twice)

5. Free Decay 2 (FDT2):
   a) $s4^*$ configuration; **motor and clutch OFF**; apply pitch initial condition at wing root (Performed Twice)
   b) $s2$ configuration; **motor and clutch OFF**; apply pitch initial condition at wing root (Performed Twice)
   c) s1 configuration; **motor and clutch OFF**; apply pitch initial condition at wing root (Performed Twice)

The no-flow data were used to generate raw time histories, histograms and power spectral densities of the noise data for a) the wind tunnel motor off, b) the wind tunnel motor on, and c) the wind tunnel motor on with clutch. The histograms served to provide information on the spread and quality of the data, and indicate biases and non-linearities; if the time history range selected produced an approximate Gaussian (normal) distribution, it was considered that the data were valid and there was no external source of noise which could interfere with the data. As an example, the baseline pitch data for the motor and clutch on for one particular test is presented in the form of time histories, a power spectral density (PSD) and histogram in the following figures. No external excitation were given, except for ambient noise.

An example of an unfiltered pitch PSD (obtained from the potentiometer), can be seen in Figure 3.20. Figure 3.20 indicates peaks located at approximately 60, 120 and 180 Hz. These values (i.e. 60 Hz, and its corresponding superharmonic peaks) are consistent with historically known wind tunnel noise, as well as ambient noise from surrounding areas and instrumentation.

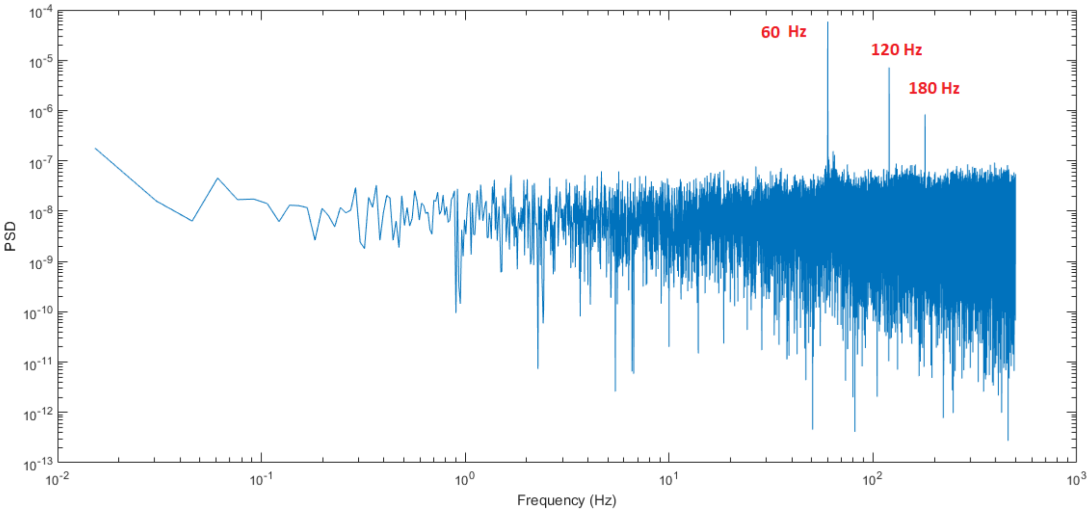

Figure 3.20: PSD for Unfiltered Wind Tunnel Potentiometer Data, Motor and Clutch On (Zero RPM) Data, Test F March 15, 2019

A summary of the unfiltered PSD peaks found for all the remaining instrumentation can be found in Table 3.13. Note that both accelerometers and both strain gauges displayed peaks around 30 Hz, which is consistent with the findings of Poirel and Yuan [5]. The bending strain gauge further showed smaller peaks at 2.564 Hz and 19.07 Hz, while the torsion strain gauge showed peaks at 10.01 and 24.01 Hz. In general, the magnitude of the peak heights for frequencies less than 30 Hz were relatively small compared to the peaks at 60 Hz and greater, as illustrated in Figure 3.21.

Table 3.13: Summary of No-Flow Unfiltered PSD Results, Motor and Clutch On (Zero RPM) Data, Tests A-F, $s4^*$ Configuration

Accelerometer 1 (Hz)	Accelerometer 2 (Hz)	Bending Strain Gauge (Hz)	Torsion Strain Gauge (Hz)
27.96	30	2.564	10.01
30.03	60	19.07	24.01
59.94	90	30	30
89.98	120	60	60
120	180	120	120
240	-	175	180
-	-	418.8	240.1
-	-	461.4	-

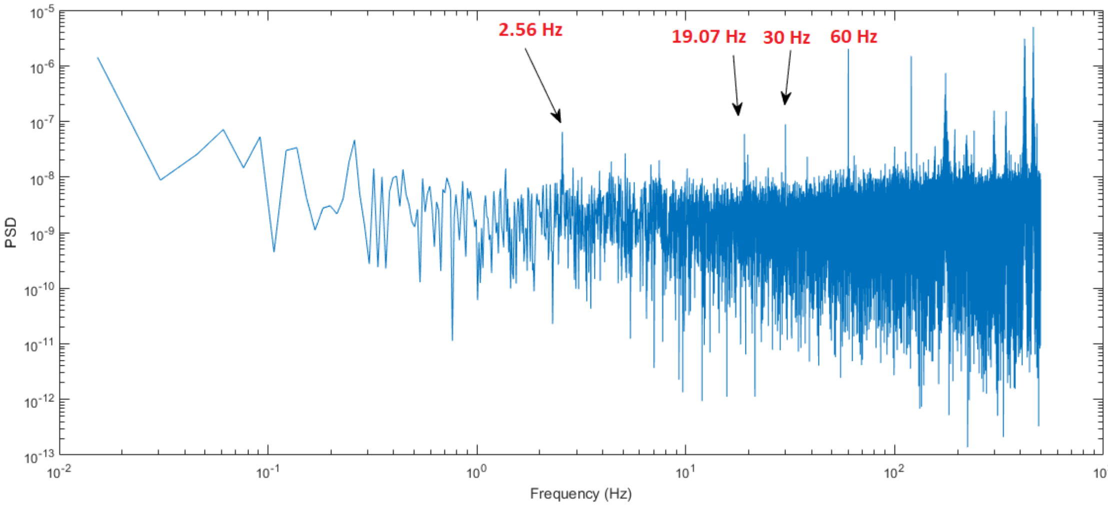

Figure 3.21: PSD for Unfiltered Wind Tunnel Bending Strain Gauge Data, Motor and Clutch On (Zero RPM) Data, Test F March 15, 2019

Recall from Sections 3.3.1 and 3.3.3 that the 1^{st} uncoupled bending modal frequency for a cantilever beam is calculated to be 4-5 Hz, while the 1^{st} modal frequency of the wing/beam combination is predicted to be at 5 Hz. Thus, it was determined that an average low-pass filter of magnitude 30-40 Hz, dependent upon review of each individual time history trace, would be sufficient to ensure that the measurement noise peaks were removed for the pitch data. Similarly, a low-pass filter of 6 Hz was applied to the bending strain gauge data; since data were only analyzed in the SAO region, this filter value was assumed to be appropriate as the higher non-linear effects would only occur in the LAO region due to the large bending deflections.

Initially, the low-pass filter for the accelerometers was 40 Hz. However, the time histories were observed to show irregular waves, especially at higher airspeeds. The filter frequency was then further lowered to 6 Hz, after further study of the time traces and unfiltered PSD's, in order to capture the effects of the dominant frequencies only.

A summary of all filter values can be seen in Table 3.14; a slightly lower filter was used for Test G as it displayed noise characteristics slightly different for Tests A-F, likely due to the use of a different beam material. In general, it is worth noting that there would have been additional noise due to significant vibration which occurred during testing as the wing/beam oscillated violently, as well as subsequent and excessive interference between moving wires.

Table 3.14: Summary of Low-Pass Filters Applied to Time History and Histogram Data

Test	Instrument	Beam #	Low-Pass Stopband Frequency (Hz)	Low-Pass Passband Frequency (Hz)
A	Potentiometer	01	40	35
B	Potentiometer	01	40	35
C	Potentiometer	01	40	35
D	Potentiometer	01	40	35
E	Potentiometer	01	40	35
F	Potentiometer	02	40	35
F	Bending Strain Gauge	02	6	5
F	Accelerometer (1,2)	02	6	5
G	Potentiometer	03	35	30

Figures 3.22 and 3.23 illustrate the unfiltered time history of the pitch response. The filtered response can be seen in Figures 3.24 and 3.25. Note that the potentiometer $0° AOA$ value was manually set to $\approx 2.5V$, which is illustrated in all plots.

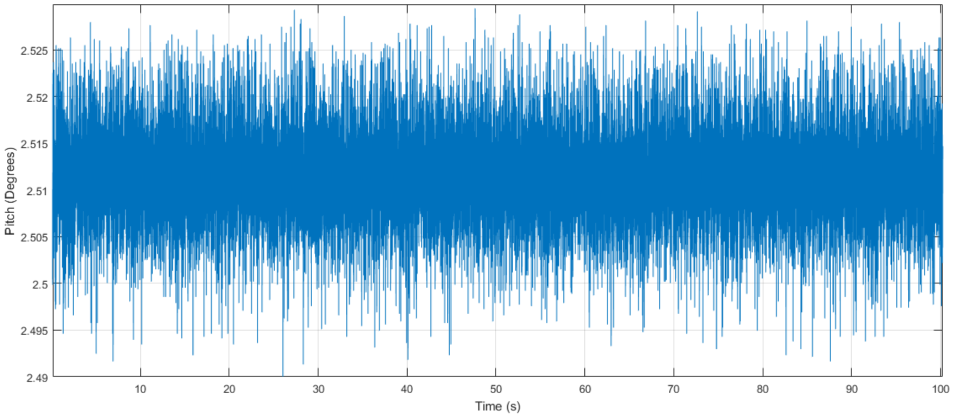

Figure 3.22: Time History for Unfiltered Wind Tunnel Potentiometer Data, Motor and Clutch On (Zero RPM), Test F March 15, 2019

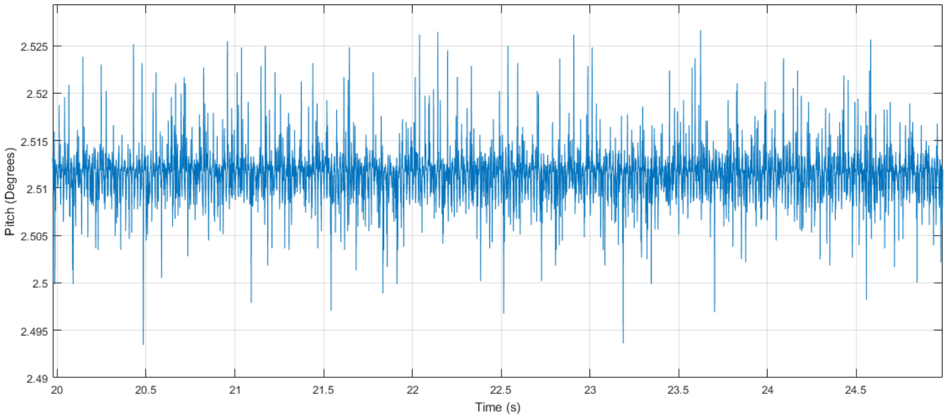

Figure 3.23: Time History for Unfiltered Wind Tunnel Potentiometer Data, Motor and Clutch On (Zero RPM), Test F March 15, 2019 (Zoomed View)

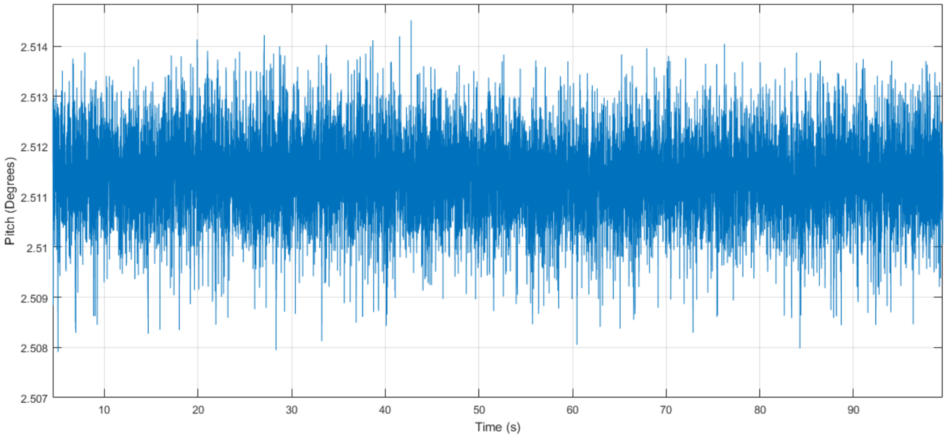

Figure 3.24: Time History for Filtered Wind Tunnel Potentiometer Data ($F_{stop} = 40$ Hz, $F_{pass} = 35$ Hz), Motor and Clutch On (Zero RPM), Test F March 15, 2019

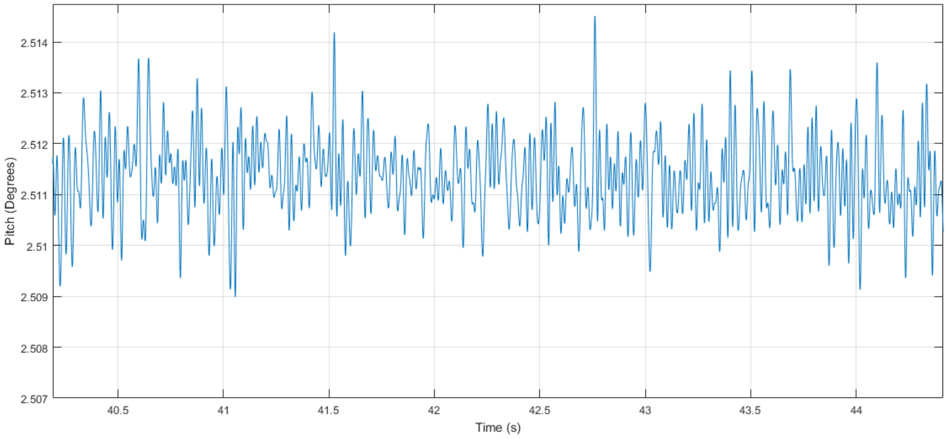

Figure 3.25: Time History for Filtered Wind Tunnel Potentiometer Data ($F_{stop} = 40$ Hz, $F_{pass} = 35$ Hz), Motor and Clutch On (Zero RPM), Test F March 15, 2019 (Zoomed View)

The corresponding filtered histogram (Figure 3.26) shows an approximately Gaussian distribution, indicating that this filtered data is reasonable and hence we can re-zero the data using the bias from the histogram.

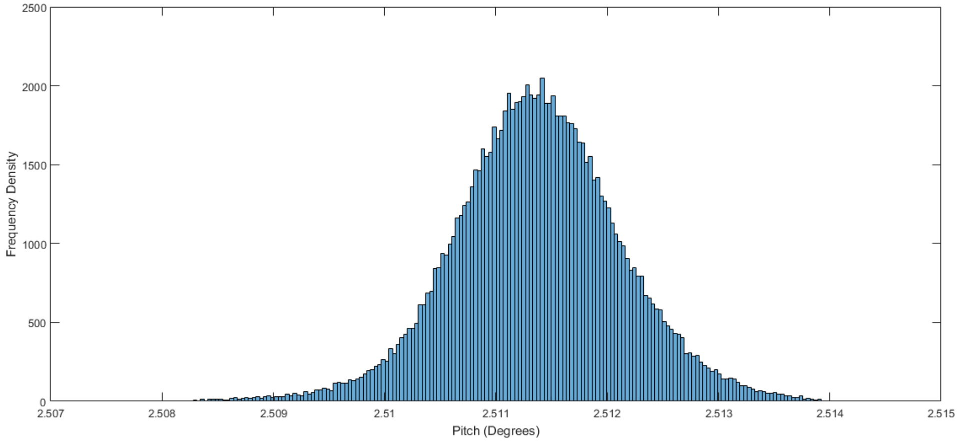

Figure 3.26: Histogram for Filtered Wind Tunnel, Motor and Clutch On (Zero RPM) Data ($F_{stop} = 40$ Hz, $F_{pass} = 35$ Hz), Test F March 15, 2019

While data from all sensors/transducers were recorded, the time history data from the potentiometer is especially critical for calculating the frequency characteristics of the system.

As laid out in the beginning of Section 3.5, FDT1 allowed determination of the difference between pre-test and post-test damped natural frequencies, damping ratios, mass moments of inertia and the damping coefficients for each set of tests, for the $s4^{*}$ configuration. FDT2, used to determine the $s2$ and $s1$ data, were only performed post-test due to time constraints during the available testing window and concerns of damaging the wing test apparatus from repeated installing/dismantling. Overall, the following sections will show that the experimentally observed free decay damped natural frequencies match well with the values calculated found in Sections 3.3.1 and 3.3.2 for all beams. Free-decay testing was performed for all beams, except Test G, where damage to the strain gauges prevented the recording of data, and Test H, where there was no pitch stiffness.

In summary, it was felt that filtering the pitch (potentimeter) flow data over 35-40 Hz satisfactorily removed the measurement noise, while filtering over 6 Hz was appropriate for the tip displacement data (bending strain gauge) and 20 Hz for the tip acceleration (accelerometers). Hence, it was considered that all measurements below this frequency range were physical and related directly to the aeroelastic dynamics, and would illustrate the contribution of all relevant modes. In the following sections, the results of the damped natural frequencies, damping ratios, and mass moments of inertia will be presented for the structural component of the wing/beam apparatus. For the damped natural frequencies and damping ratios, there will be two cases: a) free pitch and b) locked in pitch; all other data will be for case a) only. These values not only provide information on changes in the structure, but are also used for determining the damping coefficients. Finally, all data representing the pitch motion is obtained from the potentiometer, while tip bending deflection data is obtained from the bending strain gauges.

Representative Plots and and Procedure of Free Decay Analysis

The general process for obtaining the results in the following section was comprised of gathering the raw no-flow free decay data for the pre-test and post-test cases for the $s4^{*}$ configuration (free pitch and locked in pitch). The peak heights and times were collected and used to find averages of the logarithmic decrement, damping ratio, and damped natural frequency. Equation A.9 was used to find the mass moment of inertia in pitch, and in bending, respectively (Equations located in Appendix 3.5.3. Finally the damping was determined, which will be further examined in section 3.5.4.

Figure 3.34 represents an example of a free decay time history trace of the $s4^{*}$ configuration. The data were converted from voltage to degrees by using the appropriate calibration curve (Section D.1). The data were then re-zeroed and filtered, using a stopband frequency of 20 Hz, and a pass band frequency of 18 Hz (to further remove measurement noise). The initial filter characeristics were chosen such that clearly defined peaks could be obtained, without removing the characteristics of the dominant frequency and more significant superharmonic peaks, as well as to remove ambient noise. However, a lower filter was required to isolate the behaviour of the system resulting from the contribution of the first (pitch dominated) mode. Thus, Figure 3.29 shows the data filtered at $F_{stop} = 4Hz, F_{pass} = 3Hz$ in order to focus on the pitch dominated mode only. These filters were used for the pitch data seen in the ensuing sections. Since there is inertial coupling, all modes should be excited. However, upon examination of both the time histories (the apparent shift in time period, as well as the pre-perturbation oscillations are an artificial result of the filtering process) suggested that while all modes may be excited, the pitch mode is dominant for the potentiometer data recorded at the wing root.

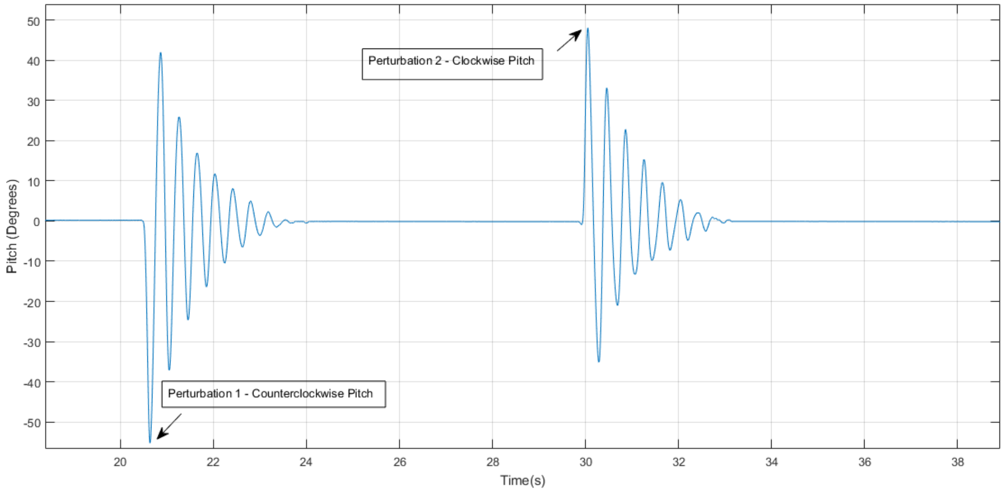

Figure 3.27: Representative Filterered Free Decay Time History For All Modes ($F_{stop} = 20$ Hz, $F_{pass} = 18$ Hz) - Post-Test C November 2, 2017, $s4^*$ Configuration, Free Pitch

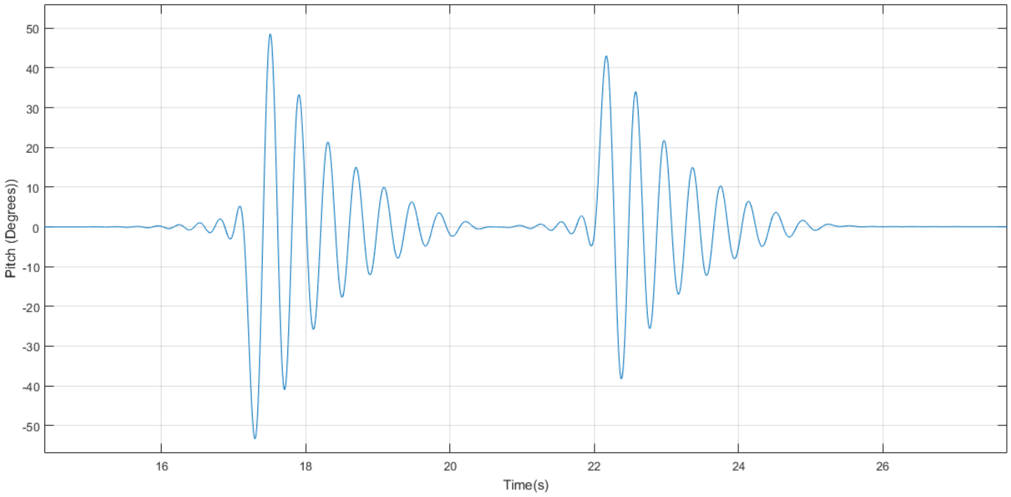

Figure 3.28: Representative Filtered Free Decay Time History For Pitch Dominated Mode ($F_{stop} = 4$ Hz, $F_{pass} = 3$ Hz) - Post-Test C November 2, 2017, $s4^*$ Configuration, Free Pitch

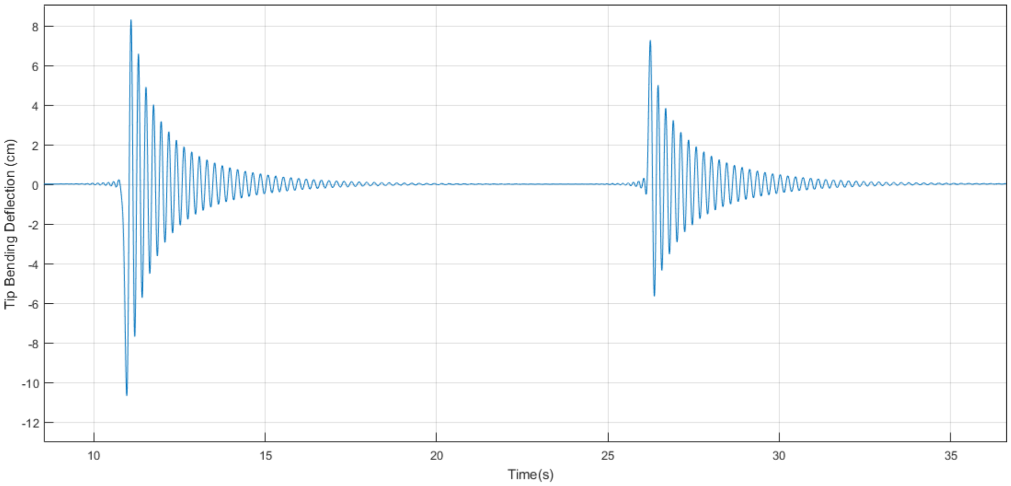

Figure 3.29: Representative Filtered Free Decay Time History For Bending (Strain Gauge) Deflection at Tip (F_{stop} = 7 Hz, F_{pass} = 6 Hz) - Post-Test C November 2, 2017, $s4^*$ Configuration, Locked in Pitch

3.5.1 Damping Ratios

In order to verify that the damping ratios obtained were valid, the instantaneous damping ratio for each set of peaks was plotted versus the height of each peak. Examples of these plots can be seen for the case of free pitch in Figure 3.30, and locked in pitch for Figure 3.31. The damping ratios for free pitch usually varied greatly for the lower peaks, where dry friction in the rotary base affects the system damping. For locked in pitch, there is freeplay between the beam and wing, as well as geometric non-linearities due to large deflections of the beam. For both the free pitch and pitch locked cases, the region which demonstrated a linear trend was selected for analysis. (See red box in Figures 3.30 and 3.31); note also that results were taken from the average of several perturbations.

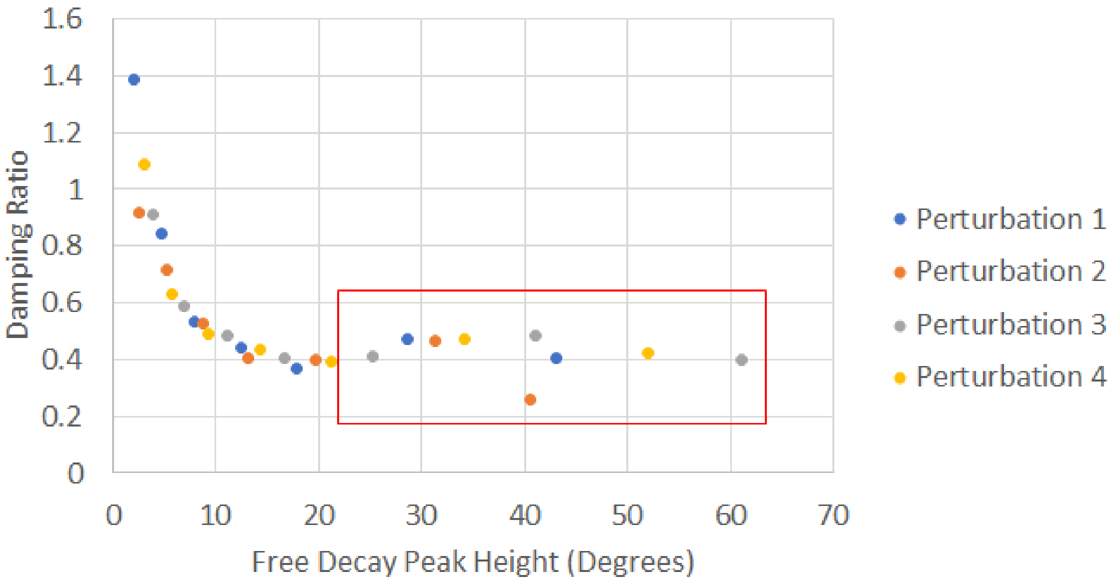

Figure 3.30: Sample Plot: Test C Free Decay Free Pitch Damping Ratio versus Height of Peaks for $s4^*$ Configuration

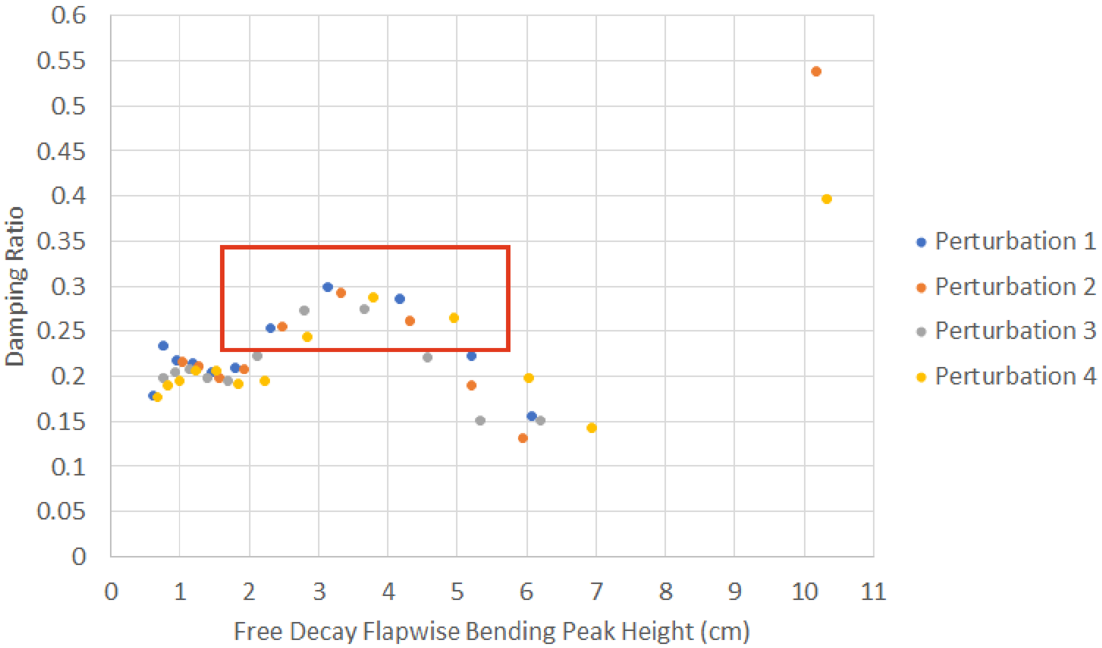

Figure 3.31: Sample Plot: Test D Free Decay Locked Pitch Flapwise Bending Damping Ratio versus Height of Peaks for $s4^*$ Configuration

3.5.1.1 Free Pitch

Figure 3.32 shows the pre-test and post-test damping ratios for the $s4^{*}$ configuration. The damping ratios generally range from 0.04 -0.11 and suggest a high degree of inconsistency between tests, but not a degree of change between pre-test and post-test results. Since the majority of damping ratios are less than 0.11, it was assumed that it was reasonable to approximate the natural frequency as the damped natural frequency.

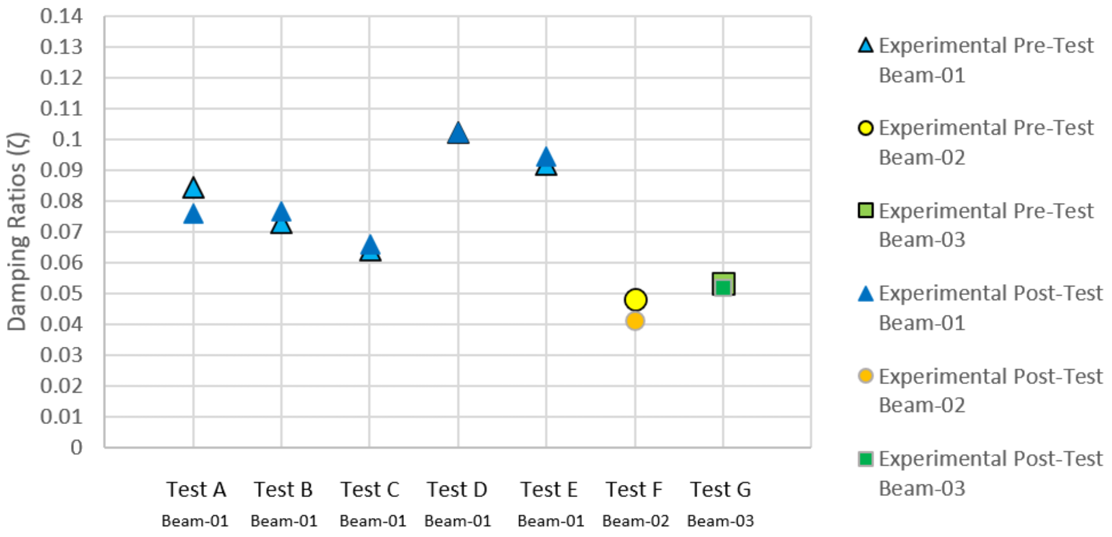

Figure 3.32: Comparison of $s4^{*}$ Free Decay Damping Ratios in Free Pitch

3.5.1.2 Locked in Pitch

Figure 3.33 shows the pre-test and post-test $s4^{*}$ damping ratios while locked in pitch. The values range from 0.024-0.042. Unlike the case of free pitch where, despite apparent beam failure for Test F, the pre-test and post-test values are similar, Figure 3.33 illustrates that the effects of the failure cause a noticeable drop in damping ratio. Furthermore, in general, there is also an appreciable difference between pre-test and post-test values for Tests C and D; the reason for this is uncertain.

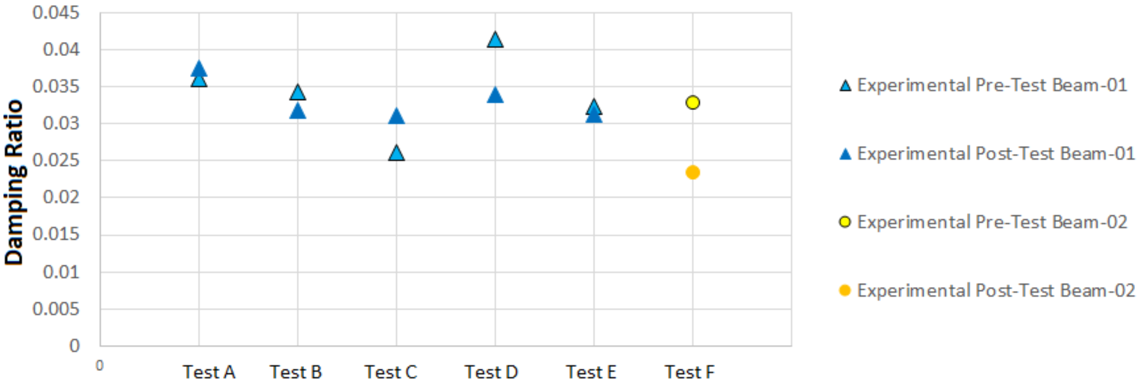

Figure 3.33: Comparison of Pre-Test and Post-Test $s4^*$ Free Decay Damping Ratios in Pure Bending

3.5.2 Damped Natural Frequencies

3.5.2.1 Free Pitch

Figure 3.34 shows the pre-test and post-test data for the $s4^*$ configuration (calculated using Equation A.9, Appendix3.5.3), as well as the analytical damped natural frequency estimations for all beams. The natural frequency estimations were made by calculating the analytical mass moment of inertia for the beam (Appendix A.3). The analytical mass moment of inertia for the $s2$ configuration can then be found via Equation A.14, Appendix A.3. Finally, the analytical $s4^*$ mass moment of inertia can be found using Equation A.15, Appendix A.3. This data is provided for Tests A-G (recall that Test H is not considered because there is no pitch stiffness). In general, the pre-test and post-test damped natural frequencies for the $s4^*$ configuration are relatively close, except for Test F where the post-test value is 1.6 Hz; similarly, the damped natural frequencies remain relatively close between tests, again with the exception of Test F. On average, the $s4^*$ values range from around 2.4-2.7 Hz. The $s4^*$ values are all on the order of magnitude of the estimated analytical $s4^*$ configuration 1^{st} modal frequencies (Beams-01,-02,-03). In terms of accuracy of the results in this section, previous research performed by Koenig has suggested that the uncertainty in the damped natural frequencies is likely approximately 3% [49] [50].

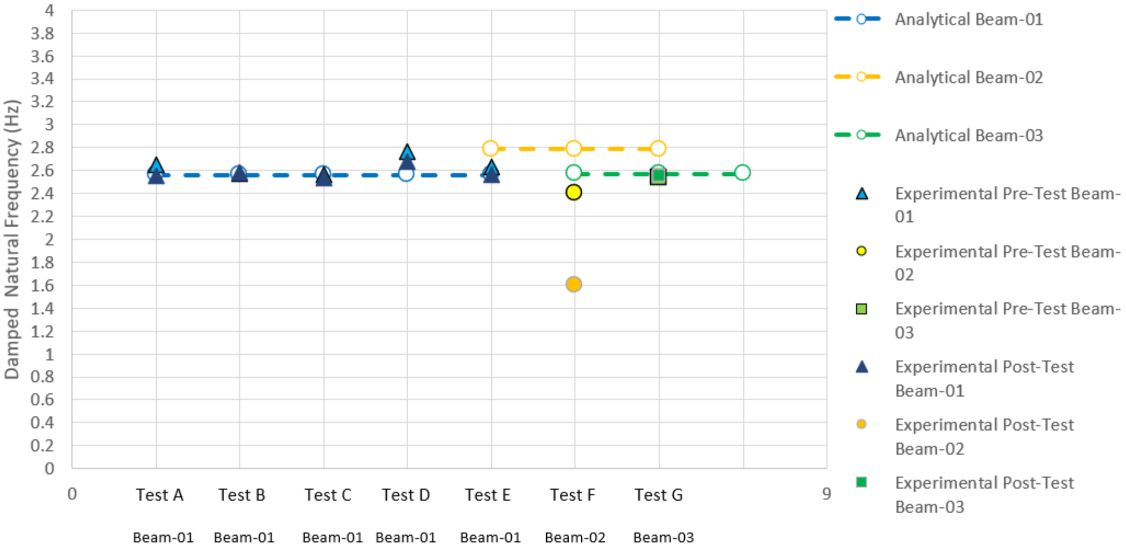

Figure 3.34: Comparison of $s4^*$ Free Decay Damped Natural Frequencies in Free Pitch, Performed Pre-Test and Post-Test

3.5.2.2 Locked in Pitch

The pre-test and post-test damped natural frequencies for the $s4^*$ configuration locked in pitch can be seen in Figure 3.35, as measured by the strain gauges (calculated by using Equation A.10, AppendixA.3.4). Note that the frequencies do not vary greatly between pre-and post-test values and the average damped natural frequencies range from around 4.1-5.0 Hz. On average, the frequency magnitudes are comparable to the estimation of the $s4^*$ configuration 1^{st} modal frequency in bending (Section 3.3.1, Table 3.6).

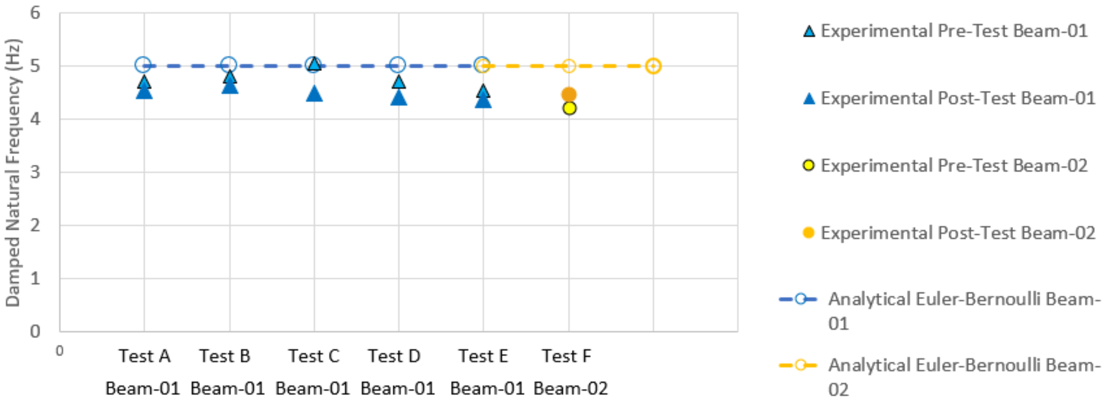

Figure 3.35: Comparison of $s4^*$ Pre-Test and Post-Test Free Decay Damped Natural Frequencies For Pitch Locked

3.5.3 Mass Moments of Inertia

Assuming that the structural terms are linear, the mass moments of inertia (about the pitch axis) of the beam, rotary base and wing can be calculated. First, the $s1$ configuration is set-up, and a perturbation is applied to the rotary base (root). The time history is recorded via the potentiometer, and by using a logarithmic decrement analysis, the natural frequency of the $s1$ system (i.e. rotary base only) is thus found. Since the average damping ratio is small ($\zeta \leq 0.11$ Per Section 3.5.1), we can assume that the natural frequency is close to the damped natural frequency. The mass moment of inertia for the $s1$ configuration can be found by applying Equation 3.3, given that we know the spring stiffness (Appendix A.2). Next, the beam is installed and a perturbation is applied to the rotary base. However, this time, the natural frequency (pitch dominated mode) found from the decaying oscillations is that of the $s2$ configuration per Equation 3.4. Finally, the wing is installed and the natural frequency of the $s4^*$ configuration is found per Equation 3.5.

$$I_{s1} = \frac{K_\theta}{\omega_{s1}^2} \tag{3.3}$$

$$I_{s2} = \frac{K_\theta}{\omega_{s2}^2} \tag{3.4}$$

$$I_{s4^*} = \frac{K_\theta}{\omega_{s4^*}^2} \tag{3.5}$$

$$I_{beam} = I_{s2} - I_{s1} \tag{3.6}$$

$$I_{wing} = I_{s4^*} - I_{s2} - m_w d^2 \tag{3.7}$$

In order to find the moment of the inertia for the beam only, we use Equation A.12 since the centre of gravity of the rotary base and beam are aligned. However, we must utilize the parallel axis theorem [41] per Equation A.13 to find the moment of inertia for the wing only (about the wing C.G.), since the centres of gravity of the wing and beam are not aligned, as was determined by a simple gravity balance test.

3.5.3.1 Free Pitch

Figure 3.36 shows the pre-test and post-test mass moments of inertia of the $s4^*$ configuration, as well as the analytically calculated mass moments of inertia for the $s4^*$ configuration, per Equation A.15. The results show good correlation between the predicted analytical mass moments of inertia and the experimental values, except for Test F, where both the pre-test and post-test values are higher than expected. Nevertheless, there is otherwise minimal variation between tests, with a range of $8X10^{-4} - 9X10^{-4} kgm^2$, excluding the aberrant Test F results.

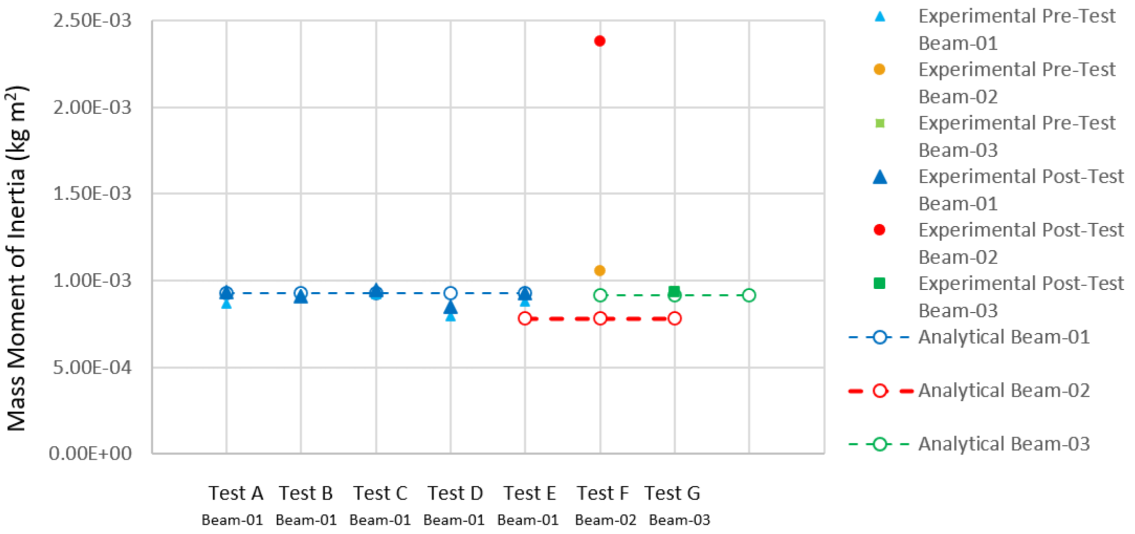

Figure 3.36: Comparison of Experimental and Analytical I_{s4^*} Free Decay Values for the Case of Free Pitch

3.5.3.2 Mass Moments of Inertia of Rotary Base, Beam and Wing

Mass Moments of Inertia of Rotary Base

Figure 3.37, represents the mass moments of inertia for the rotary base for all tests (from Equation 3.3), and indicates that the values remained consistent across all beams and tests, at around $1.6X10^{-4}kgm^2$. This was expected since the $s1$ configuration mainly experiences dry friction, freeplay, and the movement of the wires.

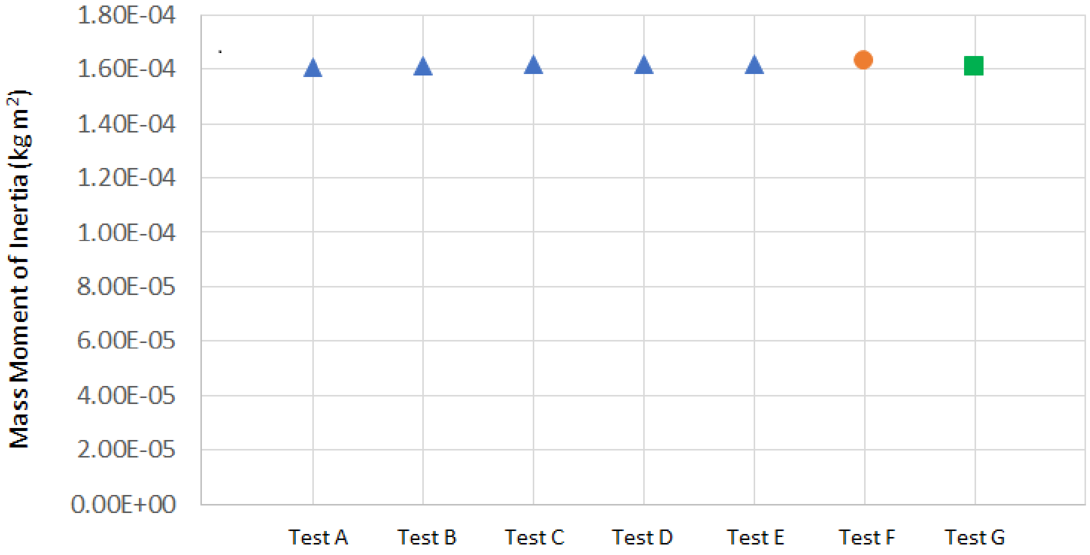

Figure 3.37: Mass Moments of Inertia For s1 (Rotary Base Only) Configuration, I_{s1}

Mass Moments of Inertia of Beam

Figure 3.38 shows the variation amongst the I_{beam} (Equation A.12) values for all beams/tests; we see that the moment of inertia of the beam appears consistent across tests at around $4X10^{-5} - 9X10^{-5}kgm^2$, except for Test F (recall that these structural properties were found from data performed post-test per FDT2, when Beam-02 has failed) and Test D (which exhibited significant freeplay issues between the beam and wing). All other test values remain on the order of the estimated analytical frequencies (Equation A.9).

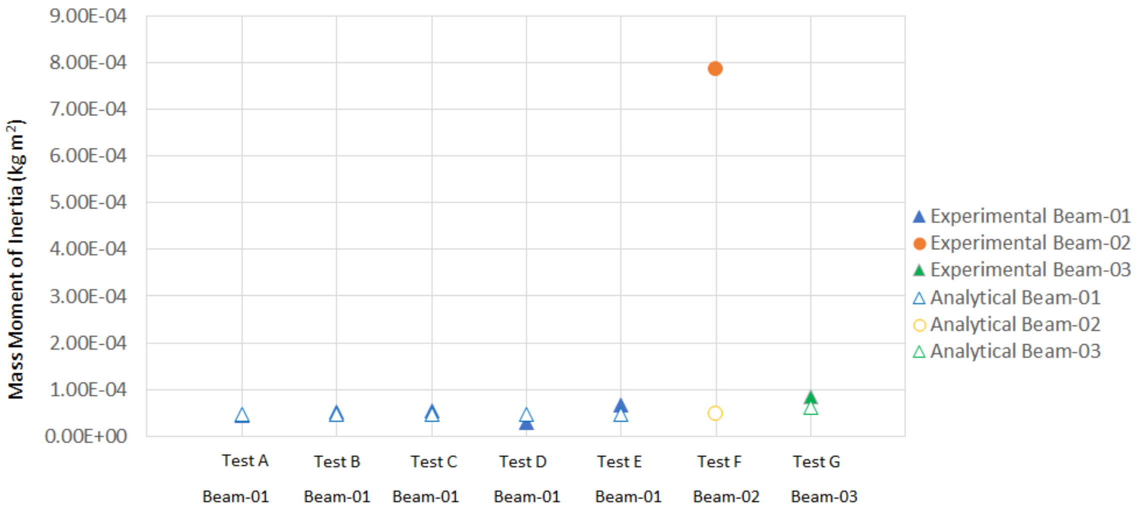

Figure 3.38: Mass Moments of Inertia of Beam Only, I_{beam}

Mass Moments of Inertia of Wing

The mass moments of inertia for the wing only, seen in Figure 3.39 (found from Equation A.13), indicate some variability between results that were not necessarily expected. On the surface, the wing is more or less unchanged. However, it is suspected that small changes in the placement and shift of the beam in the wing (freeplay), as well as difference in placement of adhesive, and putty on the surface of the wing may be to blame for so much variability. There are indications of the likely effects of cumulative calculation errors and the sensitivity of the structural system to small changes in mass distribution and freeplay.

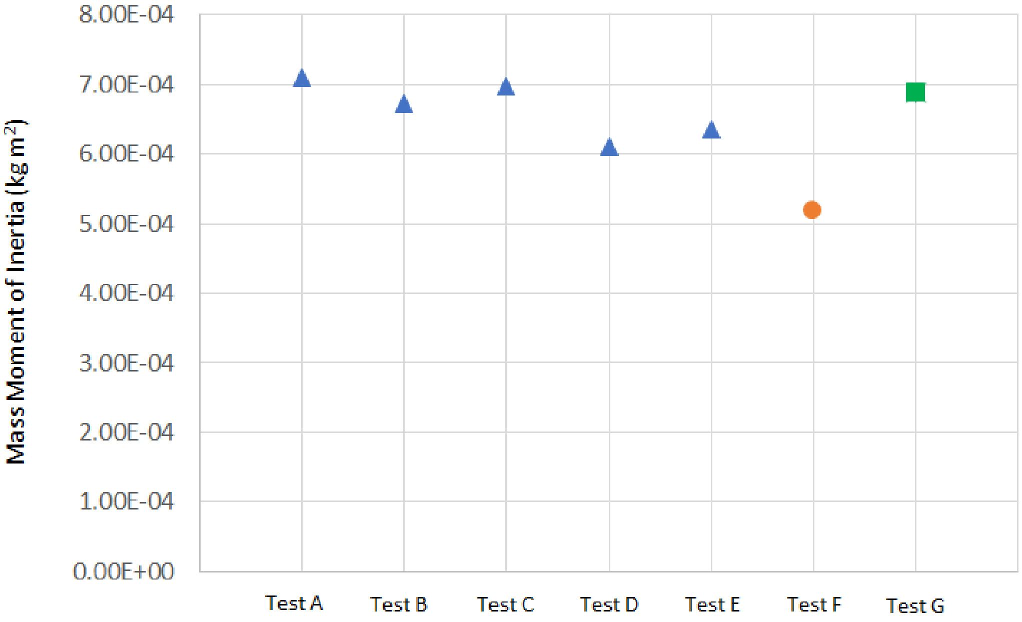

Figure 3.39: Mass Moments of Inertia of Wing Only, I_{wing}

3.5.4 Damping Coefficient

By assuming the system behaves as a 1 DOF system in pitch, the estimated damping coefficients were calculated per Equation 3.8 [36] and plotted in Figure 3.40 for the $s4^*$ configuration, for the case of free pitch motion.

$$D_{s4^*} = 2\,\zeta_{s4^*}\,\omega_{ds4^*}\,I_{s4^*} \tag{3.8}$$

3.5.4.1 Free Pitch

It can be observed that there is great variability in damping coefficient between tests, once again displaying the pattern seen in the damping ratios. Test F shows noticeably anomalous behaviour, even with the apparent variability between tests. The damping values range from $1.5X10^{-3} - 3X10^{-3} kgm^s/s$, with Test G showing the lowest damping values compared to Tests A-E. Overall, the data appears to indicate a high degree of damping is added by the addition of the wing and its components to the $s2$ configuration, and that damping may be very sensitive to beam structural properties and wing damage. Previous research performed by Koenig has suggested that the uncertainty in the damping is likely approximately 30% [49] [50].

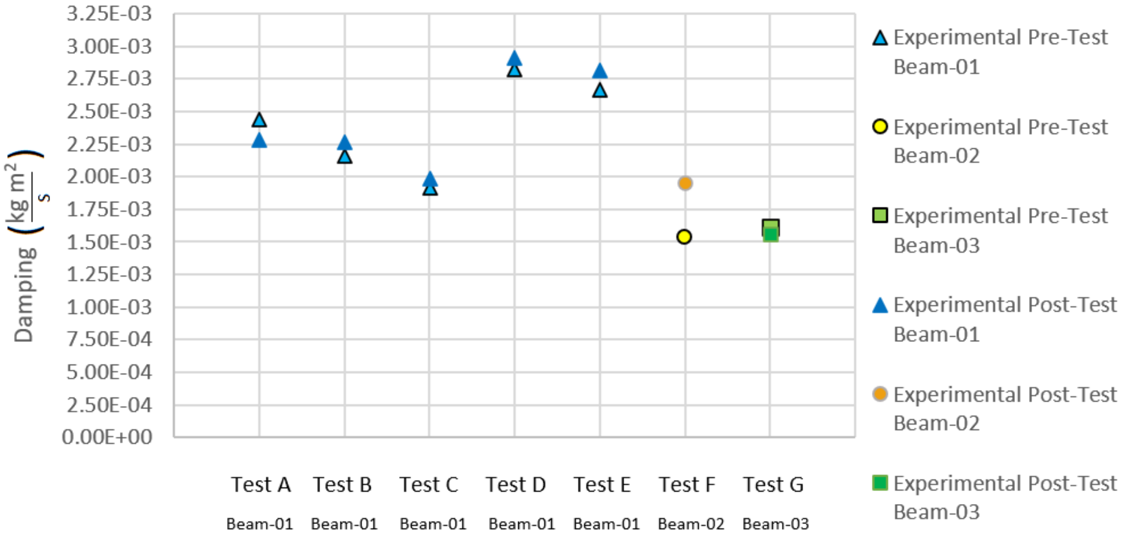

Figure 3.40: Comparison of $s4^*$ and $s2$ Free Decay Mass Damping Coefficients in Pitch-Bending-Torsion

The analysis of the free decay parameters: the damping ratio, damped natural frequency, mass moment of inertia and damping coefficient strongly suggest that the wing apparatus may be extremely sensitive to changes in the beam and wing properties. However, once again, the reason for the variability remains to be confirmed, and also indicates a profound sensitivity of the damping ratio and corresponding damping coefficient to changes in the system as well as sensitivity to changes in the properties of the beam.

3.6 Test Procedure

A total of eight valid tests are presented (Tests A-H). Tests A-E were performed with Beam-01, Test F was performed with Beam-02, and Tests G-H were performed with Beam-03. A detailed chronology of testing is presented in Appendix E.

The pitch springs were adjusted to ensure that the wing's static position was set at 0° AOA, and to allow for the amplitude of oscillations to occur without the springs becoming hyper-extended and always in tension. Prior to testing, the weight of the beam with instrumentation and wires was taken. The bending-torsion, and potentiometer calibrations were done to ensure no appreciable changes had occurred. The wires were hooked up, isolated, and secured in such a way to create support and ensuring that they would not contribute to added mass during the tests, nor would they add resistance/damping due to the tension of the wires. The equipment was allowed to warm up for a minimum of 20 mins to eliminate the effects of drift, but standard practice was closer to 1-2 hours in order to reduce its effects, without causing overheating of wires and equipment. Before and after testing, no-flow free decay tests were performed, as seen in Section 3.5. In order to assess the ambient and equipment noise for each test, three recordings were done with the wind tunnel off, motor on, and motor and clutch on at zero RPM. The sampling frequency was 1000 Hz. This data would be used two-fold: to find the baseline noise frequencies of the system and calculate the mean bias of the wing. Following this, the first type of free decay test (FDT) was performed. FDT1 consisted of two free decay tests: one test with the pitch lock off (allowing for bending, torsion, and pitch, with a pitch initial condition) and one test with the pitch lock on (bending and torsion only, with a bending initial condition). With the pre-test FDT1 complete, tests were performed at various airspeeds, in combinations of increasing or decreasing airspeed sweeps, with the goal of obtaining the behavior of different amplitudes of LCO's, as well as capturing hysteresis. In an effort to locate the LCO branches, initial conditions were applied to the wing in the form of pitch perturbations and changes in airspeed. When changing sweep direction, hysteresis was noted in response due to the change in initial conditions via airspeed. The minutiae of each test, including specific steps, incidents, behaviour and ambient conditions are noted in Appendix E.

Following the airspeed tests, FDT1 was once again performed, wherein the purpose was to check if the system parameters had changed. Following FDT1, the second type of ground vibrational test was performed FDT2, which was comprised of two free decay tests (with pitch initial conditions) for each of the three configurations, $s1$, $s2$, and $s4^*$. This data would allow us to find the decay rate and damping coefficient of the system.

All test data were first plotted raw, and the time histories were observed. If the potentiometer data indicate that a steady-state LCO had been attained, the data point (i.e. airspeed) was selected for further analysis. The time trace for each data point was truncated to choose only the steady-state regime, and the raw data PSD used to find the dominant frequency which would indicate an appropriate cut-off filter frequency. The histograms were used to check the spread and find the baseline if the wing had a bias. The data were then filtered and the bias removed, and the filtered and truncated data were used to find the time history, PSD and histogram. This data were used to find the LCO amplitude corresponding LCO frequencies.

4 Results

4.1 Overview

Table 4.1 lists all the wind tunnel tests which were performed, along with corresponding dates, ambient conditions, as well as beam and pitch spring information. Note that all tests were performed with the downstream mesh and four screws to secure the wind tunnel floor plates; the wing was set at 0° AOA and set vertically straight using a scale. There are two types of tests: trial tests (numbers), the results of which were used to refine the testing procedure, and regular tests (letters), where the data recorded was analysed and are presented in this thesis. The specific details of each test can be reviewed in Appendix E.

Table 4.1: Summary of Wind Tunnel Tests

Test #	Test Label	Date	Ambient Temperature (°C)	Ambient Pressure (Pa)	Beam #	# Pitch Springs
1	Trial 1	October 10, 2017	21.0	101850	01	2
2	Trial 2	October 11, 2017	23	102550	01	2
3	A	October 16, 2017	23.3	102200	01	2
4	B	November 1, 2017	22.1	102800	01	2
5	C	November 2, 2017	23.2	101650	01	2
6	D	December 1, 2017	20.5	102300	01	2
7	E	December 4, 2017	20.9	102250	01	2
8	Trial 8	March 14, 2018	20.8	99900	01	2
9	Trial 9	March 15, 2018	20.6	100000	01	2
10	Trial 10	March 16, 2018	20.6	101500	01	2
11	F	March 15, 2019	21.1	100600	02	2
12	G	May 27, 2019	24.7	101800	03	2
13	H	May 28, 2019	22.6	100100	03	0

In general, only the results will be presented in this section, whereas the physical interpretations and comparison with the rigid wing data, as well as special cases, will be covered in Chapters 5 and 6. All data were recorded with the chief goal of documenting motion at the wing root and tip, and the results found using Beams-01,-02 were considered the nominal cases, whereas data obtained using Beam-03 were considered a comparative case. Similarly, the results which were gained using two pitch springs are the nominal case, and the no pitch spring tests is considered comparative.

For motion at the wing root described in Section 4.2 (pitch rotation, recorded by the potentiometer), sample time histories, PSD's and histograms will be presented, representing each of the SAO and LAO branches. A bifurcation diagram of the LCO amplitude versus airspeed will be presented for Tests A-E (Beam-01, 2 pitch springs) and Test F (Beam-02, 2 pitch springs). The LCO frequencies are tabulated in Section 4.4. Test G (Beam-03, 2 pitch springs) time histories, PSD's and histograms, as well as a bifurcation diagram will be presented in Section 4.5, since Beam-03 is comprised of a different material than Beams-01,-02. Test H will be presented and discussed in Section 5.5, as it is the special case of Beam-03 with no pitch stiffness, which exhibited mainly erratic behaviour.

For motion at the wing tip (Section 4.3), only the bending strain (and thus displacement) results of Test F are presented. Due to issues in previous tests with strain gauge saturation and gain settings, only the time histories of a few select torsion results will be reviewed in Section 5.6. In general, the torsion strain results require further investigation to determine validity. In regards to the bending strain results, only the SAO data is available (Section 4.3.1 due to the effects of plastic deformation occurring in the LAO region (Section 5.7). Test F SAO Acceleration data is located in Section 4.3.2, where time histories and LCO tip acceleration are presented and compared with an analytical estimation.

In general, the accelerometer and strain gauge results of Test F were determined to be nominal since they reflected the culmination of refinements made to the wing apparatus. Furthermore, the nature of the wing/beam apparatus was well known based on the results of Tests A-E as well as the Trial tests, since they were all performed with the Normalized AISI 01 steel beam (Beams-01,-02) .

In Section 4.5, the time histories, PSD's and histograms representing SAO and LAO for the tempered 1095 spring steel beam (Beam-03, Test G) are presented, as well as a bifurcation diagram and plot of LCO frequency versus airspeed; the difference between LCO frequencies for Tests A-F (Section 4.4) and G (Section 4.5) are presented to provide a preliminary look at the effect of changing the beam material on the LCO frequency.

As previously mentioned, an average low-pass filter of 30-40 Hz was used to remove the wind tunnel and equipment noise for the pitch (potentiometer) results based on the no-flow test data. However, in order to analyse the LCO amplitudes and frequencies, the time history data were filtered just above the dominant frequency, and the flow bias was removed. The work of Poirel and Yuan suggested that when the time history data were filtered just above the dominant frequency, the motion appeared to be periodic and thus could be considered SHM [5].

4.2 Motion at the Wing Root For Beams-01,-02

The motion at the wing root was recorded by the potentiometer in voltage, and converted to degrees by using the calibration from Appendix D.1. Initially, the unfiltered potentiometer data for each test airspeed were plotted over time, and a power spectral density (PSD) was generated in order to select a) an appropriate time period of the signal where the LCO had reached steady-state b) the dominant frequency, needed to filter the data properly and c) to determine the bias of the wing in the airflow which would be used to zero the data so that the maximum and minimum peaks of the LCO amplitude were close to symmetric. The no-flow data were used to truncate, zero and filter the data, and then generate filtered histories and PSD's, as well as histograms. By using surrogate data for a simple sine wave, a code was created and vetted which was then applied to the experimental data to find the dominant frequency for each airspeed (from the PSD's), as well as determine the average of the maximum and minimum peaks in order to find the LCO amplitude (from the time histories and histograms).

Small Amplitude Oscillations (SAO)

Unfiltered Data

A sample time trace illustrating the unfiltered motion in the SAO region is shown in Figures 4.1 and 4.2. This example is not zeroed in order to demonstrate that despite removing the *no-flow* bias, there is a clear bias which is introduced when the *flow* is turned on. Further note that shape of waves are not clean sine waves, and display evidence of wave distortion caused by the 3f superharmonic (10.25 Hz) evident in Figure 4.3. Further evident in Figure 4.3 are the superharmonics of the dominant frequency, 3.42 Hz, as well as higher peaks consistent with wind tunnel noise. The peaks located at 283.28 and 290.12 Hz were not apparent in the no-flow free decay data, but may be due to vibrations of the test rig itself.

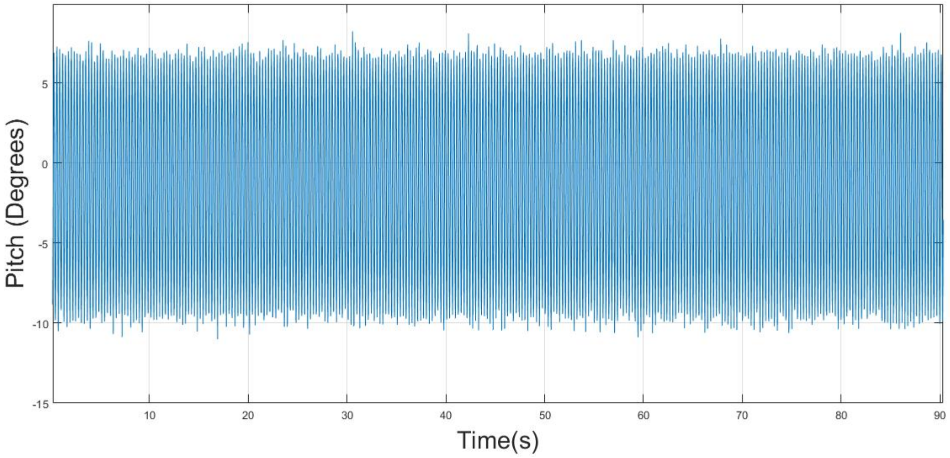

Figure 4.1: Representative Unfiltered Pitch SAO Time History, Test F March 15, 2019, for $U = 8.23$ m/s, $Re_c = 8.1 \times 10^4$

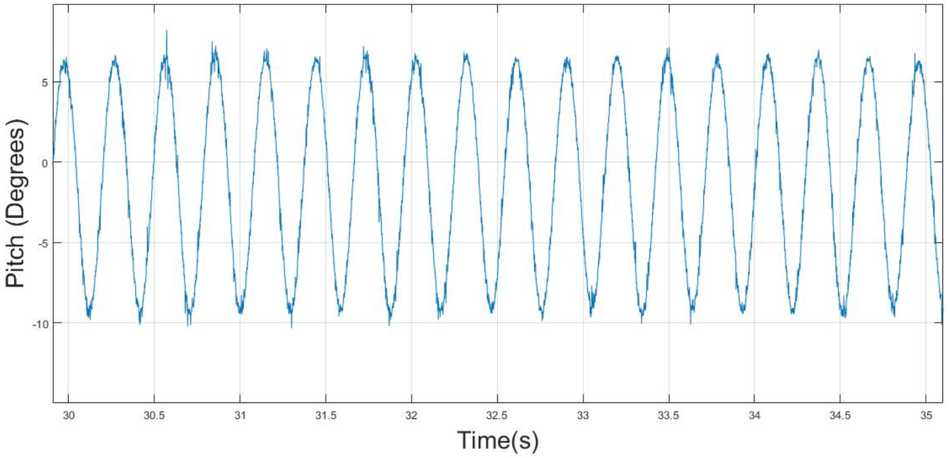

Figure 4.2: Representative Unfiltered Pitch SAO Time History, Test F March 15, 2019 (Zoomed View), for $U = 8.23$ m/s, $Re_c = 8.1 \times 10^4$

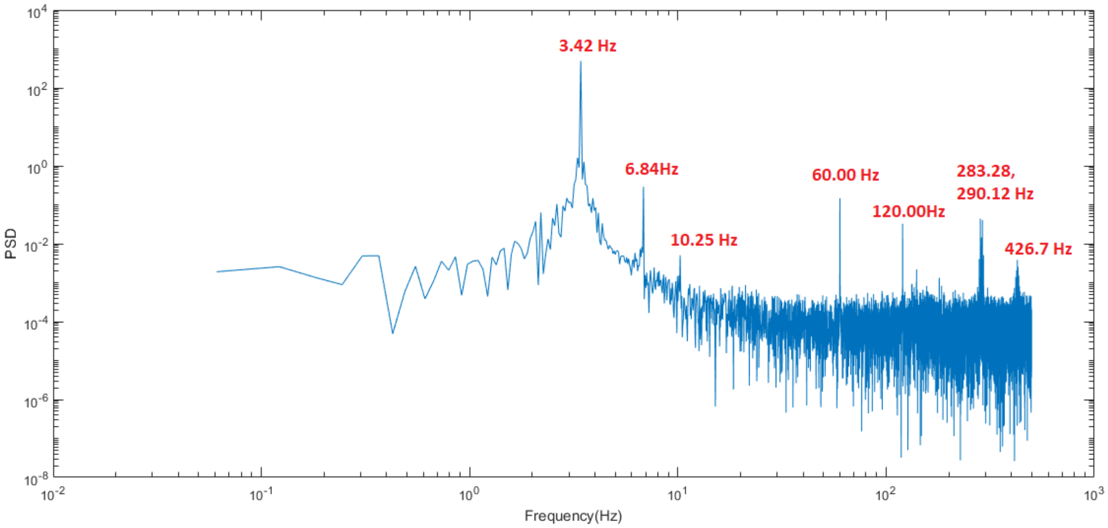

Figure 4.3: Representative Unfiltered Pitch SAO Power Spectral Density, Test F March 15, 2019, for $U = 8.23$ m/s, $Re_c = 8.1 \times 10^4$

Filtered Data

An example of the filtered test data (not zeroed), for the SAO region can be seen in Figures 4.4 and 4.5. Figure 4.6 shows the filtered PSD, clearly showing that all frequencies above the dominant frequency have been filtered out (recall that the potentiometer is capturing, for the most part, the rigid body pitch rotation). Finally, the histogram for the filtered data can be seen in Figure 4.7, and displays a rounded curve and nearly symmetrical ends, indicating a relatively harmonic signal with minimal asymmetries. Even though the flow bias is displaced from the no-flow value of 0° to approximately 1.5 °, the histogram is symmetrical about its mean. This gives us confidence that we can re-adjust the zero again to the mean with airflow.

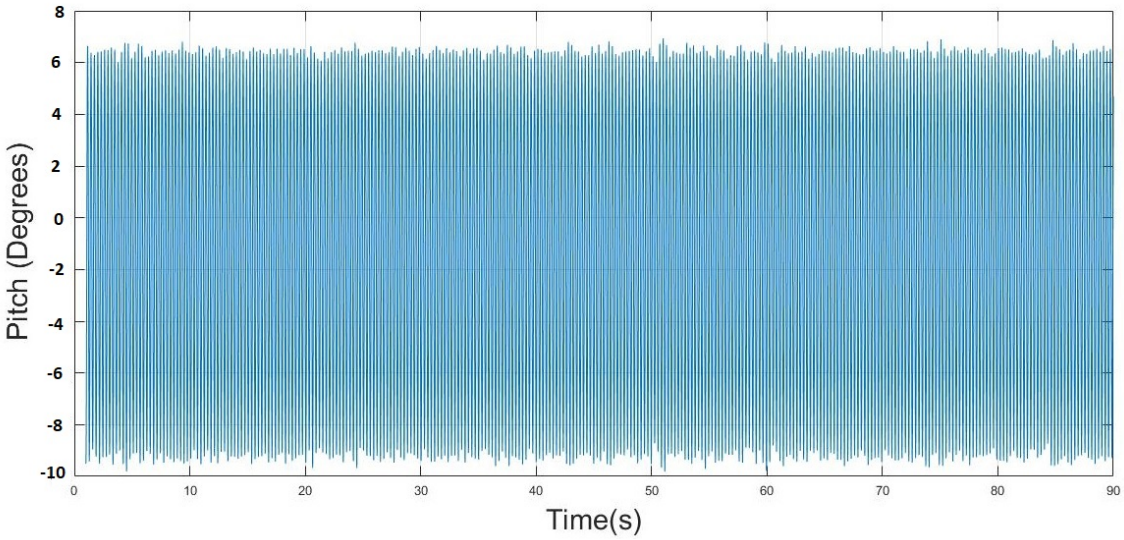

Figure 4.4: Representative Filtered Pitch SAO Time History ($F_{pass} = 40Hz, F_{stop} = 35Hz$), Test F March 15, 2019, for $U = 8.23$ m/s, $Re_c = 8.1 \times 10^4$

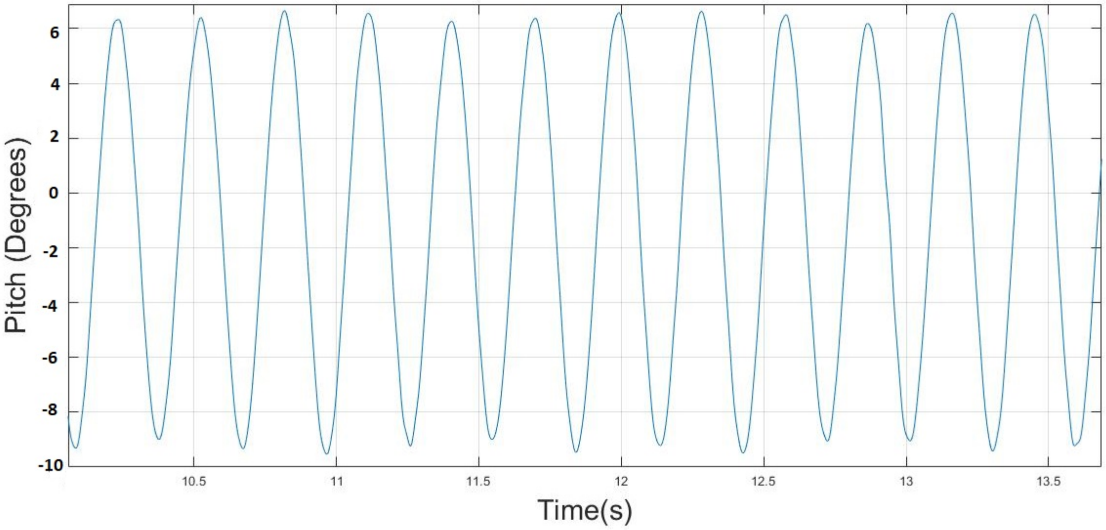

Figure 4.5: Representative Filtered Pitch SAO Time History (F_{pass} = 40 Hz, F_{stop} = 35 Hz), Test F March 15, 2019 (Zoomed View), for $U = 8.23$ m/s, $Re_c = 8.1 \times 10^4$

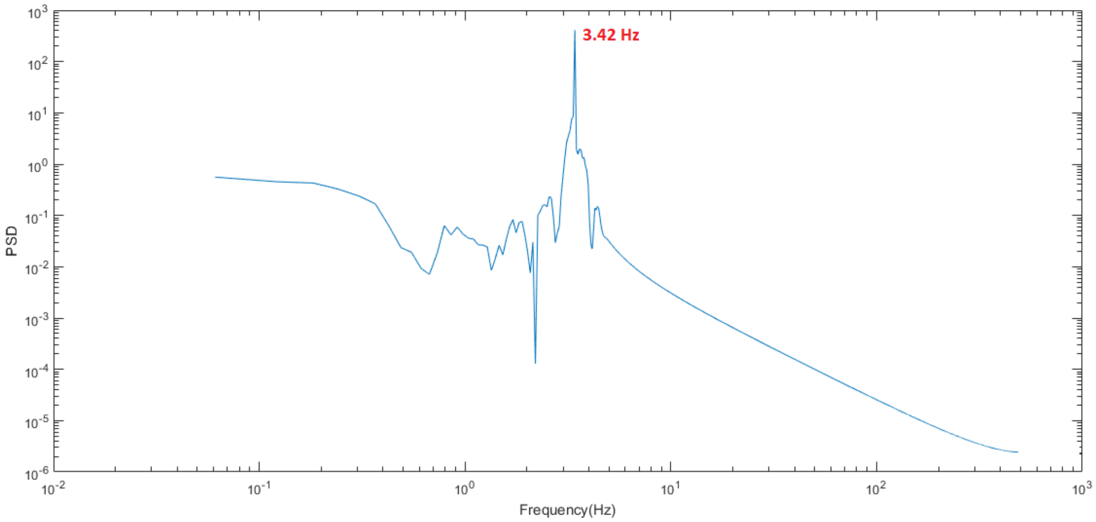

Figure 4.6: Representative Filtered Pitch SAO Power Spectral Density ($F_{pass} = 4$ Hz, $F_{stop} = 3$ Hz), Test F March 15, 2019, for $U = 8.23$ m/s, $Re_c = 8.1 \times 10^4$

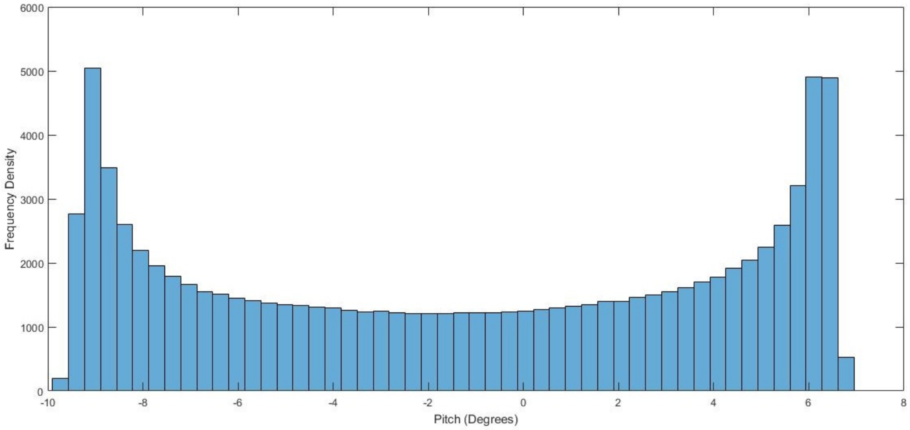

Figure 4.7: Representative Filtered Pitch SAO Histogram ($F_{pass} = 40$ Hz, $F_{stop} = 35$ Hz), Test F March 15, 2019, for $U = 8.23$ m/s, $Re_c = 8.1 \times 10^4$

Large Amplitude Oscillations (LAO)

Unfiltered Data

Similarly, the examples of the unfiltered time history (zeroed by removing the flow mean) for the LAO time traces can be seen in Figures 4.8 and 4.9. The most striking observation is that the noise in this signal is very hard to perceive. Similar to the SAO time trace, the waves appear to be distorted, per the 3f superharmonic (11.35Hz) in Figure 4.10. Interestingly, unlike the SAO PSD, the LAO PSD does not show evidence of high frequency peaks, i.e. peaks above 33.94 Hz; the reason for this is currently unknown. However, thedominant frequency (3.79 Hz) and its 2f-9f superharmonic peaks are clearly evident.

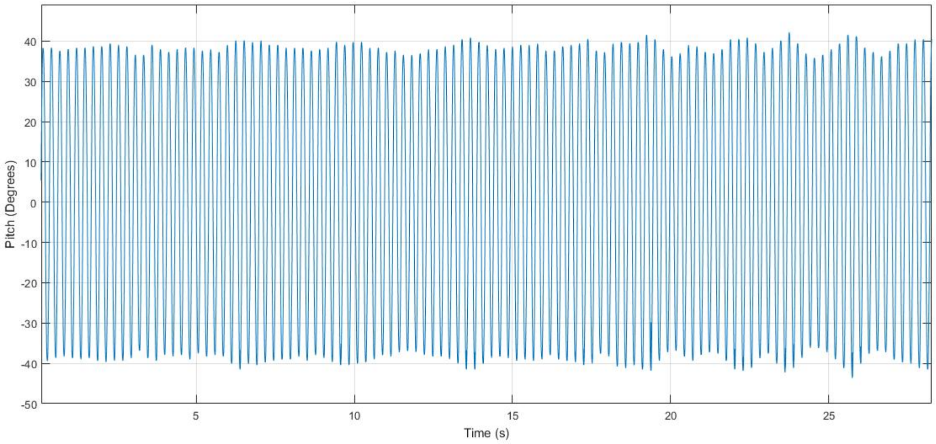

Figure 4.8: Representative Unfiltered Pitch LAO Time History for Test C November 2, 2017, for $U = 9.82$ m/s, $Re_c = 9.7 \times 10^4$

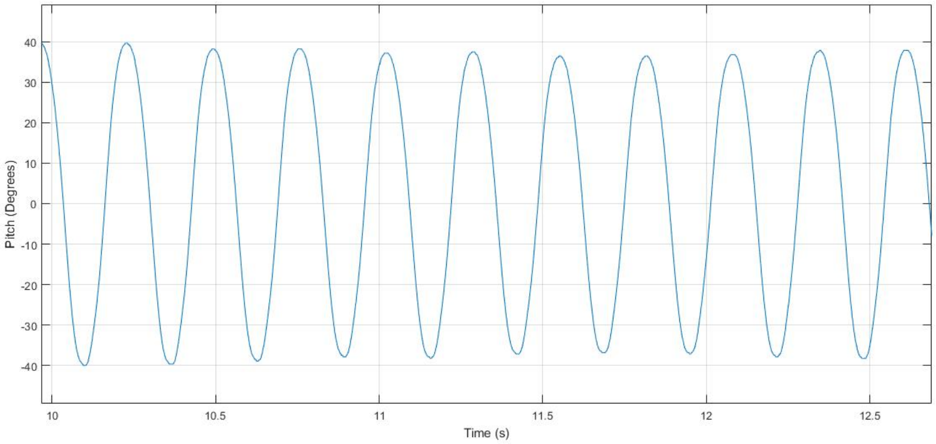

Figure 4.9: Representative Unfiltered Pitch LAO Time History for Test C November 2, 2017 (Zoomed View), for $U = 9.82$ m/s, $Re_c = 9.7 \times 10^4$

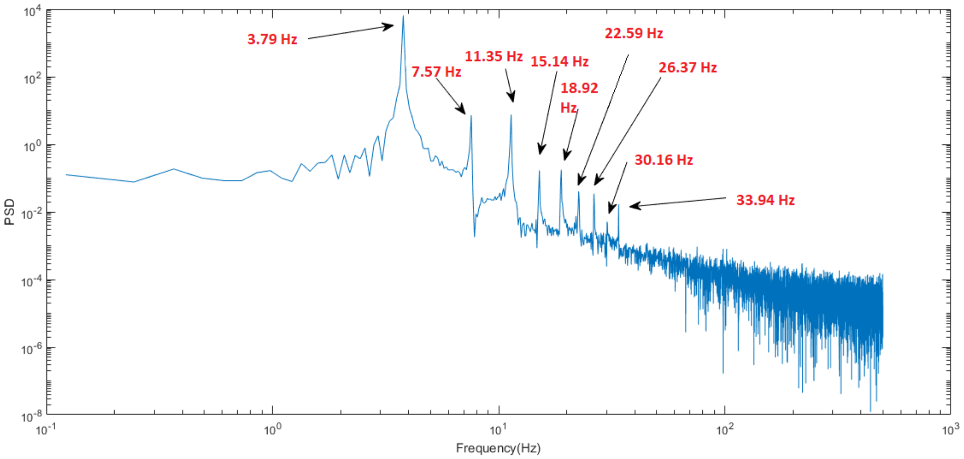

Figure 4.10: Representative Unfiltered LAO Power Spectral Density Test C November 2, 2017, for $U = 9.82$ m/s, $Re_c = 9.7 \times 10^4$

Filtered Data

Figures 4.11 and 4.12 illustrate the filtered time history sample plots for the LAO region, which look very similar to the unfiltered time traces. Figure 4.13 shows the PSD filtered to cut-of all frequencies above the dominant frequency. Figure 4.14 shows the histogram, which appears to be curved in the centre, indicating minimal non-linear content and is relatively symmetrical, suggesting there is minimal asymmetry.

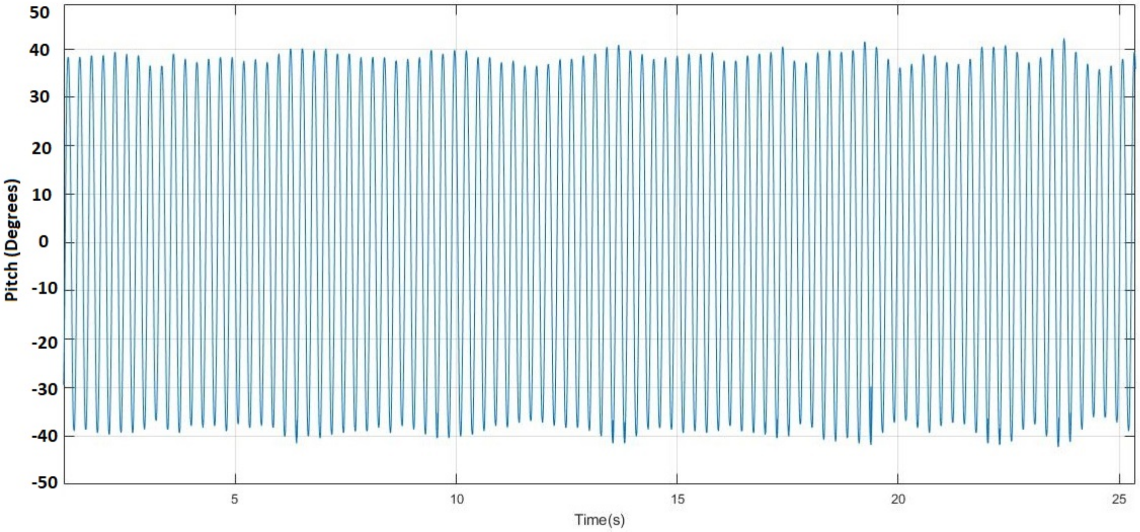

Figure 4.11: Representative Filtered Pitch LAO Time History ($F_{pass} = 40$ Hz, $F_{stop} = 35$ Hz) for Test C November 2, 2017, for $U = 9.82$ m/s, $Re_c = 9.7 \times 10^4$

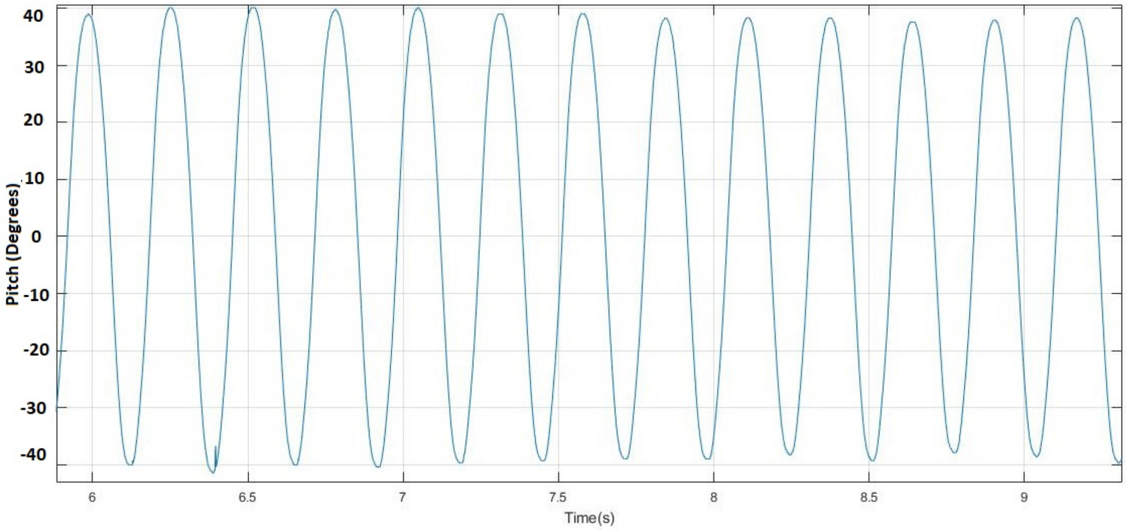

Figure 4.12: Representative Pitch LAO Time History ($F_{pass} = 40$ Hz, $F_{stop} = 35$ Hz) for Test C November 2, 2017 (Zoomed View), for $U = 9.82$ m/s, $Re_c = 9.7 \times 10^4$

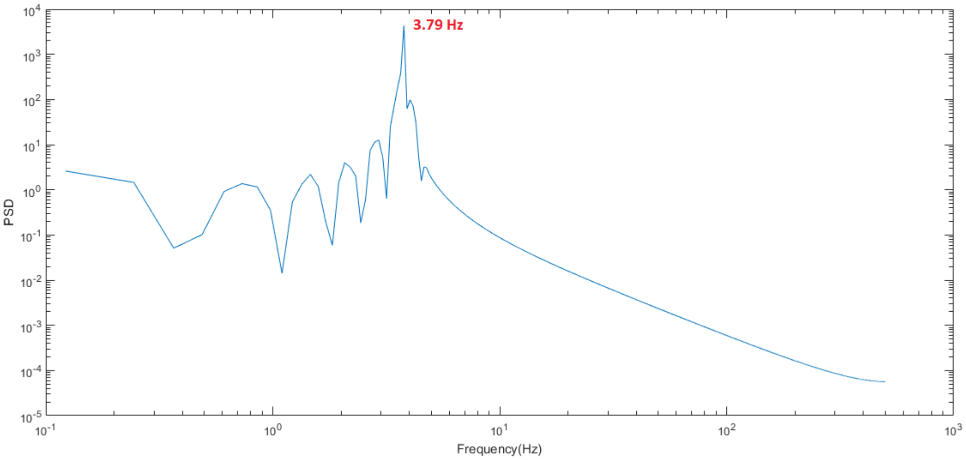

Figure 4.13: Representative Filtered LAO Power Spectral Density ($F_{pass} = 4$ Hz, $F_{stop} = 3$ Hz) Test C November 2, 2017, for $U = 9.82$ m/s, $Re_c = 9.7 \times 10^4$

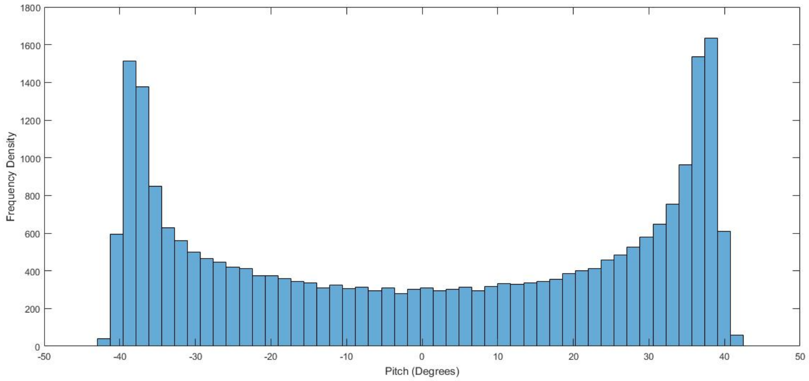

Figure 4.14: Representing Filtered Pitch LAO Histogram ($F_{pass} = 40$ Hz, $F_{stop} = 35$ Hz) Test C November 2, 2017, for $U = 9.82$ m/s, $Re_c = 9.7 \times 10^4$

4.2.1 LCO Pitch Amplitude

Methods of Instigation and Stoppage

The method used to instigate the onset of LCO's (either change in airspeed, ΔU, or pitch initial condition, $\Delta\theta$), as well as the reason for the maximum limit of each tests can be seen in Table 4.2. When the wing was stopped due to very large amplitude oscillations (VLAO), it was to prevent further damage to the wing apparatus and for safety reasons; similarly, the wing was halted at higher airspeeds, since the behaviour was unprecedented and unpredictable, and could lead to wing damage or safety issues.

Table 4.2: Initial Conditions and Reasons for Test Stoppage

Test	Initial Condition	Method of Stoppage	Reason	Beam #
A	ΔU	Manual Termination	VLAO	01
B	$\Delta\theta$(small)	Manual Termination	VLAO	01
C	ΔU	Manual Termination	VLAO	01
D	$\Delta\theta$ (small)	Manual Termination	Excessive Vibration	01
E	$\Delta\theta$ (small)	Manual Termination	VLAO	01
F	ΔU	Wing Motion Ceases	Beam Failure	02
G	$\Delta\theta$ (large)	Manual Termination	High Airspeeds	03
H	ΔU	Manual Termination	High Airspeeds	03

Results

The plot of the Pitch LCO amplitude versus airspeed can be seen in Figure 4.15. This data, presented for Tests A-E (Beam-01, Normalized AISI-01 steel, 2 pitch springs) and Test F (Beam-02, Normalized AISI-01 steel, 2 pitch springs), inherently captures the effects of the differing atmospheric conditions and ambient external vibrations, as well as sensitivity to structural parameters. In principle, these six tests should exhibit very similar dynamics, since the configurations are the same in theory). As a reminder, the data for Test G (Beam-03, Tempered 1095 spring steel, 2 pitch springs) and Test H (Beam-03, Tempered 1095 spring steel, zero pitch stiffness), will be presented and discussed in Sections 4.5 and 5.5, respectively.

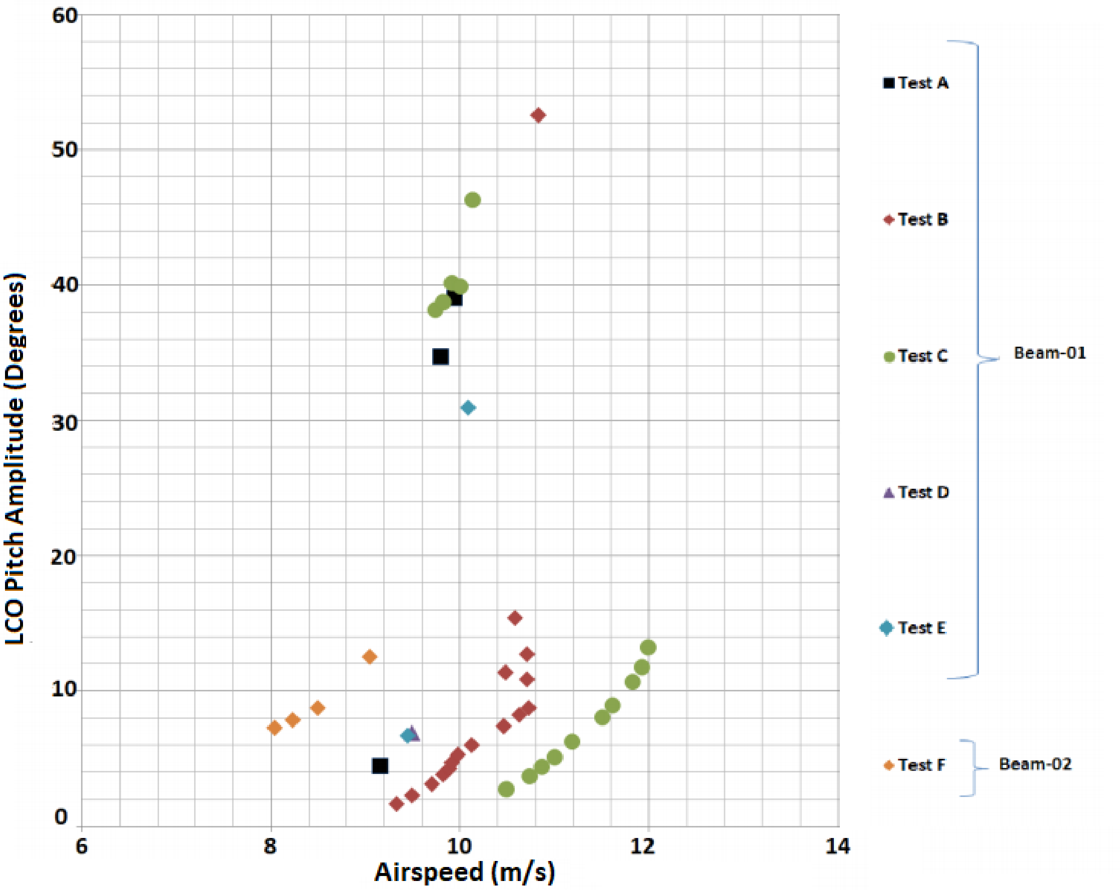

Figure 4.15: LCO Root Pitch Amplitude versus Airspeed

The range of airspeeds corresponds to a Reynolds number range of $7.9 \times 10^4 < Re_c < 1.7 \times 10^5$, which is within the transitional Reynolds number region of $10^4 - 10^6$. Additionally, previous research has observed that the range of Reynolds numbers where LCO's occur is

$5.5 \times 10^4 < Re_c < 1.2 \times 10^5$. Referring to Figure 4.15, 2 LCO branches are evident, as expected per the previous work of Poirel [51] on the rigid quasi-2D problem. These two branches illustrate the SAO and LAO regions, herein defined as LCO amplitudes of $0° - 15°$ and $30° - 60°$, respectively. The LCO onset airspeed appears to range from $\approx 8 - 10$ m/s. The SAO and LAO regions are separated by a transition region. In the SAO range, data for Tests A, C, D, E, F indicate that the LCO amplitude increases with increasing airspeed. An important distinction noted across Tests A-F was that in the SAO region, steady-state LCO's were easily attained; conversely, steady-state LCO's in the LAO region were more difficult to achieve. During testing, whether the SAO or LAO branch was attained was incumbent upon the initial condition applied (ΔU or $\Delta\theta$), as expected for such a non-linear problem.

In regards to the beams used for testing, Beam-01 was used for tests A-E (as well as Trial Tests 1 and 2), and subsequent Trial Tests 8-10; post-test examinations showed that the beam became more plastically deformed with each successive test, until Beam-01 failed during Trial Test 10. Thus, we can infer that we may also have inadvertently captured the effects of the increasing beam yield strength due to strain hardening (Section 5.7) occurring as a result of plastic deformation for Tests A-E (SAO and LAO regions). Note that since only the SAO data were plotted from Test F, this data likely did not include the effects of plastic deformation or beam failure.

It appears that there may be fold bifurcations (indicating hysteresis due to change in LSB size and movement [52]) located at 9.15 m/s, 9.33 m/s, 8.04 ms, and 10.2 m/s, i.e. where the LCO's first appear. The experimental flutter speed is currently undetermined, but would indicate the location of the possible subcritical Hopf bifurcation. However, the experimental flutter speed is likely to be lower than the predicted linear flutter speed of 12.67 m/s for coupled flutter [28] (due to the effect of the aerodynamics creating a stiffening in pitch [22]), and so the location of the Hopf bifurcation is likely in the vicinity of $U < 12.67$ m/s.

4.3 Motion at the Wing Tip For Beams-01,-02

4.3.1 Flapwise Wing Tip Bending Deflection (Beam-02, SAO Region)

The bending strain data were measured at approximately 0.12 L and related to the flapwise wing tip bending deflection in centimetres by applying the calibration curve found in Appendix D.2, as outlined in Section 3.4.1, Subsection 3.4.1. Only data for the SAO region is provided, due to progressive plastic deformation appearing to occur in the LAO region (this will be discussed in Section 5, Subsection 5.7).

Unfiltered Data

An example of an unfiltered, zeroed, time trace for the representative flapwise tip bending deflection for the SAO region is seen in Figures 4.16 and 4.17. Note that the evidence of noise is difficult to observe, but seems especially apparent in terms of resolution at the tip of the peaks. Figure 4.18 shows the unfiltered PSD, indicating evidence of higher odd harmonics, as well as wind tunnel noise, possible test rig vibration due to the large oscillations, and finally the dominant frequency (3.49 Hz) and its superharmonics.

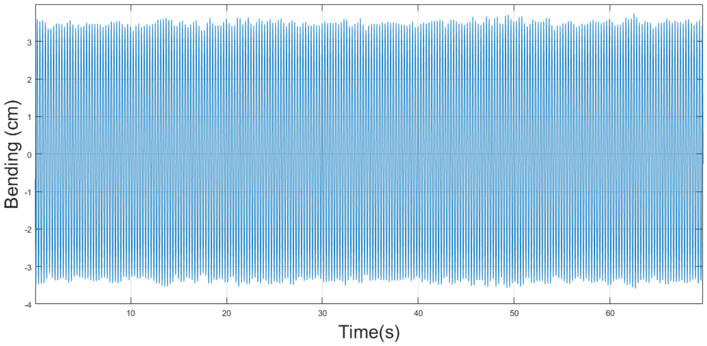

Figure 4.16: Representative Flapwise Bending SAO Time History, Test F, March 15, 2019 (Beam-02), $Re_c = 8.3 \times 10^4$, $U = 8.49$ m/s

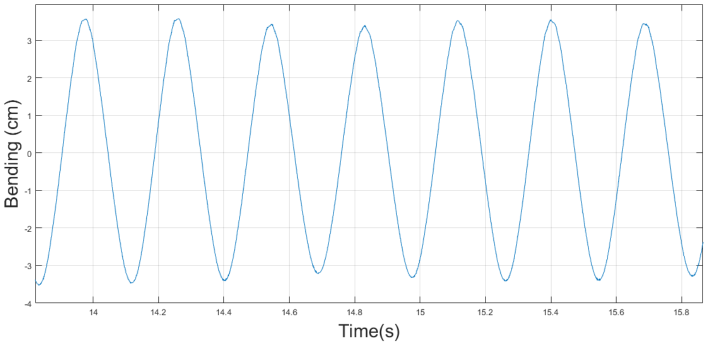

Figure 4.17: Representative Flapwise Bending SAO Time History, Test F March 15, 2019 (Zoomed View) (Beam-02), SAO Region, $Re_c = 8.3 \times 10^4$, $U = 8.49$ m/s

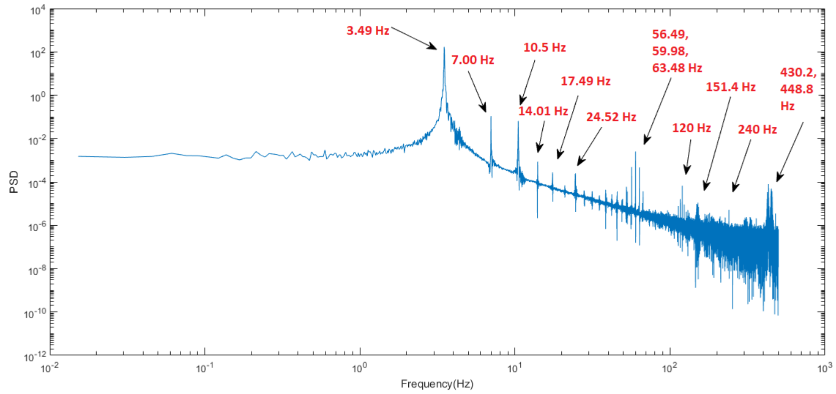

Figure 4.18: Representative Flapwise Bending SAO Time History, Test F March 15, 2019, SAO Region, $Re_c = 8.3 \times 10^4$, $U = 8.49$

Filtered Data

It is worth recalling that the data were filtered to remove frequencies above the 1^{st} bending modal frequency estimated at 4-5 Hz. Although, the LCO frequency appears to be dominated by the pitch DOF. Figures 4.19 and 4.20 show the filtered, zeroed, tip flapwise bending deflection time traces. Note that the shape of the waves are one again irregular an distorted, evident by the 3f peak in the PSD (10.5 Hz).Figure 4.21 shows the filtered PSD, with only the dominant frequency of 3.49 Hz visible. Figure 4.22 shows the filtered histogram, which is relatively curved and symmetrical.

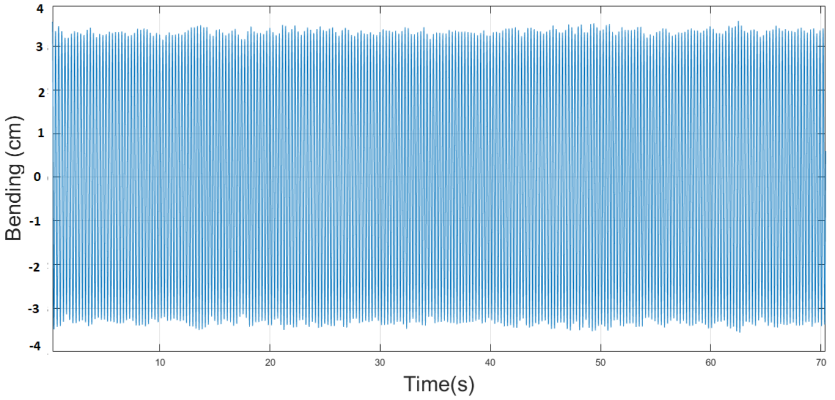

Figure 4.19: Representative Flapwise Bending SAO Time History (Filtered $F_{stop} = 6$ Hz, $F_{pass} = 5$ Hz), Test F March 15, 2019 (Beam-02), SAO Region, $Re_c = 8.3 \times 10^4$, $U = 8.49$ m/s

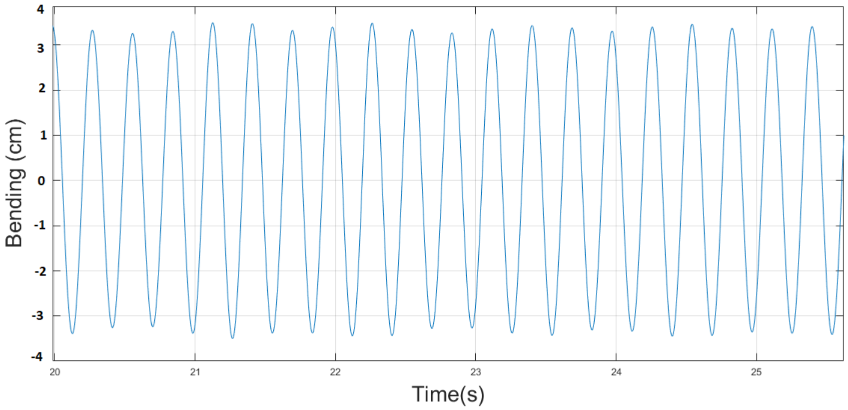

Figure 4.20: Representative Flapwise Bending SAO Time History (Filtered $F_{stop} = 6$ Hz, $F_{pass} = 5$ Hz), Test F March 15, 2019 (Zoomed View) (Beam-02), SAO Region, $Re_c = 8.3 \times 10^4$, $U = 8.49$ m/s

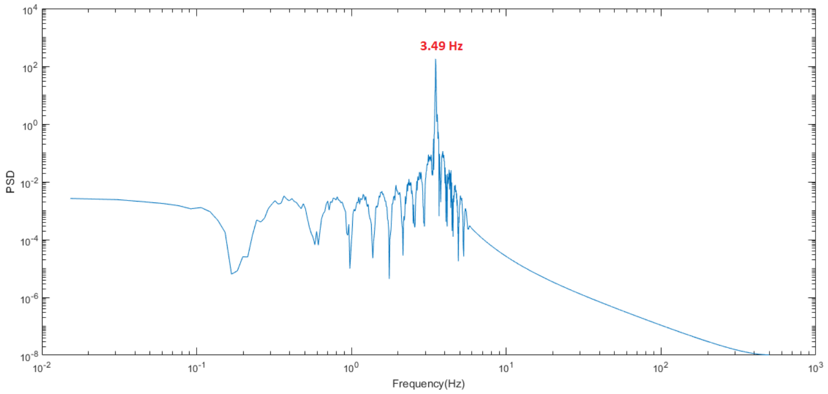

Figure 4.21: Representative Flapwise Bending SAO Time History (Filtered $F_{stop} = 6$ Hz, $F_{pass} = 5$ Hz), Test F March 15, 2019 (Zoomed View)(Beam-02), SAO Region, $Re_c = 8.3 \times 10^4$, $U = 8.49$

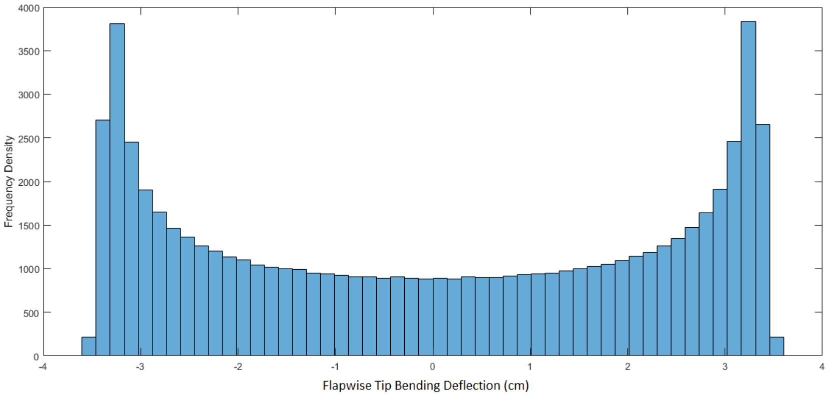

Figure 4.22: Representative Flapwise Bending SAO Histogram (Filtered $F_{stop} = 6$ Hz, $F_{pass} = 5$ Hz),Test F, March 15, 2019 (Beam-02), SAO Region $Re_c = 8.3 \times 10^4$, $U = 8.49$

Results

The flapwise wing tip bending deflection for the SAO region is presented in Figure 4.23, where the magnitude range is $2.5 - 6.1$ cm, i.e. the maximum deflection is around 13% of the wing span.

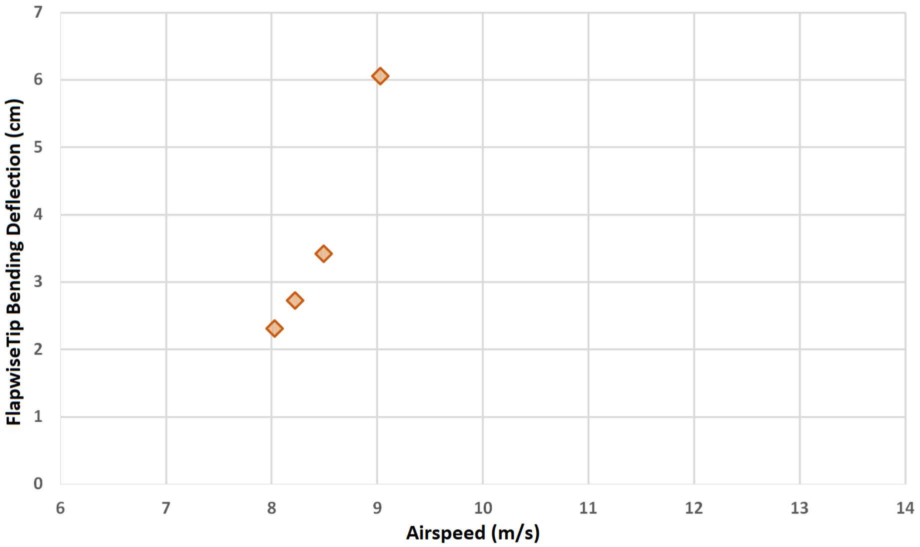

Figure 4.23: LCO Bending Deflection at Wing Tip versus Airspeed, Test F, March 15, 2019 (Beam-02), SAO Region

4.3.2 Tip Acceleration (Beam-02, SAO Region)

Accelerometer analysis is a difficult task, given the sensitivity to initial conditions, errors due to noise, as well as possibilities of drift. While the ultimate goal of using the accelerometers is to gain further insight into the total tip deflection as corroboration with the strain gauges, first the accelerations must be reviewed to ensure they are reasonable. The accelerometer data were filtered, and a review of the time traces indicated that in the SAO region, the behaviour appeared to be approximately a sine wave.

The experimental acceleration data were recorded using two accelerometers, and the data were converted to acceleration using the manufacturer provided sensitivity values. The data were filtered just above the dominant LCO frequency, and zeroed in order to accurately find the magnitude of the acceleration amplitudes.

Unfiltered Data

Figures 4.24 and 4.25 show sample plots of time traces of the (zeroed) tip acceleration in the SAO region; the noise in the signal is very evident. Figure 4.26 shows that the PSD has a dominant frequency (3.36 Hz) and its superharmonics, as well as wind tunnel noise. There is a clear peak located at 94.3 Hz.

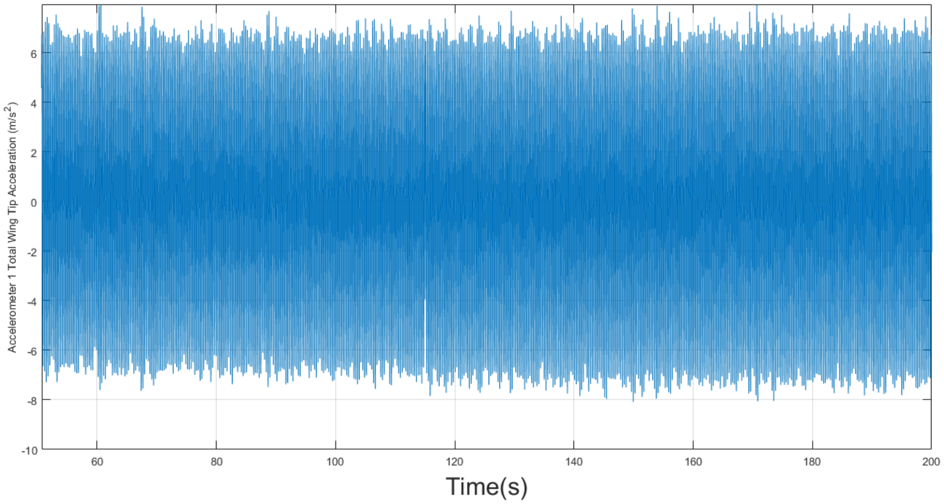

Figure 4.24: Representative Unfiltered Tip Acceleration Time History (Unfiltered), Test F March 15, 2019, for $U = 8.04$ m/s, $Re_c = 7.9 \times 10^4$

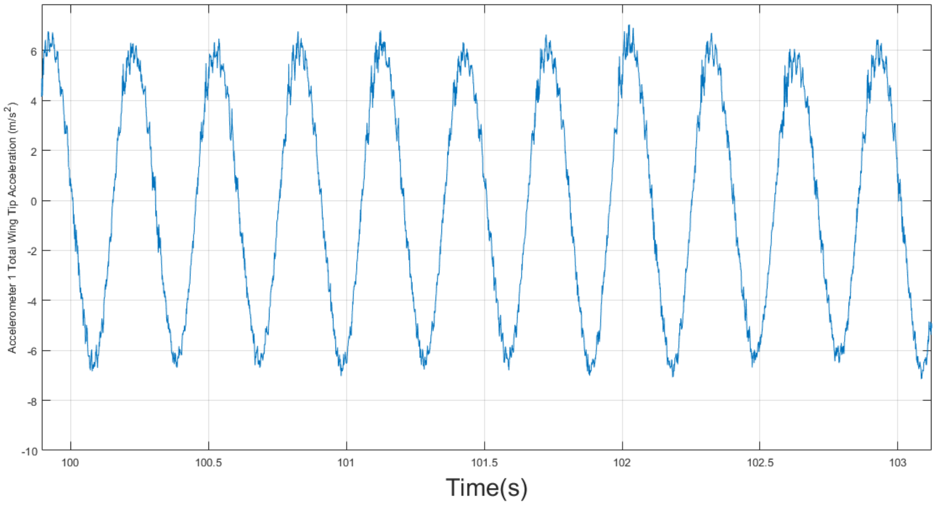

Figure 4.25: Representative Unfiltered Tip Acceleration Time History (Unfiltered), Test F March 15, 2019 (Zoomed View), for U = 8.04 m/s, $Re_c = 7.9 \times 10^4$

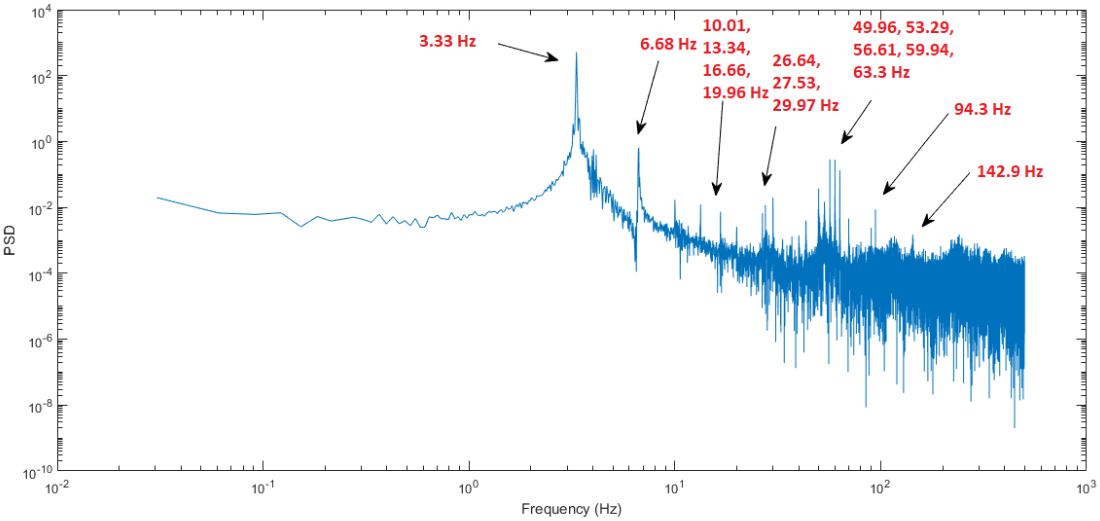

Figure 4.26: Representative Unfiltered Tip Acceleration PSD (Unfiltered), Test F March 15, 2019, for U = 8.04 m/s, $Re_c = 7.9 \times 10^4$

Filtered Data

Figures 4.27 and 4.28 show the (zeroed) filtered time histories, with smooth but modulating waves which are distorted. Figure 4.29 shows that the dominant frequency (3.33 Hz), and its 2f-5f peaks are evident, indicating that the acceleration data will include the inherent effects of non-linearities and asymmetries; the lack of even superharmonics indicates minimal misalignment [5]. Future work will almost certainly require an investigation into optimal filters for determining the acceleration, as well as the velocity and displacement, but for now this data provides a good estimation since the exact contribution of each mode to the acceleration is unknown at this point in time. The histogram can be seen in Figure 4.30, and shows a curved trend, with only very slight asymmetry.

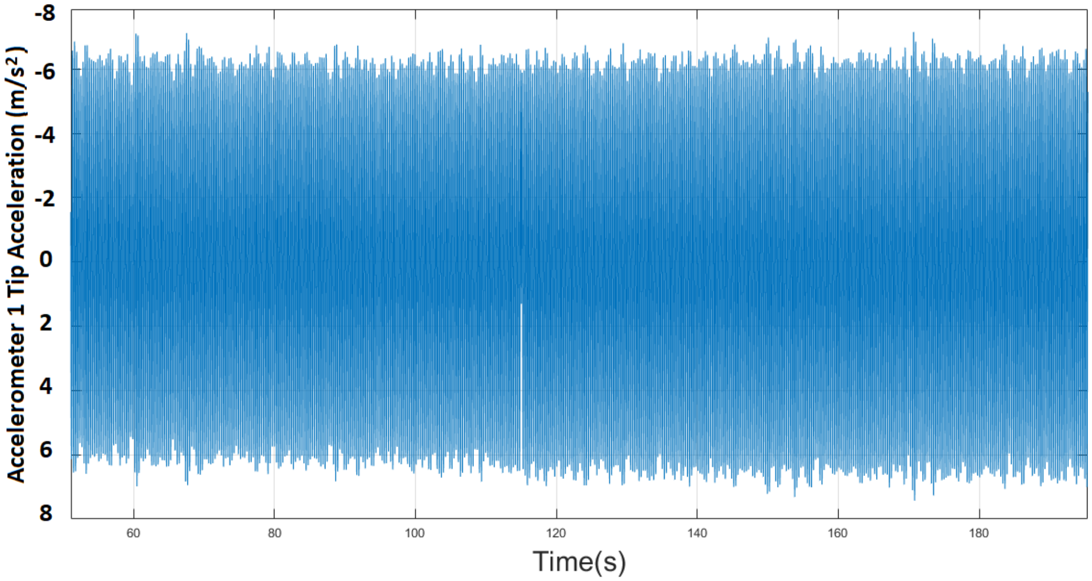

Figure 4.27: Representative Tip Acceleration Time History (Filtered $F_{stop} = 6$ Hz, $F_{pass} = 5$ Hz), Test F March 15, 2019, for $U = 8.04$ m/s, $Re_c = 7.9 \times 10^4$

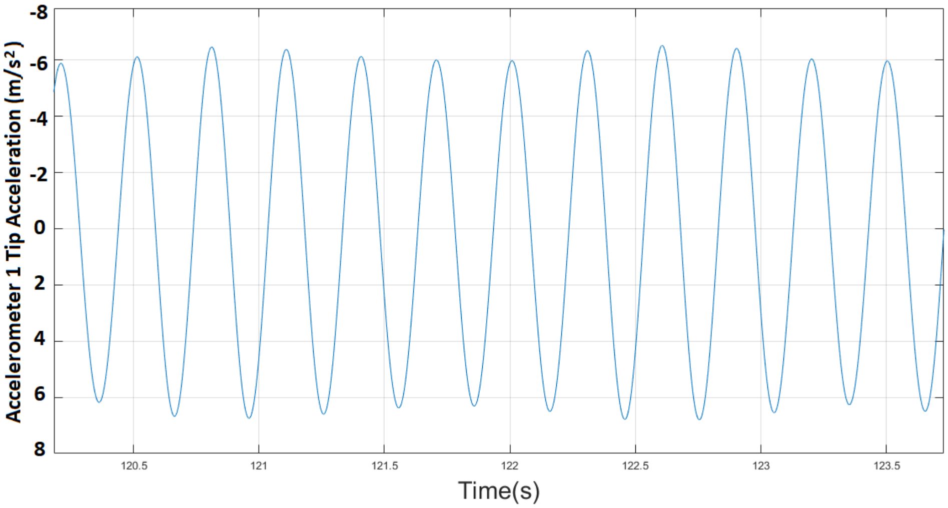

Figure 4.28: Representative Tip Acceleration Time History (Filtered $F_{stop} = 6$ Hz, $F_{pass} = 5$ Hz), Test F March 15, 2019 (Zoomed View), for $U = 8.04$ m/s, $Re_c = 7.9 \times 10^4$

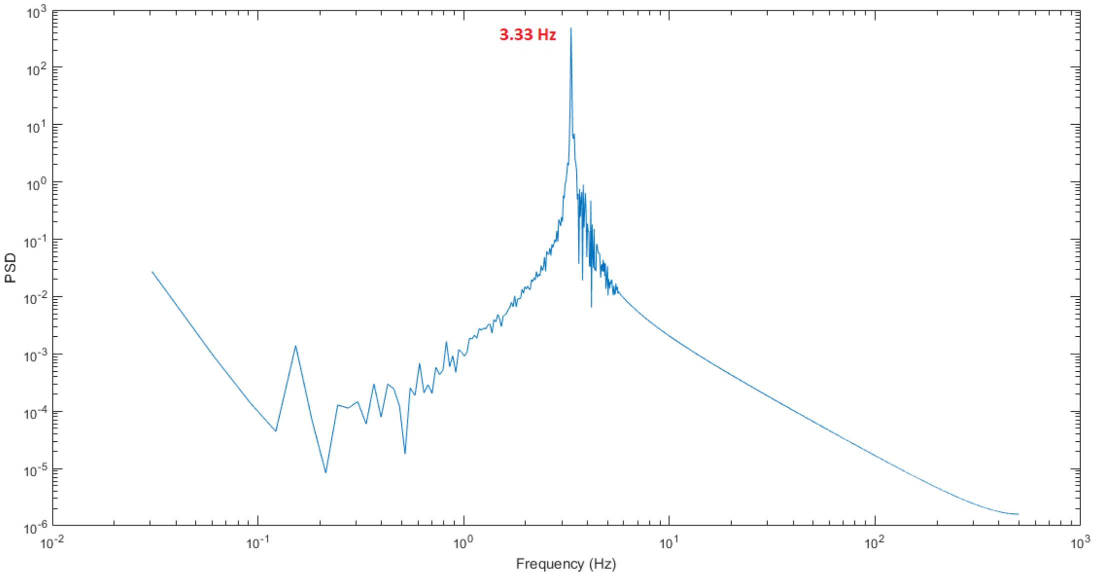

Figure 4.29: Representative Tip Acceleration PSD, Test F March 15, 2019 (Filtered $F_{stop} = 6$ Hz, $F_{pass} = 5$ Hz), for $U = 8.04$ m/s, $Re_c = 7.9 \times 10^4$

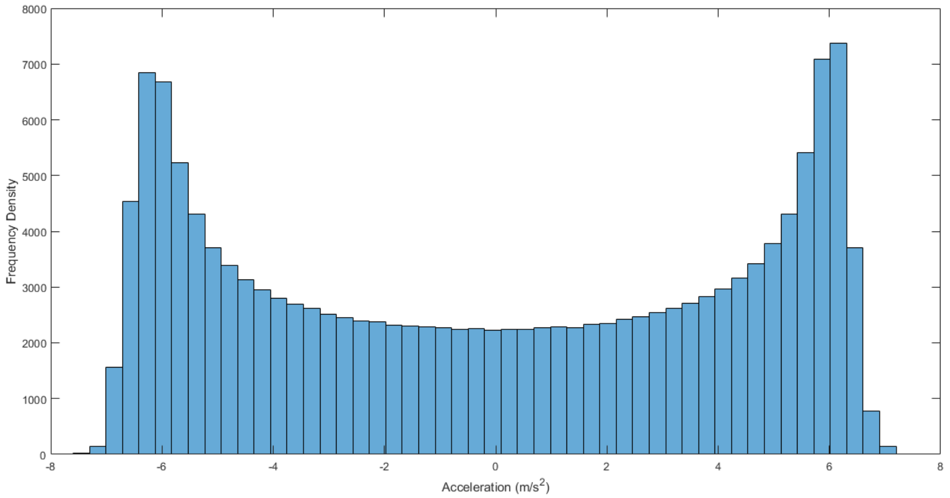

Figure 4.30: Representative Tip Acceleration Histogram, Test F March 15, 2019 (Filtered $F_{stop} = 6$ Hz, $F_{pass} = 5$ Hz), for $U = 8.04$ m/s, $Re_c = 7.9 \times 10^4$

Results

As a means to validate the acceleration results, Equation 4.1 was used to provide a rough estimate of the analytical accelerations for a system undergoing SHM. In Equation 4.1 [53],

x is the tip deflection, ω is the LCO frequency, and $\ddot{x}$ is the acceleration for each point.

$$|\ddot{x}| = |-\omega^2 x| \tag{4.1}$$

Time history data for the acceleration can be seen in Figures 4.24 and 4.25. The results of Accelerometer 1 range from 6-19 m/s^2, and Accelerometer 2 range from 5-16 m/s^2. Compared with the analytical estimations, of 10-33 m/s^2. Figure 4.31 shows that the estimated analytical accelerations are higher than the experimental accelerations for both accelerometers. However, there appear to be analogous trends in the growth of the magnitudes. This could infer that the experimental values are lower due to the fact that they are not truly SHM. Overall the trend appears to be acceptable, as it follows a quadratic which is similar to the analytical model, as seen in Equation 4.1.

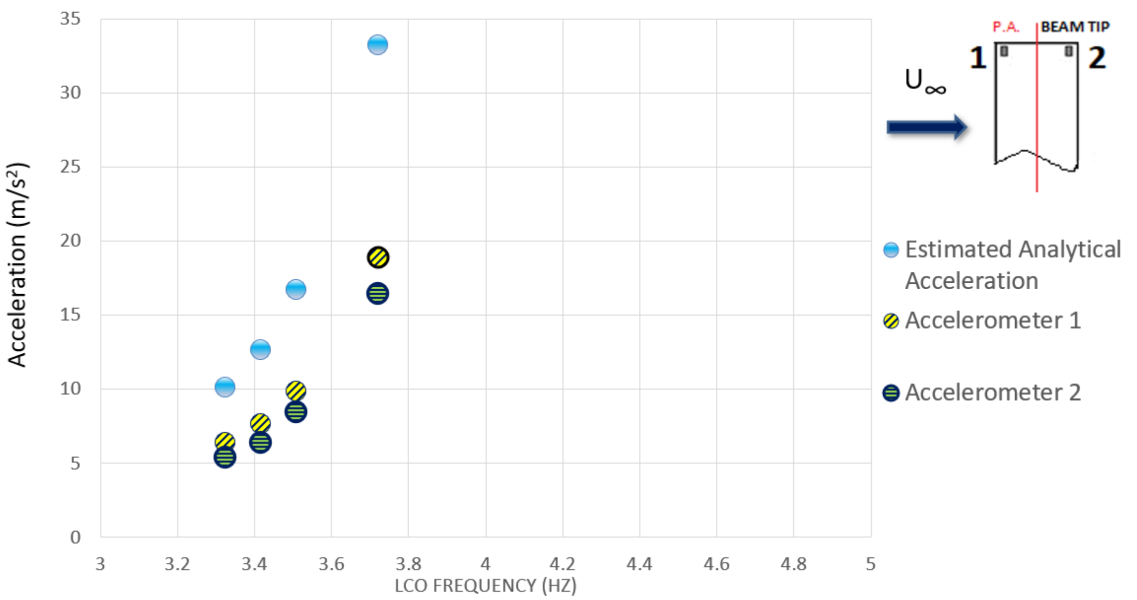

Figure 4.31: Comparison of Experimental versus Analytical Accelerations

4.4 LCO Frequencies For Beams-01,-02

The frequency results for tests A-F are presented in this section. The results of Test G will be covered in Section 4.5, and the cursory results of Test H are discussed in Section 5.5.

Frequency Resolution and LCO Filter Frequencies

Equation 4.2 [36] was used to determine the frequency resolution for each test; Δt represents the time increment between points (a constant of $1/F_s$, where $F_s = 1000$ Hz sampling rate) , and 2^n represents 2 to the power of some number (n), which is less than or equal to the length of the vector of data. The frequency resolution for each test can be seen in Table 4.3.

$$f = \frac{1}{2^n \Delta t} \tag{4.2}$$

Table 4.3: Summary of Frequency Resolutions and Filter Frequencies

Test	Frequency Resolution (Hz)	LCO Low-Pass Stopband Frequency (Hz)	LCO Low-Pass Passband Frequency (Hz)
A	0.0610	5	4
B	0.1221	5	3
C	0.2441	5	4
D	0.0610	5	3
E	0.0610	5	3
F	0.0610	5	4
G	0.0610	10	9

Results

The LCO frequencies were extracted from the PSD's of each potentiometer test point, and the data were filtered once, just above the dominant frequency. The LCO frequencies were then plotted versus airspeed as seen in 4.32; the average pre-test and post-test no-flow free decay pitch frequencies were plotted for comparison. From Fig 4.32, all LCO frequencies are observed to fall within the small frequency spectrum of 3.3 - 4.4 Hz. The reason for the appearance of multiple curves is unknown at this time, and does not correspond to the expectation of two distinct frequency curves analogous to the two LCO branches seen for the LCO amplitudes. Upon inspection of Figure 4.33, which plots the LCO frequencies based on the region, it can be seen that while the LAO region frequencies vary only minimally (3.7-3.8 Hz), the LCO frequencies in the SAO region show the most variation (3.3-4.4 Hz), and apparent sensitivity to airspeeds and other conditions.

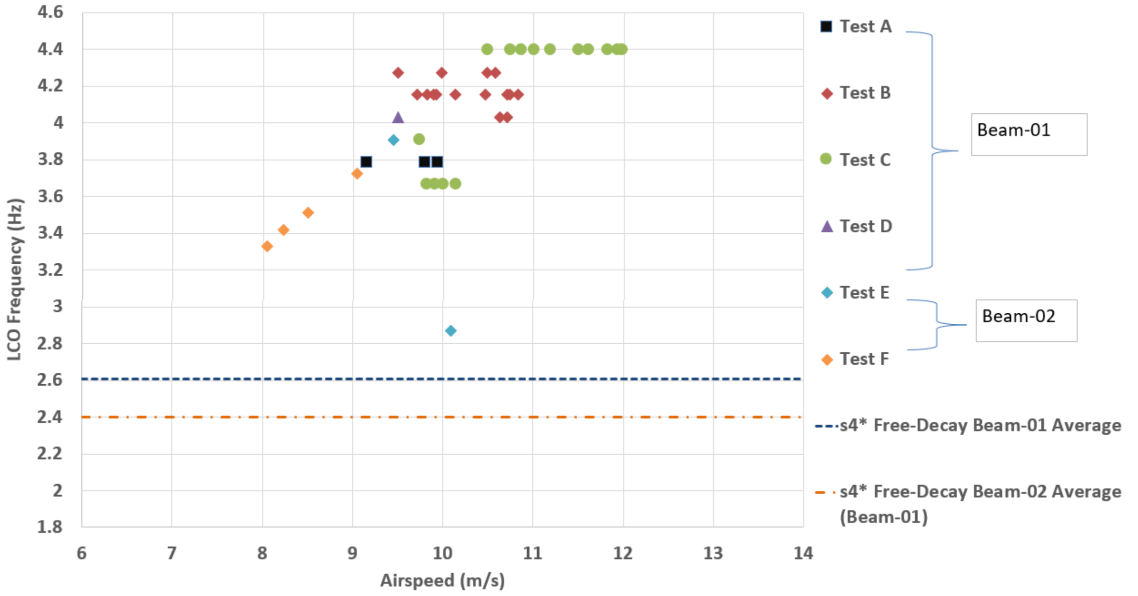

Figure 4.32: LCO Frequency

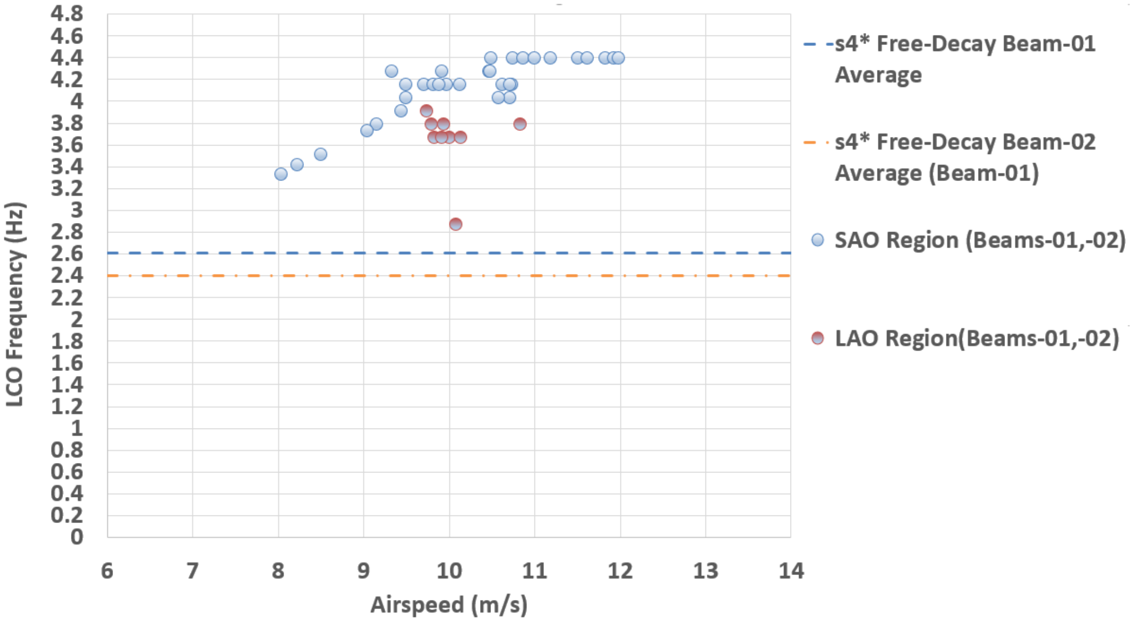

Figure 4.33: LCO Frequency: SAO and LAO Regions

4.5 Motion at the Wing Root For Beam-03

The issues of beam plastic deformation and failure in the Normalized AISI O1 steel beams (Beams-01,-02) have already been broached in a preliminary manner. However, this section provides details on the different behaviour incurred by using the stronger Tempered 1095 Spring Steel beam (Beam-03) for testing. Recall that while Beam-03 is made of a different type of steel, the beam natural frequencies are very close to the those of Beams-01,-02 (Sections 3.3.1 and 3.3.2).

In Test G, there were issues with strain gauge saturation/damage. This appeared to be corroborated by the time traces; while the potentiometer data showed a good, clean LCO of constant amplitude, the accelerometer data for the same airspeed showed two different LCO amplitudes - this brought the accuracy into question and requires further investigation. Another prominent issue was that the pressure transducer malfunctioned after Test F, and thus incorrect airspeeds were recorded for Test G. While reasonable airspeeds have been calculated based on previous tests as seen in Section E.1, this means that the effects of hysteresis have not been captured. Nevertheless, the results of Test G are included and discussed as they are an important step in understanding how to recognize and mitigate instrumentation errors, as well as provide glimpses into the effects of different beam properties.

Small Amplitude Oscillations

Unfiltered Data

Figures 4.34 and 4.35 show the zeroed, unfiltered sample time history trace for the SAO region; note that the signal is clearly noisy and once again exhibits distortion. Figure 4.36 shows the unfiltered PSD, indicating the dominant frequency of 4.94 Hz, and 2f and 3f superharmonics, indicating some asymmetries and non-linearities, as well as wind tunnel noise and possible noise from the oscillating wing/beam test rig.

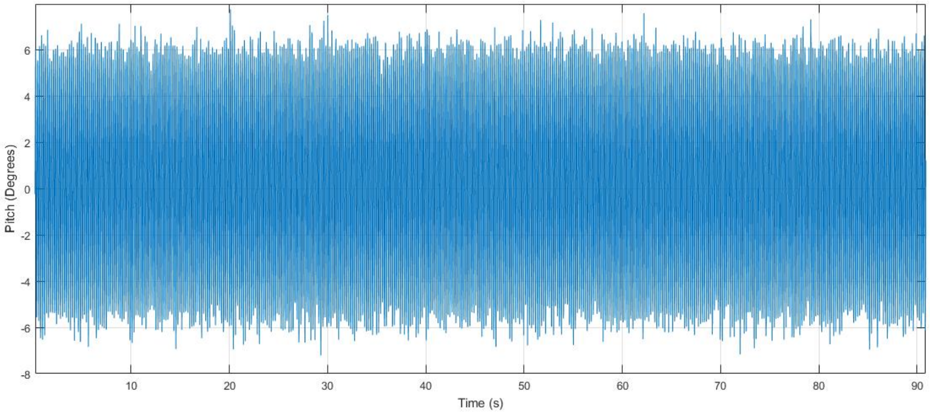

Figure 4.34: Representative Unfiltered Pitch SAO Time History, Test G May 27, 2019, $U = 13.88$ m/s, $Re_c = 1.4 \times 10^5$, Tempered 1095 Spring Steel Beam

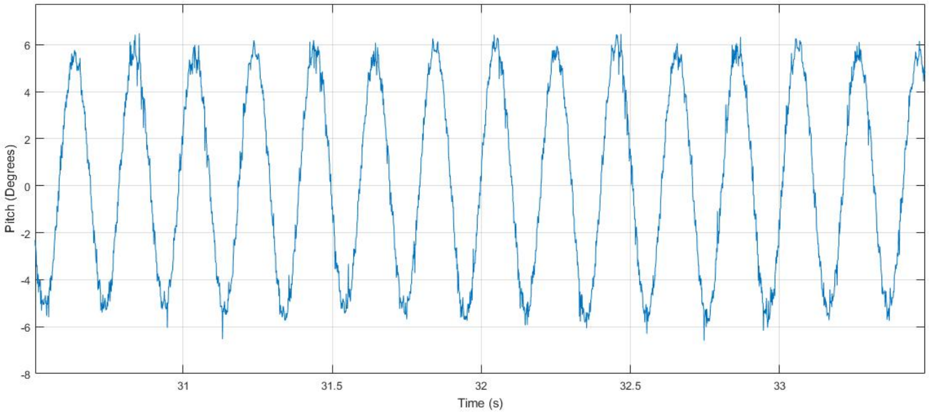

Figure 4.35: Representative Unfiltered Pitch SAO Time History, Test G May 27, 2019 (Zoomed View), $U = 13.88$ m/s, $Re_c = 1.4 \times 10^5$, Tempered 1095 Spring Steel Beam (Beam-03)

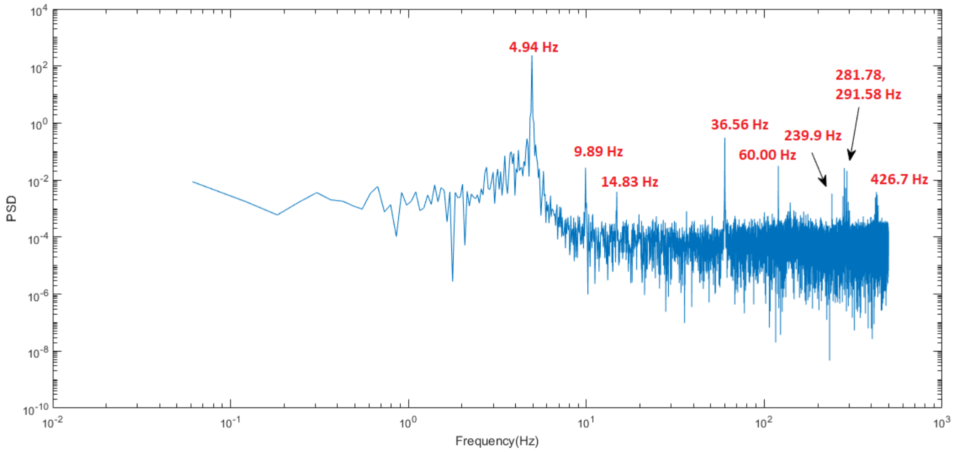

Figure 4.36: Representative Unfiltered Pitch SAO Power Spectral Density for Test G May 27, 2019, U = 13.88 m/s, $Re_c = 1.4 \times 10^5$, Reynolds number Tempered 1095 Spring Steel Beam (Beam-03)

Filtered Data

Figures 4.37 and 4.38 show the filtered, zeroed time history trace examples for the LAO region. Once again, it is evident that the waves are distorted and there is apparent modulation. Figure 4.39 shows the filtered PSD, with only the dominant frequency 4.94 Hz visible. Finally, Figure 4.40 shows a rounded and relatively symmetrical shape.

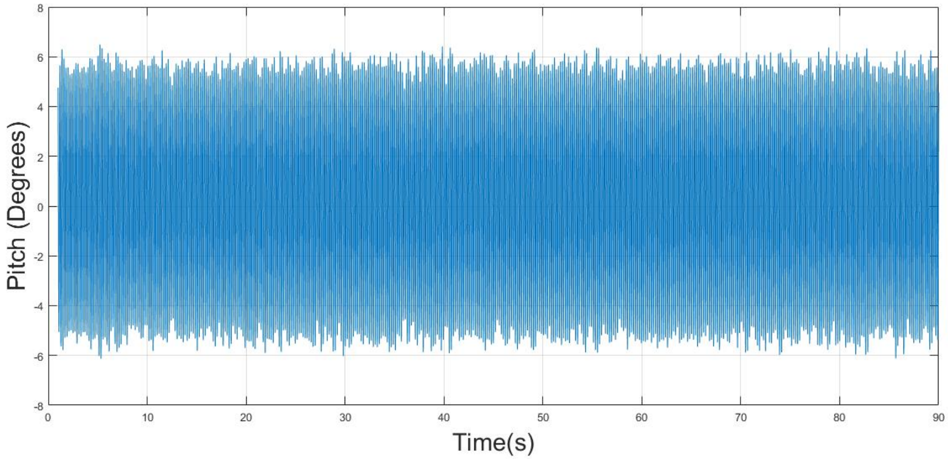

Figure 4.37: Representative Filtered Pitch SAO Time History(F_{stop} = 35 Hz, F_{pass} = 30 Hz), Test G May 27, 2019, U = 13.88 m/s, $Re_c = 1.4 \times 10^5$, Tempered 1095 Spring Steel Beam

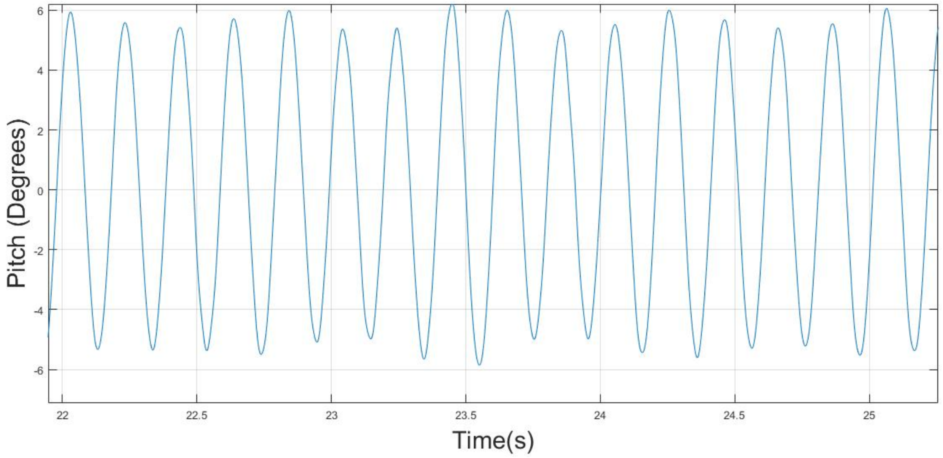

Figure 4.38: Representative Filtered Pitch SAO Time History Close-Up ($F_{stop} = 35$ Hz, $F_{pass} = 30$ Hz), Test G May 27, 2019 (Zoomed View), $U = 13.88$ m/s, $Re_c = 1.4 \times 10^5$, Tempered 1095 Spring Steel Beam (Beam-03)

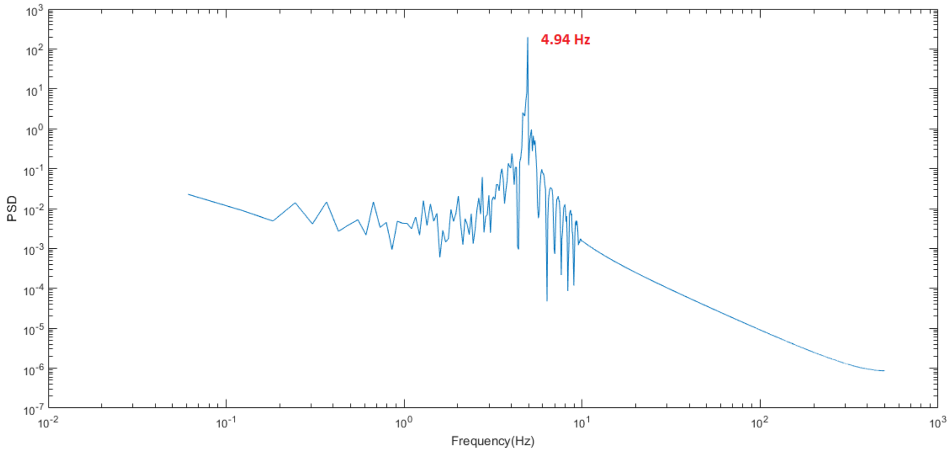

Figure 4.39: Representative Filtered Pitch SAO Power Spectral Density for Test G May 27, 2019 ($F_{stop} = 10$ Hz, $F_{pass} = 9$ Hz), $U = 13.88$ m/s, $Re_c = 1.4 \times 10^5$, Reynolds number Tempered 1095 Spring Steel Beam (Beam-03)

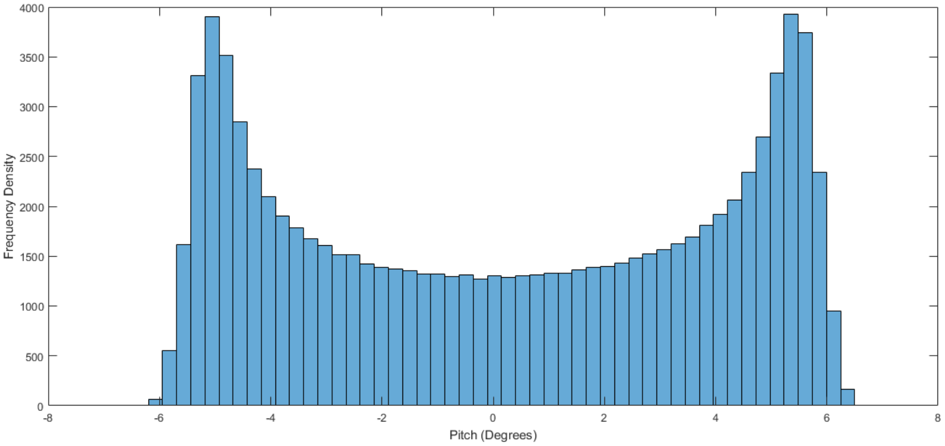

Figure 4.40: Representative Filtered Pitch SAO Histogram for Test G May 27, 2019, ($F_{stop} = 35$ Hz, $F_{pass} = 30$ Hz), $U = 13.88$ m/s, $Re_c = 1.4 \times 10^5$, Tempered 1095 Spring Steel Beam (Beam-03)

Large Amplitude Oscillations

Unfiltered Data

Figures 4.41 and 4.42 show the zeroed, unfiltered sample time trace for the LAO region, which clearly show evidence of a noisy signal. The unfiltered PSD is seen in Figure 4.43, where the dominant frequency of 4.88 Hz is observed, along with 2f-7f peaks, indicating asymmetry and non-linearities, as well as wind tunnel noise and possible wing/beam test rig vibration.

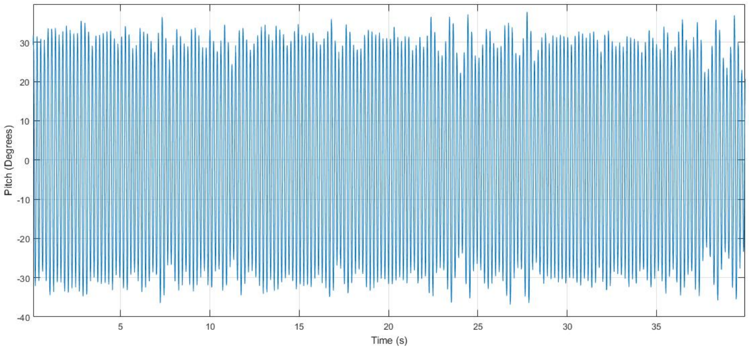

Figure 4.41: Representative Pitch LAO Time History, Test G May 27, 2019, $U = 16.3$ m/s, $Re_c = 1.6 \times 10^5$, Tempered 1095 Spring Steel Beam (Beam-03)

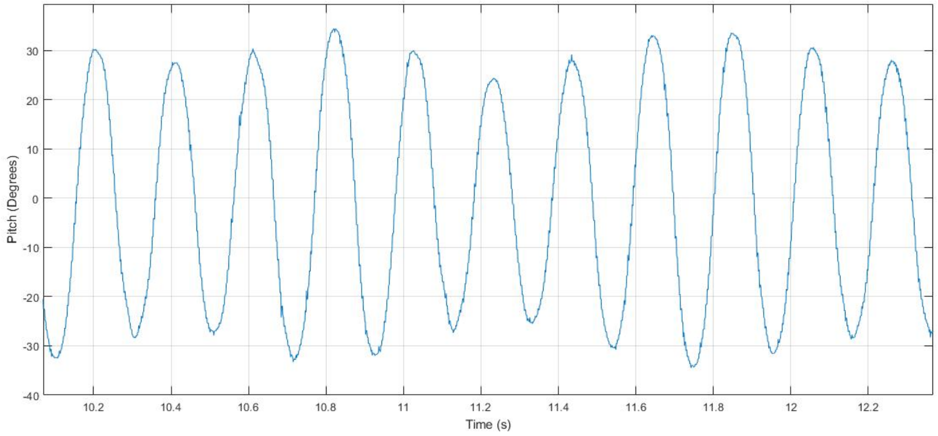

Figure 4.42: Representative Pitch LAO Time History, Test G May 27, 2019 (Zoomed View), U = 16.3 m/s, $Re_c = 1.6 \times 10^5$, Tempered 1095 Spring Steel Beam (Beam-03)

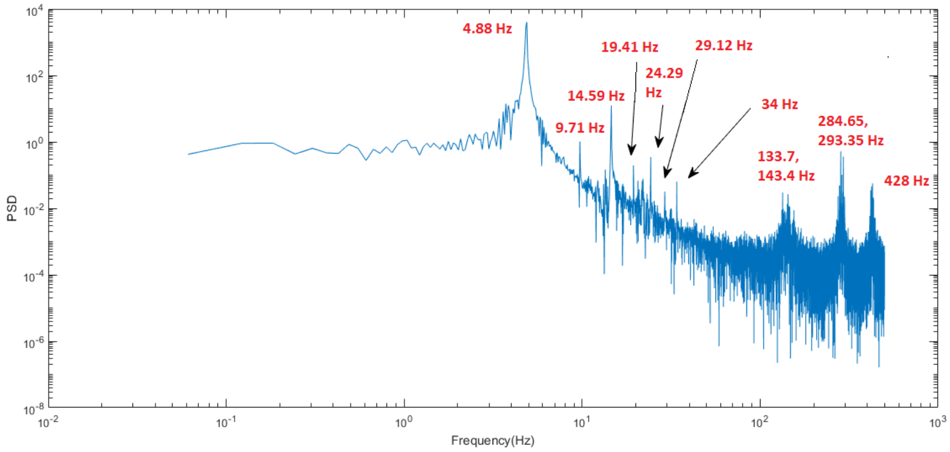

Figure 4.43: Representative Pitch LAO Power Spectral Density, Test G May 27, 2019, U = 16.3 m/s, $Re_c = 1.6 \times 10^5$, Tempered 1095 Spring Steel Beam (Beam-03)

Filtered Data

Figures 4.44 and 4.45 show the zeroed, filtered pitch LAO time trace, indicating significant modulation and distorted waves. The filtered PSD, Figure 4.46, shows that only the dominant frequency of 4.88 Hz is present. Finally Figure 4.46 shows the relatively symmetrical, rounded histogram.

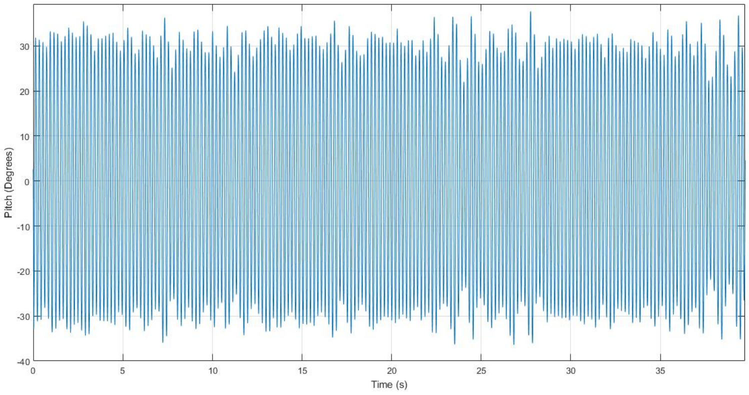

Figure 4.44: Representative Filtered Pitch LAO Time History,(F_{stop} = 35 Hz, F_{pass} = 30 Hz), Test G May 27, 2019, U = 16.3 m/s, $Re_c = 1.6 \times 10^5$, Tempered 1095 Spring Steel Beam (Beam-03)

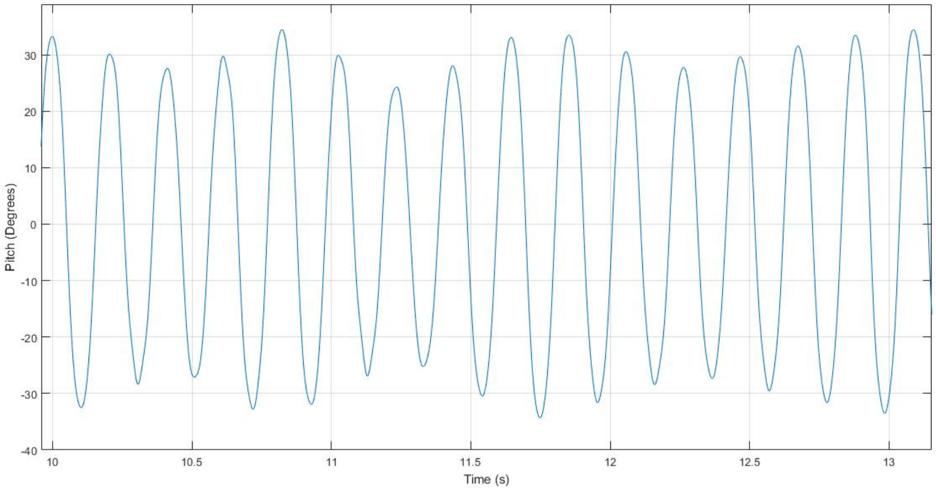

Figure 4.45: Representative Filtered Pitch LAO Time History (F_{stop} = 35 Hz, F_{pass} = 30 Hz), Test G May 27, 2019 (Zoomed View), U = 16.3 m/s, $Re_c = 1.6 \times 10^5$, Tempered 1095 Spring Steel Beam (Beam-03)

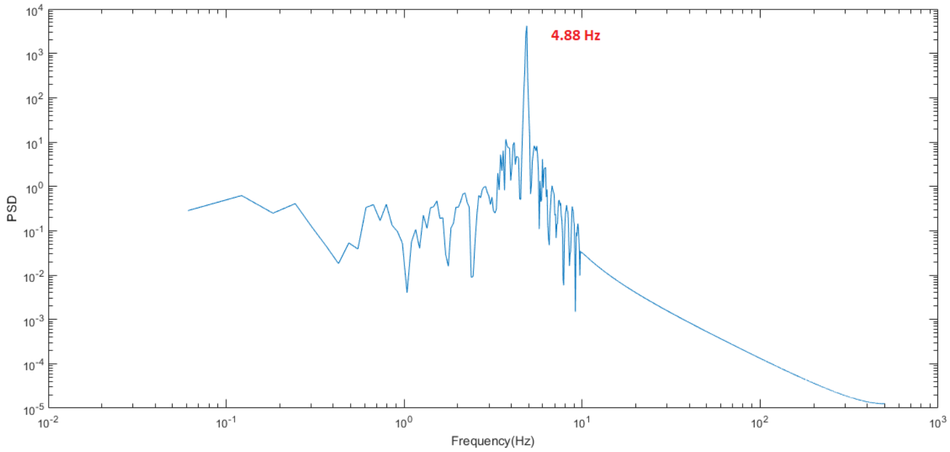

Figure 4.46: Representative Filtered Pitch LAO Power Spectral Density for Test G May 27, 2019, (F_{stop} = 10 Hz, F_{pass} = 9 Hz), U = 16.3 m/s, $Re_c = 1.6 \times 10^5$, Tempered 1095 Spring Steel Beam (Beam-03)

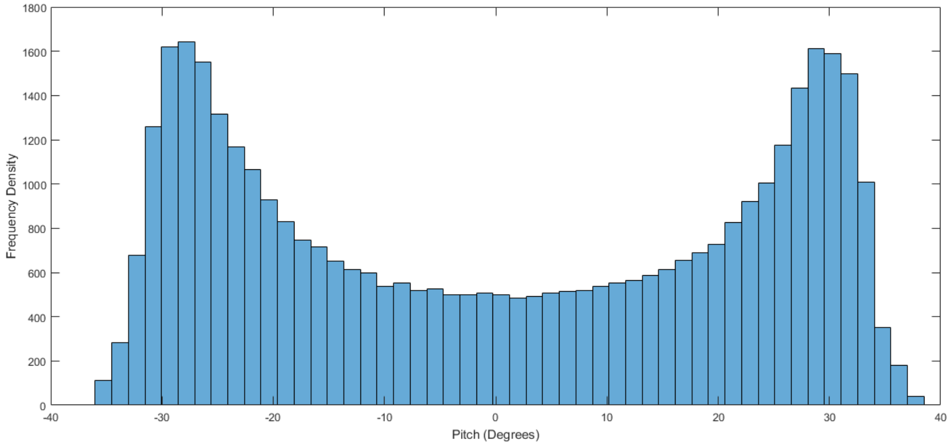

Figure 4.47: Representative Filtered Pitch LAO Histogram for Test G May 27, 2019, (F_{stop} = 35 Hz, F_{pass} = 30 Hz), U = 16.3 m/s, $Re_c = 1.6 \times 10^5$, Tempered 1095 Spring Steel Beam (Beam-03)

Results

LCO Pitch Amplitudes

The LCO amplitudes for Test G are presented in Figure 4.48. Once again, there are two apparent branches, as with Beams-01,-02; however the onset of LCO's, at around 13.8 m/s, occurred at much higher airspeeds than previously seen with Beams-01,-02 (8-10 m/s). The SAO region is consistent with the range of $0-15°$, but the LAO region is now in the range of $30-35°$. Qualitatively, observations during testing suggested that in the LAO region, the wing/beam experienced (tip) bending deflections of a lesser magnitude (relative to Beams-01,-02), coexisting with larger pitch deflections at the root. Thus, a detailed analysis of the Test G strain gauge and accelerometer data will be necessary for future work.

Only two points were gleaned in the LAO region since, as with Beams-01,-02 steady-state was difficult to achieve. Furthermore, the onset of LAO for Beam-03 was over 16 m/s, in contrast to 12 ms for Beams-01,-02. It is important to note that at these higher airspeeds, there was uncertainty as to whether the oscillations might become so catastrophic that they would cause damage to the wing apparatus or tunnel, as well as posing health and safety concerns. Thus, the test airspeed was limited to less than 18 m/s.

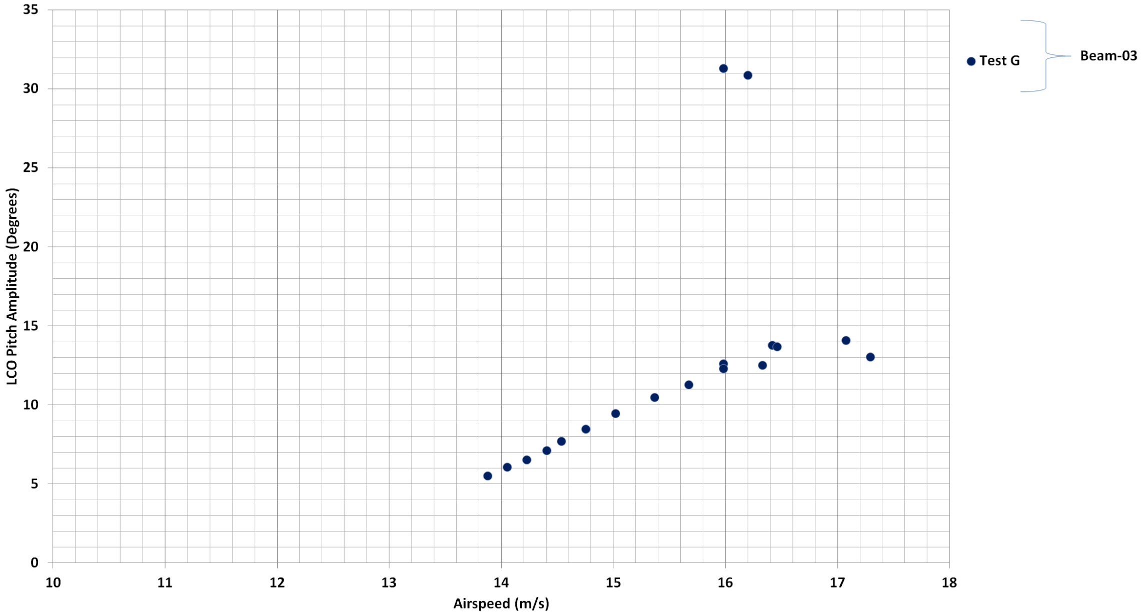

Figure 4.48: LCO Pitch Amplitude versus Airspeed, Test G May 27, 2019 for Tempered 1095 Spring Steel Beam (Beam-03)

LCO Frequencies

The LCO frequencies for Test G are seen in Figure 4.49 along with the no-flow free decay $s4^*$ frequency. The Test G LCO frequencies are generally higher than for Beams-01,-02 as seen in Figure 5.3. Referring to Figure 5.3, we see that all frequencies fall in the range of 3-5.1 Hz. The Beam-03 frequencies are higher than the frequencies found for Beams-01,-02 . However, both sets of data show that the frequencies grow with airspeed until they reach a peak, and then decrease (around 3.7 Hz at 8.5 m/s and 5.1 Hz at 14.8 m/s, for Beams-01,-02 and Beam-03 respectively). Figure 5.3 shows the difference between the magnitudes of the LCO frequencies for Beams-01,-02 (Normalized AISI O1 steel) versus Beam-03 (Tempered 1095 spring steel). Note that while the Beam-01,-02 frequencies range from 3.3-4.4 Hz, the Beam-03 frequencies span from 4.7 - 5.1 Hz.

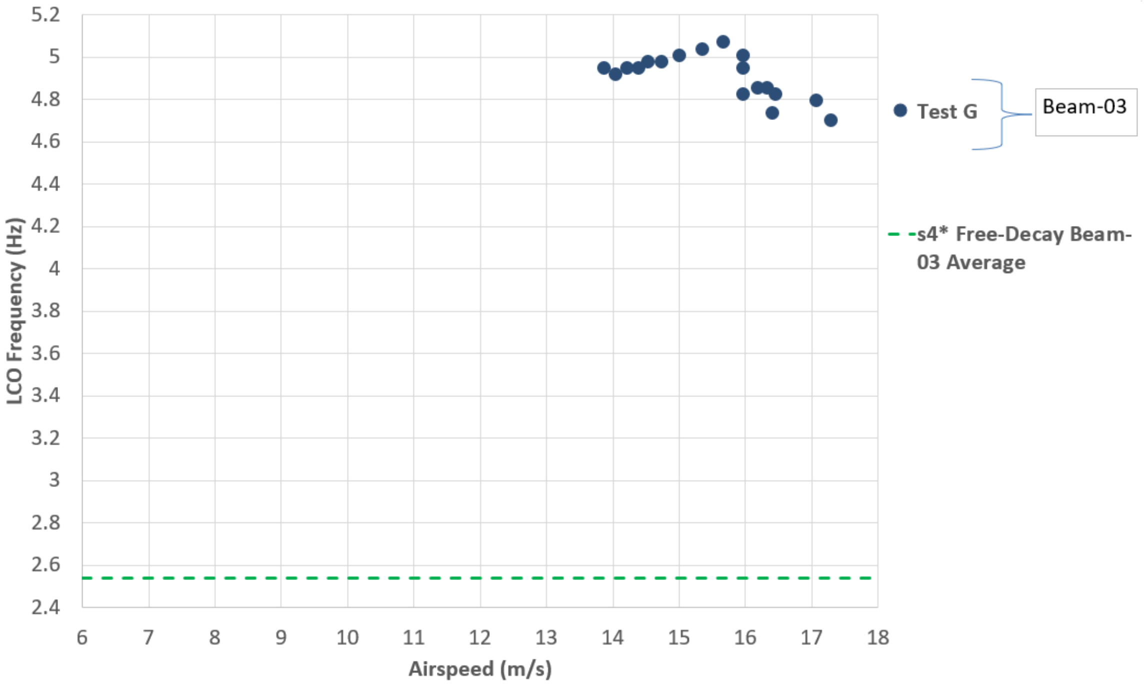

Figure 4.49: LCO Frequency versus Airspeeds, Test G May 27, 2019, for Tempered 1095 Spring Steel Beam (Beam-03)

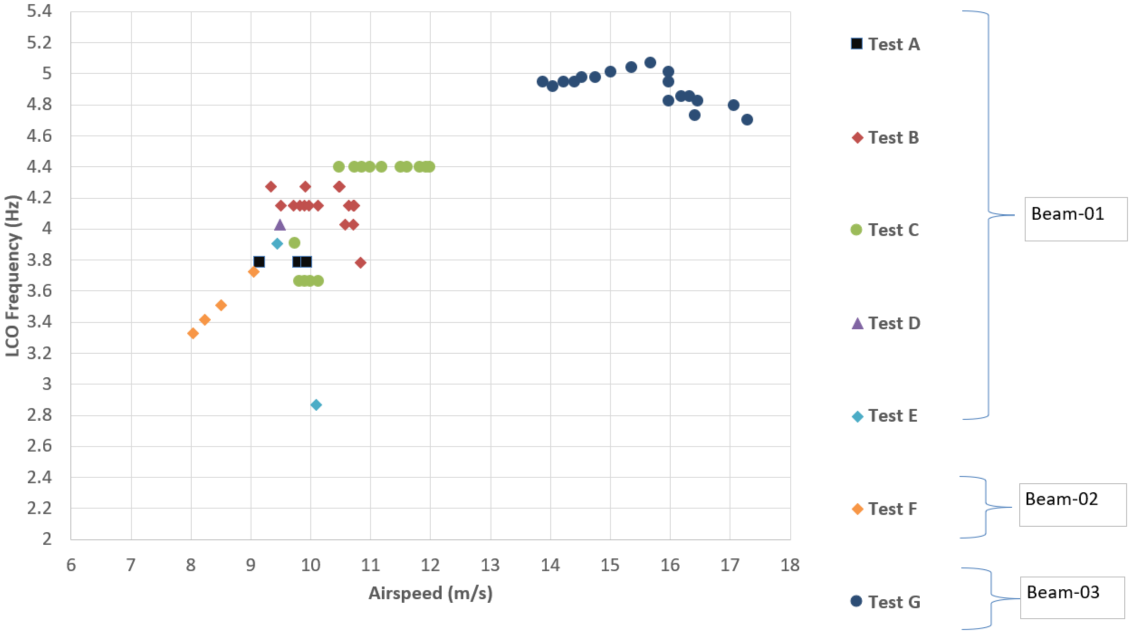

Figure 4.50: Comparison of LCO Frequencies for Normalized AISI Steel (Beams-01,-02) and Tempered 1095 Spring Steel (Beam-03)

5 Discussion

5.1 Pitch LCO Amplitude Comparisons

Figure 5.1 shows the LCO amplitudes for Tests A-G, encompassing the usage of both the Normalized AISI O1 steel and Tempered 1095 spring steel beams. All LCO's were instigated by means of an initial condition (ΔU or $\Delta \theta$). This is consistent with the knowledge that a critical speed and a perturbation (either by physical application of an initial condition to the root of the apparatus, or by means of a change in airspeed) are required to instigate LCO's. Another interesting note is the reminder that Tang and Dowell (2000) found that LCO amplitudes are proportional to the magnitude of freeplay of the system (for the flexible wing, prominent sources of freeplay are internal ball-bearings, and the fit between the beam/wing); Marsden further confirmed this correlation, as well as that the static bias affects the mean LCO amplitude [2]. Hence, this suggests that there may also be a correlation occurring for this data. Finally, the very existence of LCO's confirms that non-linearities are present.

In Figure 5.1, it is evident that the SAO and LAO regions occur over the same range of airspeeds. This behaviour was also observed in the research of Mendes and Goyaniuk [21][22]. There is also a transition region in between the SAO and LAO regions, which is consistent with the findings of Mendes, who stated that for an elastic axis at 27%, there was a "tendency to jump to large amplitude at high airspeeds [21]." In Figure 5.1, the jump appears between approximately 15° - 30°. Generally speaking, the work done by Poirel et al. proved that these LCO's which are occurring are self-sustaining [5].

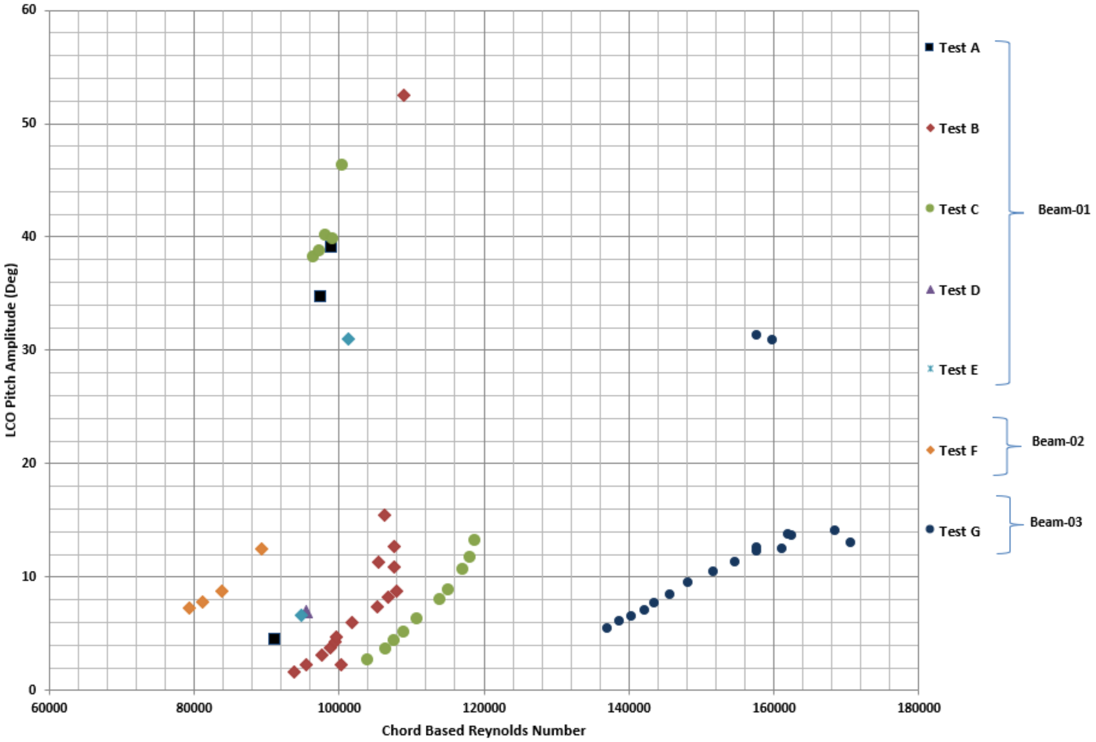

Figure 5.1: LCO Root Pitch Amplitude versus Reynolds Number

Figure 5.2 shows both the (root) pitch and flapwise tip bending deflections plotted simultaneously. The maximum value of 14 cm chosen for the tip bending deflection scale was not arbitrary, but rather, represents a maximum estimated by both visual observation, and rough data obtained from Test F in the LAO region, used as guides. The plot serves as a preliminary means to convey the motion of the wing at the root and tip locations. It is worth noting that McCroskey [1] found that the plunge DOF (analogous 1^{st} flapwise bending) generally intensified the overall amplitude of the LCO oscillations.

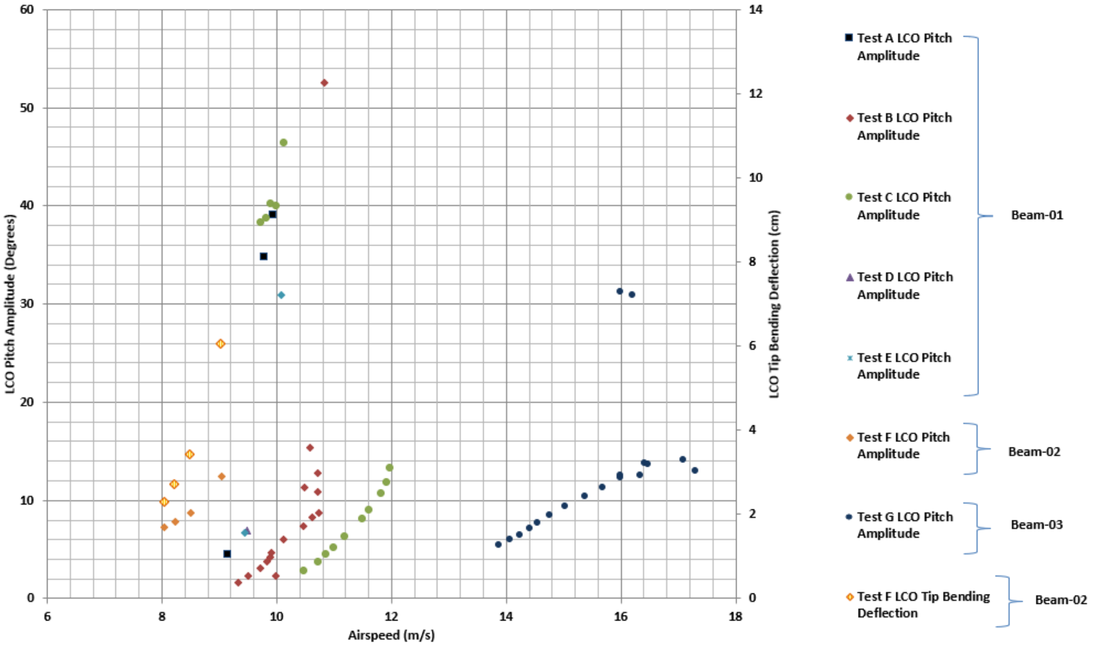

Figure 5.2: LCO Root Pitch Amplitude (Degrees) and LCO Tip Bending Deflection (cm) versus Airspeed, Tests A-G

In order to gain perspective on the validity of these results, it is useful to compare them with previous results from the rigid wing, in order to determine if the LCO amplitudes and frequencies appear reasonable, as well as to provide clues for the possible types of flutter which may be occurring.

5.2 Flutter Characteristics and Mechanisms

5.2.1 Small Amplitude Oscillations

The current flexible wing SAO results (Beams-01,-02) occur in the range of $7.9 \times 10^4 < Re_c < 1.2 \times 10^5$ (E.A. located at 25%) and exhibit LCO amplitudes of $1 - 15°$. For this wing, the E.A. is located at 25% of the chord. In general, the appearance of an SAO region indicates the existence of Reynolds number effects, and that the airfoil is smooth. While the LCO onset speed is different for each test, all SAO branches appear to follow the same increasing trend with airspeed. The magnitudes of the LCO amplitudes also appear to be fairly consistent across all tests. There is a strong dependence of SAO amplitude on airspeed, consistent with the work of Rocha Da Costa [27].

Table 5.1 presents select data from the works of Mendes, Goyaniuk, and Robinson along with results from this thesis: over all, it can be observed that while the parameters (i.e. elastic axis and frequency ratio) from previous tests with the rigid wing are not an exact match with the current flexible wing parameters, nonetheless they provide a good estimation of the magnitude of the LCO amplitudes that might be expected for the SAO region. Note that the frequency ratio for the rigid wing is estimated as the ratio of 1^{st} flapwise bending to pitch ($\bar{\omega} = {}^{\omega_{w1}}/_{\omega_\theta}$)for this case.

Table 5.1: Comparison of Pitch SAO Amplitudes [21] [22] [28]

Author	$\bar{\omega}$	Re_c Range	E.A. Location (%)	Pitch Amplitude (Deg.)	Type of Flutter
Mendes	1.59	$6 \times 10^4 - 8.5 \times 10^4$	18.6	4.5-7.5	Laminar Separation
Mendes	< 1	$6.5 \times 10^4 - 1.1 \times 10^5$	27	1.9-3.8	2 DOF Laminar Separation
Mendes	< 1	$6 \times 10^4 - 7 \times 10^4$	27	4.5-5	1 DOF Laminar Separation
Robinson	1.95	1.4×10^5	25	20	Unknown
Itwar Barrett	1.95	$7.9 \times 10^4 - 1.2 \times 10^5$	25	0-15	Unknown

For $\bar{\omega} < 1$, with an E.A. at 27%, Mendes found the overall range of amplitudes is $1.9 - 5°$. These values fall into the lower end of the flexible wing SAO region LCO amplitudes. For $\bar{\omega} > 1$, with an E.A. at 18.6%, Mendes found SAO due to LSF, with amplitudes around $4.5 - 7.5°$. Overall it appears that SAO for the flexible wing occurs over a much larger range of Reynolds numbers than for the rigid wing. Furthermore, the maximum SAO amplitude is higher than previously seen for the rigid wing.

Comparing the numerical results of Robinson for the parameters seen in Table 3.2, for $Re_c = 1.4 \times 10^5$, the pitch amplitude is 20°. Experimentally, this value falls into the transitional region, where no data could be captured due to the previously mentioned "jump" in airspeed.

5.2.1.1 Evidence of Laminar Separation Flutter

Goyaniuk noted that LSF exhibited small amplitude LCO's (SAO), which were due to the feedback between the LSB behaviour and the reaction of the wing itself; this in turn created negative aerodynamic damping in the non-linear region at low AOA. These effects could be suppressed if the boundary layer was tripped with a wire or sandpaper, or if the wing surface itself was not smooth [22] [21]. Thus the very existence of SAO suggests that LSF is occurring. The rigid wing SAO, which was caused by LSF, also appeared to be strongly sensitive to the Reynolds number. Similarly, the flexible wing SAO results show a clear sensitivity to Reynolds number. Finally, Mendes found that for an E.A. at 27%, the mechanism which caused the LCO's was LSF, and that both the pitch and heave increased greatly with airspeed (for $\bar{\omega} > 1$). Data in Section 4.5 illustrates that both the pitch and flapwise bending LCO amplitudes also increase with airspeed.

5.2.2 Large Amplitude Oscillations

The current flexible wing LAO results (Beams-01,-02) occur in the range of $9.2 \times 10^4 < Re_c < 1.1 \times 10^5$ and exhibit LCO amplitudes in the range of $31° - 53°$. As a reminder, for this wing, the E.A. is located at 25% of the chord. It appears that data in the LAO region are not as sensitive to the airspeed as data in the SAO range. Furthermore, converse to what occurs in the SAO region, Harris noted that there was a positive effective aerodynamic stiffness in the LAO region which increases with airspeed (for the rigid wing), which may explain why the LCO amplitudes from all tests in the LAO region appear to collapse onto one curve in a manner similar to Harris' findings [2]. Table 5.2 provides comparative rigid wing data from Mendes and Goyaniuk [22][21].

Table 5.2: Comparison of Pitch LAO Amplitudes [21] [22]

Author	$\bar{\omega}$	Re_c Range	E.A. Location (%)	Pitch Amplitude (Deg.)	Type of Flutter
Mendes	1.41	$6.4 \times 10^4 - 6.6 \times 10^4$	35	29-33	Stall
Mendes	1.47	$1.2 \times 10^5 - 1.6 \times 10^5$	27	20-25	L Stall
Mendes	1.59	6.7×10^4	27	20-25	Coupled
Mendes	1.59	6.7×10^4	18.6	60	Coupled
Goyaniuk	1.34	$8 \times 10^4 - 1.5 \times 10^5$	27	40-45	Coupled
Goyaniuk	1.43	$8 \times 10^4 - 1.5 \times 10^5$	35	37-47	Stall
Itwar Barrett	1.95	$9.2 \times 10^4 - 1.1X10^5$	25	30-60	Unknown

For an E.A. located at 18.6, % Mendes observed a pitch amplitude of 60° caused by coupled flutter, which is comparable with the maximum flexible wing pitch LCO amplitude.

For an E.A. located at 35%, Mendes found amplitudes on the order of $29° - 33°$, while Goyaniuk encountered LCO amplitudes in the range of $37° - 47°$. In both cases, the LCO's were caused by stall flutter.

For an E.A. at 27%, Goyaniuk found that for $8 \times 10^4 < Re_c < 1.5 \times 10^5$, coupled flutter occurred and the corresponding LCO amplitudes were approximately $40° - 45°$. Similarly, Mendes found that coupled flutter occurred for $Re_c = 6.7 \times 10^4$, with amplitudes around $20° - 25°$, and stall flutter for $1.2 \times 10^5 < Re_c < 1.6 \times 10^5$ with amplitudes around $20° - 25°$. Thus, the LCO amplitudes found by Mendes and Goyaniuk for an E.A. located at 27% are less than or equal to the flexible wing LAO amplitudes for the E.A. located at 25%.

Hence, when the E.A. position is located at 27% of the chord (which is very close to 25%), and for frequency ratios in the range of $1 < \bar{\omega} < 1.95$, two types of flutter are possible: *coupled flutter* in the *lower* Reynolds number range, and *stall flutter* in the *higher* Reynolds number range. Therefore, the flexible wing LCO's in the LAO region could possibly be due to either coupled flutter or stall flutter. Sections 5.2.2.1 and 5.2.2.2 will present evidence comparing and contrasting which types of flutter may be occurring.

5.2.2.1 Evidence of Coupled Flutter

The flapwise bending LCO amplitudes, which can be seen in Figure 4.23, indicate a growth in the LCO amplitude versus airspeed in the SAO region. Furthermore, coupled flutter is known to be sensitive to the frequency ratio, and thus may explain why the amplitudes are larger for the flexible wing since it has a larger frequency ratio relative to the comparative rigid wings tests seen in Table 5.2. Harris also noted that for tests where the E.A. coincided with the A.C., the highest LCO amplitudes were experienced; hence, given that the analogous flexural centre and quarter-chord point for the flexible wing are also aligned, as such these LCO amplitudes could also possibly represent maximum values. If the mechanism for LAO is indeed coupled flutter, per the work of Da Costa, Poirel, and Mendes, coupled flutter would then simply describe the instability, with the amplitude then limited by flow separation [27][20].

In their work, Goyaniuk and Mendes generally found coupled flutter occurring in the range of $6.7 \times 10^4 < Re_c < 1.5 \times 10^5$ for an E.A. located at 27% of the chord. For $\bar{\omega} > 1$, Goyaniuk commented that the LCO pitch amplitudes all converged towards a common value with increasing Reynolds number. However, this was not the case for the flexible wing. Also, for the rigid wing, the heave LCO amplitudes increased, as did the flexible wing flapwise bending amplitudes (SAO region).

The evidence of a static bias for symmetric LCO's could also shed light on the possibility of coupled flutter. While a non-zero bias could also be due to stall flutter, this typically occurs past the divergence airspeed, which is theoretically infinite for the flexible wing [22]. Unfortunately, most of the data for Tests A-F are not a trustworthy indicator of the change in static bias solely as a result of the aerodynamics, since there was a clear change in flow bias due to the plastic deformation and beam failure which could taint the information (Figure 5.4). However, the data from Test G could possibly be analysed in future to track and plot the static bias with airspeed.

The numerical work of Robinson suggested that flutter was due to the coalescence of the rigid pitch and 1^{st} flapwise bending dominated mode, with the latter going unstable. The linear flutter speed was found to be 12.67 m/s. However due to the effects of a likely subcritical Hopf bifurcation, LCO's occurred below this predicted linear flutter speed (around 8-10 m/s). However, this does not necessarily imply that coupled flutter is not occurring, since the effect of the stiffening in pitch due to Reynolds number effects could cause the experimental test apparatus to have a lower flutter speed than predicted by the linear model [22].

5.2.2.2 Evidence of Stall Flutter

The LCO amplitude plots show the suggestion of multiple attractors, which were noted by Goyaniuk and Mendes for stall flutter. Specifically, Mendes noted that for an E.A. located at 27% both coupled flutter (2 DOF) and stall flutter (1 DOF) could be possible, depending on whether the flow was laminar or turbulent. He also noted that the 27% E.A. location was a transition point for coupled to stall flutter, dependent upon the frequency ratio. However, Mendes found that for $\bar{\omega} > 1$, for stall flutter, SAO occurred towards the lower end of the Reynolds number range, while the jump and subsequent shift to LAO occurred in the higher end of the range. This was not true in the case of the flexible wing, where both SAO and LAO occupied the same Reynolds number region. Finally, Mendes found that Reynolds number effects are not significant for LAO caused by stall flutter, and the flexible wing data indicates a low sensitivity to Reynolds number for LAO.

Goyaniuk commented that for $\bar{\omega} > 1$, the LCO pitch amplitudes tended to increase and then plateau with increasing Reynolds number, and the heave LCO amplitudes also increased. The flexible wing flapwise bending LCO amplitudes (Figure 4.23), indicate a growth in the LCO amplitude versus airspeed in the SAO region.

5.2.3 Hysteresis and Sensitivity to Ambient and Initial Conditions

Figure 4.15 shows that the onset of LCO oscillations varies between tests, and ranges from 8.1-10.4 m/s. It also clearly illustrates that in the airspeed range of 9.8-10.9 m/s, both SAO and LAO co-exist. The possible reason for the change in LCO onset could be attributed to multiple factors. The gradual beam failure occurring over Tests A-E may have affected the LCO onset as this would alter the static AOA at the wing tip, as well as the beam properties, and thus the mass moment of inertia of the system. There would certainly also have been a difference in the applied I.C.'s (pitch perturbation or change in airspeed).

The observance of a shift in the SAO/LAO boundary, difference in airspeed for a single RPM value, co-existence of SAO and LAO in the same airspeed range, and notable variation of LCO amplitude with small change in airspeed all point towards a dependence upon initial conditions, critical airspeed, multiple attractors, mean pitch angle and hysteresis. These observations are consistent with the results found by Tang and Dowell [9] [10], Poirel et al. [20], Mendes [21], Goyaniuk [22], Da Costa [27] and Patil et al. [54] as presented in

Section 1.2. Appendix F contains specific examples of experimentally encountered instances of hysteresis.

5.3 Comparison of Flapwise Wing Tip Bending Deflection and Heave

Table 5.3 compares the flexible wing flapwise bending LCO amplitudes (Beam-02, SAO region) at the wing tip with the rigid wing heave LCO amplitude results. The only rigid wing heave LCO amplitudes which are comparable to the flexible wing are for the cases of $\bar{\omega} = 1.59$, with an E.A. located at 18.6% of the chord, with an amplitude of 5.5 cm (coupled flutter) and $\bar{\omega} = 1.34$, and at an E.A. of 27% of the chord (coupled flutter) with an amplitude range of 3-3.5 cm. All these values were obtained in the range of $6 \times 10^4 < Re_c < 6.7 \times 10^4$. However, the flexible wing experiences flapwise bending SAO amplitudes which are on the order of magnitude seen for the LAO region for the rigid wing. Note that Robinson's numerical prediction appears to serve as a modest estimate of scale of the flapwise bending LCO amplitudes.

Overall, Goyaniuk and Mendes noted that while SAO (due to LSF) is a fundamentally 1 DOF problem, the contribution of the heave/flapwise bending DOF increased the energy transferred from the airflow to the airfoil.

Table 5.3: Comparison of Heave/1^{st} Flapwise Bending LCO Amplitudes

Author	$\bar{\omega}$	Chord Reynolds Number Range	Elastic Axis Location (%)	Amplitude (cm)	DOF/Mode	Flutter Type	Region
Mendes	1.59	$6 \times 10^4 - 8.5 \times 10^4$	18.6	0.025-0.27	Heave	Laminar Separation	SAO
Mendes	1.59	6.7×10^4	18.6	5.5	Heave	Coupled	LAO
Mendes	1.41	$6.4 \times 10^4 - 6.6 \times 10^4$	35	0.5-0.6	Heave	Stall	LAO
Goyaniuk	1.34	$6.4 \times 10^4 - 6.6 \times 10^4$	27	3-3.5	Heave	Coupled	LAO
Goyaniuk	1.43	$8 \times 10^4 - 1.1 \times 10^5$	35	0.5-2	Heave	Stall	LAO
Robinson	1.95	1.4×10^5	25	1.5	Flapwise Bending	Coupled	LAO
Itwar Barrett	1.95	$7.9 \times 10^4 - 8.9 \times 10^4$	25	2.3-6.1	Flapwise Bending	Unknown	SAO

5.4 LCO Frequency Spectra

In contrast to the two LCO branches found when considering the rigid pitch and 1^{st} flapwise bending amplitudes, three curves (Curves 1, 2 and 3) were found for the LCO frequencies for Beams-01,-02 (Figure 4.32). This may be due to the sensitivity of the LCO frequencies to changes in the structural properties, since we know that there were differences in damping ratio, damped natural frequency, damping and mass moment of inertia between tests, as seen in Section 3.5, A comparison of the dominant LCO frequencies can be seen in Table 5.4, where the LCO frequencies found by Mendes and Goyaniuk are compared to the current flexible wing results (Beams-01,-02).

Table 5.4: Comparison of LCO Frequencies

Author	$\bar{\omega}$	Re_c Range	E.A.	LCO Frequency(Hz)	LCO Range	Type of Flutter
Mendes	1.59	$6 \times 10^4 - 8.5 \times 10^4$	18.6%	2.9-3.1	SAO	LSF
Mendes	1.59	$6.4 \times 10^4 - 7.4 \times 10^4$	18.6%	3.7	1 DOF	Stall Flutter
Mendes	< 1	$6 \times 10^4 - 7 \times 10^4$	27%	2.8-2.7	SAO	2 DOF LSF
Mendes	< 1	$6.1 \times 10^4 - 1.2 \times 10^5$	27%	2.8-3.8	SAO	1 DOF LSF
Mendes	N.A.	$1.2 \times 10^5 - 1.6 \times 10^4$	27%	2.5-2.6	N.A.	1 DOF Stall Flutter
Mendes	0.72	$6.1 \times 10^4 - 1.1 \times 10^5$	35%	3.5-4.2	N.A.	2 DOF Stall Flutter
Goyaniuk	1.34	$6 \times 10^4 - 6.1 \times 10^4$	27%	3.4-3.5	LAO	Coupled flutter
Goyaniuk	1.43	$8 \times 10^4 - 1.1 \times 10^5$	35%	2.5-3	LAO	Stall fluter
Robinson	1.95	1.4×10^5	25%	4.959	SAO	Coupled Flutter
Itwar Barrett	1.95	$7.9 \times 10^4 - 1.1 \times 10^5$	25%	2.8-3.9	SAO	Unknown
Itwar Barrett	1.95	$7.9 \times 10^4 - 1.1 \times 10^5$	25%	3.3-3.4	LAO	Unknown

Table 5.4 suggests that the LCO frequencies for Curve 1 match the values found for LSF, found by Mendes in the SAO region. The frequencies for Curve 2 more closely match those for 2 DOF stall flutter. The values found for Curve 3 are larger than any of the previous results presented. Compared to the numerical results from Robinson, we find that the predicted LCO frequency is higher than the maximum encountered during testing. This perhaps illustrates the effects of the imperfections in the physical rig, such as slight misalignments or freeplay between the wing and beam, and also changes in the internal structure of the wing which may not be evenly distributed. This discrepancy may also suggest the effects of both structural and aerodynamic non-linearities combined. Metivier [17] found that a small change in the moment of inertia impacted characteristics of oscillations (frequency especially); however, Robinson suggested that a change in pitch stiffness would have a more pronounced effect.

Focussing on coalescence for Tests A-F (Section 3.3.3), the FDM results indicate that the first two modes for the $s4^*$ configuration are 2.56 Hz (Rigid Pitch Dominated Mode) and 5.0 Hz (1^{st} Flapwise Bending Dominated Mode). These frequencies are close, indicating that these modes are likely to coalesce. Furthermore, Robinson found that for his analysis, the rigid pitch mode had a frequency of 2.289 Hz, while the 1^{st} flapwise bending mode had a frequency of 4.959 Hz. Once again, these frequencies are very close to each other, and are comparable to the FDM results. In section 3.3, it is seen that 1^{st} modal frequency predicted for the $s4^*$ configuration is 5 Hz, and from Section 3.5.2, the damped natural frequencies of the system for the $s4^*$ configuration are approximately on the order of 2.3-2.6 Hz. Thus, by comparing the free decay natural frequencies of the experimental $s4^*$

system, Euler-Bernoulli uncoupled bending, the FDM and the numerical results, there is a strong suggestion that coalescence may be occurring.

Figure 5.3 illustrates the range of frequency characteristics, dependent upon on the E.A. location, and compared to the 1^{st} and 2^{nd} FDM modal results. In general, the range of flexible wing LCO frequencies (E.A. of 25%) surpasses the ranges seen for the rigid wing (E.A. of 18.6%, 27%, and 35%).

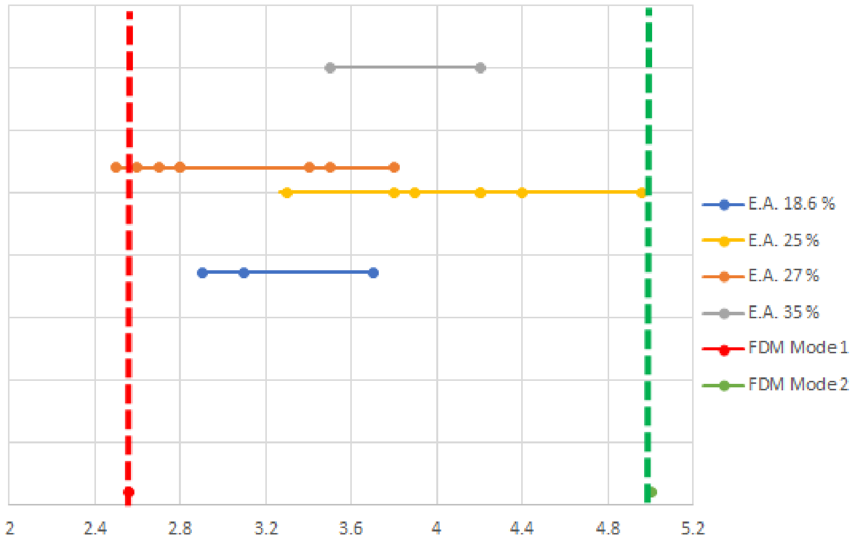

Figure 5.3: Comparison of LCO Frequencies for Rigid and Flexible Wings and FDM Modal Results [21] [22]

Upon general review of the LCO frequency results, a point which contradicts the possibility of stall flutter is that Mendes found that the LCO frequencies generally increased with increasing airspeed for stall flutter; the flexible wing results indicate that LCO frequencies reached a peak before descending.

5.5 Zero Pitch Stiffness Test

This section briefly reviews the results of Test H (Appendix E.4.8) seen in Appendix G, which was performed with no pitch springs (zero pitch stiffness). It is important to note that, as with Test G, the recorded airspeeds were erroneous and required correction. Despite this, the results of Test H are briefly discussed as they are important to help understand the effect of changing the spring stiffness.

The RPM test range for Test H was chosen based on data from Tests A-G. The results show that at 270 RPM there was some motion occurring, which may be attributed to LCO's or Reynolds number effects. The RPM was then swept up to 430 RPM, and then swept down to 211 RPM, where no motion was noted. While sweeping up the second time and recording distinct points, it was noted that vibration occurred around 225 RPM. At around 400 RPM, strange motion in the time trace was observed on the potentiometer oscilloscope, and so the airspeed was swept down in an attempt to capture this behaviour. The behaviour evident in the time traces is currently unexplainable, as the potentiometer data were carefully vetted in the early stages, and there were no signs of damage to the equipment wires or any other related instrumentation. Furthermore, this behaviour consistently happened only between 400 RPM-430 RPM. Hence, it seems that something interesting may be occurring in this airspeed range when there is no pitch stiffness. These results seem consistent with Harris' observations in 2007, where he noted erratic oscillations for the case of no springs.

5.6 Torsion Data

While torsion data were recorded for Tests A-G, there were frequent issues with wire snapping, possible noise pollution, and saturation. Furthermore, data did not appear reasonable in terms of magnitude, based on visual corroboration during testing.

A qualitative test was done with the rigid pitch motion locked in order to determine if there was bending-torsion coupling occurring. The airspeed was increased far in excess of values where known LCO's appear, and no motion occurred. Furthermore, it is known that bending-torsion coupling would not occur until far higher airspeeds, as seen in Section 3.3.2, since the uncoupled torsion natural frequency is 103-107 Hz, far in excess of the pitch and flapwise bending modal frequencies (Section 3.3.3). Thus, detailed analysis of the torsion motion was not performed. Nevertheless, some sample torsion data can be found in Appendix H.

5.7 Effects of Plastic Deformation in Beam

Beam-01 gradually failed over the course of Trial Test 1 - Test E and was subsequently replaced by Beam-02, which was an identical material. Beam-02 subsequently failed over the course of Test F, and exhibited signs of plastic deformation where the beam was clamped into the support, which translated into a static tip deflection of up to 3 cm in the negative z direction (Figure 1.2). The beam also showed signs of strain hardening, and the beam properties appeared to change over time (Section 3.5). During testing, Beam-02 experienced a growing bias during testing which reached a maximum, which culminated in the wing slowing down before ceasing motion.

Figure 5.4 (where the data are not zeroed) illustrates the suspected process of plastic deformation, followed by failure. The change in the flow mean bias (data not zeroed, therefore the mean bias of the LCO's are plotted) as the airspeeds increases, indicates that the bias changes sign from *positive to negative* before reaching a plateau as failure occurs.

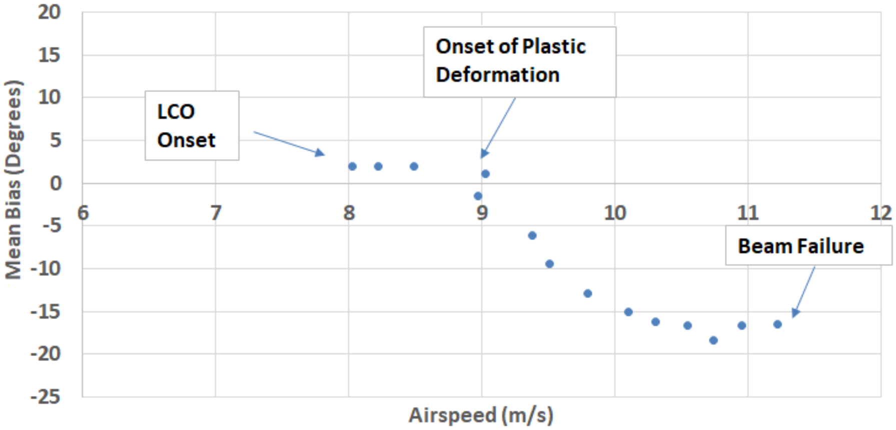

Figure 5.4: Test F March 15, 2019 Normalized AISI 01 Steel (Beam-02) Illustrating Evolution of Mean Bias

Qualitatively, it appears likely that cyclic failure occurred, since it is known that the material is soft, and has a high strain hardening ratio (Section A.5). Furthermore, during testing it was observed that in the LAO region, the wing/beam settled on a new LCO with a larger bias than in the SAO region, before stopping after 11000 cycles (based on an average LCO frequency and the length of the test time); it was noted that post-test, the beam appeared severely deformed and was noted to be "harder" in the region exhibiting damage (suggesting strain hardening had occurred, at the location above where the beam was clamped near the root). This process is consistent with behaviour which is representative of cyclic failure [55].

It is known that a conservative estimation of the maximum bending deflection is 10 cm based on qualitative observations (Section A.1), suggesting a maximum bending stress estimate of 286 MPa (for the static deflection case). This estimated maximum bending stress is less than the yield strength of the normalized AISI O1 beam, which is 350 MPa. However, based on Figure 2.19 in Section 2.4.5, it is also known that the endurance limit of steel is 186 MPa. Given that a) the beam was estimated to have failed after 11000 cycles, b) the conservative beam maximum bending stress (static) exceeds the endurance limit (Equation A.4), and c) qualitative observations (both during the experiment and subsequent examination of the material post-test), it seems likely that the beam did indeed plastically deform before failing.

5.8 Error discussion

5.8.1 Deviation

Figure 5.5 shows a plot of the LCO amplitudes, and the corresponding average deviation ($\bar{\delta}$) between the height of each individual LCO peak and the mean of the LCO amplitude, for each test (Equation 5.1). Overall, the magnitude of the average deviation appears to remain low in the SAO region for all beams; conversely, the average deviation magnitude is consistently larger in the LAO region.

$$\bar{\delta} = \frac{\sum(|\theta_{peak} - \bar{\theta}_{peak}|)}{\#ofPeaks} \tag{5.1}$$

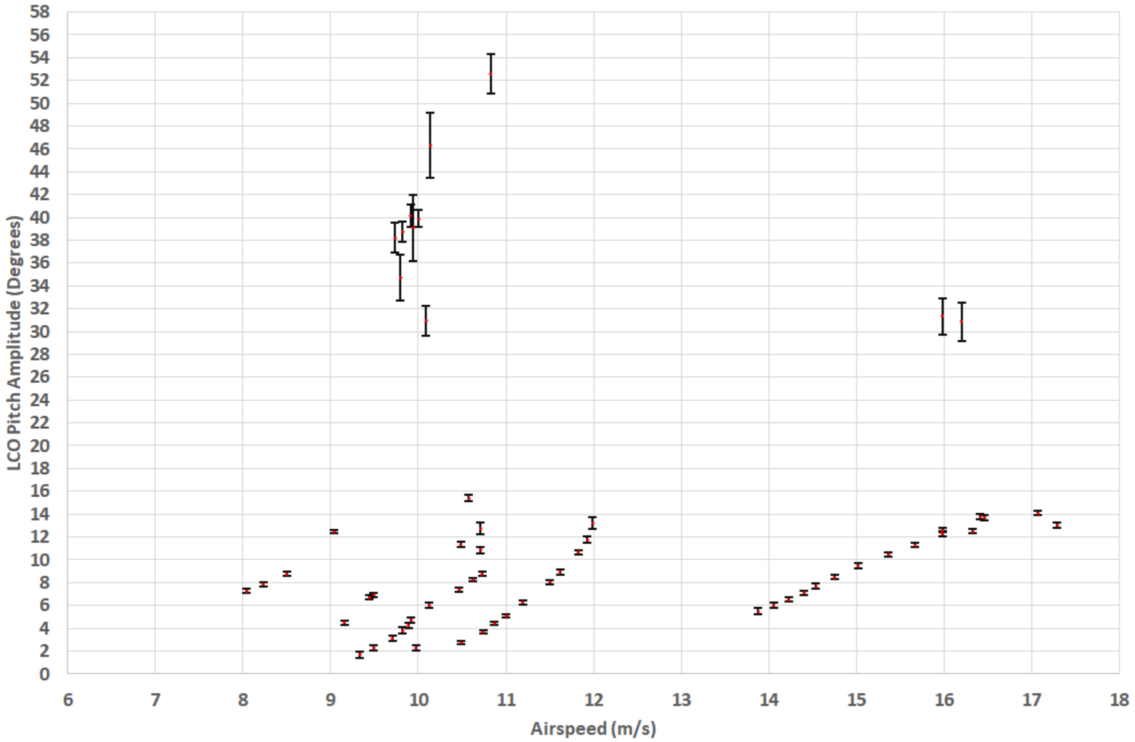

Figure 5.5: Deviation Between Mean LCO Pitch Amplitude and Mean of LCO Pitch Peaks

5.8.2 Wing/Beam Assembly

In regards to the wing-beam assembly, there were issues encountered due to the repeated opening and re-sealing of the wing in order to install and then remove the beam for instrumentation applications, as well as to perform FDT2 after every test. This posed issues with maintaining the integrity of the leading edge of the wing, which needed to remain as smooth as possible to ensure that the flow would be laminar across the wing surface. Hence, wing re-design needs to be explored in order to eliminate these leading edge issues, and also create a better fit between the beam and wing thereby reducing the amount of freeplay between them.

5.8.3 Instrumentation Damage

In general, during testing there were instances where there was equipment saturation, due to amplitudes which were greater than expected and thus outside of the limiting bounds of the equipment settings and gains; the intense nature of the oscillations led to significant strains being placed on wires, and compression/tension damage on the instruments themselves. The indication of experimental errors on the strain gauges and accelerometers were evident by a live-feed on the displays during testing. Saturation was usually indicated by the truncation of the peaks of the real-time time histories, or the abrupt loss of a ”sine-like” shape despite being on an LCO. For the accelerometers specifically, a pseudo-sine wave which showed a marked global increase in time suggested strong effects of drift, possibly due to damage, or a need for re-calibration. A case of significant drift was found for Accelerometer Number 151337 based on simple gravity drop tests, and led to its replacement with Accelerometer Number 151335.

5.8.4 Test Procedure

Great care was taken to choose data where the LCO was as close to steady-state as possible; each point included on the final LCO amplitude and frequency curves was reviewed in detail, by using the time histories, PSD’s and histograms to determine if the point was suitable and would provide accurate information. Detailed notes observed instances of instrumentation errors during testing and these points were omitted to remove doubt. However, in some cases, the damage to the equipment was gradual and cumulative, indicating that there may be inherent errors which are unavoidable due to the physicality of the test rig.

6 Recommendations and Future Work

Future tests should include performing a full test with a fresh beam which will not fail, to find the SAO/LAO boundaries. It also recommended that tests be performed with varying pitch stiffnesses and beam parameters, in order to test the effects of changing the frequency ratio. This will not only provide interesting data in terms of sensitivity to changing the structural parameters, but provide further evidence to support whether or not this may be coupled flutter occurring (for LAO), since coupled flutter is sensitive to changes in the frequency ratio [56]. From Tang and Dowell, we also know that a non-zero AOA can decrease the system stiffness and stability [9] [10], and so it may be useful to perform sensitivity tests where small static AOA's are purposefully an carefully set to test the sensitivity and effect of the onset of SAO and LAO.

A wing apparatus re-design (i.e. updated materials and improvement on the wing/beam fit) would be useful to ensure less variation of parameters between tests, as well as to lessen wing/beam freeplay and reduce wing damage which was caused by re-building and taking apart the wing after each test. With a sufficient redesign (which will hopefully allow for easier installation and removal of the beam, as well as lead to less deterioration of the wing due to the oscillations) it would be possible to perform FDT2 prior testing as well. A new, more efficient design would hopefully provide more consistent FDT results.

In terms of current strain gauges results, it would be useful to use modelling techniques such as ANSYS to find the relation between strain gauge values at 0.09-0.15 L and wing tip displacement, for the non-linear large deflections. The calibration of the accelerometers to find the velocity and position data is also a notable future goal.

The importance of I.C.'s and test conditions have already been clearly demonstrated and so in future, it is imperative to be able to apply a controlled and consistent magnitude or change in airspeed to better understand how they affect the system. The moment when the amplitude of the I.C. is applied is also important i.e. pitch up or pitch down, since it may determine how the effective aerodynamic stiffness is changing [2]. It would be useful in future to implement more constant and controlled initial conditions, perhaps by means of a hammer strike as for full scale aircraft GVT. Additionally, it is recommended to monitor the real time airspeed, by means of the Labview oscilloscope showing the pressure transducer oscillations, which will be calibrated to show the instantaneous airspeed. This would allow more refined adjustment of the airspeed, instead of using the RPM value.

The bulk of the current flexible wing test results were obtained while sweeping up in airspeeds. Since we know that hysteresis occurs, depending on whether ascending or descending in airspeed [2], it would be useful to perform more focussed tests only sweeping down, to match the test points obtained for sweeping up, and compare these more diligently.

When pitching down, the separation point moves faster than reattachment point [5] and the movement of the separation bubble along the chord changes for pitch up versus pitch down [26]. Thus, the use of a high speed camera, by extending and applying the work of Poels would be useful to capture the effects of the laminar separation bubble for both SAO and LAO regions.

The information from the rigid wing has thus far been very important in inferring the behaviour of the flexible wing, thus it would be useful to have more data from the rigid wing, for an E.A. located at 27% chord, but with a frequency ratio closer to 1.95. Thus, the amplitude and frequency results would provide a better estimate of the LCO amplitudes and frequencies expected for the rigid wing. Of course, in order to confirm the type of flutter, tests performed with trip wires and sandpaper could be done. Tripping the boundary layer for the rigid wing showed that no LCO's occurred and thus SAO was due to laminar separation flutter[2]. If future tests are performed with sandpaper on the flexible wing, this might allow determination if a) SAO still occurs when there is no laminar boundary layer, and b) LAO still occurs when there is turbulence.

In order to further determine if stall flutter may be occurring, it would be useful to perform experiments with a trip wire to allow the flow to remain attached to the wing. In the absence of laminar separation, if LCO's still occur, then they are likely due to coupled flutter and not stall flutter [22] [21]. Furthermore, it will be useful to generate the moment and lift curves for the data; the moment curve will indicate the overall work done and any hysteresis present (non-linear behaviour) and provide details of whether dynamic stall has occurred (required for stall flutter to occur). Performing tests where both the pitch and flapwise bending amplitudes are found for the LAO region will also be useful, as we know from Mendes that for coupled flutter, when the amplitude of one mode increases, the other decreases; conversely, for stall flutter, both modal amplitudes increased. For stall flutter, Goyaniuk noted higher non-linear content in pitch compared to heave; however, the reverse was true for the flexible wing data.

Mendes noticed that a change in phase difference occurred where there was a jump in LCO amplitude (from SAO to LAO). Thus, It would be interesting to calculate the phase difference for the flexible wing tests and check if a decrease in the phase difference behaviour indicates where the SAO/LAO boundary may be for $\bar{\omega} > 1$; this may hold promise as a future prediction tool. Furthermore, for coupled flutter, Mendes noted that when one mode increased, the other decreased with increasing airspeed. Hence more strain gauge data is needed in order to determine if there was a post-jump decrease in flapwise bending deflection with airspeed, which could also possibly prove the existence of coupled flutter.

Poirel and Mendes [20] determined that pitch-heave coupling feeds energy into the LCO's (for coupled flutter), and not negative aerodynamic damping. Depending on the frequency ratio, the motion can be either pitch or heave driven and so determining the phase angle is key. Previously, Poirel found that heave was the driving force for energy transfer, while in 2018, Goyaniuk determined that for frequencies ratios not close to 1, the pitch drives the heave for 2 DOF stall flutter. Determining the phase angle and work done for the data would be useful to compare to previous work done with the rigid quasi-2D pitch-plunge wing, in order to determine which motion is driving the energy transfer, as indicated by positive/negative work done.

In terms of considering the kinetics in future work, installation of the strain gauges and accelerometers could be modified. It would be interesting to apply some strain gauges in a standard rosette pattern, and using Mohr's circle determine the principal strains and corresponding stresses. The strain gauges were placed as such for Tests A-H, since we were focused on obtaining frequency and deflection data. However, using the rosette patterns would allow stress-strain analysis, which has proven to be non-trivial given the issues with cyclic failure and plastic deformation of the beam. In terms of installation, the use of the manufacturer mounting system for accelerometers should be considered and sensitivity tests done to determine if adding these mounting systems would significant change the system in terms of mass distribution. If it is determined that the mounting system does not interfere with the data, then it is recommended that tests be performed with this in future.

7 Conclusions

A series of tests were performed on a free pitching flexible cantilever NACA 0012 wing, in order to characterize the dynamics at transitional Reynolds numbers. The wing apparatus is composed of a thin steel beam, enclose by a plastic, foam and epoxy wing. The frequency ratio is 1.95 when using the ratio of pitch to flapwise bending. The flexural centre and pitch axis are aligned and located at 25% of the chord. The data were recorded using a potentiometer, strain gauges (in bending and torsion) and accelerometers.

The potentiometer data for a Normalized AISI O1 beam was low-pass filtered and used to generate plots of rigid pitch dominant mode LCO amplitudes versus airspeed and LCO frequency versus airspeed. Two LCO branches were found corresponding to SAO $(0 - 15^\circ)$ and LAO $(30 - 60^\circ)$. The data generally indicated steady-state LCO's in both the SAO and LAO regions; all data appeared valid based on the histograms. The LCO onset speed varied, and the airspeed values of 8.04 m/s, 9.15 m/s, 9.33 m/s, and 10.2 m/s may indicate the locations of fold bifurcations. The subcritical Hopf bifurcation may be located near the linear flutter speed, analytically predicted as 12.67 m/s. A sharp jump occurs between SAO and LAO; no data could be recorded in this transition region, in which there may be a supercritical Hopf bifurcation. The data for a tempered 1095 spring steel beam were investigated, and two LCO regions were found: SAO $(0 - 15^\circ)$ and LAO $(30 - 35^\circ)$.

The bending strain gauges yielded data in pure bending, and results were found by calibrating the voltage at approximately 0.12 L to the tip of the beam, assuming that deflection of a cantilever beam closely approximated the 1^{st} mode shape of a cantilever beam. The data generally indicated that steady-state LCO's occurred in the SAO region; all data appeared valid based on the histograms. The flapwise bending tip deflections were found and plotted for the SAO region. Data for the LAO region could not be found due to apparent beam failure. The results appeared reasonable, given that the maximum qualitative tip deflection observed was on the order of 10-14 cm. The SAO region for the flapwise tip bending deflections are defined as 0-7 cm.

Despite evidence of superharmonics indicating asymmetries and non-linearities for much of the data (for all instrumentation), SHM was assumed, since the peak of the dominant frequency was relatively much higher than its superharmonic peaks.

The LCO frequency range was found for both types of beams. The Normalized AISI O1 steel beam yielded frequencies ranging from 3.3-4.4 Hz, and there were three branches present; the Tempered 1095 spring steel beam yielded LCO frequencies ranging from 4.7-5.1 Hz and there was only one branch. The LCO frequency results indicate higher LCO frequencies for the Tempered 1095 spring steel beam, compared to the Normalized AISI O1 steel beam. In general, the LCO frequency results indicated a trend of the frequency increasing with airspeed, until a peak was reached, where the frequency would then decrease with airspeed.

The results for total tip acceleration in the SAO region were determined and compared with a simple analytical estimation, assuming SHM. The results appear to follow analogous trends, but the differing magnitudes suggest the effects of physical non-linearities present.

The effects of plastic deformation and cyclic failure were briefly touched upon, and evidence provided suggests that these phenomena did occur. There was also evidence of hysteresis, effects of initial conditions, and multiple attractors.

It is theorized that the SAO is caused by laminar flow separation at small angles of attack due to transitional Reynolds number and its interaction with the free pitching wing, which in turn causes negative aerodynamic damping. The LCO amplitude results were comparable but higher than the amplitude found for the SAO region of the rigid wing which was concluded to have experienced laminar separation flutter. The mechanism responsible for LAO has yet to be confirmed through future testing and analysis. The range of Reynolds numbers where LAO's are observed, as well as the LCO frequencies, are comparable with previously published work suggesting either coupled or stall flutter in these cases. However, for comparable frequency ratios and and elastic axis positions, the LAO data appears overlapping or in excess of rigid wing flutter amplitudes.

Bibliography

[1] McCroskey, W.J. “The Phenomenon of Dynamic Stall,” Technical Report. NASA, March in 1981.

[2] Harris, Y. “The Aeroelastic Dynamics of a NACA 0012 Airfoil Oscillating in Pitch at Transitional Reynolds Numbers,” Master’s thesis. Royal Military College of Canada, May 2007.

[3] Mueller, T.J. “Low Reynolds Number Vehicles,” *Technical Report*. AGARD AG-288, March 1985.

[4] Schreck, S.J., and Helin, H.E. “Unsteady Vortex Dynamics and Surface Pressure Topologies on a Finite Pitching Wing,” *Journal of Aircraft*, Vol. 31, No. 4, October 1994, pp. 899–907.

[5] Poirel, D., and Yuan, W. “Aerodynamics of Laminar Separation Flutter at a Transitional Reynolds Number,” *Journal of Fluids and Structures*, June 2010, pp. 1174–1194.

[6] Huang, R.F., and Lin, C.L. “Vortex Shedding and Shear-Layer Instability of Wing at Low-Reynolds Numbers,” *AIAA Journal*, Vol. 33, No. 8, August 1995.

[7] Dunn, P., Dugundji, J. "Nonlinear Stall Flutter and Divergence Analysis of Cantilevered Graphite/Epoxy Wings," *AIAA Journal*, Vol. 30, January 1992.

[8] Dunn, P. “Stall Flutter of Graphite/Epoxy Wings with Bending-Torsion Coupling,” Master of science in aeronautics and astronautics, Massachusetts Institute of Technology, May 1985.

[9] Tang, D.M., and Dowell, E.H. “Experimental and Theoretical Study for Nonlinear Aeroelastic Behavior of a Flexible Rotor blade,” *AIAA Journal*, Vol. 31, No. 6, June 1993.

[10] Tang, D.M., and Dowell, E.H. “Effects of Geometric Structural Nonlinearity on Flutter and Limit Cycle Oscillations of High-Aspect-Ratio Wings,” *Journal of Fluids and Structures*, October 2000, .pp. 291–306.

[11] Dowell, E.H., and Tang, D.M. “Nonlinear Aeroelasticity and Unsteady Aerodynamics,” *40th AIAA Aerospace Sciences Meeting and Exhibit*, January 2002.

[12] Dimitriadis, G., and Li, J. “Bifurcation Behavior of Airfoil Undergoing Stall Flutter Oscillations in Low-Speed Wind Tunnel,” *AIAA Journal*, Vol. 47, No.11, November 2009.

[13] Razak, N.A., Andrianne, T., and Dimitriadis, G. “Flutter and Stall Flutter of a Rectangular Wing in a Wind Tunnel,” AIAA Journal, Vol. 49, No. 10, October 2011.

[14] Marsden, C.C., and Price, S.J. “The Aeroelastic Response of a Wing Section with Structural Freeplay Nonlinearity: An Experimental Investigation,” *Journal of Fluids and Structures*, May 2005, pp. 257–276.

[15] Poirel, D., Harris, Y., and Benaissa, A. "Self-sustained Aeroelastic Oscillations of a NACA 0012 airfoil at Low-to-Moderate Reynolds Numbers," *Journal of Fluids and Structures*, November 2008, pp. 700–719.

[16] Dowell, E.H., and Tang, D.H. "Nonlinear Aeroelasticity and Unsteady Aerodynamics," *AIAA Journal*, Vol. 40, No. 9, September 2002.

[17] Metivier, V., Dumas, G., and Poirel, D. "Effects of Inertia and Boundary Layer Tripping on Aeroelastic, Self-Excited Pitch Osillcations of an Airfoil," *Canadian Aeronautics and Space Institute Aero '09 Conference Aerodynamics Symposium*, 2009.

[18] Poirel, D. "Aeroelastic Stability in Transitional Reynolds Number Flow - A Canadian Overview," Royal Military College of Canada, May 2012.

[19] Peristy, L. "Examination of Small and Large Amplitude Aeroelastic Oscillations in Pitch of a NACA0012 Airfoil," Master's thesis, Royal Military College of Canada, October 2014.

[20] Poirel, D., and Mendes, F. "Experimental Small-Amplitude Self-Sustained Pitch-Heave Oscillations at Transitional Reynolds Numbers," *AIAA Journal*, Vol. 52, No. 8, August 2014.

[21] Da Costa Mendes, F. "Self-Sustained Aeroelastic Oscillations of a Two Degree of Freedom NACA 0012 Airfoil at Transitional Reynolds Numbers," Master's thesis. Royal Military College of Canada. August 2014.

[22] Goyaniuk, L.B. "The Potential for Energy Extraction from Flutter," Master's thesis, Royal Military College of Canada, June 2018.

[23] Fung, Y.C. *An Introduction to the Theory of Aeroelasticity*, Dover Publications, Inc., 1993.

[24] Pigolotti, L., Mannini, C., and Bartoli, G. "Experimental Study on the Flutter-Induced Motion of Two-Degree-of-Freedom Plates," *Journal of Fluids and Structures*, July 2017, pp. 77–98.

[25] Rudmin, D., Benaissa, A., and Poirel, D. "Detection of Laminar Flow Separation and Transition on a NACA-0012 Airfoil Using Surface Hot-Films," *Journal of Fluids Engineering*, Vol. 135, October 2013.

[26] Poels, A., Rudmin, D., Benaissa, A., Poirel, D."Localization of Flow Separation and Transition Over a Pitching NACA0012 Airfoil at Transitional Reynolds Numbers Using Hot-Films," *Journal of Fluids Engineering*, Vol. 137, December 2015, pp. 124501–1–6.

[27] Da Costa, R. "Nonlinear Aeroelastic Modeling of a Flexible Wing and Comparison with Experiments," Master's thesis, Royal Military College of Canada, 2016.

[28] Robinson, B. "Aeroelastic Oscillations of a Pitching Cantilever with Structural Geometric Nonlinearities: Theory, Numerical Simulation and Global Sensitivity Analysis," Master's thesis, Carleton University, August 2018.

[29] Hodges, D.H., and Dowell, E.H. "Nonlinear Equations of Motion for the Elastic Bending and Torsion of Twisted Nonuniform Rotor Blades," *NASA TN D-7818*, 1974.

[30] Guckenheimer, J., and Holmes, P. *Nonlinear Oscillations, Dynamical Systems, and Bifurcations of Vector Fields*, North-Holland, 1994.

[31] Argyris, J., Faust, G., and Haase, M. *An Exploration of Chaos, Vol. 7.* North-Holland, 1994.

[32] Thompson, J.M.T., and Stewart, H.B. *Nonlinear Dynamics and Chaos Geometrical Methods for Engineers and Scientists*, John Wiley & Sons, 1986.

[33] Dowell, E., Edwards, J., and Strganac, T. "Nonlinear aeroelasticity," *Journal of Aircraft*, Vol. 40, No. 5, September-October 2003.

[34] Anderson Jr., J.D., *Fundamentals of Aerodynamics, Fifth Edition*. McGraw-Hill Series on Aeronautical and Aerospace Engineering, 2005.

[35] Huang, R.F., Shy, W.W., Lin, S.W. "Influence of Surface Flow on Aerodynamic Loads of a Cantilever Wing," *AIAA Journal*, Vol. 34, No. 3, March 199

[36] Poirel, D. "AEE 463: Aeroelasticity." Royal Military College of Canada. Department of Mechanical and Aerospace Engineering. Winter 2017.

[37] Halfman, R.L., Johnson, H.C., Haley, S.M. "Evaluation of High-Angle -of-Attack Aerodynamic - Derivative Data and Stall-flutter Prediction Techniques," *Technical Note 2533*, Massachusetts Institute of Technology, November 1951.

[38] Meirovitch, L. *Fundamentals of Vibrations*. McGraw Hill Higher Education, 2001, pp. 383-400.

[39] Jaworksi, J.W., and Dowell, E.H."Comparison of Theoretical Strucutural Models with Experiment for a High-Aspect-Ratio Aeroelastic Wing," *Journal of Aircraft*, Vol. 46, No. 2, March-April 2009.

[40] Wright, J.R., and Cooper, J.E. *Introduction to Aircraft Aeroelasticity*. John Wiley & Sons, Ltd., 2007.

[41] Benham, P.P., Crawford, R.J., and Armstrong, C.G. *Mechanics of Engineering Materials Second Edition*, Pearson Prentice Hall, 1996

[42] Hodges, D.H., Pierce, G.A. *Introduction to Structural Dynamics and Aeroelasticity*, Cambridge University Press, 2002, pp. 31-41.

[43] Callister Jr., W.D. *Materials Science and Engineering An Introduction Sixth Edition*, John Wiley & Sons, Inc., 2003.

[44] Hibbeler, R.C. *Mechanics of Materials Eighth Edition*, Prentice Hall. 2011.

[45] Jehan, D.J. "Effect of Sensor Placement on Measuring Higher Modes of Vibration for a Thin Flexible Cantilever Beam in Free Vibration," Master's thesis, Royal Military College of Canada, May 2008.

[46] Hac, A., and Liu, L. "Sensor and Actuator Location in Motion Control of Flexible Structures," *Journal of Sound and Vibration*, No. 167(2), 1993, pp. 239-261.

[47] Beckwidth, T.G,. Marangoni, R.D., and Lienhard, V.J.H. *Mechanical Measurements Sixth Edition. Pearson Learning Solutions*, 2011.

[48] Asghar, A. “Personal Communication,” Discussion Regarding Effect of Changing Strain Gauges on Calibration Curve, Royal Military College of Canada, May 2019.

[49] Koenig, K. “Problems of System Identification in Flight Vibration Testing,” *Technical Report*. AGARD-R-720, April 1984.

[50] Koenig, K. "Pretension and Reality of Flutter-Relevant Tests, Advanced Aeroservoelastic Testing and Data Analysis," *Technical Report*, AGARD-CP-566, 1995. pp.17.1-17.1

[51] Poirel, D., Harris, Y., and Benaissa, A. “Aeroelastic Dynamics of a NACA 0012 Airfoil in the Transitional Reynolds Number Regime,” *2006 ASME Pressure Vessels and Piping Division Conference, Vancouver, B.C., Canada, Proceedings of PVP2006-ICPVT-11*, July 27 2006. pp. 23-27.

[52] Lissaman, P. “Low-Reynolds-Number Airfoils,” *Ann. Rev. Fluid Mech.*, Vol. 15:223-39, AeroVironment Inc., Pasadena, California 91107, 1983.

[53] Thomson, W.T., and Dahleh, M.D. *Theory of Vibration with Applications Fifth Edition*, Pearson Education, 2005.

[54] Patil, M.J., Hodges, D.H., and Cesnik, C.E.S. “Limit Cycle Oscillations in High-Aspect-Ratio Wings,” *American Institute of Aeronautics and Astronautics*, Vol. AIAA-99-1464, 1999.

[55] DuQuesnay, D. “Personal Communication,”Discussion Regarding Steel Selection and Properties, Royal Military College of Canada, May 2019.

[56] Poirel, D., Price, S.J. “Post-Instability Behaviour of a Structurally Nonlinear Airfoil in Longitudinal Turbulence,” *Journal of Aircraft*, Vol. 34, 1997, pp. 619–626.

[57] Gere, J. and Goodno, B. Mechanics of Materials Seventh Edition. Cengage Learning, 2009.

[58] Dowling, N.E. Mechanical Behavior of Materials: Engineering Methods of Deformation, Fracture and Fatigue Fourth Edition, Prentice Hall, 1993.

[59] Cimbala, J.M. “The Turbulent Flat Plate Boundary Layer (Section 10-6, C¸ engel and Cimbala),” Online Resources for PennState College of Engineering, 2015.

[60] Schlichting, H. Boundary-Layer Theory Seventh Edition, McGraw-Hill Series in Mechanical Engineering, 1979.

[61] Pope, A. Low Speed Wind Tunnel Testing, John Wiley & Sons, 1999.

[62] “https://www.mcmaster.com/9075K371/,” McMaster Carr Website, 2019.

[63] “https://www.engineersedge.com/materials/spring-steel.htm,” Engineers Edge Website, 2019.

Appendices

A Structural Physics

A.1 Bending Stresses

$$F_{max} = \frac{\delta_{max} 3 E I_y}{L^3} = 13.99 kN \tag{A.1}$$

$$|\sigma_{max}| = \frac{F_{max} L y}{I_y} = 286 MPa \tag{A.2}$$

$$|\sigma_{max}| < |\sigma_y| \quad (For \quad Beams - 01, -02) \tag{A.3}$$

$$|\sigma_{max}| > |(S_{el})_{steel}| \quad (For \quad Beams - 01, -02) \tag{A.4}$$

A.2 Spring Stiffness Calculation

The plot of force applied versus displacement for the two pitch springs can be seen in Figures A.1 and A.2; these plots provide the spring stiffness coefficient for each spring. The pitch springs showed no signs of hyper-extension and therefore there it was presumed that there were no non-linearities in the pitch stiffness due to plastic deformation.

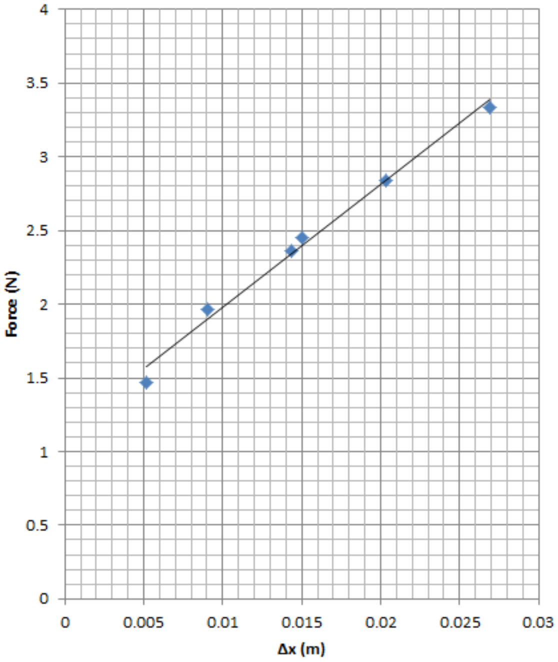

Figure A.1: Pitch Stiffness for Spring 1

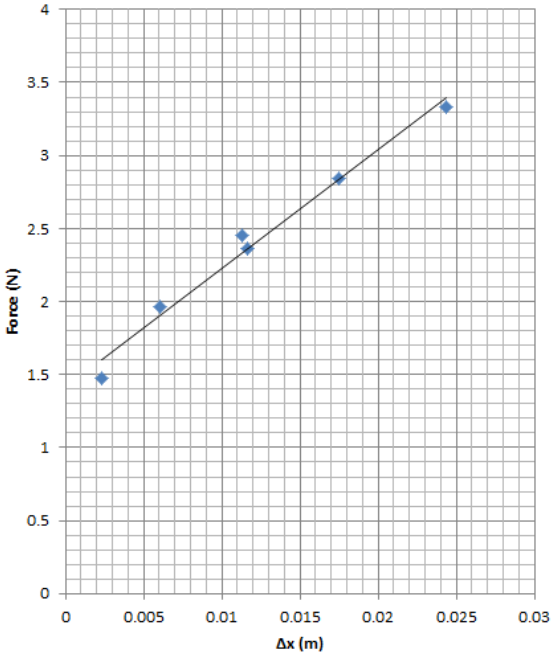

Figure A.2: Pitch Stiffness for Spring 2

Inserting the spring stiffness values into Equation A.5 and taking the average of both springs yields the total pitch stiffness as seen in Table A.1.

$$k_\theta = Nkr^2 \tag{A.5}$$

Table A.1: Stiffness in Pitch

k (N/m)	Spring 1	83.092
k (N/m)	Spring 2	81.522
Radius of Pulley	0.0381 m	NA
Number of Springs	2	NA
k_θ	Spring 1	0.2412 Nm/rad
k_θ	Spring 2	0.2366 Nm/rad
k_θ	Total Pitch Stiffness	0.24 Nm/rad

A.3 Moments of Inertia

A.3.1 Area Moment of Inertia

Equation A.6 is used to calculate the area moment of inertia for a thin rectangular section through its centroid, about the y axis [41].

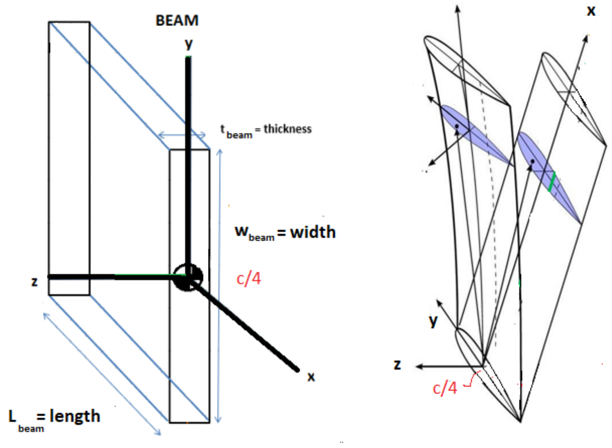

Figure A.3: Area Moment of Inertia - Axes [41]

$$I_y = \frac{1}{12} w_{beam} t_{beam}^3 \tag{A.6}$$

A.3.2 Polar Second Moment of Area

Equation A.7 is used to calculate the polar second moment of area (also known as the torsion constant) for a thin rectangular section [41].

$$J = \frac{1}{3}(w_{beam} t_{beam}^3) \tag{A.7}$$

A.3.3 Area Polar Moment of Inertia

Equation A.8 is used to calculate the polar second moment of area for a thin rectangular section [57]. The relevant axes and coordinate system can be seen in Figure A.3.

$$I_p = \frac{w_{beam} t}{12}(w_{beam}^2 + t_{beam}^2) \tag{A.8}$$

A.3.4 Experimental Beam Mass Moments of Inertia

The experimental beam mass moments of inertia for the $s4^*$ configuration were calculated using Equation A.9 (free pitch), using the first modal frequency for pitch and Equation A.10 (pitch locked), using the first modal frequency for bending.

$$I_{s4^*(\theta)} = \frac{k_\theta}{(\omega_{\theta 1})^2} \tag{A.9}$$

$$I_{s4^*(w)} = \frac{k_{ben}}{(\omega_{w1})^2} \tag{A.10}$$

A.3.5 Analytical Beam Mass Moment of Inertia

The analytical beam only mass moment of inertia can be calculated using Equation A.11 [40].

$$I_{beam} = \frac{m}{12}(w_{beam}^2 + t_{beam}^2) \tag{A.11}$$

A.3.6 Analytical $s2$ and $s4^*$ Mass Moments of Inertia

The analytical $s2$ and $s4^*$ configuration mass moments of inertia can be calculated as follows. Equation A.12 can be re-arranged to solve for I_{s2}, and Equation A.13 can be re-arranged to solve for Equation I_{s4^*}.

$$I_{beam} = I_{s2} - I_{s1} \tag{A.12}$$

$$I_{wing} = I_{s4^*} - I_{s2} - m_w d^2 \tag{A.13}$$

Equation A.14 is found by adding the analytical beam mass moment of inertia to the experimentally determined I_{s1} values. Equation A.15 is found by adding the experimentally determined mass moment of inertia of the wing only to the value from Equation A.14, plus an additional term to account for the offset in axes, per the parallel axis theorem. Finally, the frequency can be estimated via the standard Equation $\omega = \sqrt{k/I}$, where k is the total pitch stiffness (k_θ).

$$I_{s2_{ANALYTICAL}} = I_{beam_{ANALYTICAL}} + I_{s1_{EXPERIMENTAL}} \tag{A.14}$$

$$I_{s4^*_{ANALYTICAL}} = I_{wing_{EXPERIMENTAL}} + I_{s2_{ANALYTICAL}} + m_w d^2 \tag{A.15}$$

A.4 Rockwell C Hardness Tests and Tensile Strength Estimation

Initial hardness tests were performed using a Rockwell C tip (diamond cone with 150 Kg load, and a standard loading rate). The hardness value was read off the appropriate scale (Rockwell B or C, the latter being for harder materials). In general, if a test yields a big divot, it is a soft material, and if there is small divot it is a hard material.

The results yielded a Rockwell C of 3. However, a value of 20 was expected based on the fact that the beam was supposedly composed of AISI O1 steel. Furthermore, there was a very large divot, indicating a soft material. Hence, the results of the Rockwell C test indicated that the steel was normalized.

The hardness tests were repeated, using a Rockwell B tester (steel ball tip, 100 Kg load), per table A.2. This yielded an initial estimation of a tensile strength of 83 ksi (based on the NewAge Industries chart provided with the instrumentation).

Table A.2: Rockwell B Hardness Tests

Test #	Rockwell B Hardness Value
2	86
3	85
4	86
5	86
6	87 (opposite end of specimen)

Using the test specimen dimensions (12 mm x 1.27mm), a maximum force of about 10 kN was found at the yield point. Therefore, a 20kN Instron machine was elected for tensile testing. The specimen and strain rate parameters can be seen in Table A.3.

Table A.3: Tensile Test Results

Specimen	Width (mm)	Thickness (mm)	Strain rate(mm/min)
C1	12.8	1.27	20
C2	12.78	1.27	10
C3	12.76	1.27	10
C4	12.82	1.27	10
C5	12.8	1.27	10
C6	12.79	1.27	10

The Modulus of Elasticity is found by analysing the slope of the linear portion (for specimens C2-C6 with the standard strain rate) of curve and the yield strength is located at a strain offset of 0.002. For an isotropic material, and assuming Poisson's ratio of 0.30 for steel, the shear modulus of Beams-01,-02 is found to per Equation A.16.

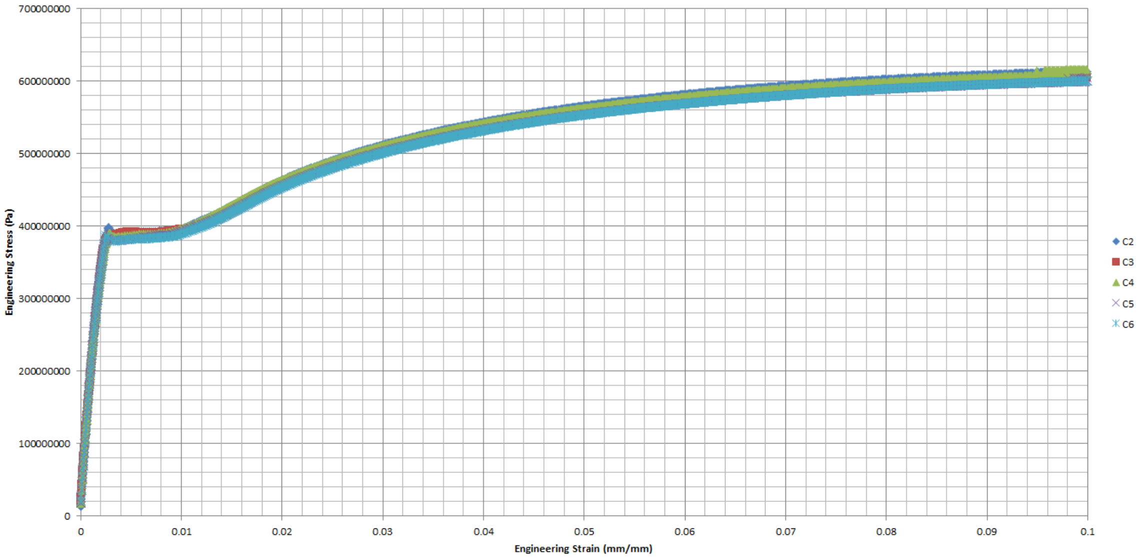

Figure A.4: Stress-Strain Curves: Tests 2-6

$$G = \frac{E}{2(1+\nu)} \tag{A.16}$$

The Rockwell B Test yielded an Ultimate Tensile Strength (defined in Equation A.17) of 572 MPa; however, the Uniaxial Test yielded an Ultimate Tensile Strength of 620 MPa.

$$\sigma_{UTS} = \frac{F_{applied}}{A_0} \tag{A.17}$$

Table A.4: Material Properties of a Normalized AISI O1 Steel Beam-01

E	200 GPa
ν	0.30
G	77 GPa
Ultimate Tensile Strength	620 MPa
σ_y	350 MPa
ρ	6629 kg/m^3

A.5 Strain Hardening and Cyclic Failure

The data in Table A.5 were gleaned from the tensile tests and basic knowledge of the material properties of steel. Using the information in Table A.5 and Equation A.18 [58], the strain hardening ratio was calculated as 1.77 (Beams-01,-02). The definition of strain hardening is ”the rise in the stress-strain curve following yielding [44] [58].” This information provides us with a means to quantify the material's' increasing resistance with increasing strain. Notably, values above 1.4 indicate a material which can become very strain hardened. This is expected since this material is relatively ”soft”, as predicted by the low yield strength for Beams-01,-02 [58].

Table A.5: Normalized AISI O1 Tool Steel Parameters

Modulus of Elasticity	200 GPa
Poisson's Ratio	0.30
Shear Modulus	77 GPa
Ultimate Tensile Strength	620 MPa
Yield Strength	350 MPa

$$\frac{UTS}{YieldStrength} = \frac{\sigma_o}{\sigma_y} = 1.77 \tag{A.18}$$

$$1.77 > 1.2 \tag{A.19}$$

A.6 Sensitivity of Damped Natural Frequency to Movement of Wire Mass

The mass and motion of the wires connecting the sensors to the outputs are non-trivial, since they can affect the wing motion via the damping. In general, if the wires are secured too tightly, the will restrict the motion of the wing and create added damping; conversely, if they are too loose, the mass of the wires will add to the mass moment inertia of the system. Thus, some preliminary sensitivity tests were performed by qualitatively varying the security of the wires. Per Figure A.5, there is minimal change in the damped natural frequency (from the potentiometer results), with an approximately 3.7% difference in the maximum and minimum values. Thus, further investigation into this sensitivity, as well as custom designed wire holders are suggested.

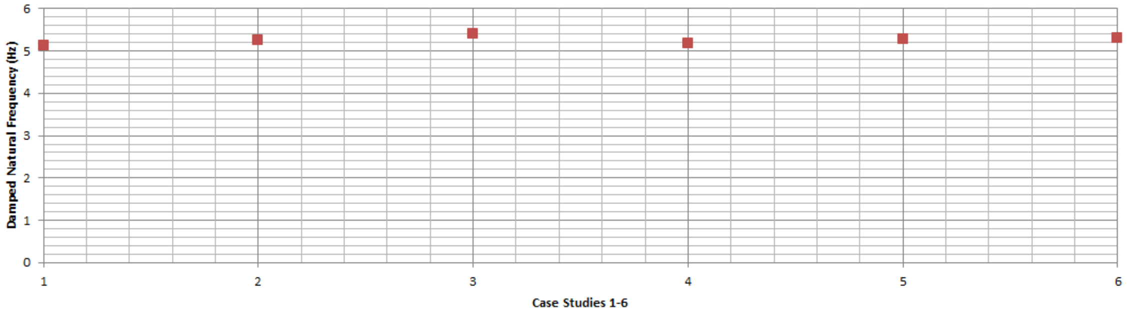

Figure A.5: Instrumentation Wire Mass Sensitivity

B Aerodynamic Considerations

B.1 Boundary Layer Thickness

Calculations were performed in order to approximate the thickness of the boundary layer (Figure B.1). The solutions for the Blasius [34], the one-seventh-power law [59] and Spalding's law of the wall [59] [60] were plotted for comparison; however since $Re_x > 500000$, the Blasius solution is not valid. Thus, the results for the One-Seventh Law and Spalding's Law of the Wall indicate that the wing tip is not immersed in the boundary layer.

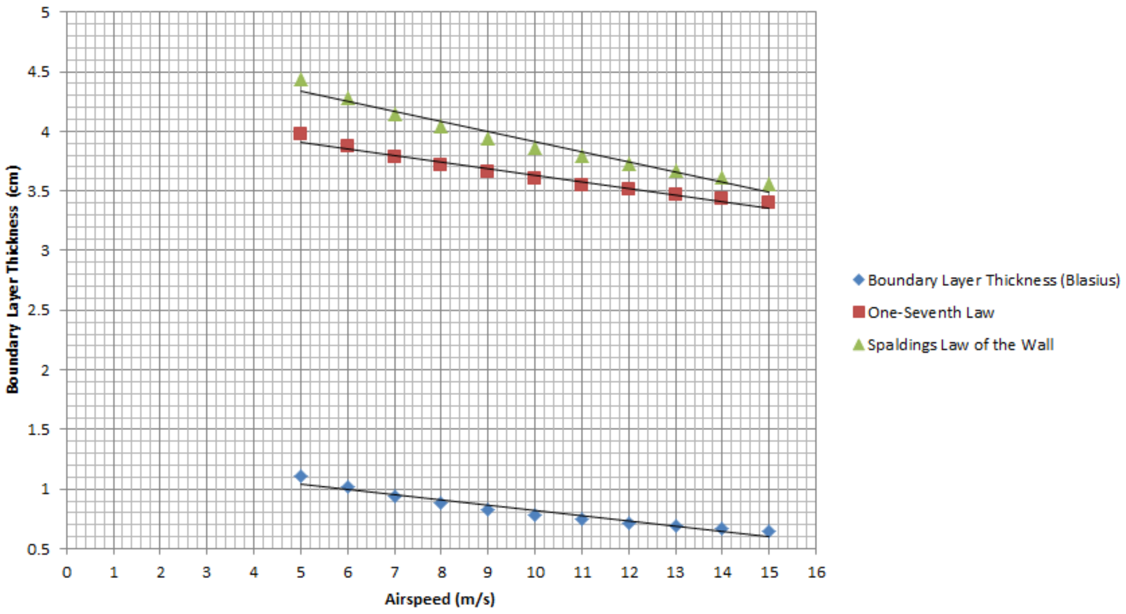

Figure B.1: Boundary Layer Thickness

B.2 Vortex Shedding Frequency

The Von Karman vortex shedding frequency (Equation B.1) was calculated using the Strouhal number of the cylindrical support with a diameter of 1.5774 cm (for a cylinder, $St = 0.2.$). The results in Figure B.2, show that the vortices are shed at frequencies much higher than the frequency of the mode which goes unstable first [28].

$$f = \frac{StU}{D} \tag{B.1}$$

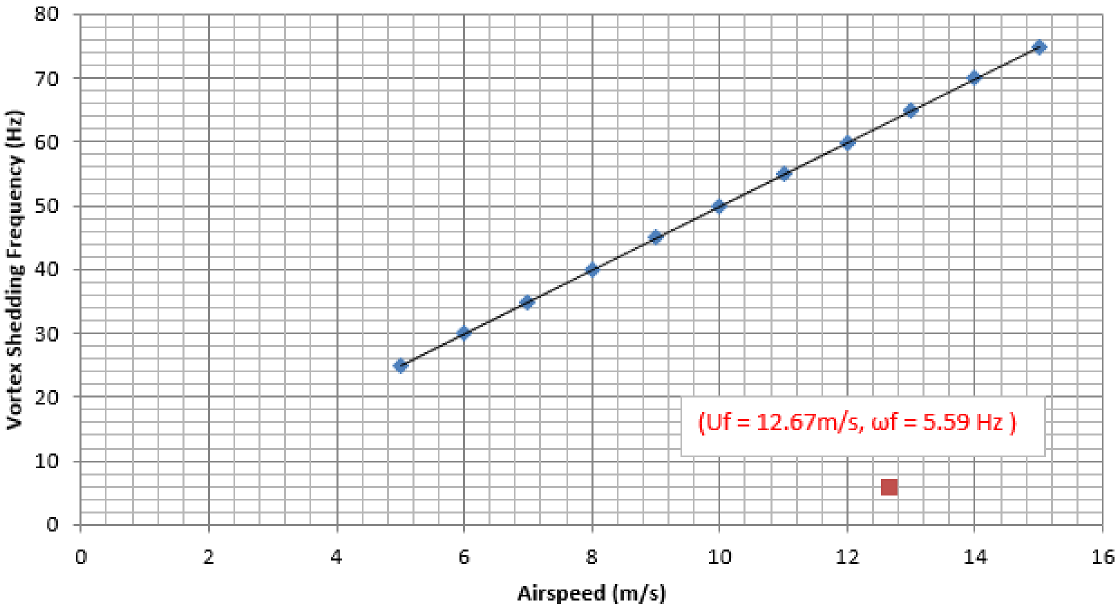

Figure B.2: Vortex Shedding Frequency

B.3 Wing Span Versus Wind Tunnel Width

Pope [61] provided a simple rule of thumb which stated that the span of the wing should be no more than 0.8 of the tunnel width. As can be seen in equation B.2 the ratio of wing span to tunnel width appears reasonable.

$$\frac{wingspan}{tunnelwidth} = \frac{44.5cm}{75cm} = 0.5855 < 0.8 \tag{B.2}$$

B.4 Blockage Ratios

The maximum blockage ratios for all beams were calculated by means of simple geometry, given that all apparatus dimensions are known. The wing blockage rations for al beams are listed in Table B.1.

Table B.1: Blockage Ratios for Beams-01,-02,-03

Maximum Blockage Ratio (Wing at 90°)	8.3%
Maximum Blockage Ratio (Wing at 0°)	1.0%

C Aeroelasticity

C.1 Intensity of Flutter

The three types of flutter intensity are presented in Figure C.1.

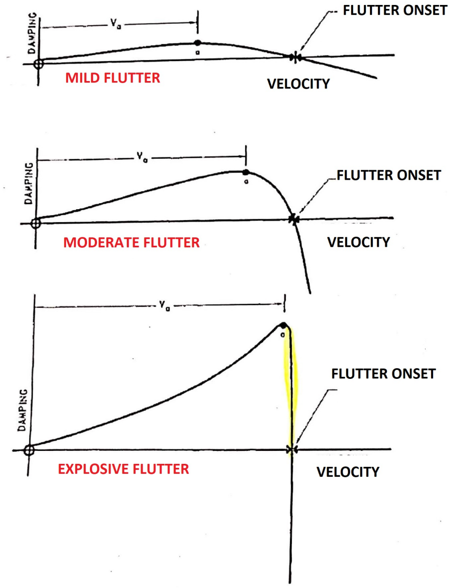

Figure C.1: Examples of Mild, Moderate and Explosive Flutter [36]

C.2 Equations of Motion for Unsteady Aerodynamic Model with Geometric Non-Linearities

It is useful to briefly review the equations of motion for unsteady aerodynamics and geometric non-linearities; the particulars of the exact symbols will not be provided, since the purpose is to simply demonstrate the ubiquitous non-linear terms.

$$\begin{aligned}&I_\theta\ddot{\theta}+D_\theta\dot{\theta}+K_\theta\theta+\\&\int_0^S\{\bar{I}_O(\ddot{\theta}+\ddot{\phi})+\bar{m}\ddot{w}(e_p+e)+\bar{m}e\ddot{\phi}e_p+2\bar{m}e\ddot{\theta}(e_p+w\phi)+\bar{m}\ddot{\theta}(w^2+e_p^2)+2\bar{m}\dot{\theta}e+\dot{w}(e\phi+w)+\dot{\phi}ew\}dx=\bar{W}_\theta\end{aligned} \tag{C.1}$$

$$\{EI_yw'''' + EC_1^*\phi''''\} + \{\bar{m}\ddot{w} + \bar{m}e\ddot{\phi} + \bar{m}\ddot{\theta}(e_p + e) - \bar{m}\dot{\theta}^2(e\phi + w)\} = \bar{W}_w \tag{C.2}$$

$$\begin{aligned}W_\theta = \int_0^S \sqrt{1-(\frac{x}{S^2})}(\frac{1}{4}\rho c^2\pi(((e_c+e_p)-\frac{c}{4})(-wcos(\theta)-\ddot{v}sin(\theta))-U(\frac{c}{2}-e_c)\dot{\phi}-U(\frac{c}{2}-(e_c+e_p))\dot{\theta}\\
-(((e_c+e_p)-\frac{1}{4}c)(e_c-\frac{1}{4}c)+\frac{1}{32}c^2))\ddot{\phi}-(((e_c+e_p)-\frac{1}{4}c))^2+\frac{1}{32}c^2))\ddot{\theta})\\
+\frac{1}{2}\rho Uc2\pi e_c(1-A_1-A_2)w_{3c/4}\\
+\dot{z}(t)(A_1b_1+A_2b_2)+z(t)b_1b_2(A_1+A_2))\end{aligned} \tag{C.3}$$

$$\begin{aligned}W_w = \sqrt{1-(\frac{x}{S^2})}(\frac{1}{4}\rho c^2\pi(((-wcos(\theta)-\ddot{v}sin(\theta))+U(\dot{\phi}+\dot{\theta})-(e_c-c/4)\ddot{\phi}-((e_c+e_p-c/4)\ddot{\theta})\\
+\frac{1}{2}\rho Uc2\pi(1-A_1-A_2)w_{3c/4}+\dot{z}(t)(A_1b_1+A_2b_2)\\
+z(t)b_1b_2(A_1+A_2))) \times cos(\theta)\end{aligned} \tag{C.4}$$

The equations of motion that Robinson [28] derived for the flexible wing system can be seen in Equations C.1, C.2, C.3 and C.4; specifically, details of the structural portion are seen in Equations C.1 and C.2 and the corresponding aerodynamic portion seen in detail in Equations C.3 and C.4. The equations include terms representing the structural non-linearities, as well as the coupling between DOF.

D Calibrations

The test section was installed and lined up to ensure symmetry with the wind tunnel. The wing was set to $0^\circ AOA$ by using a protractor, and using the centre of the wind tunnel as the $0^\circ AOA$ position. The wing was set vertically straight relative to the in-plane and out-of-plane bending directions. The details of the calibration jig can be seen in Figure D.1, as well as the physical installation in the wind tunnel, which can be seen in Figure D.2.

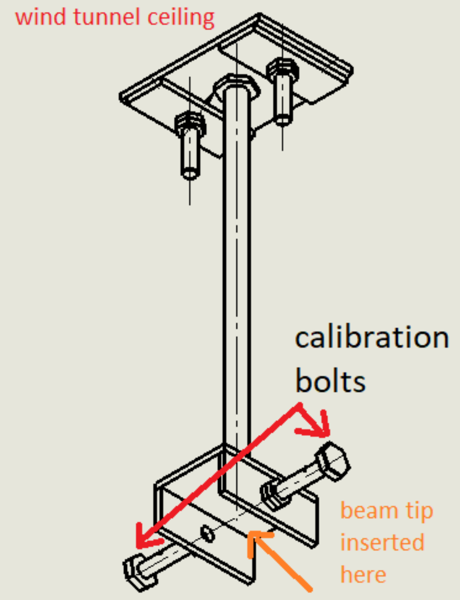

Figure D.1: Calibration Jig

Figure D.2: Potentiometer Calibration In-Situ

D.1 Potentiometer Calibration Curve

The results from the potentiometer calibrations can be seen in Figures D.3 and D.4. The results were used to obtain the relationship between voltage an pitch angle in degrees, seen in Equations D.1 and D.2.

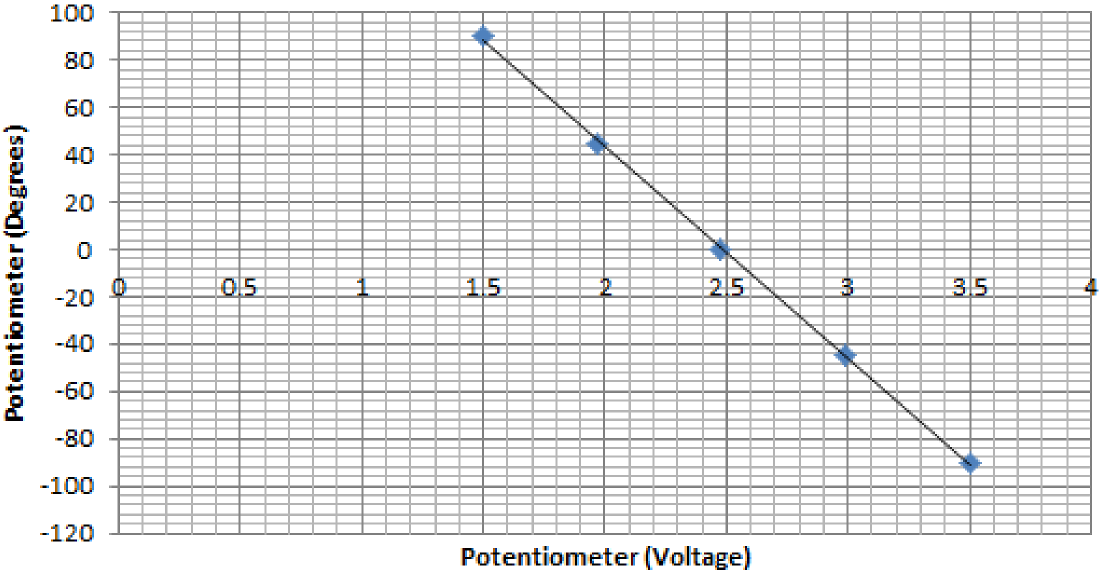

Figure D.3: Potentiometer Calibration Curve Tests A-F

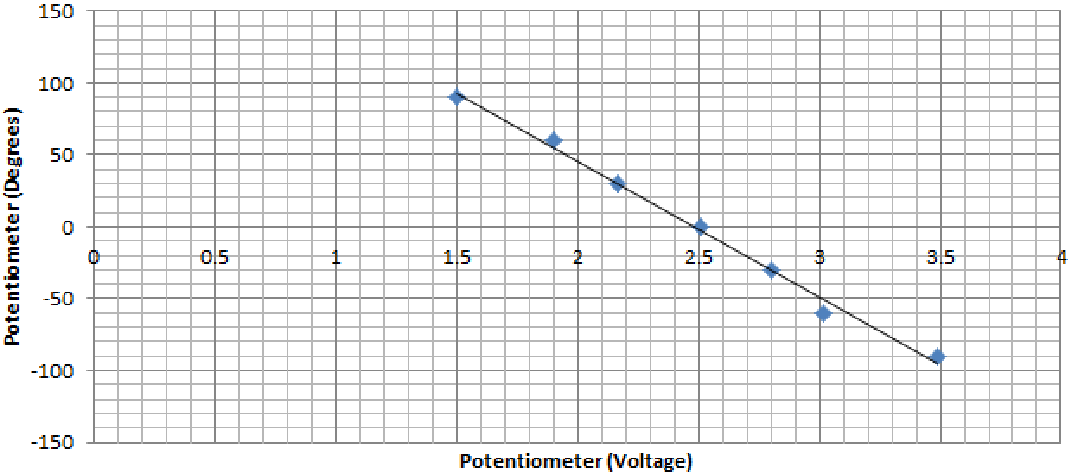

Figure D.4: Potentiometer Calibration Curve Tests G-H

$$\theta = -89.614V + 223.01; R^2 = 0.9997 \tag{D.1}$$

$$\theta = -94.542V + 234.99; R^2 = 0.9939 \tag{D.2}$$

D.2 Flapwise Tip Deflection Calibration and Validation

In order to relate the strain gauge voltage data (located at approximately 0.12 L) to the tip deflection of the beam, a simple physical calibration was used, where a prescribe tip deflection was applied and the corresponding bending strain at around 0.12 L recorded. However, in order to validate that this linear relation was valid, several cases were compared: free vibration of the 1^{st} mod shape (for a linear system, i.e. small angles as this is not quantifiable at larger angles where there are non-linearities) along with some standard analytical cases (Figure 3.18 indicates that there is a close correlation between all cases, especially at the tip and the location of the strain gauges). Thus, the bending calibration results were plotted (Figure D.5), and the equation relating tip bending deflection (in centimetres) to voltage was found (Equation D.3).

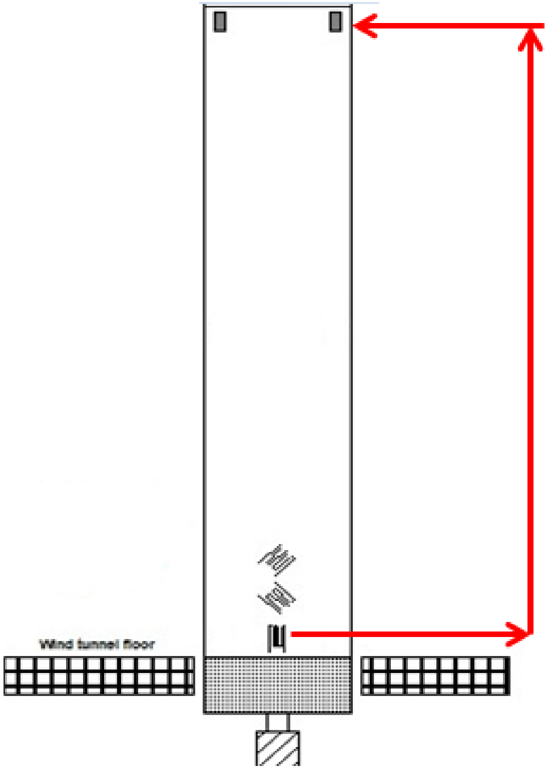

Figure D.5: Relating Strain Gauge Data at 0.12 1L to Tip Deflection

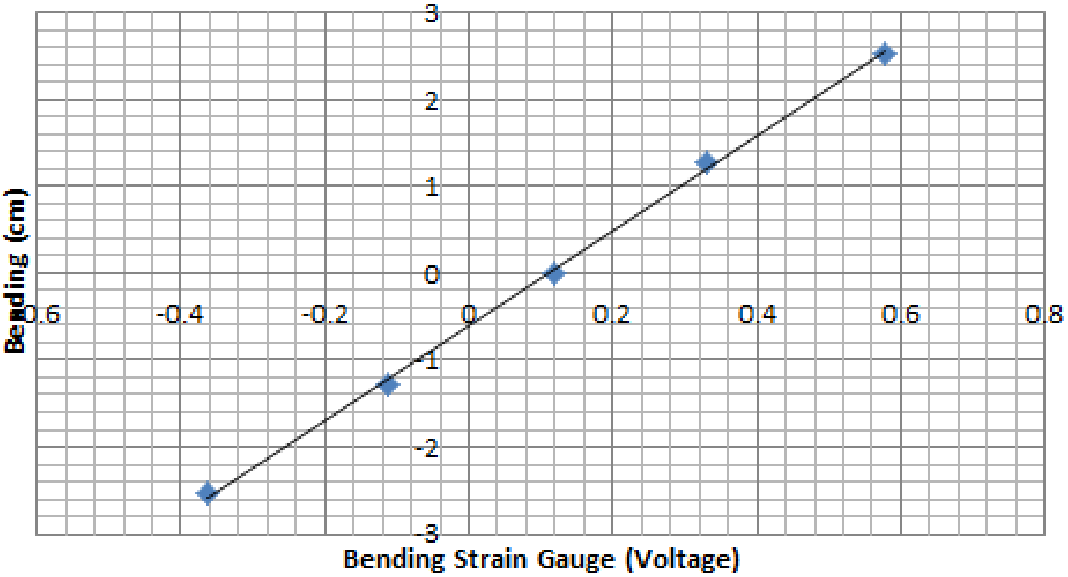

Figure D.6: Bending Calibration Curve Test F

$$w = 5.4512V - 0.6019; R^2 = 0.9994 \tag{D.3}$$

E Wind Tunnel Testing

E.1 Airspeed Calculations and Drift

E.1.1 Airspeed Calculations

Tests A-F

For Tests A-F, the rotations per minute (RPM) of the wind tunnel, baseline zero voltage (prior to testing), and each individual airspeed voltage (due to change in total pressure) were recorded. The RPM was read off of the wind tunnel control manifold. The airspeeds were found via the pitot static voltage readings (either manually read, or recorded through Labview). The local ambient conditions were recorded and used to find the air density (Equation E.1, where $R = 287\ J/kgK$). A simple linear relation between the dynamic pressure, baseline and experimental voltages was found by means of calibration with manometers. Finally the dynamic pressure(Equation E.2) was used to calculate the airspeeds.

$$\rho = \frac{P}{RT} \tag{E.1}$$

$$\Delta P = 673.7 - 631.98(V - V_0) \tag{E.2}$$

$$U = \sqrt{\frac{2\Delta P}{\rho}} \tag{E.3}$$

Tests G-H

For Tests G-H, there was a leak in the pressure transducer tubes, causing erroneous readings of the pitot static results and thus incorrect values of airspeeds. This was substantiated by comparison to a) previous data from the rigid wing b) the calibrated pressure transducer data and c) the results of Test F (Figure E.3).

Since the rigid wing's behaviour can be represented by a simple aerodynamic model, the experimental airspeeds could be compared with analytical predictions to justify their accuracy. In 2018, baseline tests were done with the pressure transducer, where the RPM value was systematically increased for the case of an empty test section; this data were recorded simultaneously with manometer readings. Since the results matched, it indicated that this calibrated pressure transducer data could be trusted.

Finally, anecdotal airspeed evidence was taken from Test F (for the current flexible wing), where there was no indication of erroneous readings. The rigid wing data, calibrated pressure transducer data and manometer data, as well as the results of Test F collectively display the same consistent trend; however, Tests G and H do not match this trend. Note that the corrected curves for Test G and H appears slightly higher, likely due the influence of the Test F data on the calibration curve characteristics.

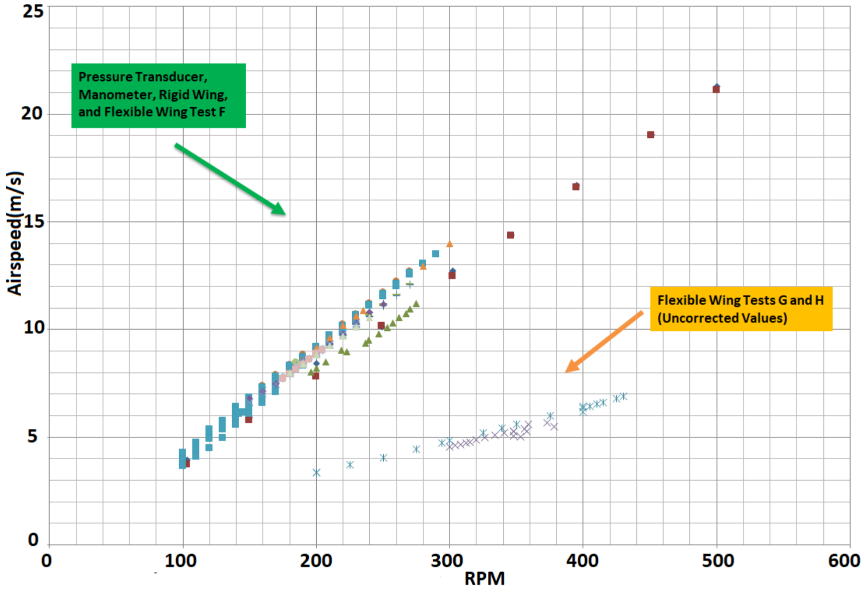

Figure E.1: Airspeed versus Wind Tunnel Rotations Per Minute

Thus, the calibrated pressure transducer, manometer, and Test F data were was used to generate the equation seen in Figure E.2.

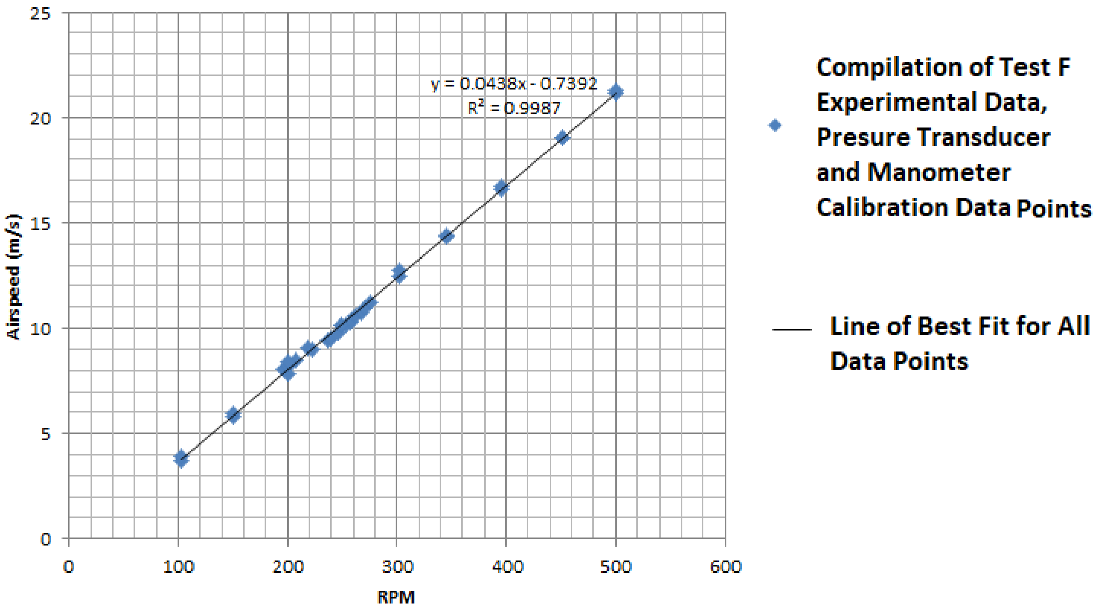

Figure E.2: Relation of RPM to Airspeed (m/s) Using Pressure Transducer, Manometer Calibration Data and Test F Experimental Data

This Equation was then used to correct the airspeeds for Tests G and H, as seen in Figure E.3. Note that due to the airspeed correction, the effects of hysteresis were not captured in Tests G and H.

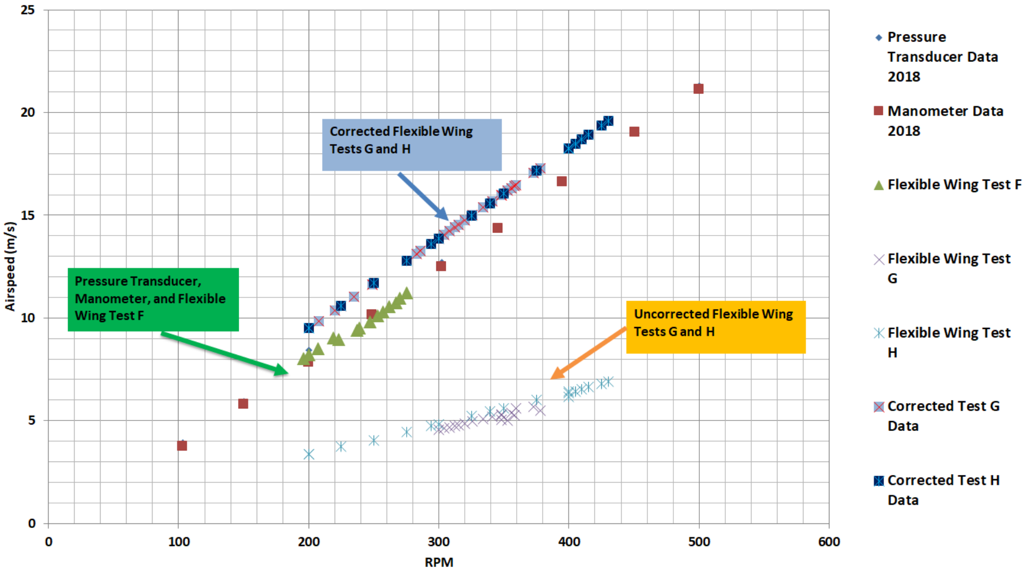

Figure E.3: Airspeed versus Wind Tunnel Rotations Per Minute

E.1.2 Airspeed Drift

Based on the work of Goyaniuk [22], as well as an analysis performed to estimate the drift due to instrumentation, the airspeed can vary by approximately a maximum of $\pm 0.7 m/s$.

E.2 Chronology of Experiments

Trial Tests 1 and 2 focussed on locating the onset of LCO's, as well as capturing the effects of hysteresis and locating the saddle-node/fold bifurcation; videos were taken to help characterize the behaviour. Additionally, these tests provided an estimation of the maximum beam deflection and root pitch rotation. These results were also used in a manner similar to surrogate data, that is to to develop and refine the techniques for filtering and analysis; knowledge of the data from the rigid wing was also used to infer the behaviour of the LCO's.

From a practical standpoint, Trials Tests 1 and 2 focussed on details regarding installation of the wing apparatus, reducing freeplay, sealing cracks, proper application of adhesive at various locations, and proper setting of the wing to a 0° baseline, as well as application of putty on the wing to ensure a smooth surface. Initial observations of any aberrations such as rough portions of the wing and cracks were noted as well.

After refining the test apparatus based on the results of Trial Tests 1 and 2, Test A was performed, with an airspeed test range of 100-250 RPM. Test A indicated the extreme sensitivity of the onset of LCO's to a change in airspeed (initial conditions), and it was decided that a much slower, systematic approach must be undertaken for the following test (Test B). Analytically, it was discussed that there were possibly two types of classical flutter pertinent to these tests: 1) low speed (pitch-1^{st} bending) and 2) high speed (1^{st} torsion and 1^{st} bending) [27]. The approximate locations of the onset of LCO and the SAO/LAO boundaries were noted; it was noted that no motion occurred below 196 RPM; motion occurred from 196-207 RPM when a perturbation was applied but then decayed back to zero.

Test B was performed for an airspeed range of 190-245 RPM, with the lower end of the range dictated by the onset of LCO's observed in Test A and the upper end of the range bounded due to the observance of very large and potentially damaging LCO amplitudes; the LCO onset and SAO/LAO boundaries were found. This test was done with multiple sweeps, providing more detailed information on SAO and LAO behaviour as the airspeed was varied in smaller increments. Test C (230-264 RPM) focussed on capturing more details of the LAO limits, as well as refining and adjusting the spring and pulley tensions. Three ascending airspeed sweeps were performed which , along with Test B, showed a good indication of the effects of changes in initial conditions (by means of a shift in airspeed) on hysteresis, LCO onset and SAO/LAO boundaries. Time history data observed from

Tests B and C indicated that steady-state was difficult to achieve in the LAO region which suggested that perhaps more time needed to be spent on a particular airspeed. Significantly, by this point in testing, damage to the wing, such as cracks in the leading edge near where the beam was clamped, was noticed to be accruing, as well as gradual deformation of the beam (again, evident by the deformation of the beam near the beam clamped-end location). Furthermore, these early tests indicated LCO pitch amplitude in excess of 100° ("VLAO"), much higher than expected based on previous rigid wing data.

Due to the now well-observed violent nature of the motion in the LAO/VLAO region, Test D (210-231 RPM) was performed with the focus of attaining more LAO data, as well as more clearly capturing the jump from SAO to LAO. Test E (209-261 RPM) once again focussed on only the LAO region as, hitherto, it was noted that a significant amount of data had been collected for the SAO region.

Generally, Tests A-E (which all utilized Beam-01) indicated the existence of small, large and very large (on the order of 100°) amplitude LCO's . However, the very large amplitude oscillations were found to be an artefact of a spring extension issue. Comparing the LCO amplitudes to data from the rigid wing, and observation of spring extension behaviour during testing suggested that data in the LCO amplitude range of approximately $0 - 80^\circ$ was valid for Tests A-E.

Following the first five valid tests (Tests A-E), a further three trial tests were performed, with the focus of refining the wing apparatus. More importantly, given that the LCO amplitude data from the potentiometer appeared valid and reasonable, focus was now also placed on observing the strain gauge and accelerometer data. Trial Test 8 (209-261 RPM) is very significant as only a few test airspeeds were gleaned due to a significant amount of freeplay between the beam and wing. Upon post-test examination, it became clear that the plastic deformation of the beam had made it more difficult to obtain a smooth fit between the beam and wing, leading to larger amounts of freeplay and cracks in the wing located on the L.E. at the beam clamped-end, coincident with the area of localized plastic deformation. This led to the requirement of extensive shimming to set the wing vertically straight, but created a notable offset of the wing relative to the W.T. centreline in the process. For Trial Test 9 (217-263 RPM) great adjustments involving adhesive and shimming were used to ensure the wing apparatus was adequately straight, aligned and at 0° AOA. Multiple sweeps were performed with the hopes of capturing further details of boundaries and gaining more data points. The final test performed with Beam-01, Trial Test 10 (167-286 RPM), was performed in a manner similar to Trial Test 9. However, new spring anchors were installed, which fully eliminated the spring extension issues, and thus the goal was replication of Trial Test 9, with the new set-up. At this point in time, the effects of the beam plastic deformation were extremely apparent in the visual sense.

Thus Trial Test 10 was attempted. However, only two test points were gained, for 153 RPM, and 175 RPM, before the wing apparatus abruptly stopped by itself during testing above 175 RPM; a post-test examination strongly suggested that the cause was the plastic deformation of the beam; the plastic deformation which occurred near the beam clamped-end meant that when beam was installed in the wing and clamped into the rotary base, the wing tip was displaced in the -z direction by a qualitatively noticeable amount.

After the events of Trial Test 10 (final test performed with Beam-01) it was decided that further testing would not be accurate due to such a significant amount of plastic deformation experienced by Beam-01, while the wing was still viable but noted to be gently disintegrating internally, and losing some smoothness at the L.E. It is important to note that the wing was continued to be used since the internal damage could be corrected with adhesive, while the external damage appeared trivial in the sense that the continued appearance of SAO in all subsequent tests confirmed the existence of Reynolds numbers effects due to a ”smooth” wing surface.

After obtaining a new beam, Beam-02, with identical dimensions and parameters as the old beam, Test F (167-286 RPM) was performed. Unfortunately, Test F was plagued with issues of the wing splitting due to the cracks which had already formed at the L.E., near the beam clamped-end. However, each time the wing split (3 times in total), the airspeed was dropped and the wing was repaired in-situ with more adhesive to ensure a smooth L.E. with mitigated cracks. Testing continued until 286 RPM was reached, when the wing stopped abruptly by itself. Upon post-test inspection, it appeared to be be due to a significant amount of plastic deformation, which had caused beam failure. When the beam was installed in the wing and clamped into the free rotary base, the wing tip exhibited a maximum deflection of about 2.5 cm (Using the coordinates of Figure 1.2, wing tip located at [44.5 cm, 0,-2.5 cm]).

Tests F is significant, as beam failure for Beam-02 occurred quickly over the course of one test; conversely, Beam-01 experienced gradual plastic deformation over the course of Trial Test 1 - Trial Test 10 (see Table 4.1) and then beam failure in Trial Test 10. By plotting the bifurcation diagram for Test F and analysing the change in the wing bias by means of the histograms for all test points, it was determined that only data gleaned from the SAO region was valid, but data from the LAO region was significantly affected by the plastic deformation of the beam.

The unexpected phenomena of beam failure due to a soft beam material (Appendix A.5) led to the decision to switch from Normalized AISI-01 steel (Beams-01,-02) to Tempered 1095 spring steel (Beam-03).

After research into selecting a beam with the same Young's modulus and similar dimensions to Beams-01,-02 but with a higher yield strength, the best material option was found to be Tempered 1095 spring steel. It was known that normalized 1095 spring steel had a yield strength of 500 MPa, which is greater than the 350 MPa for Normalized AISI 01 steel (Appendix A.4). The manufacturer's data indicated that the normalized spring steel would have a Rockwell C (RC) hardness value of approximately 60 [62], suggesting that the tempered spring steel would have a lower value on the order of around RC50 [55], which meant a yield strength estimate of around 570 MPa [55] [63]. The beam stock material was available in a thickness of 0.062" (1.57 mm) [62], which is thicker than Beam-01. While Beam-03 was initially going to be ground down to match the thickness of Beams-01,02 (1.4 mm), this idea was cancelled as grinding/sanding the surface of the tempered steel might remove the martensite coating which contributed to its increased strength [55].

Thus, Test G (209-378 RPM) utilized Beam-03 (Tempered 1095 spring steel). Prior to testing, there was notable freeplay between the beam and wing due to the thicker beam. It was noted that strain gauge application required some sanding and heating of the areas where the strain gauges were applied at 0.09-0.13 L, possibly changing the properties of the beam material in this localized area. The position near the wing tip on the L.E. was noticeably worn and down and not as smooth as for previous tests. Post-test, a new potentiometer calibration was done, and the weight of the beam with instrumentation was recorded. Several airspeed sweeps were done, both up and down, in order to capture LCO's, as before.

For Test G, LCO's did not appear until 294 RPM, and after applying several pitch perturbations; thus the instigation of LCO's occurred at a much higher airspeed than seen with tests conducted with Beams-01,02. Additionally, there appeared to be a possible beat frequency at 235 RPM (beating phenomenon defined as an "interference pattern resulting from the interaction of two very close fundamental frequencies" [22]). Clean LCO's appeared at approximately 300 RPM, indicating the presence of the fold bifurcation. One possible SAO/LAO boundary (subcritical Hopf bifurcation) appeared to be located at 339 RPM, after several sweeps in both directions. During testing, cracks appeared in the wing, and the strain gauge scopes indicated that they had become damaged or saturated. A post-test inspection suggested the strain gauges shorted out due to large deflections compressing the strain gauge films, causing them to touch the metal beam. This instrumentation damage, in tandem with the unpredictable nature of the new beam being tested at higher airspeeds, (close to approximately 20 m/s), led to manual termination of the test.

Finally Test H was performed (200-415 RPM) with a 0 pitch spring configuration. No strain gauge data were recorded and accelerometers were not applied as this test was mostly qualitative in nature. It is important to note that only one possible clean LCO was observed at 430RPM; from approximately 400-425 RPM some interesting patterns noticeable in the time histories appeared but remain unexplained (Section 5.5). The test was manually terminated at 430 RPM, again due to an airspeed in excess of 20 m/s, where the behaviour of this configuration was unpredictable.

E.3 Trial Tests

E.3.1 Trial Test 1

$V\#$: Indicates that a video of the behaviour was taken

1. Noise Data:
    a) $s3$ configuration; **pitch lock OFF**; **wind tunnel OFF**
    b) $s3$ configuration; **pitch lock OFF**; **motor ON** [1]
    c) $s3$ configuration; **pitch lock OFF**; **motor and clutch ON (zero RPM)** [2]
2. FDT1:
    a) $s3$ configuration; **pitch lock OFF**; **motor and clutch ON (zero RPM)**; pitch I.C. X 2
    b) $s3$ configuration; **pitch lock ON**; **motor and clutch ON (zero RPM)**; bending I.C. X 2 [3]
3. Varying Speed Testing:
    a) $s3$ configuration, 100 RPM; small pitch I.C., large pitch I.C. [4]
    b) $s3$ configuration, 115 RPM; small pitch I.C., large pitch I.C. [5]
    c) $s3$ configuration, 130 RPM; small pitch I.C., large pitch I.C.
    d) $s3$ configuration, 145 RPM; small pitch I.C., large pitch I.C. [6]
    e) $s3$ configuration, 160 RPM; small pitch I.C., large pitch I.C. [7]
    f) $s3$ configuration, 175 RPM; small pitch I.C., large pitch I.C. [8]
    g) $s3$ configuration, 190 RPM; small pitch I.C., large pitch I.C.
    h) $s3$ *configuration, 205 RPM; small pitch I.C.[V1], large pitch I.C.[V2]* [9]
    i) $s3$ configuration, 220 RPM [V3]; small pitch I.C., large pitch I.C.
    j) $s3$ configuration, 230 RPM [V4]; small pitch I.C. [10]
    k) $s3$ configuration, 235 RPM [V5]; small pitch I.C.[V6]
    l) $s3$ *configuration, 250 RPM Attempt 1; small pitch I.C. - behaviour appeared divergent, dropped speed quickly and returned to zero RPM; inspected rig, and found no damage or loose supports, etc. Perhaps beam in wing slightly loose but not major.*
    m) $s3$ *configuration, 250 RPM Attempt 2; small pitch I.C. - recorded airspeed voltage and took video of divergent behaviour following small perturbation. [V7]*

---

[1] confirmed that pipe water is running, gauge is at non-zero

[2] Changed to 1 time column output; display shows Voltage not Pitch Angle

[3] Opened Door to give bending I.C. then closed before Varying Speed Testing

[4] Lowest possible tunnel speed where reasonable results can be gleaned, due to freeplay; from discussion with L. Goyaniuk

[5] Large I.C.'s test effects of non-linearities

[6] Audible sound begins

[7] Watch for LCO due to subcritical saddle-node bifurcation per Dr. Poirel

[8] Some residual oscillations after perturbation

[9] LCO occurs due to saddle-node bifurcation; manually stopped movement after each perturbation

[10] Previous testing qualitatively indicated that this is where the onset of flutter occurs (when the downstream mesh grate is used)

4. FDT1:
    a) $s3$ configuration; **pitch lock OFF**; **motor and clutch ON (zero RPM)**; pitch I.C.
    b) $s3$ configuration; **pitch lock ON**; **motor and clutch ON (zero RPM)**; bending I.C. [11]
5. FDT2:
    a) $s3$ configuration; **pitch lock OFF**; **motor and clutch OFF**; Pitch I.C. X 2
    b) $s2$ configuration; **pitch lock OFF**; **motor and clutch OFF**; Pitch I.C. X 2
    c) s1 configuration; **pitch lock OFF**; **motor and clutch OFF**; Pitch I.C. X 2

E.3.2 Trial Test 2

1. Noise Data:
    a) $s4^*$ configuration; **pitch lock OFF**; **wind tunnel OFF**
    b) $s4^*$ configuration; **pitch lock OFF**; **motor ON**
    c) $s4^*$ configuration; **pitch lock OFF**; **motor and clutch ON (zero RPM)**
2. FDT1:
    a) $s4^*$ configuration; **pitch lock ON**; **motor and clutch ON (zero RPM)**; bending I.C. X 2
    b) $s4^*$ configuration; **pitch lock OFF**; **motor and clutch ON (zero RPM)**; pitch I.C. X 2
3. Sweep 1:
    a) 100 RPM; Give wing small I.C.
    b) increase to 115 RPM; record behaviour
    c) increase to 130 RPM; record behaviour
    d) increase to 145 RPM; record behaviour
    e) increase to 160 RPM; record behaviour
    f) increase to 175 RPM; record behaviour
    g) increase to 175 RPM; record behaviour
    h) increase to 190 RPM; record behaviour
    i) increase to 205 RPM; record behaviour
    j) increase to 220 RPM; record behaviour
    k) increase to 235 RPM; record behaviour
    l) increase to 250 RPM; record behaviour
    m) repeat previous steps until LAO achieved; continue to raise airspeed while comfortable with behavior
    n) when test limit reached, return to Zero RPM
4. Sweep 2:
    a) 100 RPM; Give wing large I.C.
    b) Sweep through increasing airspeed until LAO achieved; record data from this point, in increments of 10-15 RPM

---

[11] Opened Door to give bending I.C., left open for FDT2

    c) when no longer comfortable with behaviour, sweep back down in airspeed until no LCO
5. FDT1:
    a) $s4^*$ configuration; **pitch lock OFF**; **motor and clutch ON (zero RPM)**; pitch I.C.
    b) $s4^*$ configuration; **pitch lock ON**; **motor and clutch ON (zero RPM)**; bending I.C.
6. FDT2:
    a) $s4^*$ configuration; **motor and clutch OFF**; Pitch I.C. X 2
    b) $s2$ configuration; **motor and clutch OFF**; Pitch I.C. X 2
    c) s1 configuration; **motor and clutch OFF**; Pitch I.C. X 2

E.3.3 Trial Test 8

1. Noise Data:
    a) $s4^*$ configuration; **pitch lock OFF**; **wind tunnel OFF**
    b) $s4^*$ configuration; **pitch lock OFF**; **motor ON**
    c) $s4^*$ configuration; **pitch lock OFF**; **motor and clutch ON (zero RPM)**
2. FDT1:
    a) $s4^*$ configuration; **pitch lock OFF**; **motor and clutch ON (zero RPM)**; pitch I.C. X 2
    b) $s4^*$ configuration; **pitch lock ON**; **motor and clutch ON (zero RPM)**; bending I.C. X 2
3. Sweep 1:
    a) $s4^*$ configuration, 209 RPM, SPIC
    b) $s4^*$ configuration, 237 RPM
    c) $s4^*$ configuration, 242 RPM
    d) $s4^*$ configuration, 254 RPM
    e) $s4^*$ configuration, 261 RPM
    f) $s4^*$ configuration, 210 RPM
4. FDT1:
    a) $s4^*$ configuration; **pitch lock OFF**; **motor and clutch ON (zero RPM)**; pitch I.C.
    b) $s4^*$ configuration; **pitch lock ON**; **motor and clutch ON (zero RPM)**; bending I.C.
5. FDT2:
    a) $s4^*$ configuration; **pitch lock OFF**; **motor and clutch OFF**; Pitch I.C. X 2
    b) $s2$ configuration; **pitch lock OFF**; **motor and clutch OFF**; Pitch I.C. X 2
    c) s1 configuration; **pitch lock OFF**; **motor and clutch OFF**; Pitch I.C. X 2

- Ambient Pressure = 1022.5 mbar
- Ambient Temperature = 20.9°
- $V_o = 1.1345$V

E.3.4 Trial Test 9

1. Noise Data:
   a) $s4^*$ configuration; **pitch lock OFF**; **wind tunnel OFF**
   b) $s4^*$ configuration; **pitch lock OFF**; **motor ON**
   c) $s4^*$ configuration; **pitch lock OFF**; **motor and clutch ON (zero RPM)**
2. FDT1:
   a) $s4^*$ configuration; **pitch lock OFF**; **motor and clutch ON (zero RPM)**; pitch I.C. X 2
   b) $s4^*$ configuration; **pitch lock ON**; **motor and clutch ON (zero RPM)**; bending I.C. X 2
3. Sweep 1,Up:
   a) pitch initial condition given
   b) $s4^*$ configuration, 217/218 RPM
   c) $s4^*$ configuration, 222 RPM
   d) $s4^*$ configuration 225 RPM
   e) $s4^*$ configuration, 226/227 RPM
   f) $s4^*$ configuration, 228/229 RPM
   g) $s4^*$ configuration, 230 RPM
   h) $s4^*$ configuration, 233 RPM
   i) $s4^*$ configuration, 235 RPM
   j) $s4^*$ configuration, 238 RPM
   k) $s4^*$ configuration, 243 RPM
   l) $s4^*$ configuration, 247/248 RPM
   m) $s4^*$ configuration, 253 RPM
   n) $s4^*$ configuration, 258 RPM
   o) $s4^*$ configuration, 262 RPM
4. Sweep 2, Down: cable slipped out of spring towards outer loop of wing tunnel at 262 RPM, dropped to 140 RPM and fixed it.
5. Sweep 3, Up:
   a) bottom of L.E. split
   b) $s4^*$ configuration, 229 RPM with pitch initial condition
   c) $s4^*$ configuration, 262 RPM
6. Sweep4, Down: dropped to 224 RPM LAO/VLAO obtained too fast, springs appear to be okay.
7. Sweep 5, Up:
   a) $s4^*$ configuration, 263RPM
8. Sweep 6, Down: dropped again, same abrupt LAO behaviour as before
9. Sweep 7, Up:
   a) $s4^*$ configuration No airspeed captured
10. Sweep 8, Down: Again LAO/VLAO too abrupt, dropped to 191 RPM
11. Sweep 9, Up:
    a) $s4^*$ configuration, 235 RPM pitch initial conditions

In order to properly capture LAO, airspeed needed to be increased to 284 RPM. Unfortunately, the testing was halted as beam failure appeared to occur, ending the test.

12. FDT1:
    a) $s4^*$ configuration; **pitch lock OFF**; **motor and clutch ON (zero RPM)**; pitch I.C.
    b) $s4^*$ configuration; **pitch lock ON**; **motor and clutch ON (zero RPM)**; bending I.C.
13. FDT2:
    a) $s4^*$ configuration; **pitch lock OFF**; **motor and clutch OFF**; Pitch I.C. X 2
    b) $s2$ configuration; **pitch lock OFF**; **motor and clutch OFF**; Pitch I.C. X 2
    c) s1 configuration; **pitch lock OFF**; **motor and clutch OFF**; Pitch I.C. X 2

- Ambient Pressure Pre-test = 1000 mbar
- Ambient Temperature Pre-Test = 20.6°

E.3.5 Trial Test 10

1. Noise Data:
    a) $s4^*$ configuration; **pitch lock OFF**; **wind tunnel OFF**
    b) $s4^*$ configuration; **pitch lock OFF**; **motor ON**
    c) $s4^*$ configuration; **pitch lock OFF**; **motor and clutch ON (zero RPM)**
2. FDT1:
    a) $s4^*$ configuration; **pitch lock OFF**; **motor and clutch ON (zero RPM)**; pitch I.C. X 2
    b) $s4^*$ configuration; **pitch lock ON**; **motor and clutch ON (zero RPM)**; bending I.C. X 1 (pitch lock would not secure properly at this moment)
3. Sweep 1,Up:
    a) $s4^*$ configuration, 153 RPM
    b) $s4^*$ configuration, 175 RPM WING APPARATUS STOPS MOVING ABRUPTLY, STATICALLY STOPPING ON A BIAS
4. FDT2:
    a) $s4^*$ configuration; **pitch lock OFF**; **motor and clutch OFF**; Pitch I.C. X 2
    b) s2 configuration; **pitch lock OFF**; **motor and clutch OFF**; Pitch I.C. X 2
    c) s1 configuration; **pitch lock OFF**; **motor and clutch OFF**; Pitch I.C. X 2

- Ambient Pressure Pre-test = 1022.5 mbar
- Ambient Temperature Pre-Test = 20.9°
- V_o = 1.1345V

Table E.1: Trial Test 10 Airspeeds

RPM	**Voltage**
Sweep 1	
209 SPIC	1.2107
237	1.2214
242	1.2260
254	1.2362
261	1.2426
210	1.2099

E.4 Wind Tunnel Tests A-H

E.4.1 Test A

1. Noise Data:
   a) $s4^*$ configuration; **pitch lock OFF**; **wind tunnel OFF**
   b) $s4^*$ configuration; **pitch lock OFF**; **motor ON**
   c) $s4^*$ configuration; **pitch lock OFF**; **motor and clutch ON (zero RPM)**
2. FDT1:
   a) $s4^*$ configuration; **pitch lock ON**; **motor and clutch ON (zero RPM)**; bending I.C. X 2
   b) $s4^*$ configuration; **pitch lock OFF**; **motor and clutch ON (zero RPM)**; pitch I.C. X 2
3. Varying Speed Testing:
   a) Started at 203 RPM - Recorded Data [12]
   b) Increased to 230 RPM - Recorded Data
   c) Decreased to approx. 210 RPM, then increased to 225 RPM - Recorded Data
   d) Decreased to 220 RPM - Recorded Data
   e) Decreased to 217 RPM - Recorded Data
   f) Increased to 230 RPM - Recorded Data [13]
   g) Decreased to 203 RPM - Recorded Data [14]
4. FDT1:
   a) $s4^*$ configuration; **pitch lock OFF**; **motor and clutch ON (zero RPM)**; pitch I.C.
   b) $s4^*$ configuration; **pitch lock ON**; **motor and clutch ON (zero RPM)**; bending I.C.
5. FDT2:
   a) $s4^*$ configuration; **motor and clutch OFF**; Pitch I.C. X 2
   b) s2 configuration; **motor and clutch OFF**; Pitch I.C. X 2

---

[12] This is where small amplitude LCO begins

[13] To capture LAO

[14] To check consistency of data

c) s1 configuration; **motor and clutch OFF**; Pitch I.C. X 2

- Ambient Pressure = 1022 mbar
- Ambient Temperature = 23.3°C
- $V_o = 1.443$V

Table E.2: Test A Airspeeds

Airspeed (RPM)	Voltage	Voltage (During Oscillations)	Airspeed (m/s)
203 (1^{st} test)	1.2153	N/A	N/A
203 (2nd test)	1.2148	N/A	N/A
217	1.2262	N/A	N/A
220	1.2256	N/A	9.15
225	1.2334	1.2280	9.80
230	1.2370	1.2252	9.94

E.4.2 Test B

1. Noise Data:
   a) $s4^{*}$ configuration; **pitch lock OFF**; **wind tunnel OFF**
   b) $s4^{*}$ configuration; **pitch lock OFF**; **motor ON**
   c) $s4^{*}$ configuration; **pitch lock OFF**; **motor and clutch ON (zero RPM)**
2. FDT1:
   a) $s4^{*}$ configuration; **pitch lock OFF**; **motor and clutch ON (zero RPM)**; pitch I.C. X 2
   b) $s4^{*}$ configuration; **pitch lock ON**; **motor and clutch ON (zero RPM)**; bending I.C. X 2
3. SAO Boundaries:
   a) $s4^{*}$ configuration, 190 RPM; small pitch I.C. [15]
   b) $s4^{*}$ configuration, 192 RPM; small pitch I.C.
   c) $s4^{*}$ configuration,194 RPM; small pitch I.C.
   d) $s4^{*}$ configuration, 196 RPM; small pitch I.C. [16]
   e) $s4^{*}$ configuration, 198 RPM; small pitch I.C.
   f) $s4^{*}$ configuration, 200 RPM; small pitch I.C.
   g) $s4^{*}$ configuration, 202 RPM; small pitch I.C.
   h) $s4^{*}$ configuration, 204 RPM; small pitch I.C.
   i) $s4^{*}$ configuration, 205 RPM; small pitch I.C.
   j) $s4^{*}$ configuration, 206 RPM; small pitch I.C.
   k) $s4^{*}$ configuration, 207 RPM; small pitch I.C. [17]
   l) $s4^{*}$ configuration, 210 RPM
   m) $s4^{*}$ configuration, 215 RPM
4. LAO Boundaries (Sweep 1):
   a) $s4^{*}$ configuration, 217 RPM [18]
   b) $s4^{*}$ configuration, 218 RPM
   c) $s4^{*}$ configuration, 219 RPM
   d) $s4^{*}$ configuration, 220 RPM
   e) $s4^{*}$ configuration, 224 RPM
   f) $s4^{*}$ configuration, 230 RPM
   g) $s4^{*}$ configuration, 234 RPM.
   h) $s4^{*}$ configuration, 236 RPM
   i) $s4^{*}$ configuration, 240 RPM; small pitch I.C.]
   j) $s4^{*}$ configuration, 245 RPM; small pitch I.C. [19] [20]

---

[15] Test 1 - Oct. 10 2017 indicates that onset of SAO between 190 RPM and 205 RPM

[16] Faintly audible noise appeared

[17] Determined to be where onset of SAO occurs

[18] Test 3 - Oct. 16 2017 indicates that onset of LAO between 217 RPM and 220 RPM

[19] Onset of LAO, qualitatively appeared to be approx. ≥ 100 °

[20] Test 3 - Oct. 16 2017 indicates that onset of pitch angles of ≥ 100 ° occurs approximately at 230 RPM when triggered by large I.C.

Pitch angles of ≥ 100 ° experienced at 245 RPM. Proceeded to drop airspeed down to 212 RPM and wait for wing to reach steady-state. The wing was manually stopped a couple times. The Airspeed was raised to 220 RPM and behaviour was noted to have returned to what was seen in Sweep 1. Proceeded attempt of Sweep 2 to catch onset of approx. ≥ 50 ° pitch angles.

5. LAO Boundaries (Sweep 2):
   a) $s4^*$ configuration, 236 RPM; small pitch I.C.
   b) $s4^*$ configuration, 238/239 RPM; small pitch I.C. [21]

   Following the vents of Sweep 2, the airspeed was again dropped to 216 RPM and attempts made to manually stop the wing. One final sweep was done attempting to capture the onset of predicted LAO.
6. LAO Boundaries (Sweep 3):
   a) $s4^*$ configuration, 231 RPM; small pitch I.C.
   b) $s4^*$ configuration, 234 RPM; small pitch I.C.
   c) $s4^*$ configuration, 235 RPM; small pitch I.C. [22]
7. FDT1:
   a) $s4^*$ configuration; **pitch lock OFF**; **motor and clutch ON (zero RPM)**; pitch I.C.
   b) $s4^*$ configuration; **pitch lock ON**; **motor and clutch ON (zero RPM)**; bending I.C.
8. FDT2:
   a) $s4^*$ configuration; **pitch lock OFF**; **motor and clutch OFF**; Pitch I.C. X 2
   b) s2 configuration; **pitch lock OFF**; **motor and clutch OFF**; Pitch I.C. X 2
   c) s1 configuration; **pitch lock OFF**; **motor and clutch OFF**; Pitch I.C. X 2

- Ambient Pressure = 1028 mbar
- Ambient Temperature = 22.1°C
- $V_o = 1.1357$V

---

[21] Experienced LAO which qualitatively looked like approx. ± 100 ° again

[22] Onset of LAO approx. ± 60°

Table E.3: Test B Airspeeds

RPM	**Voltage**	**Voltage (During SS Oscillations)**	**Comment**	Airspeed (m/s)
Sweep 1				
190	1.1984			
192	1.1993			
194	1.2005			
196	1.2022-1.2030		Faintly Audible Noise	
198	1.2040	1.2029-1.2047	LCO which decays when SS reached	
200	1.2046-1.2052	1.2050	LCO which decays when SS reached	
204	1.2082	1.2085	LCO which decays when SS reached	
205	1.2088	1.2088	LCO which decays when SS reached	
206	1.2095	1.2095	LCO which decays when SS reached	
207		1.2102	Onset of SAO	9.33
210		1.2128	SAO	9.49
215		1.2163	SAO, potentiometer in order of ± 3° pitch angles	9.71
217		1.2182	SAO, potentiometer in order of ± 4° pitch angles	9.82
218		1.2193	SAO, potentiometer in order of ± 4,5° pitch angles	9.89
219		1.2198	SAO, potentiometer in order of ± 4,6° pitch angles	9.92
220		1.2208	SAO, potentiometer in order of ± 5,6° pitch angles	9.97
224		1.2234	SAO, potentiometer in order of ± 6,8° pitch angles	10.13
230		1.2294	SAO, potentiometer in order of ± 6,9° pitch angles	10.46
234		1.2323	SAO, potentiometer in order of ± 6,10° pitch angles	10.48
236/237		1.2342	SAO, potentiometer in order of ± 8,10° pitch angles	10.587
240		1.2382	SAO, potentiometer in order of ± 9,12° pitch angles	
245		N.A.	LAO, potentiometer qualitatively in order of ± 100° pitch angles	
Sweep 2				
236		1.2338	LAO, potentiometer qualitatively in order of ± 10,13° pitch angles	10.63
238/239		1.2338	LAO, potentiometer qualitatively in order of ± 100° pitch angles	10.71
Sweep 3				
231		1.2297		10.71
234		1.2314		10.73
235		1.2360	Onset of LAO, potentiometer in order of ± 60° pitch angles	10.83

E.4.3 Test C

1. Noise Data:
    a) $s4^*$ configuration; **pitch lock OFF**; **wind tunnel OFF**
    b) $s4^*$ configuration; **pitch lock OFF**; **motor ON**
    c) $s4^*$ configuration; **pitch lock OFF**; **motor and clutch ON (zero RPM)**
2. FDT1:
    a) $s4^*$ configuration; **pitch lock OFF**; **motor and clutch ON (zero RPM)**; pitch I.C. X 2
    b) $s4^*$ configuration; **pitch lock ON**; **motor and clutch ON (zero RPM)**; bending I.C. X 2
3. Sweep 1 (All $s4^*$ config.):
    a) 230 RPM; recorded airspeed and Labview data
    b) 235 RPM; recorded airspeed and Labview data
    c) 238 RPM; recorded airspeed and Labview data
    d) 240 RPM; recorded airspeed and Labview data
    e) 245 RPM; recorded airspeed and Labview data
    f) 251 RPM; recorded airspeed and Labview data
    g) 254 RPM; recorded airspeed and Labview data
    h) 258 RPM; recorded airspeed and Labview data
    i) 260/261 RPM; recorded airspeed and Labview data
    j) 262 RPM; recorded airspeed and Labview data
    k) 264 RPM [23]

    Dropped Speed down to reduce amplitude of oscillations and increased to 230 RPM again to try and capture LAO boundary and data. Slowly swept down in speed to gain results.
4. Sweep 2 (All $s4^*$ config.):
    a) 230 RPM, SPIC; recorded airspeed and Labview data
    b) 226 RPM, SPIC; recorded airspeed and Labview data
    c) 224 RPM; recorded airspeed and Labview data
    d) 222 RPM; recorded airspeed and Labview data
    e) 219/220 RPM [24]
5. Sweep 3 (All $s4^*$ config.):
    a) 221 RPM; recorded airspeed and Labview data [25]
    b) 228 [26]
6. FDT1:
    a) $s4^*$ configuration; **pitch lock OFF**; **motor and clutch ON (zero RPM)**; pitch I.C.

---

[23] artificial VLAO due to spring hyper-extension, onset between 262 and 264 RPM

[24] No data recorded at this speed, observed that this is the boundary of LAO and SAO

[25] Appears to be in the cusp of LAO and artificial VLAO due to spring hyper-extension

[26] Onset of VLAO

   b) *s*4* configuration; **pitch lock ON**; **motor and clutch ON (zero RPM)**; bending I.C.

7. FDT2:
   a) *s*4* configuration; **pitch lock OFF**; **motor and clutch OFF**; Pitch I.C. X 2
   b) s2 configuration; **pitch lock OFF**; **motor and clutch OFF**; Pitch I.C. X 2
   c) s1 configuration; **pitch lock OFF**; **motor and clutch OFF**; Pitch I.C. X 2

The Onset of limits of SAO were successfully found. However, the LAO behaviour still needs to be further investigated. Based on this experiment, it is recommended that tests be done in the region of 231 RPM-240 RPM, perhaps with and without initial conditions.

- Ambient Pressure = 1016.5 mbar
- Ambient Temperature = 23.2°C
- V_o = 1.1425V

Table E.4: Test C Airspeeds

RPM	Voltage (During SS Oscillations)	Comment	Airspeed(m/s)
Sweep 1			
230	1.2352	±4°	9.74
235	1.2397	N.A.	9.82
238	1.2420	±5°	9.91
240	1.2445	±5,6°	10.00
245	1.2480	N.A.	10.14
251	1.2540	N.A.	10.49
254	1.2562	±10°	10.74
258	1.2603	N.A.	10.87
260/261	1.2624	N.A.	11.00
262	1.2636	±14°	11.19
264		VLAO	
Sweep 2			
230	1.2291	SPIC	11.50
226	1.2268	SPIC	11.62
224	1.2253	N.A.	11.82
222	1.2238	N.A.	11.92
219/220		**Boundary of SAO and LAO**	
Sweep 3			
221	1.2224	**cusp of LAO and VLAO**	11.99
228		VLAO	

* Note all angles refer to pitch angles only, i.e. the values gleaned from Labview and the potentiometer

E.4.4 Test D

1. Noise Data:
    a) $s4^*$ configuration; **pitch lock OFF**; **wind tunnel OFF**
    b) $s4^*$ configuration; **pitch lock OFF**; **motor ON**
    c) $s4^*$ configuration; **pitch lock OFF**; **motor and clutch ON (zero RPM)**
2. FDT1:
    a) $s4^*$ configuration; **pitch lock OFF**; **motor and clutch ON (zero RPM)**; pitch I.C. X 2
    b) $s4^*$ configuration; **pitch lock ON**; **motor and clutch ON (zero RPM)**; bending I.C. X 2
3. LAO Boundaries (Sweep 1):
    a) $s4^*$ configuration, 210 RPM
    b) $s4^*$ configuration, 210 RPM, small pitch initial condition
    c) $s4^*$ configuration, 227 RPM
    d) $s4^*$ configuration, 230 RPM

    Dropped to 190 RPM as VLAO obtained too soon (recorded airspeed for reference). While increasing airspeed again (at about 198 RPM) noticed wing biased to one side. Note that no further I.C.'s given prior to next 2 sweeps
4. LAO Boundaries (Sweep 2):
    a) $s4^*$ configuration, 224 RPM
    b) $s4^*$ configuration, 226 RPM
    c) $s4^*$ configuration, 227 RPM
    d) $s4^*$ configuration, 229 RPM
    e) $s4^*$ configuration, 231 RPM
5. LAO Boundaries (Sweep 3):
    a) $s4^*$ configuration, 227 RP
6. FDT1:
    a) $s4^*$ configuration; **pitch lock OFF**; **motor and clutch ON (zero RPM)**; pitch I.C.
    b) $s4^*$ configuration; **pitch lock ON**; **motor and clutch ON (zero RPM)**; bending I.C.
7. FDT2:
    a) $s4^*$ configuration; **pitch lock OFF**; **motor and clutch OFF**; Pitch I.C. X 2
    b) s2 configuration; **pitch lock OFF**; **motor and clutch OFF**; Pitch I.C. X 2
    c) s1 configuration; **pitch lock OFF**; **motor and clutch OFF**; Pitch I.C. X 2

Stopped testing as sounds indicated violent connecting wire movements. Airspeed dropped to zero RPM; inspections yielded that no wires or pulley loose. No new cracks in wing. Further tests should ensure that wires better supported.

- Ambient Pressure = 1023 mbar
- Ambient Temperature = 20.5°
- V_o = 1.1321V

Table E.5: Test D Airspeeds

RPM	Voltage	Airspeed(m/s)
Sweep 1		
210	1.2088	9.49
210S SPIC	1.2092	N.A.
227	1.2138	N.A.
230	1.2147	N.A.
Sweep 2		
224	1.2116	N.A.
226	1.2116	N.A.
227	1.2126	N.A.
229	1.2134	N.A.
231	1.2164	N.A.
Sweep 3		
227	1.2113	N.A.

E.4.5 Test E

1. Noise Data:
    a) $s4^*$ configuration; **pitch lock OFF**; **wind tunnel OFF**
    b) $s4^*$ configuration; **pitch lock OFF**; **motor ON**
    c) $s4^*$ configuration; **pitch lock OFF**; **motor and clutch ON (zero RPM)**
2. FDT1:
    a) $s4^*$ configuration; **pitch lock OFF**; **motor and clutch ON (zero RPM)**; pitch I.C. X 2
    b) $s4^*$ configuration; **pitch lock ON**; **motor and clutch ON (zero RPM)**; bending I.C. X 2
3. Sweep 1:
    a) $s4^*$ configuration, 209 RPM, SPIC
    b) $s4^*$ configuration, 237 RPM
    c) $s4^*$ configuration, 242 RPM
    d) $s4^*$ configuration, 254 RPM
    e) $s4^*$ configuration, 261 RPM
    f) $s4^*$ configuration, 210 RPM
4. FDT1:
    a) $s4^*$ configuration; **pitch lock OFF**; **motor and clutch ON (zero RPM)**; pitch I.C.
    b) $s4^*$ configuration; **pitch lock ON**; **motor and clutch ON (zero RPM)**; bending I.C.
5. FDT2:
    a) $s4^*$ configuration; **pitch lock OFF**; **motor and clutch OFF**; Pitch I.C. X 2
    b) s2 configuration; **pitch lock OFF**; **motor and clutch OFF**; Pitch I.C. X 2
    c) s1 configuration; **pitch lock OFF**; **motor and clutch OFF**; Pitch I.C. X 2

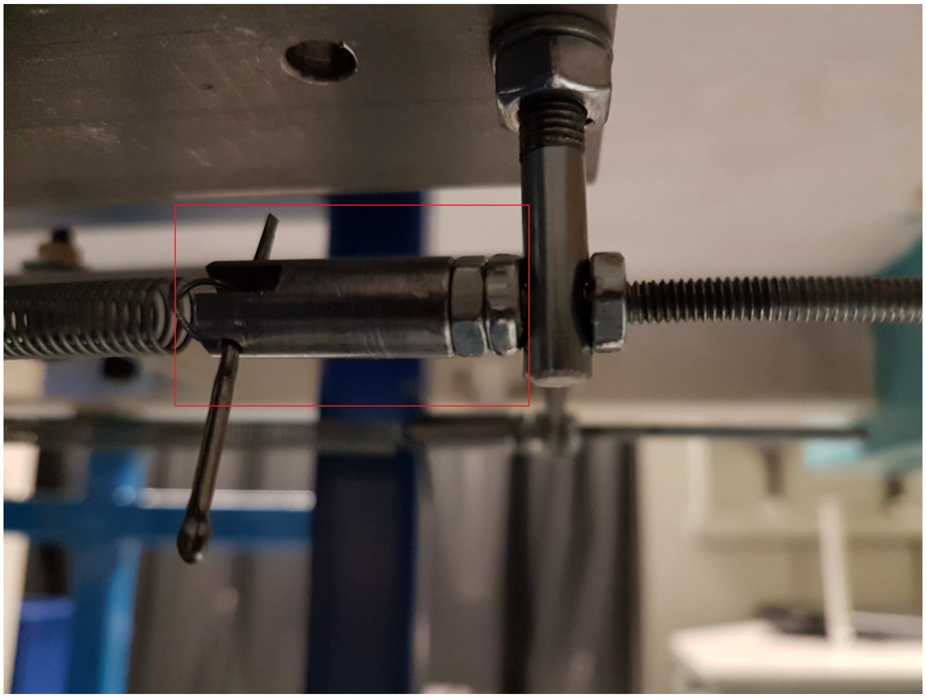

Figure E.4: Spring screw

- Ambient Pressure = 1022.5 mbar
- Ambient Temperature = 20.9°
- V_o = 1.1345V

Table E.6: Test E Airspeeds

RPM	**Voltage**	Airspeed(m/s)
Sweep 1		
209 SPIC	1.2107	9.44
237	1.2214	N.A.
242	1.2260	N.A.
254	1.2362	N.A.
261	1.2426	N.A.
210	1.2099	10.09

E.4.6 Test F

1. Noise Data:
    a) $s4^*$ configuration; **pitch lock OFF**; **wind tunnel OFF**
    b) $s4^*$ configuration; **pitch lock OFF**; **motor ON**
    c) $s4^*$ configuration; **pitch lock OFF**; **motor and clutch ON (zero RPM)**
2. FDT1:
    a) $s4^*$ configuration; **pitch lock OFF**; **motor and clutch ON (zero RPM)**; pitch I.C. X 2
    b) $s4^*$ configuration; **pitch lock ON**; **motor and clutch ON (zero RPM)**; bending I.C. X 2

    Test started at approx. 7:37pm.
3. LAO Boundaries (Sweep 1 Up):
    a) $s4^*$ configuration, 196 RPM
    b) $s4^*$ configuration, 200 RPM
    c) $s4^*$ configuration, 207 RPM
    d) $s4^*$ configuration, 219 RPM
    e) $s4^*$ configuration, 223 RPM
    f) $s4^*$ configuration, 224 RPM (no info recorded)

    Swept down dropped to 167 RPM L.E. bottom tape split. spent approx. 3-4 mins at 224 RPM, added 2nd layer of tape on L.E. and decided to try testing again
4. LAO Boundaries (Sweep 2, Up):
    a) $s4^*$ configuration, 237 PIC RPM
    b) $s4^*$ configuration, 239 RPM
    c) $s4^*$ configuration, 242 RPM

    Swept down Dropped to 199 RPM from 242 RPM, due to second L.E. split and added 3rd layer of tape. .
5. LAO Boundaries (Sweep 3, Up):
    a) $s4^*$ configuration, 242 RPM Pic
    b) $s4^*$ configuration, 247 RPM
    c) $s4^*$ configuration, 253 RPM
    d) $s4^*$ configuration, 257 RPM
    e) $s4^*$ configuration, 262 RPM
    f) $s4^*$ configuration, 267 RPM
    g) $s4^*$ configuration, 270 RPM
    h) $s4^*$ configuration, 275 RPM
    i) $s4^*$ configuration, 286 RPM

    Beam failure! wing motion halted due to failure, excessive loads only on one side. Final P = 1006.5 mbar, temp = 20.9 deg. Bottom of trailing cracked open. Post-Test breakdown reveals that the torsion wire snapped some point early in testing.
6. FDT1:
    a) $s4^*$ configuration; **pitch lock OFF**; **motor and clutch ON (zero RPM)**; pitch I.C.

   b) $s4^*$ configuration; **pitch lock ON**; **motor and clutch ON (zero RPM)**; bending I.C.
7. FDT2:
   a) $s4^*$ configuration; **pitch lock OFF**; **motor and clutch OFF**; Pitch I.C. X 2
   b) s2 configuration; **pitch lock OFF**; **motor and clutch OFF**; Pitch I.C. X 2
   c) s1 configuration; **pitch lock OFF**; **motor and clutch OFF**; Pitch I.C. X 2

- Ambient Pressure = 1006 mbar
- Ambient Temperature = 21.1°
- V_o = 1.0474 V
- Time approx. 6:45pm

Table E.7: Test F Airspeeds

RPM	Voltage	Airspeed (m/s)
Sweep 1	N.A.	
196	1.1084	9.64
200	1.1113	9.84
207	1.1156	10.18
219	1.1245	10.78
223	1.1235	10.97
224	N.A.	N.A.
Sweep 2		
237	1.1.1306	N.A.
226	1.1329	N.A.
227	N.A.	N.A.
Sweep 3		
247	1.1380	12.15
253	1.1439	12.45
257	1.1439	12.64
262	1.1525	12.89
267	1.1565	13.13
270	1.1609	13.28
275	1.1666	13.53
227	N.A.	N.A.

E.4.7 Test G

1. Noise Data:
   a) $s4^*$ configuration; **pitch lock OFF**; **wind tunnel OFF**
   b) $s4^*$ configuration; **pitch lock OFF**; **motor ON**
   c) $s4^*$ configuration; **pitch lock OFF**; **motor and clutch ON (zero RPM)**
2. FDT1:
   a) $s4^*$ configuration; **pitch lock OFF**; **motor and clutch ON (zero RPM)**; pitch I.C. X 2
   b) $s4^*$ configuration; **pitch lock ON**; **motor and clutch ON (zero RPM)**; bending I.C. X 2

   Test started at approx. 7:37pm.
3. Sweep Up:
   a) $s4^*$ configuration, 209 LPIC
   b) $s4^*$ configuration, 219-220 LPIC
   c) $s4^*$ configuration, 225 LPIC
   d) $s4^*$ configuration, 235 (noticed beat frequency i.e. 2 frequencies close together - see Luba's thesis [22] for further details)
   e) $s4^*$ configuration, 249 RPM
   f) $s4^*$ configuration, 256 RPM

   Hitherto, no LCO's visually evident, despite being in LAO region based on previous tests with Normalized AISI O1 steel beam.
4. Continue to Sweep Up:
   a) $s4^*$ configuration, 267 RPM
   b) $s4^*$ configuration, 268 RPM
   c) $s4^*$ configuration, 274-278 RPM; only last test point recorded

   @ 294, LCO's begin after several pitch perturbations.
5. Continue to Sweep Up:
   a) $s4^*$ configuration, 295 RPM

   Drop to catch beginning of SAO/LAO boundary.Dropped to 260 RPM.
6. Sweep Down Second Time:
   a) $s4^*$ configuration, 286 RPM → 283 RPM: no LCO's/SAO's evident

   Sweep upto 294 RPM again.
7. After Sweep Up to 294 RPM:
   a) $s4^*$ configuration, 300-301 RPM: appearance of "clean" LCO's
   b) $s4^*$ configuration, 304 RPM
   c) $s4^*$ configuration, 307-308 RPM → took video of "SAO"
   d) $s4^*$ configuration, 311-312 RPM
   e) $s4^*$ configuration, 320-321 RPM
   f) $s4^*$ configuration, 326/328 RPM
   g) $s4^*$ configuration, 334-335 RPM
   h) $s4^*$ configuration, 341 RPM

   Dropped airspeed to capture LCO with PIC.

8. Sweep down - run of several airspeeds:
    a) *s*4* configuration, 300 RPM w/ PIC
    b) *s*4* configuration, 305 RPM
    c) *s*4* configuration, 310 RPM
    d) *s*4* configuration, 315 RPM
    e) *s*4* configuration, 320 RPM
    f) *s*4* configuration, 325 RPM
    g) *s*4* configuration, 330 RPM
    h) *s*4* configuration, 335 RPM
    i) *s*4* configuration, 339 RPM → apparent LAO boundary

    Increase airspeed again, i.e. sweep up again.
9. Sweep down - run of several airspeeds:
    a) *s*4* configuration, 340 RPM
    b) *s*4* configuration, 348 RPM
    c) *s*4* configuration, 353 RPM
    d) *s*4* configuration, 358 RPM

    Airspeed was dropped and extra tape layer added where the crack was located.Airspeed swept down.
10. Sweep Up after wing repair:
    a) *s*4* configuration, 348 RPM → BENDING S.G¿ APPEARS SATURATED OR DAMAGED
    b) *s*4* configuration, 348 RPM → (R2)

    Are these are LCO's or due to Reynolds number effects.
11. Sweep Up again:
    a) *s*4* configuration, 356 RPM → (R2) BOTH BENDING AND TORSION S.G.'S NOW APPEARS SATURATED OR DAMAGED

    There is an airspeed sweep, run up where some data were recorded spontaneously. Airspeed sweep - RPM's recorded are noted from data text files.
12. Sweep Up, Run
    a) *s*4* configuration, 356 RPM (as in previois item) → (359 RPM) → 369 RPM → (373 RPM) → 378 RPM *APPARENT SAO/LAO BOUNDARY
    b) END OF TESTING

    ** NOTE, Due to both strain gauges being damaged/saturated, standard post-test FDT not performed.
13. FDT1:
    a) *s*4* configuration; **pitch lock OFF**; **motor and clutch ON (zero RPM)**; pitch I.C.
    b) *s*4* configuration; **pitch lock ON**; **motor and clutch ON (zero RPM)**; bending I.C.
14. FDT2:
    a) *s*4* configuration; **pitch lock OFF**; **motor and clutch OFF**; Pitch I.C. X 2
    b) s2 configuration; **pitch lock OFF**; **motor and clutch OFF**; Pitch I.C. X 2
    c) s1 configuration; **pitch lock OFF**; **motor and clutch OFF**; Pitch I.C. X 2

Table E.8: Test G Airspeeds

RPM	Voltage	Airspeed (m/s)
Sweep 1	N.A.	
300	N.A	14.76
304	N.A	14.96
308	N.A	15.15
312	N.A	15.35
315	N.A	15.50
320	NA	15.74
326	NA	16.03
334	NA	16.43
341	NA	16.78
348	NA	17.12
Sweep 2	N.A.	
348	N.A	17.12
353	N.A	17.37
358	N.A	17.61
Sweep 3	N.A.	
348	N.A	17.12
356	N.A	17.52
359	N.A	17.66
373	N.A	18.35
378	N.A	18.60

- Ambient Pressure = 1018 mbar
- Ambient Temperature = 24.7°
- V_o = 1.0252 V
- Time approx. N.A.

* Note that airspeed voltages were recorded using LabView.

E.4.8 Test H

1. Qualitative Observstions only:
    a) $s4^*$ configuration, 270 RPM - possible LCO's or Reynolds number effects

    Swept up to 400 RPM, and then down to 211 RPM; at 211 RPM, wing no longer oscillating.
2. Sweep Up
    a) $s4^*$ configuration, 200 RPM, with and without pitch initial condtion - no LCO's commence
    b) $s4^*$ configuration, 225 RPM - vibrations begin to occur
    c) $s4^*$ configuration, 250 RPM
    d) $s4^*$ configuration, 275 RPM
    e) $s4^*$ configuration, 294 RPM - chosen because of previous data
    f) $s4^*$ configuration, 300 RPM
    g) $s4^*$ configuration, 325 RPM
    h) $s4^*$ configuration, 339 RPM - chosen because of previous data
    i) $s4^*$ configuration, 350 RPM
    j) $s4^*$ configuration, 375 RPM
    k) $s4^*$ configuration, 400 RPM - unusual behavior noted at this airspeed
    l) $s4^*$ configuration, 425 RPM
    m) $s4^*$ configuration, 430 RPM
3. Sweep Down to Capture Unusual Behaviour
    a) $s4^*$ configuration, 415 RPM
    b) $s4^*$ configuration, 410 RPM
    c) $s4^*$ configuration, 405 RPM
    d) $s4^*$ configuration, 400 RPM
4. END OF TESTING
5. FDT1:
    a) $s4^*$ configuration; **pitch lock ON**; **motor and clutch ON (zero RPM)**; bending I.C.
6. FDT2:
    a) $s4^*$ configuration; **pitch lock OFF**; **motor and clutch OFF**; Pitch I.C. X 2
    b) s2 configuration; **pitch lock OFF**; **motor and clutch OFF**; Pitch I.C. X 2
    c) s1 configuration; **pitch lock OFF**; **motor and clutch OFF**; Pitch I.C. X 2

- Ambient Pressure = 1010 mbar
- Ambient Temperature = 22.6°
- V_o = recorded
- Time approx. N.A.

* Note that airspeed voltages were recorded using LabView.

Table E.9: Test H Airspeeds

RPM	Voltage	Airspeed (m/s)
400	N.A	19.68
400	N.A	19.68
400	N.A	19.68
405	N.A	19.93
410	N.A	20.17
415	NA	20.42
425	NA	20.91
430	NA	21.16

F Hysteresis

Delving deeper in to the details of specific tests provides preliminary insight can be found in regards to the SAO/LAO boundary. In Appendix E.4, there is a of this information shows a clear change in the SAO/LAO boundary between tests. For example, Test B (Section E.4.2) had an SAO/LAO boundary which occurred at 240 RPM ($\approx$ 10.6 m/s). However, for Test C, (Section E.4.3) the boundary appeared at around 219/220 RPM ($\approx$ 11.9 m/s). Evidence of differing airspeeds for the same test RPM can also be seen in Table F.1. This table is a compilation of RPM and airspeed data, comprising several tests,and shows for data obtained while sweeping both up and down. This gives a good indication of how much variability there is between tests. In terms of effect on amplitude, Test B shows that during the first sweep up in airspeed, an RPM of 236 translated to an airspeed of 10.587 m/s.The airspeed was dropped, and a second sweep was done, yielding an airspeed of 10.63 m/s. While this small change may appear trivial, consider that a change of $\Delta 0.043$ m/s leads to a increase in LCO amplitude, from $8 - 10^\circ$ to $10 - 13^\circ$.

Table F.1: Difference in Airspeeds

RPM	U(m/s)	$\Delta U_{max}(m/s)$
210	9.47, 9.36	0.10
220	9.72, 9.95	0.22
224	10.10, 9.81, 9.62	0.48
226	9.90, 9.61	0.29
227	9.75, 9.61, 9.60	0.15
230	9.70, 10.44, 10.38, 10.03, 9.80	0.74
231	10.45, 9.90	0.55
234	10.60, 10.55	0.05
235	10.80, 10.63	0.17
236	10.70, 10.68	0.02
238	10.68, 10.75	0.63
262	11.87, 11.21	0.65

G Test H: Zero Pitch Stiffness

Figures G.1 and G.2 illustrate the generally erratic motion observed. However at 400 RPM (Figures G.3 and G.4), we see the motion which appears to be similar to a sine wave, but with large spikes appearing at certain intervals. On a final note, Figure G.5 shows the one possibly good LCO captured during the tests. The resolution for this potentiometer is 0.18 degrees, so it is unlikely that the inconsistent amplitude is due to experimental error.

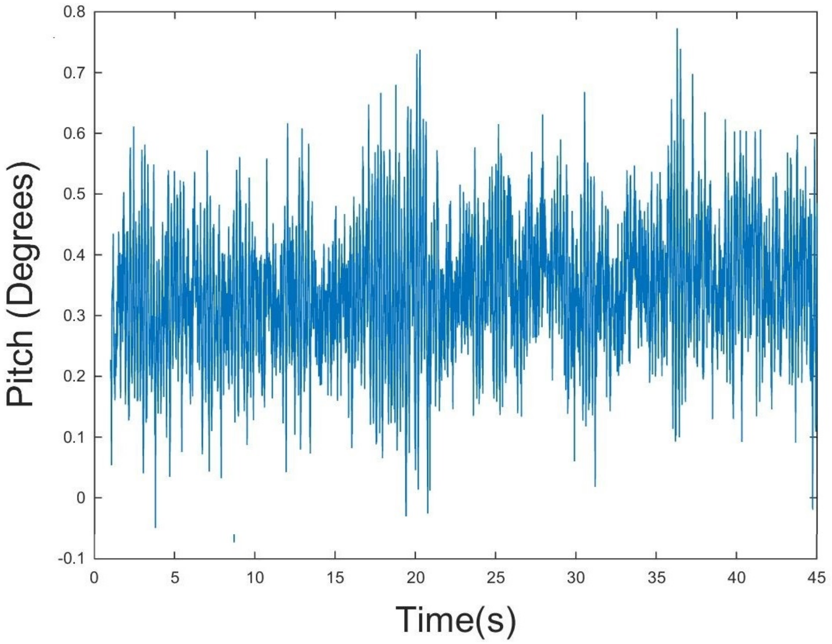

Figure G.1: Representative Pitch Time History for Zero Pitch Stiffness at 9.84 m/s

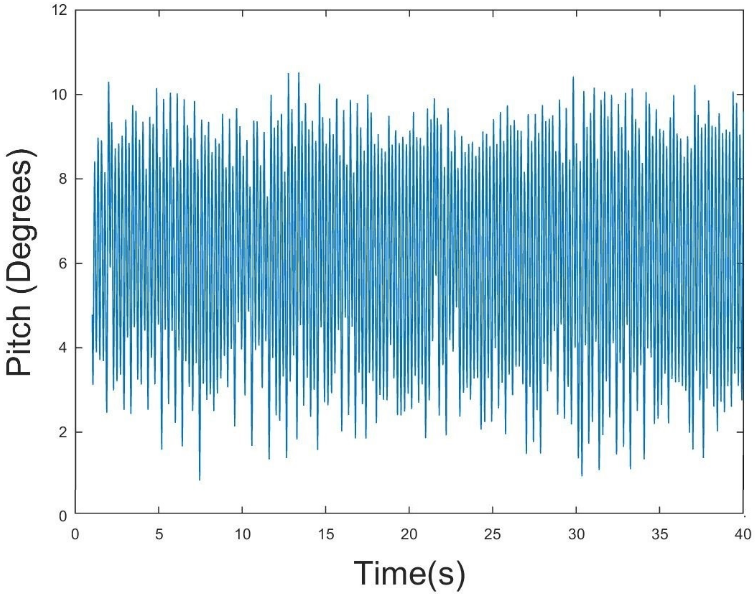

Figure G.2: Example Rigid Pitch Dominated Mode Time History for Zero Pitch Stiffness at 18.45 m/s

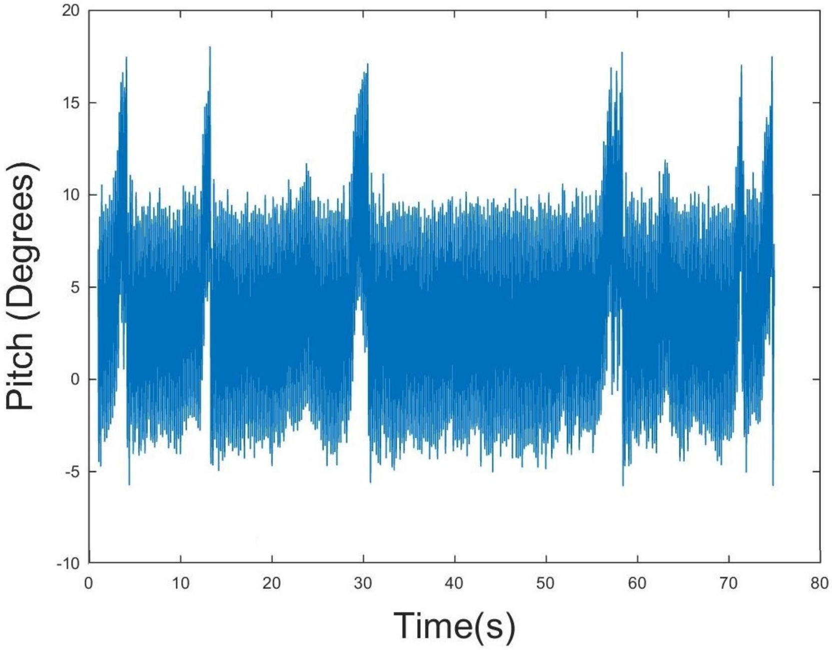

Figure G.3: Representative Pitch Time History for Zero Pitch Stiffness at 19.68 m/s

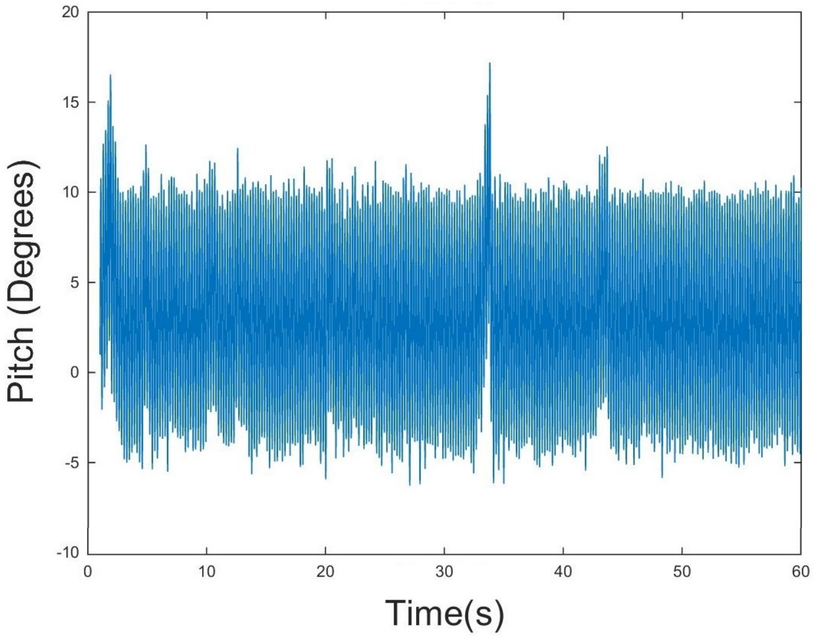

Figure G.4: Example Rigid Pitch Dominated Mode Time History for Zero Pitch Stiffness at 20.42 m/s

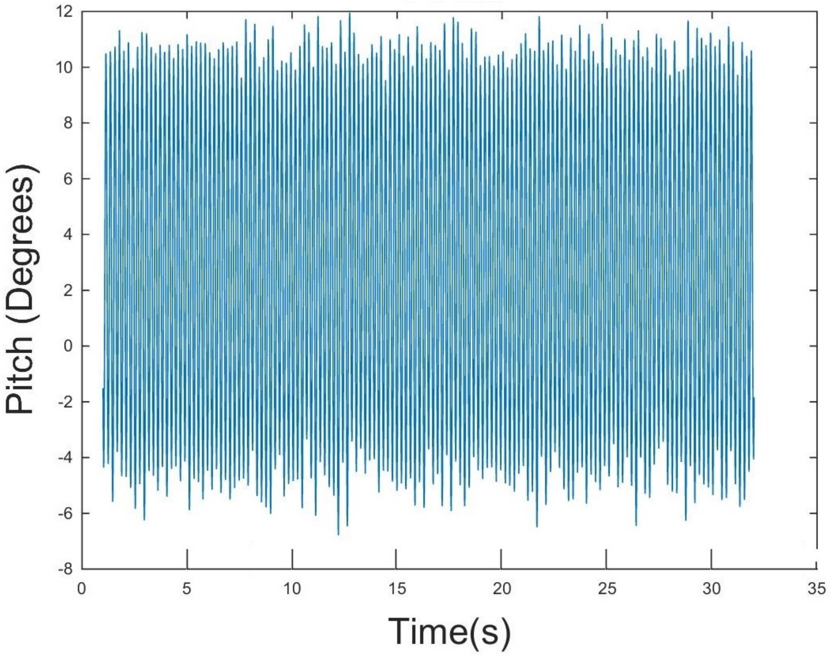

Figure G.5: Representative Pitch Time History for Zero Pitch Stiffness at 21.16 m/s

H Torsion Data Plots

Some example torsion histories are provided for demonstrative purposes in Appendix H. Figure H.1 shows an example of what may be a reasonable time history. A close-up of this, seen in Figure H.2 illustrates the non-sine wave behaviour which has yet to be explained.

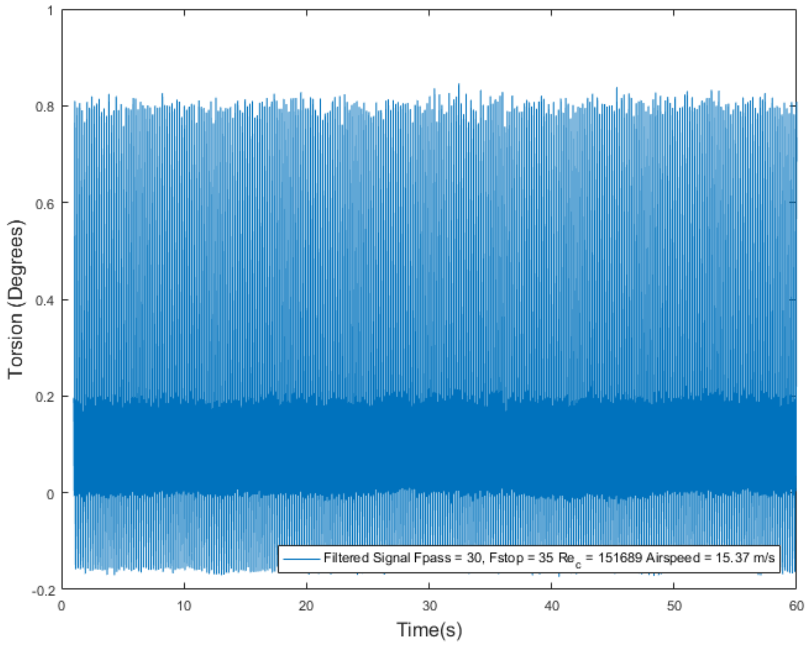

Figure H.1: Representative Torsion Time History 15.37 m/s

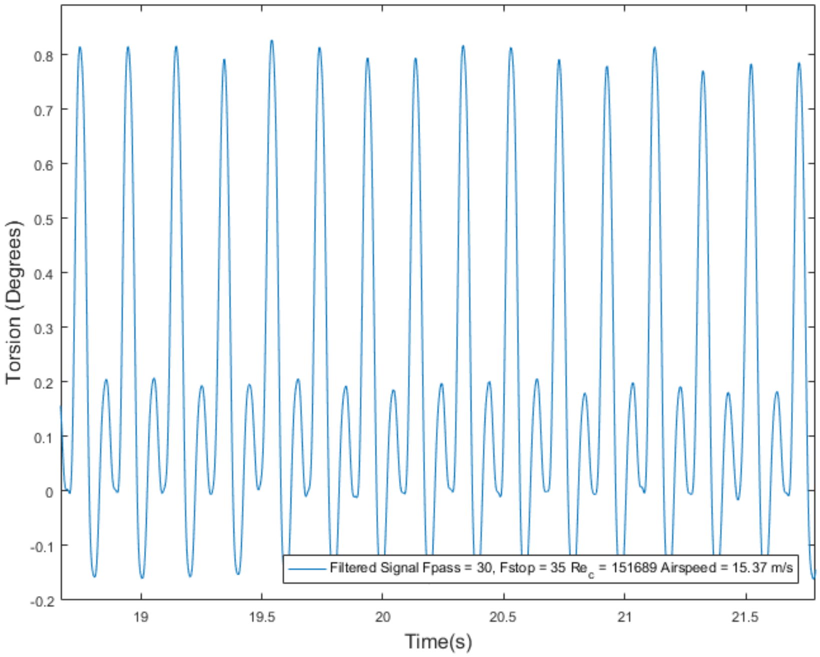

Figure H.2: Representative Torsion Time History 15.37 m/s Close-Up